Pre-Clinical Investigation of Histotripsy for Non-Invasive Ablation of Liver Cancer

by

Tejaswi Umesh Worlikar

A dissertation submitted in partial fulfillment
of the requirements for the degree of
Doctor of Philosophy
(Biomedical Engineering)
in the University of Michigan
2022

Doctoral Committee:

Professor Zhen Xu, Chair
Professor Clifford Cho
Professor J. Brian Fowlkes
Dr. Joan Greve
Research Scientist Timothy Hall
Associate Professor Zhongming Liu
Assistant Professor Man Zhang

Sometimes the smallest things take up the most room in your heart

– A.A. Milne

Tejaswi Worlikar

wtejaswi@umich.edu

ORCID iD: 0000-0001-6828-022X

Dedication

For Science and Humanity

Acknowledgements

In my years as a PhD student, Dr. Zhen Xu has been my staunchest support and the fiercest critic of my research. I have been extremely lucky to have her as my advisor and she has always been just a phone call away whenever I needed anything. She has nurtured my understanding of science and conducting research, motivated me to aim higher and learn from life's disappointments and successes. The most important lesson she taught me was to never give up. I am also grateful for the constant support of my dissertation committee: Drs. Timothy Hall, Clifford Cho, J. Brian Fowlkes, Zhongming Liu, Man Zhang, and Joan Greve. I learnt about histotripsy from Dr. Hall, who is an amazing scientist and researcher. My research work would not have been feasible without the transducers and electronics developed by Dr. Hall. Dr. Cho introduced me to the complex and fascinating world of cancer immunology and our collaboration with his lab has been at the forefront of investigating histotripsy immunomodulation. Dr. Fowlkes taught me about hands-on medical imaging many years ago and has been a valuable resource in learning contrast-enhanced ultrasound for histotripsy applications. Dr. Liu been an irreplaceable resource for MR imaging. Dr. Zhang has taught me small animal ultrasound imaging skills without which this research would not have been possible. I also want to highlight the support I received from Dr. Joan Greve, who not only taught me small animal MR imaging, but also about becoming a better scientist and educator.

I also want to thank all past and present members of the Histotripsy Lab. Dr. Kim Ives taught me about humanely working with research animals. Adam Fox, Dave Choi, and Ashley Cornett have been terrific research specialists. Dr. Tyler Gerhardson got me started in the lab and

I am extremely grateful to him for sharing his knowledge. Dr. Jonathan Sukovich has always inspired me in our conversations, and I admire his work ethic. During my time in the lab, I am also grateful to have interacted with Eli Vlaisavljevich, Jonathan Lundt, Jonathan Macoskey, Yige Li, Hedieh Tamaddoni, Sang Won Choi, Ryan Hubbard, Ning Lu, Greyson Stocker, Ellen Yeats, Scott Haskell, Christina Hendren, Dinank Gupta, Jeremy Deniega, Sarah Duclos, Varsha Kuma, Reliza McGinnis, Mikey Komaiha, Tarana Kaovasia. I owe special thanks to Sang, Ryan, Sarah and Reliza have always been there to help me with my projects whenever I needed an extra hand. I could not have asked for a more fun, collaborative, and intellectually stimulating lab environment.

I am immensely indebted to our collaborators outside of the Histotripsy Lab for accomplishing this research, it has been a team effort. I would like to thank Drs. Theodore Welling and Eli Vlaisavljevich for beginning the work on liver cancer histotripsy. Drs. Shanshan Wan and Sibu Kuruvilla taught me cell culture and developing animal models for research. Dr. Mishal Mendiratta-Lala helped me with histotripsy ablation of orthotopic tumors and provided valuable feedback on my research. I have also been fortunate to work with and learn from Tahra Luther, Mariam Toma, Ashley Pepple, Shibin Qu, Joe Guy, Amy Felsted, Alicia Kevelin, and Hannah Garavaglia during my time collaborating with Dr. Cho's lab. Dr. Anutosh Ganguly has been a tremendous resource in learning about immunostaining and histology techniques and I am grateful to him for sharing his expertise. Dr. Cho's lab has been essential to the immune response investigations presented in this dissertation. Dr Jan Stegemann graciously allowed us to use their cell culture space. Brandan Walters, Nick Schott, and Nicole Friend from the CMITE lab were always available to help. Dr. Ulrich Scheven has helped debug MRI issues on countless occasions and I am thankful for his support. Dr. Jiaqi Shi has shared her expertise on histopathology. Dr. Lily Zhao has helped me with statistical analyses. Dr. Fred Lee has provided valuable feedback on my research projects. Dr. Sunitha Nagrath and Dr. Mina Zeinali have extensively collaborated with our lab to initiate the investigation of circulating tumor cells using their Labyrinth device.

I also want to highlight the role of ULAM (Unit for Laboratory Animal Medicine) and VA Animal Research Program in our research. I received all my animal certifications and surgical training at ULAM. Faculty veterinarians Drs. Lucy Kennedy, Deanna Renner, Helen Noack, have been valuable resources. The contribution of animal care supervisors Scot Pittman, Allen Lindsey, Jacques Corey and Tamara Tanner, animal technicians and truck drivers has been indispensable in making animal research possible.

The past and present staff from Department of Biomedical Engineering: Maria Steele, Kathleen McCrumb, Rebecca Green, Dana Jackson, Chuck Nicholas, Erik Keup and Claire Truskowski deserve a special mention for patiently keeping our department running smoothly.

Finally, I would like to acknowledge the support of my all my friends and family here in US. They have been such an integral part of my journey to the US as an international student and have made me feel at home away from home. I met my best friend and husband Satyum Joshi at University of Michigan. I started my PhD a few months before we got married. I am grateful to Satyum's parents Bharati and Shivdarshan Joshi for welcoming me into their family with much love and affection. Satyum has been my rock as we navigated the ups and downs of married-PhD life together. I am so grateful to have him around. The last two years have been especially difficult with some irreparable, personal losses and we have only grown stronger with each challenge. Although they will never read this, I want to thank my fur-babies Simba and Mowgli for providing me comfort, teaching me to find happiness in the little things and showing me how to live every moment to the fullest. You have filled my heart with so much joy. I am thankful for my loving sister Vidula for always being there for me, I wish we could spend more time together.

Finally, I want to acknowledge my parents, Drs. Pranita and Umesh Worlikar, who always believed in me, taught me the meaning of unconditional love and made many sacrifices to give me the wings to fly.

Table of Contents

List of Tables

List of Figures

Abstract

Liver cancer, including hepatocellular carcinoma (HCC) is one of the top ten causes of cancer related deaths worldwide and in the United States. The liver is also a frequent site for metastases originating from colorectal cancer, pancreatic cancer, melanoma, lung cancer and breast cancer. Depending on the location, severity and staging of liver cancer, multiple treatment options are currently available including surgical resection, liver transplantation, chemotherapy, radiation therapy, targeted drug therapy, immunotherapies, and ablation techniques including radiofrequency ablation (RFA), microwave ablation (MWA), cryoablation, high intensity focused ultrasound (HIFU), yet the prognosis of HCC remains poor with five-year survival rates reported at only 18% in the US. Even after treatment, the high prevalence of tumor recurrence and metastasis highlights the clinical need for improving outcomes of liver cancer.

Histotripsy is a novel non-invasive, non-ionizing, and non-thermal ablation technique that mechanically destroys target tissue by controlled acoustic cavitation. High pressure (focal peak negative pressure P- >30MPa), microsecond-length ultrasound pulses cause endogenous nanometer-scale gas nuclei in the target tissue to rapidly expand and collapse, generating high mechanical stress and strain to disrupt the cellular structure into an acellular homogenate. This dissertation presents histotripsy as a therapeutic ultrasound technology for effective treatment of liver cancer and other solid tumors.

The first study evaluated the safety and feasibility and survival benefits of histotripsy for in vivo tumor ablation. Results showed that non-invasive histotripsy ablation reduced local tumor progression of subcutaneous human-derived HCC tumor and improved survival outcomes

in immunocompromised mice. This study also characterized the radiological features correlating to the histotripsy tumor response.

The second study evaluated the safety, feasibility, and tumor volume reduction effects of histotripsy for liver cancer ablation in an orthotopic, immune-competent in vivo rat HCC model. For the first time, it was demonstrated that complete as well as partial histotripsy ablation of tumors can result in complete tumor regression with no recurrence.

The third study evaluated the effects of partial histotripsy tumor ablation on tumor response, risk of metastases and immune infiltration in an orthotopic, immunocompetent, metastatic rodent hepatocellular carcinoma (HCC) model. Results showed that histotripsy significantly improved survival outcomes with no increased risk of metastasis compared to controls and demonstrated that augmented tumor immune infiltration may have contributed to the eventual regression even with partial treatment of tumors.

The fourth study evaluated the anti-tumor immune response generated by histotripsy ablation of subcutaneous murine melanoma and HCC tumors. Histotripsy stimulated potent local intratumoral infiltration of innate and adaptive immune cell populations, promoted abscopal immune responses at untreated tumor sites and inhibited growth of pulmonary metastases. Histotripsy was capable of releasing tumor antigens with retained immunogenicity and was able to amplify the efficacy of checkpoint inhibition immunotherapy.

The fifth study compared the tumor response and survival outcomes with single and repeat histotripsy treatment in human-derived and mouse HCC murine models. One week after the initial histotripsy treatment, animals received a repeat histotripsy treatment. Results showed that both histotripsy groups significantly improved survival outcomes over control.

Overall, this dissertation demonstrated the potential of histotripsy for successful non-invasive tumor ablation, reduction of local tumor burden and prevention of metastasis. Future studies will continue to investigate the safety, efficacy, and biological effects of histotripsy for potential translation to clinic.

Chapter 1 Introduction

This dissertation is focused on the investigation of pulsed cavitational ultrasound therapy (histotripsy) as a noninvasive ultrasound ablation therapy with primary emphasis on the treatment of liver cancer. This dissertation also contains preliminary investigations into histotripsy mediated immunomodulatory effects in melanoma and liver cancer. Although focused primarily on HCC, the insights, and technical developments can be translated to the treatment of other solid tumors (e.g., pancreatic and breast cancer). The dissertation is presented in five main parts: 1) The in-vivo feasibility and safety concerns for tumor ablation using histotripsy are investigated through subcutaneous mouse tumor model with characterization of long-term radiological observations. 2) The safety, feasibility, and survival outcomes of complete and partial histotripsy ablation in an orthotopic rodent liver tumor model. 3) Investigation of partial histotripsy ablation on the risk of metastasis development in an orthotopic rodent liver tumor model. 4) The first investigation into immune effects induced by histotripsy in subcutaneous HCC and melanoma tumor models. 5) Preliminary evaluation into safety concerns for repeat histotripsy ablation. This chapter will give a brief background of liver cancer and current clinically available treatment options followed by a brief introduction cancer immune therapy and context for the immunomodulation studies contained within this dissertation. This is followed by an overview of histotripsy therapy, the histotripsy system used in this dissertation and the anticipated role of histotripsy in clinical HCC treatments in future. This chapter will then be concluded with an outline of the dissertation, which provides an overview of each chapter.

1.1 Liver Cancer

Liver cancer is one of the top ten causes of cancer related deaths worldwide and in the United States [1]. Hepatocellular carcinoma (HCC) accounts for >75% of all liver cancer cases, most frequently occurring in patients with chronic liver diseases from etiologies such as hepatitis B and C, alcohol abuse, non-alcoholic steatohepatitis (NASH) and non-alcoholic fatty liver disease (NAFLD) resulting in cirrhosis [2]. When diagnosed at intermediate or late stages, HCC may present as multinodular due to synchronic carcinogenesis or early intra-hepatic spread, and has also been observed to invade the portal or hepatic veins [3]. The liver is also a frequent site for metastases originating from colorectal cancer, pancreatic cancer, melanoma, lung cancer and breast cancer [4]. Despite the availability of multiple treatment options, the prognosis of HCC is poor with five-year survival rates reported at only 18% in the US [1]. Symptoms associated with liver cancer may not show at early stages, placing the patients at an increased risk for nodal and distant metastases which further lowers their 5-year survival rate to an estimated 3-11% [5]. Even after treatment, high prevalence of tumor recurrence and metastasis [6] highlights the clinical need for improving outcomes of liver cancer. In fact, metastasis accounts for >90% of all cancer-associated deaths and metastatic progression is predominantly regulated by the complex signaling pathways between the primary tumor and stromal cells, especially the immune cells [7, 8].

1.2 Current Treatment Modalities

Currently, curative treatment options for HCC include surgical resection, liver transplantation or thermal ablation [6, 7, 9]. Surgical resection and liver transplantation are the first-choice treatments, but only a small percentage of patients qualify depending on the severity of underlying liver disease, other medical co-morbidities, or extent of their HCC [8, 10, 11]. The

Barcelona-Clinic-Liver Cancer (BCLC) classification is one of the main clinical algorithms for the stratification of patients according to HCC stages. Local ablation therapy is considered as a conventional treatment option for patients with early stage hepatocellular carcinoma (HCC) according to BCLC [12]. Such options include radiofrequency ablation (RFA), microwave ablation (MWA), cryoablation, and percutaneous ablation and stereotactic body radiotherapy (SBRT) [13, 14]. Patients with intermediate-stage HCC, characterized by multinodular disease but preserved liver function are typically treated with chemoembolization and radioembolization strategies such as TACE (transarterial chemoembolization) and TARE (transarterial radioembolization)[15]. However, each locoregional therapy also has limitations based on tumor location and extent of disease, as well as morbidity based on degree of underlying liver dysfunction secondary to cirrhosis [16-19]. Thermal ablation modalities often suffer from inconsistent heat dissipation due to heat sink effect and achieve inefficient, incomplete tumor necrosis especially in hepatic tumors [20-22]. The heat sink effect refers to ineffectual ablation observed in thermally ablated lesions that are within 1 cm of a blood vessel ≥ 3 mm in diameter because of the cooling effect exerted by the flowing blood which acts to shrink the ablation volume [23]. Thermal ablation methods are also less suitable for ablating larger tumors (>3 cm) due to longer treatment times and potential complications resulting from thermal injuries [24-27]. Since cancer therapies such as radiation, chemotherapy and thermal ablation destroy tumor and surrounding tissues via necrosis, an inflammatory immune response can be triggered which may be either pro-tumor or anti-tumor depending on the tumor microenvironment and the expression of immune mediators and modulators [28-31]. Cryoablation destroys target tumor by causing direct cellular injury and indirect cellular death by arteriovenous injury with extremely low temperatures but has been associated with adverse outcomes such as cryoshock syndrome, liver failure, thrombocytopenia amongst others [32, 33]. Yet, cryoablation has demonstrated anti-cancer immune responses, likely because the intact intracellular contents of cryoablated tumor cells induce an immune-specific reaction [34]. There is ongoing interest in combining various therapies in the adjuvant setting to maximize therapeutic efficacy against HCC.

High intensity focused ultrasound (HIFU) is a non-invasive thermal ablation method guided by real time magnetic resonance imaging (MRI) or ultrasound that has been investigated to treat liver tumors [35], however it has drawbacks related to the heat sink effect, ablating through rib obstruction, respiratory motion, and long procedure times [36]. Additional complications such as unintentional tissue damage due to overheating of ribs and surrounding tissue, skin burns, and subcostal edema have been reported with HIFU [37, 38]. There is pre-clinical and clinical evidence to suggest that HIFU could elicit a systemic anti-tumor immune response[39].

Finally, there are palliative therapies available for late-stage HCC patients such as sorafenib, lenvatinib, and regorafenib [12, 40, 41]. Even with multiple treatment options available, up to 70% patients experience recurrence at 5 years [6] and require repeat treatment such as repeat resection, thermal ablation, or transplantation. Thus, there is an unmet clinical need for an effective locoregional liver tumor therapy to achieve local tumor control and improve survival outcomes while preventing thermal-related collateral damage and inefficacy.

1.3 Cancer Immunotherapy in HCC

Cancer progression and metastases is affected by the immune system. There is increasing evidence that ablative therapies can either positively or negatively impact tumor progression and metastasis by regulating both adaptive and innate immunity [42-45]. For effective anti-tumor immune surveillance, the innate and adaptive immune systems need to work together otherwise immune evasion can occur due to impaired antigen recognition or immunosuppressive tumor microenvironment [46, 47]. To prevent an over-response, the immune system also employs several immune checkpoints, which act to inhibit effector lymphocytes, however, this physiological mechanism is often exploited by tumors to evade immune responses [48]. A few examples of inhibitory receptors that block immune responses include cytotoxic T lymphocyte-associated antigen 4 (CTLA4), PD1, T cell immunoglobulin and mucin domain containing-3 (TIM3), and lymphocyte-activation gene 3 (LAG3)[49]. To overcome these blocks, antibodies targeting these inhibitory receptors and ligands (PD-L1) expressed on T lymphocytes, antigen presenting cells and tumor cells are used as immune checkpoint inhibitors [50, 51]. Immune checkpoint inhibitors, such as ipilimumab (anti-CTLA-4), nivolumab (anti-PD-1) and pembrolizumab (anti-PD-1) are currently used for HCC treatment [52, 53]. Cancer immunotherapy also encompasses other treatments such as targeted antibodies, cancer vaccines, adoptive cell transfer, tumor-infecting viruses, and cytokines to stimulate the patient's immune system to recognize and eliminate tumor cells [54]. Since tumors express varying levels of immunogenicity, ICI treatment is more likely to be effective when there either is pre-existing anti-tumor immunity or T cell infiltration in the tumor microenvironment [55]. In HCC, the tumor microenvironment is complex, with the presence of hepatic non-parenchymal resident cells, tumor cells, immune cells, and tumor-associated fibroblasts [53]. Various studies have demonstrated that both innate and adaptive immune responses in patients with HCC are diminished due to various factors such as expression of inhibitory receptors, MDSC-mediated immune suppression, dysfunctional NK cells, and exhausted or dysfunctional tumor-infiltrating lymphocytes[56-60]. The presence of multiple immunosuppressive aspects in the HCC tumor microenvironment further highlights the need for combinatorial therapies, such as immunotherapeutic and locoregional therapeutic modalities.

1.4 Histotripsy Overview

Histotripsy is the first non-invasive, non-ionizing, non-thermal ablation method that ablates tissue through precise control of acoustic cavitation [61-63]. Microsecond-length, high-amplitude ultrasound pulses (<2 cycles) generate cavitation bubbles from endogenous gas pockets in the target tissue [61, 63, 64]. Depending on the pulsing parameters, the nanometer gas pockets can expand to ~100 µm cavitation microbubbles and collapse within a few hundred microseconds. The rapid expansion and collapse of the cavitation microbubbles creates high strains to destroy cellular structure in the target region and form a liquid acellular homogenate [63, 65]. To enable the initiation of inertial cavitation, the generated focal peak negative pressure must exceed the intrinsic threshold of the soft-tissue target (typically >26MPa); this is the mechanism of intrinsic threshold histotripsy. Histotripsy was invented and pioneered by the Histotripsy Group at University of Michigan as an extremely precise, controlled, and predictable ultrasonic ablation technique to destroy targeted tissue.

The low duty cycle of the ultrasound pulses (on-time/ (on- + off- time) < 0.1%) prevents undesirable thermal effects and allows sufficient cooling. Thus, histotripsy is not impeded by the heat sink effect and may safely achieve homogeneous cell disruption even in vascular organs such as liver [66]. Large vessels possess higher mechanical strength [67, 68] and resistance to fractionation compared to surrounding soft tissue, and thus remain intact during histotripsy ablation [69, 70]. Ultrasound is used to guide and monitor histotripsy in real-time since cavitation is easily detectable on ultrasound imaging [71]. However, histotripsy ablation can be visualized on both ultrasound and MRI [72-74]. There is an alternative approach to mechanical histotripsy, termed as boiling histotripsy (BH), which uses milliseconds-long HIFU pulses with shock waves to generate boiling bubbles; the interaction of shock fronts with the bubbles cause cellular destruction at the focus [75]. Previous *in vivo* studies using boiling histotripsy have demonstrated local and systemic immune responses [76, 77]. The rest of this dissertation refers to and discusses intrinsic-threshold histotripsy as histotripsy.

Previous in vivo studies have shown that histotripsy can completely destroy normal liver tissue in porcine and rodent models, resulting in a liquefied acellular homogenate [71, 78-80] which is completely absorbed by the body within a month. Based on these results, we hypothesize that histotripsy can destroy the target tumor tissue to form acellular homogenate, which is resorbed over time, resulting in effective control of local tumor progression and improvement in survival outcomes.

1.5 Histotripsy in Current Treatment Landscape

Histotripsy is a promising option that can overcome the limitations of currently available ablation modalities and provide safe and effective non-invasive liver tumor ablation. Additionally, since histotripsy can mechanically ablate cells without denaturing them, we hypothesize that histotripsy may also be capable of releasing tumor antigens which can be recognized by the immune system to stimulate strong anti-tumor response as a robust adjuvant to cancer immunotherapy. Histotripsy may also be useful as a downstaging treatment modality either alone or in combination with other therapies in HCC patients, enabling them to meet the criteria for curative HCC options such as resection and transplantation.

1.6 Histotripsy System used in this Dissertation

Our rodent histotripsy setup consists of a custom-built 1 MHz therapy transducer mounted to a motorized 3-axis positioning system. The ring configuration therapy transducer (f number = 0.6, focal distance = 32.5mm) contains 8 individually focused lead zirconate titanate elements (20 mm diameter). The histotripsy transducer is driven by a custom-built high-voltage pulser controlled by a field-programmable gate array (FPGA) development board (DE0-Nano Terasic Technology, HsinChu, Taiwan), enabling the therapy transducer to generate and output 1-2 cycle histotripsy pulses. The value of peak negative pressure in the tissue is estimated based on pressure measurements from fiber optic hydrophone in free field. In the free-field medium (degassed water), the pressure measurements from individual transducer elements were summed to calculate the peak negative pressure of 37.8MPa and the peak positive pressure of 43.9 MPa. The spatial peak temporal peak intensity (I_{SPTP}) was estimated to be ~130kW/cm^2, spatial peak pulse average intensity (I_{SPPA}) is estimated to be ~24kW/cm^2 and spatial peak temporal average (I_{SPTA}) is estimated to be ~8W/cm^2. The single focal ablation volume is typically an elliptical shape of 1-2 mm in width and 3-4 mm in the length, depending on the parameters. The single focal volume can be repositioned within the tumor to form a user-defined larger ablation zone with desired volume and shape.

1.7 Outline of This Dissertation

This dissertation is comprised of seven chapters that document the details of the work done on the investigation and development of histotripsy therapy for the pre-clinical treatment of liver tumors.

1.7.1 Chapter 2

This chapter investigates the feasibility of using histotripsy for non-invasive subcutaneous tumor ablation. As histotripsy is a relatively novel ablation technique, there were no pre-clinical studies addressing the long-term safety and biological effects of histotripsy and providing detailed radiological characterization of histotripsy-induced tumor response. This is the first study to demonstrate that non-invasive histotripsy ablation reduced local tumor progression of human-derived HCC tumor and significantly prolonged survival time compared to untreated controls in immunocompromised mice. This study also reports the MR imaging features correlating to the histotripsy tumor response immediately following ablation up to a 3-month post-treatment follow-up period. To allow MR and histology characterization of differences between ablated and unablated tumor, both partial ablation (50% tumor volume targeting) and complete ablation (100% tumor volume targeting) were used in this study.

1.7.2 Chapter 3

This chapter presents the first study to evaluate the safety, feasibility, and tumor volume reduction effects of histotripsy for liver cancer ablation in an orthotopic, immune-competent in vivo rat HCC model. Tumors were targeted entirely (100%) or partially (50-75% tumor volume). The choice of ablation volumes (viable residual tumor intentionally left untargeted versus tumor completely ablated with additional margin of healthy liver tissue) was selected to observe the differences in treatment response and survival outcomes. MRI revealed effective post-histotripsy reduction of tumor burden with near-complete resorption of the ablated tumor in 93.3% animals in both partial and complete treatment groups. Gross morphology showed shrunken, non-tumoral, fibrous tissue at original site. There was no evidence of histotripsy-induced adjacent tissue injury.

1.7.3 Chapter 4

Histotripsy mechanically disrupts the targeted tumor cells, yet there is insufficient evidence regarding the effects of histotripsy on the risk of recurrence and metastases following tumor debulking. This chapter evaluates the effect of different partial histotripsy tumor ablation volumes (<25% tumor volume targeted, or ~50-75% tumor volume targeted) on tumor response, risk of metastases and immune infiltration in an orthotopic, immunocompetent, metastatic rodent hepatocellular carcinoma (HCC) model. The choice of partial ablation (50-75% tumor volume targeted) was repeated from Chapter 3 to observe if similar outcomes can be achieved in a highly metastatic tumor model and to determine if a minimal tumor volume percentage ablation (<25% tumor volume targeted) can achieve meaningful treatment response. Even with partial ablation (50-75% tumor volume targeted), complete local tumor regression was observed in 81% treatment rats with no recurrence or metastasis. In contrast, 100% untreated control animals showed local tumor progression and intrahepatic metastases. Histotripsy-treated animals had statistically significant improved survival outcomes compared to controls (p-value < 0.0001). Histotripsy-treated animals had increased immune infiltration as compared to controls which may have contributed to the eventual regression of the untargeted tumor region in partial histotripsy-treated tumors. When <25% tumor volume was targeted for ablation, immune infiltration was minimal and there were no tumor reduction benefits observed.

1.7.4 Chapter 5

This chapter evaluates in-depth the immune response generated by histotripsy ablation of subcutaneous murine melanoma and hepatocellular carcinoma tumors. Partial histotripsy ablation (~80% tumor volume targeted) of subcutaneous murine melanoma tumors stimulated potent local intratumoral infiltration of innate and adaptive immune cell populations. The selection of partial ablation was done to allow evaluation of immune infiltration within the residual viable tumor. Histotripsy promoted abscopal immune responses at distant non-targeted tumor sites and inhibited growth of pulmonary metastases. Histotripsy ablation released tumor antigens with retained immunogenicity, and this immunostimulatory effect was associated with danger associated molecular patterns such as calreticulin translocation to the cellular membrane and local and systemic release of high mobility group box protein 1. Histotripsy also enhanced the efficacy of checkpoint inhibition immunotherapy.

1.7.5 Chapter 6

This chapter presents a preliminary evaluation of the safety and efficacy of repeat histotripsy tumor ablation on tumor response and survival outcomes in an *in vivo* human hepatocellular carcinoma (HCC) xenograft model and a mouse-derived HCC model. A repeat histotripsy ablation session controlled local tumor growth compared to animals receiving a single dose of histotripsy and control animals receiving no interventions. Survival outcomes were significantly improved in both histotripsy treatment groups as compared to controls.

1.7.6 Chapter 7

This chapter summarizes the information presented in this dissertation and discusses the future work towards clinical translation of histotripsy therapy for liver cancer ablation. The unique non-invasive, non-ionizing and non-thermal features of histotripsy make it a promising alternative to the current locoregional ablation modalities.

1.8 References

1. R. L. Siegel, K. D. Miller, H. E. Fuchs, and A. Jemal, "Cancer Statistics, 2021," (in eng), CA Cancer J Clin, vol. 71, no. 1, pp. 7-33, 01 2021, doi: 10.3322/caac.21654.

2. D. Anwanwan, S. K. Singh, S. Singh, V. Saikam, and R. Singh, "Challenges in liver cancer and possible treatment approaches," (in eng), Biochim Biophys Acta Rev Cancer, vol. 1873, no. 1, p. 188314, 01 2020, doi: 10.1016/j.bbcan.2019.188314.

3. J. M. Llovet et al., "Hepatocellular carcinoma," (in eng), Nat Rev Dis Primers, vol. 2, p. 16018, 04 14 2016, doi: 10.1038/nrdp.2016.18.

4. J. de Ridder, J. H. de Wilt, F. Simmer, L. Overbeek, V. Lemmens, and I. Nagtegaal, "Incidence and origin of histologically confirmed liver metastases: an explorative case-study of 23,154 patients," (in eng), Oncotarget, vol. 7, no. 34, pp. 55368-55376, 08 23 2016, doi: 10.18632/oncotarget.10552.

5. American Cancer Society, "Cancer Facts & Figures 2021," 2021.

6. R. Inchingolo, A. Posa, M. Mariappan, and S. Spiliopoulos, "Locoregional treatments for hepatocellular carcinoma: Current evidence and future directions," (in eng), World J Gastroenterol, vol. 25, no. 32, pp. 4614-4628, Aug 2019, doi: 10.3748/wjg.v25.i32.4614.

7. Y. K. Cho, H. Rhim, and S. Noh, "Radiofrequency ablation versus surgical resection as primary treatment of hepatocellular carcinoma meeting the Milan criteria: a systematic review," (in eng), J Gastroenterol Hepatol, vol. 26, no. 9, pp. 1354-60, Sep 2011, doi: 10.1111/j.1440-1746.2011.06812.x.

8. R. Small, N. Lubezky, and M. Ben-Haim, "Current controversies in the surgical management of colorectal cancer metastases to the liver," (in eng), Isr Med Assoc J, vol. 9, no. 10, pp. 742-7, Oct 2007.

9. J. D. Yang, P. Hainaut, G. J. Gores, A. Amadou, A. Plymoth, and L. R. Roberts, "A global view of hepatocellular carcinoma: trends, risk, prevention and management," (in eng), Nat Rev Gastroenterol Hepatol, Aug 2019, doi: 10.1038/s41575-019-0186-y.

10. C. L. Tinkle and D. Haas-Kogan, "Hepatocellular carcinoma: natural history, current management, and emerging tools," (in eng), Biologics, vol. 6, pp. 207-19, 2012, doi: 10.2147/BTT.S23907.

11. V. Mazzaferro et al., "Liver transplantation for the treatment of small hepatocellular carcinomas in patients with cirrhosis," (in eng), N Engl J Med, vol. 334, no. 11, pp. 693-9, Mar 1996, doi: 10.1056/NEJM199603143341104.

12. A. Forner, J. M. Llovet, and J. Bruix, "Hepatocellular carcinoma," (in eng), Lancet, vol. 379, no. 9822, pp. 1245-55, Mar 31 2012, doi: 10.1016/S0140-6736(11)61347-0.

13. T. Ruers and R. P. Bleichrodt, "Treatment of liver metastases, an update on the possibilities and results," (in eng), Eur J Cancer, vol. 38, no. 7, pp. 1023-33, May 2002, doi: 10.1016/s0959-8049(02)00059-x.

14. S. M. Sawrie, J. B. Fiveash, and J. J. Caudell, "Stereotactic body radiation therapy for liver metastases and primary hepatocellular carcinoma: normal tissue tolerances and toxicity," (in eng), Cancer Control, vol. 17, no. 2, pp. 111-9, Apr 2010, doi: 10.1177/107327481001700206.

15. J. M. Llovet and J. Bruix, "Systematic review of randomized trials for unresectable hepatocellular carcinoma: Chemoembolization improves survival," (in eng), Hepatology, vol. 37, no. 2, pp. 429-42, Feb 2003, doi: 10.1053/jhep.2003.50047.

16. T. Livraghi, H. Mäkisalo, and P. D. Line, "Treatment options in hepatocellular carcinoma today," (in eng), Scand J Surg, vol. 100, no. 1, pp. 22-9, 2011, doi: 10.1177/145749691110000105.

17. L. Rossi et al., "Current approach in the treatment of hepatocellular carcinoma," (in eng), World J Gastrointest Oncol, vol. 2, no. 9, pp. 348-59, Sep 2010, doi: 10.4251/wjgo.v2.i9.348.

18. J. Balogh et al., "Hepatocellular carcinoma: a review," (in eng), J Hepatocell Carcinoma, vol. 3, pp. 41-53, 2016, doi: 10.2147/JHC.S61146.

19. T. Livraghi, L. Solbiati, M. F. Meloni, G. S. Gazelle, E. F. Halpern, and S. N. Goldberg, "Treatment of focal liver tumors with percutaneous radio-frequency ablation: complications encountered in a multicenter study," (in eng), Radiology, vol. 226, no. 2, pp. 441-51, Feb 2003.

20. A. J. Aschoff et al., "How does alteration of hepatic blood flow affect liver perfusion and radiofrequency-induced thermal lesion size in rabbit liver?," (in eng), J Magn Reson Imaging, vol. 13, no. 1, pp. 57-63, Jan 2001, doi: 10.1002/1522-2586(200101)13:1<57::aid-jmri1009>3.0.co;2-n.

21. M. Kudo, "Radiofrequency ablation for hepatocellular carcinoma: updated review in 2010," (in eng), Oncology, vol. 78 Suppl 1, pp. 113-24, Jul 2010, doi: 10.1159/000315239.

22. S. Mulier, Y. Ni, J. Jamart, T. Ruers, G. Marchal, and L. Michel, "Local recurrence after hepatic radiofrequency coagulation: multivariate meta-analysis and review of contributing factors," (in eng), Ann Surg, vol. 242, no. 2, pp. 158-71, Aug 2005, doi: 10.1097/01.sla.0000171032.99149.fe.

23. K. Pillai et al., "Heat sink effect on tumor ablation characteristics as observed in monopolar radiofrequency, bipolar radiofrequency, and microwave, using ex vivo calf liver model," (in eng), Medicine (Baltimore), vol. 94, no. 9, p. e580, Mar 2015, doi: 10.1097/MD.0000000000000580.

24. S. A. Curley, "Radiofrequency ablation of malignant liver tumors," (in eng), Oncologist, vol. 6, no. 1, pp. 14-23, 2001.

25. D. S. Lu et al., "Influence of large peritumoral vessels on outcome of radiofrequency ablation of liver tumors," (in eng), J Vasc Interv Radiol, vol. 14, no. 10, pp. 1267-74, Oct 2003, doi: 10.1097/01.rvi.0000092666.72261.6b.

26. J. A. Marrero and S. Pelletier, "Hepatocellular carcinoma," (in eng), Clin Liver Dis, vol. 10, no. 2, pp. 339-51, ix, May 2006, doi: 10.1016/j.cld.2006.05.012.

27. E. Lahat et al., "Complications after percutaneous ablation of liver tumors: a systematic review," (in eng), Hepatobiliary Surg Nutr, vol. 3, no. 5, pp. 317-23, Oct 2014, doi: 10.3978/j.issn.2304-3881.2014.09.07.

28. S. I. Grivennikov, F. R. Greten, and M. Karin, "Immunity, inflammation, and cancer," (in eng), Cell, vol. 140, no. 6, pp. 883-99, Mar 19 2010, doi: 10.1016/j.cell.2010.01.025.

29. J. Vakkila and M. T. Lotze, "Inflammation and necrosis promote tumour growth," (in eng), Nat Rev Immunol, vol. 4, no. 8, pp. 641-8, 08 2004, doi: 10.1038/nri1415.

30. M. J. Smyth, G. P. Dunn, and R. D. Schreiber, "Cancer immunosurveillance and immunoediting: the roles of immunity in suppressing tumor development and shaping tumor immunogenicity," (in eng), Adv Immunol, vol. 90, pp. 1-50, 2006, doi: 10.1016/S0065-2776(06)90001-7.

31. W. W. Lin and M. Karin, "A cytokine-mediated link between innate immunity, inflammation, and cancer," (in eng), J Clin Invest, vol. 117, no. 5, pp. 1175-83, May 2007, doi: 10.1172/JCI31537.

32. K. D. Song, "Percutaneous cryoablation for hepatocellular carcinoma," (in eng), Clin Mol Hepatol, vol. 22, no. 4, pp. 509-515, Dec 2016, doi: 10.3350/cmh.2016.0079.

33. L. Z. Niu, J. L. Li, and K. C. Xu, "Percutaneous Cryoablation for Liver Cancer," (in eng), J Clin Transl Hepatol, vol. 2, no. 3, pp. 182-8, Sep 2014, doi: 10.14218/JCTH.2014.00017.

34. B. M. Aarts et al., "Cryoablation and immunotherapy: an overview of evidence on its synergy," (in eng), Insights Imaging, vol. 10, no. 1, p. 53, May 20 2019, doi: 10.1186/s13244-019-0727-5.

35. H. Fukuda et al., "Treatment of small hepatocellular carcinomas with US-guided high-intensity focused ultrasound," (in eng), Ultrasound Med Biol, vol. 37, no. 8, pp. 1222-9, Aug 2011, doi: 10.1016/j.ultrasmedbio.2011.04.020.

36. S. Bobkova, L. Gavrilov, V. Khokhlova, A. Shaw, and J. Hand, "Focusing of high-intensity ultrasound through the rib cage using a therapeutic random phased array," (in eng), Ultrasound Med Biol, vol. 36, no. 6, pp. 888-906, Jun 2010, doi: 10.1016/j.ultrasmedbio.2010.03.007.

37. S. E. Jung, S. H. Cho, J. H. Jang, and J. Y. Han, "High-intensity focused ultrasound ablation in hepatic and pancreatic cancer: complications," (in eng), Abdom Imaging, vol. 36, no. 2, pp. 185-95, Apr 2011, doi: 10.1007/s00261-010-9628-2.

38. F. Wu et al., "Extracorporeal high intensity focused ultrasound ablation in the treatment of 1038 patients with solid carcinomas in China: an overview," (in eng), Ultrason Sonochem, vol. 11, no. 3-4, pp. 149-54, May 2004, doi: 10.1016/j.ultsonch.2004.01.011.

39. F. Wu, L. Zhou, and W. R. Chen, "Host antitumour immune responses to HIFU ablation," (in eng), Int J Hyperthermia, vol. 23, no. 2, pp. 165-71, Mar 2007, doi: 10.1080/02656730701206638.

40. J. M. Llovet et al., "Sorafenib in advanced hepatocellular carcinoma," (in eng), N Engl J Med, vol. 359, no. 4, pp. 378-90, Jul 24 2008, doi: 10.1056/NEJMoa0708857.

41. J. Bruix et al., "Efficacy and safety of sorafenib in patients with advanced hepatocellular carcinoma: subanalyses of a phase III trial," (in eng), J Hepatol, vol. 57, no. 4, pp. 821-9, Oct 2012, doi: 10.1016/j.jhep.2012.06.014.

42. H. Takaki, F. Cornelis, Y. Kako, K. Kobayashi, N. Kamikonya, and K. Yamakado, "Thermal ablation and immunomodulation: From preclinical experiments to clinical trials," (in eng), Diagn Interv Imaging, vol. 98, no. 9, pp. 651-659, Sep 2017, doi: 10.1016/j.diii.2017.04.008.

43. R. Slovak, J. M. Ludwig, S. N. Gettinger, R. S. Herbst, and H. S. Kim, "Immuno-thermal ablations - boosting the anticancer immune response," (in eng), J Immunother Cancer, vol. 5, no. 1, p. 78, 10 17 2017, doi: 10.1186/s40425-017-0284-8.

44. L. Qian, Y. Shen, J. Xie, and Z. Meng, "Immunomodulatory effects of ablation therapy on tumors: Potentials for combination with immunotherapy," (in eng), Biochim Biophys Acta Rev Cancer, vol. 1874, no. 1, p. 188385, 08 2020, doi: 10.1016/j.bbcan.2020.188385.

45. S. P. Haen, P. L. Pereira, H. R. Salih, H. G. Rammensee, and C. Gouttefangeas, "More than just tumor destruction: immunomodulation by thermal ablation of cancer," (in eng), Clin Dev Immunol, vol. 2011, p. 160250, 2011, doi: 10.1155/2011/160250.

46. R. D. Schreiber, L. J. Old, and M. J. Smyth, "Cancer immunoediting: integrating immunity's roles in cancer suppression and promotion," (in eng), Science, vol. 331, no. 6024, pp. 1565-70, Mar 25 2011, doi: 10.1126/science.1203486.

47. G. A. Rabinovich, D. Gabrilovich, and E. M. Sotomayor, "Immunosuppressive strategies that are mediated by tumor cells," (in eng), Annu Rev Immunol, vol. 25, pp. 267-96, 2007, doi: 10.1146/annurev.immunol.25.022106.141609.

48. L. Chen and D. B. Flies, "Molecular mechanisms of T cell co-stimulation and co-inhibition," (in eng), Nat Rev Immunol, vol. 13, no. 4, pp. 227-42, Apr 2013, doi: 10.1038/nri3405.

49. X. He and C. Xu, "Immune checkpoint signaling and cancer immunotherapy," (in eng), Cell Res, vol. 30, no. 8, pp. 660-669, 08 2020, doi: 10.1038/s41422-020-0343-4.

50. R. E. Royal et al., "Phase 2 trial of single agent Ipilimumab (anti-CTLA-4) for locally advanced or metastatic pancreatic adenocarcinoma," (in eng), J Immunother, vol. 33, no. 8, pp. 828-33, Oct 2010, doi: 10.1097/CJI.0b013e3181eec14c.

51. B. Lee et al., "Emerging biomarkers for immunomodulatory cancer treatment of upper gastrointestinal, pancreatic and hepatic cancers," (in eng), Semin Cancer Biol, vol. 52, no. Pt 2, pp. 241-252, 10 2018, doi: 10.1016/j.semcancer.2017.12.009.

52. B. Sangro et al., "A clinical trial of CTLA-4 blockade with tremelimumab in patients with hepatocellular carcinoma and chronic hepatitis C," (in eng), J Hepatol, vol. 59, no. 1, pp. 81-8, Jul 2013, doi: 10.1016/j.jhep.2013.02.022.

53. B. Sangro, P. Sarobe, S. Hervás-Stubbs, and I. Melero, "Advances in immunotherapy for hepatocellular carcinoma," (in eng), Nat Rev Gastroenterol Hepatol, vol. 18, no. 8, pp. 525-543, 08 2021, doi: 10.1038/s41575-021-00438-0.

54. Y. Yang, "Cancer immunotherapy: harnessing the immune system to battle cancer," (in eng), J Clin Invest, vol. 125, no. 9, pp. 3335-7, Sep 2015, doi: 10.1172/JCI83871.

55. J. B. Jacob, M. K. Jacob, and P. Parajuli, "Review of immune checkpoint inhibitors in immuno-oncology," (in eng), Adv Pharmacol, vol. 91, pp. 111-139, 2021, doi: 10.1016/bs.apha.2021.01.002.

56. E. Cariani et al., "HLA and killer immunoglobulin-like receptor genes as outcome predictors of hepatitis C virus-related hepatocellular carcinoma," (in eng), Clin Cancer Res, vol. 19, no. 19, pp. 5465-73, Oct 01 2013, doi: 10.1158/1078-0432.CCR-13-0986.

57. E. Cariani et al., "Natural killer cells phenotypic characterization as an outcome predictor of HCV-linked HCC after curative treatments," (in eng), Oncoimmunology, vol. 5, no. 8, p. e1154249, Aug 2016, doi: 10.1080/2162402X.2016.1154249.

58. B. Hoechst et al., "Myeloid derived suppressor cells inhibit natural killer cells in patients with hepatocellular carcinoma via the NKp30 receptor," (in eng), Hepatology, vol. 50, no. 3, pp. 799-807, Sep 2009, doi: 10.1002/hep.23054.

59. Q. F. Zhang et al., "Liver-infiltrating CD11b," (in eng), Cell Mol Immunol, vol. 14, no. 10, pp. 819-829, Oct 2017, doi: 10.1038/cmi.2016.28.

60. T. Flecken et al., "Immunodominance and functional alterations of tumor-associated antigen-specific CD8+ T-cell responses in hepatocellular carcinoma," (in eng), Hepatology, vol. 59, no. 4, pp. 1415-26, Apr 2014, doi: 10.1002/hep.26731.

61. J. E. Parsons, C. A. Cain, G. D. Abrams, and J. B. Fowlkes, "Pulsed cavitational ultrasound therapy for controlled tissue homogenization," (in eng), Ultrasound Med Biol, vol. 32, no. 1, pp. 115-29, Jan 2006, doi: 10.1016/j.ultrasmedbio.2005.09.005.

62. W. W. Roberts, T. L. Hall, K. Ives, J. S. Wolf, Jr., J. B. Fowlkes, and C. A. Cain, "Pulsed cavitational ultrasound: a noninvasive technology for controlled tissue ablation (histotripsy) in the rabbit kidney," (in eng), J Urol, vol. 175, no. 2, pp. 734-8, Feb 2006, doi: 10.1016/s0022-5347(05)00141-2.

63. Z. Xu et al., "Controlled ultrasound tissue erosion," (in eng), IEEE Trans Ultrason Ferroelectr Freq Control, vol. 51, no. 6, pp. 726-36, Jun 2004, doi: 10.1109/tuffc.2004.1308731.

64. A. D. Maxwell, C. A. Cain, T. L. Hall, J. B. Fowlkes, and Z. Xu, "Probability of cavitation for single ultrasound pulses applied to tissues and tissue-mimicking materials," (in eng), Ultrasound Med Biol, vol. 39, no. 3, pp. 449-65, Mar 2013, doi: 10.1016/j.ultrasmedbio.2012.09.004.

65. A. D. Maxwell et al., "Cavitation clouds created by shock scattering from bubbles during histotripsy," (in eng), J Acoust Soc Am, vol. 130, no. 4, pp. 1888-98, Oct 2011, doi: 10.1121/1.3625239.

66. E. Vlaisavljevich et al., "Non-Invasive Liver Ablation Using Histotripsy: Preclinical Safety Study in an In Vivo Porcine Model," (in eng), Ultrasound Med Biol, vol. 43, no. 6, pp. 1237-1251, Jun 2017, doi: 10.1016/j.ultrasmedbio.2017.01.016.

67. G. Zhao et al., "Mechanical stiffness of liver tissues in relation to integrin β1 expression may influence the development of hepatic cirrhosis and hepatocellular carcinoma," (in eng), J Surg Oncol, vol. 102, no. 5, pp. 482-9, Oct 2010, doi: 10.1002/jso.21613.

68. S. Umale et al., "Experimental in vitro mechanical characterization of porcine Glisson's capsule and hepatic veins," (in eng), J Biomech, vol. 44, no. 9, pp. 1678-83, Jun 2011, doi: 10.1016/j.jbiomech.2011.03.029.

69. E. Vlaisavljevich, Y. Kim, G. Owens, W. Roberts, C. Cain, and Z. Xu, "Effects of tissue mechanical properties on susceptibility to histotripsy-induced tissue damage," (in eng), Physics in Medicine and Biology, vol. 59, no. 2, pp. 253-70, Jan 20 2014, doi: 10.1088/0031-9155/59/2/253.

70. E. Vlaisavljevich, A. Maxwell, M. Warnez, E. Johnsen, C. Cain, and Z. Xu, "Histotripsy-induced cavitation cloud initiation thresholds in tissues of different mechanical properties," (in eng), IEEE Transactions on Ultrasonics, Ferroelectrics, and Frequency Control, vol. 61, no. 2, pp. 341-52, Feb 2014, doi: 10.1109/TUFFC.2014.6722618.

71. E. Vlaisavljevich et al., "Image-guided non-invasive ultrasound liver ablation using histotripsy: feasibility study in an in vivo porcine model," (in eng), Ultrasound Med Biol, vol. 39, no. 8, pp. 1398-409, Aug 2013, doi: 10.1016/j.ultrasmedbio.2013.02.005.

72. S. P. Allen, T. L. Hall, C. A. Cain, and L. Hernandez-Garcia, "Controlling cavitation-based image contrast in focused ultrasound histotripsy surgery," (in eng), Magn Reson Med, vol. 73, no. 1, pp. 204-13, Jan 2015, doi: 10.1002/mrm.25115.

73. T. L. Hall, J. B. Fowlkes, and C. A. Cain, "A real-time measure of cavitation induced tissue disruption by ultrasound imaging backscatter reduction," (in eng), IEEE Trans Ultrason Ferroelectr Freq Control, vol. 54, no. 3, pp. 569-75, Mar 2007.

74. X. Zhang et al., "Real-time feedback of histotripsy thrombolysis using bubble-induced color Doppler," (in eng), Ultrasound Med Biol, vol. 41, no. 5, pp. 1386-401, May 2015, doi: 10.1016/j.ultrasmedbio.2014.12.006.

75. T. D. Khokhlova, M. S. Canney, V. A. Khokhlova, O. A. Sapozhnikov, L. A. Crum, and M. R. Bailey, "Controlled tissue emulsification produced by high intensity focused ultrasound shock waves and millisecond boiling," (in eng), J Acoust Soc Am, vol. 130, no. 5, pp. 3498-510, Nov 2011, doi: 10.1121/1.3626152.

76. G. R. Schade, Y. N. Wang, S. D'Andrea, J. H. Hwang, W. C. Liles, and T. D. Khokhlova, "Boiling Histotripsy Ablation of Renal Cell Carcinoma in the Eker Rat Promotes a Systemic Inflammatory Response," (in eng), Ultrasound Med Biol, vol. 45, no. 1, pp. 137-147, 01 2019, doi: 10.1016/j.ultrasmedbio.2018.09.006.

77. K. J. Pahk et al., "Boiling Histotripsy-induced Partial Mechanical Ablation Modulates Tumour Microenvironment by Promoting Immunogenic Cell Death of Cancers," (in eng), Sci Rep, vol. 9, no. 1, p. 9050, 06 21 2019, doi: 10.1038/s41598-019-45542-z.

78. E. Vlaisavljevich et al., "Non-Invasive Ultrasound Liver Ablation Using Histotripsy: Chronic Study in an In Vivo Rodent Model," (in eng), Ultrasound Med Biol, vol. 42, no. 8, pp. 1890-902, 08 2016, doi: 10.1016/j.ultrasmedbio.2016.03.018.

79. A. R. Smolock et al., "Robotically Assisted Sonic Therapy as a Noninvasive Nonthermal Ablation Modality: Proof of Concept in a Porcine Liver Model," (in eng), Radiology, vol. 287, no. 2, pp. 485-493, 05 2018, doi: 10.1148/radiol.2018171544.

80. T. L. Hall, K. Kieran, K. Ives, J. B. Fowlkes, C. A. Cain, and W. W. Roberts, "Histotripsy of rabbit renal tissue in vivo: temporal histologic trends," (in eng), J Endourol, vol. 21, no. 10, pp. 1159-66, Oct 2007, doi: 10.1089/end.2007.9915.

Chapter 2 Non-Invasive Tumor Ablation using Histotripsy in an In Vivo, Subcutaneous Murine Hepatocellular Carcinoma (HCC) Model

A majority component of this chapter has been published in *2018 40th Annual International Conference of the IEEE Engineering in Medicine and Biology Society (EMBC)* © 2018 IEEE.

Reprinted, with permission, from T. Worlikar et al., "Histotripsy for Non-Invasive Ablation of Hepatocellular Carcinoma (HCC) Tumor in a Subcutaneous Xenograft Murine Model," (in eng), Conf Proc IEEE Eng Med Biol Soc, vol. 2018, pp. 6064-6067, 07 2018, doi: 10.1109/EMBC.2018.8513650.

2.1 Introduction

Hepatocellular carcinoma (HCC) is the most common primary hepatic malignancy, the sixth most common cancer worldwide, and one of the top ten leading causes of cancer-related deaths in the United States [1, 2]. The incidence of HCC continues to rise in the United States, largely secondary to the increasing rate of cirrhosis from chronic viral hepatitis, obesity, diabetes, non-alcoholic fatty liver disease (NAFLD) and excessive alcohol use [3].

Currently, curative treatment options for HCC include surgical resection, liver transplantation or thermal ablation [4, 5]. Surgical resection remains the gold standard but is performed in a small percentage of patients secondary to severity of underlying liver disease, other medical co-morbidities, or extent of their HCC [6-8]. Other existing HCC treatment options include locoregional liver therapies such as: radiofrequency ablation (RFA), microwave ablation (MWA), cryoablation, transcatheter arterial chemoembolization (TACE), transarterial radioembolization (TARE), and stereotactic body radiotherapy (SBRT) [9, 10]. However, each locoregional therapy also has limitations based on tumor location and extent of disease, as well as morbidity based on degree of underlying liver dysfunction secondary to cirrhosis [11-14].

High intensity focused ultrasound (HIFU) is a non-invasive thermal ablation method guided by real time magnetic resonance imaging (MRI) or ultrasound that has been investigated to treat liver tumors [15, 16], however it has drawbacks related to the heat sink effect, ablating through ribs, respiratory motion, and long procedure times. Despite the availability of multiple treatment options, the prognosis of HCC is poor with five-year survival rates reported at only 18% in the US [1].

Histotripsy is the first non-invasive, non-ionizing, non-thermal ablation method that ablates tissue through precise control of acoustic cavitation [17-19]. Microsecond-length, high-amplitude ultrasound pulses (<2 cycles) generate cavitation from endogenous gas pockets in the target tissue [17, 19, 20]. The nanometer gas pockets expand to ~100 um cavitation microbubbles and collapse within a few hundred microseconds. The rapid expansion and collapse of the cavitation microbubbles produces high strains and disrupts cells in the target region into a liquid acellular homogenate [19, 21]. The single focal ablation volume is typically an elliptical shape of 1-2 mm in width and 3-4 mm in the length, depending on the parameters. The single focal volume can be repositioned within the tumor to form a user-defined larger ablation zone with desired volume and shape. Additionally, the low duty cycle of the ultrasound pulses (on-time/ (on- + off- time) < 0.1%) prevents undesirable thermal effects. Thus, histotripsy is not impeded by the heat sink effect and may safely achieve homogeneous cell disruption even in vascular organs such as liver [22]. Large vessels remain intact since they possess higher mechanical strength [23, 24] and resistance to fractionation compared to surrounding soft tissue [25, 26]. Since cavitation can be readily detected on ultrasound imaging, ultrasound is used to guide and monitor histotripsy in real-time [27]. Histotripsy ablation can be visualized on ultrasound and MRI [28-30].

Previous in vivo studies have shown that histotripsy can completely destroy normal liver tissue in porcine and rodent models, resulting in a liquefied acellular homogenate [22, 31-33] which is completely absorbed by the body within a month. Based on these results, we hypothesize that histotripsy can destroy the target tumor tissue to form acellular debris, which is resorbed over time, resulting in effective reduction of local tumor progression and improvement in survival outcomes. In this study, the effect of noninvasive histotripsy tumor ablation on local tumor progression and survival time was investigated in human-derived HCC subcutaneous xenograft murine models. Our secondary objective was to characterize the radiological and histopathologic appearance of the acute and chronic response of the histotripsy treated HCC tumors.

2.2 Materials and Methods

2.2.1 Experimental Design

This study was approved by the Institutional Animal Care and Use Committee at the University of Michigan (UM-IACUC). Two human-derived xenograft murine subcutaneous HCC tumor models were developed in immune-compromised NOD-scid (NOD.C.B17-Prkdc^{scid}) and NSG (NOD-Prkdc^{scid} IL2rγ^{null}) murine hosts, which are well suited for engraftment of solid tumors like HCC [34]. In both models, the NOD strain background confers deficiencies in innate immunity, whereas the Prkdc^{scid} mutation generates defects in adaptive immunity [35]. The fundamental difference between the two models is the complete lack of the IL2rγ gene (responsible for high affinity signaling for many interleukin receptors) in the NSG mice [35-37]. The absence of signaling disables innate and adaptive immunity and makes the NSG mouse more receptive to human cells and primary tumor engraftment compared to a NOD-scid mouse. In this study, histotripsy treated animals from both models were monitored for up to 3 months by MRI for local tumor regression or progression, as well as evaluated by pathology for the development of any metastasis following histotripsy ablation. The primary tumor growth characteristics, response to histotripsy, tumor recurrence and survival outcomes were compared between the two models.

The study protocol is shown in Figure 2-1A. Hep3B HCC tumor cells were injected subcutaneously in the flanks of 16 NSG and 11 NOD-scid male mice aged 6-7 weeks to generate tumors. The mice were categorized into four groups based on the tumor volume targeted for ablation: A) partially targeted acute (n=9), B) entirely targeted acute (n=6), C) entirely targeted chronic (n=6), D) partially targeted chronic (n=2) and E) control (n=4) as indicated in Table 1-1. Histotripsy ablation was performed once the tumor measured a minimum of 5 mm in its largest diameter, based on caliper measurements. Tumors reached this treatment timepoint more rapidly in NSG mice (3-5 weeks post inoculation) as compared to NOD-scid mice (8-15 weeks post inoculation), likely due to differences in immunological makeup. The mice in acute groups A and B were euthanized within 3 days after ablation. The mice in chronic group C and D were monitored weekly post treatment using caliper measurements and MRI after ablation for up to 3 months or euthanized when they reached tumor endpoint (maximum tumor diameter exceeded 1.8 cm). For the partial ablation groups A and D, approximately 50% of the tumor volume was targeted for ablation by histotripsy. Tumors were ablated partially to allow evaluation and characterization of distinctive appearance of the targeted and non-targeted tumor regions on ultrasound imaging, MRI imaging, as well to confirm that there is a sharp demarcation between targeted and non-targeted tissue on histology without any intermediate zones of tissue damage as typically observed in thermal ablation. In the entire tumor ablation groups B and C, the entire tumor was targeted for ablation, with an additional small margin (<2 mm) of muscle tissue beyond the tumor boundary (along the far edge) included in the target region to ensure adequate treatment along the margin. However, the subcutaneous location of tumors often did not allow even a small (<2 mm) ablation margin along the superficial border of the tumor due to the risk of possible skin perforation.

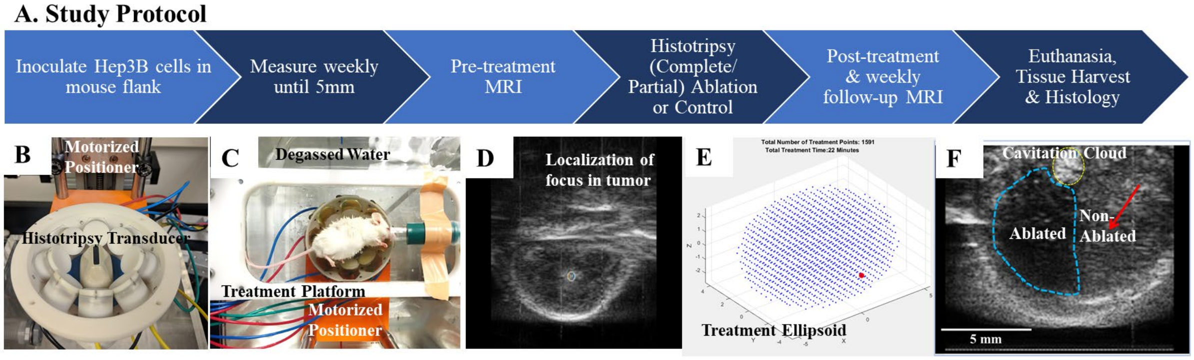

Figure 2-1 (A) ***Study Protocol****: Histotripsy ablation (either partial or entire tumor) was performed once the tumor measured a minimum of 5 mm in largest diameter. The acute mice were euthanized within 3 days after ablation. The chronic mice were survived and monitored weekly using caliper measurements and MRI for up to 3 months post treatment or until the maximum tumor diameter exceeded 1.8 cm. For the partial ablation groups 50% of the tumor volume was ablated by histotripsy. In the entire tumor ablation groups, the entire tumor was targeted for ablation. The control group mice received no treatment. (B) Custom 8 element 1 MHz focused therapy transducer with coaxially aligned imaging probe used for histotripsy treatment and real-time US guidance respectively, mounted to a motorized 3-axis positioning system. (C) The mouse is placed on a custom-built treatment platform just over the water tank, such that the tumor region to be treated is immersed in water. (D) Histotripsy generated hyperechoic cavitation cloud at the focus of the therapy transducer at a target location within the tumor (E) Generation of ellipsoid treatment grid of locations for delivering histotripsy pulses within the tumor (F) Cavitation cloud (yellow), and ablated region (blue) is visualized in real-time as hypoechoic zone distinct from the speckled appearance of the non-targeted tumor (red arrow) on ultrasound imaging.*

2.2.2 Cell Preparation

Hep3B (ATCC® HB-8064™) cells derived from human HCC tumors were cultivated in MEM (+Glutamine, +Earle's Salts) media supplemented with 10% FBS, 1% Antimycotic-Antibiotic, 1% Minimum non-essential amino acids (MNEAA), 1% Sodium pyruvate and 1 mL Gentamicin. The cells were maintained at 37 °C in a 5% CO2/95% humidified air atmosphere.

2.2.3 Animal Preparation

In both tumor models, mice were injected with 1-2 million Hep3B cells subcutaneously into the flank to generate xenograft tumors. All mice were monitored weekly and tumor diameter measurements were quantified using calipers. Once tumor diameters reached 5 mm in the largest dimension, the mice in treatment groups A, B, C and D were treated with histotripsy. The mice in control group E did not receive histotripsy or other treatment.

Table 2-1 Control and Treatment Cohorts

	Group (n=27)	**Ablation Target**	**Survival Timepoints**	**NSG (n=16)**	**NOD-scid (n=11)**
Treatment Cohort	A (n=9)	Partial Tumor	Acute	n=5	n=4
	B (n=6)	Entire Tumor	Acute	n=6	
	C (n=6)	Entire Tumor	Chronic	n=2	n=4
	D (n=2)	Partial Tumor	Chronic		n=2
Control Cohort	E (n=4)	Control		n=3	n=1

Histotripsy HCC study mice sub-groups in NSG and NOD-scid models based on ablation target and post treatment survival timepoints.

Prior to and during histotripsy, the mice were induced and maintained on general anesthesia by inhalation of isoflurane gas (1.5-2.0%) in 1 L/min of oxygen (SurgiVet V704001, Smiths Medical, Waukesha, Wisconsin, USA). The hair covering the subcutaneous tumor region was removed with an electric clipper followed by treatment with a depilatory cream. Core body temperature was recorded using a rectal probe and was maintained between 35-37 °C with an overhead heating lamp. The mice were injected with Carprofen (Rimadyl, Pfizer, NY, USA) analgesic (5 mg/kg) subcutaneously before delivery of histotripsy treatment and once every 24 hours for 2 days after treatment. Immediately after histotripsy, the mice were transferred to a recovery chamber fitted with an overhead heating lamp and were placed on a heated pad. Once the mice recovered from anesthesia and were mobile, they were transferred back to their housing cages. The mice were monitored daily for one week following treatment and then twice weekly for the duration of the study. All efforts were made to minimize suffering. Tumor dimensions were measured using calipers until they reached 5 mm in largest dimension and using MR imaging beginning from the histotripsy timepoint. Treatment outcomes were monitored using MR imaging. Animals were survived up to 3 months or until the tumors reached a diameter of 1.8cm in any two dimensions (tumor endpoint). Additionally, end stage illness and humane endpoints guidelines were determined as follows: animals exhibiting signs of dehydration, emaciation or cachexia, impaired mobility, systemic infection, or abdominal or thoracic bleeding during or immediately after histotripsy treatment were to be euthanized. The primary method of euthanasia was exposure to CO2 in compressed gas form followed by a secondary method of euthanasia, bilateral pneumothorax, to ensure animal cannot revive, in accordance with UM-IACUC guidelines.

2.2.4 Experimental Setup

Our lab has designed and built a custom 8 element 1 MHz focused ultrasound therapy transducer specifically for rodent histotripsy therapy (Figure 2-1B). The histotripsy transducer was driven by a custom-built high-voltage pulser controlled by a field-programmable gate array (FPGA) development board (DE0-Nano Terasic Technology, HsinChu, Taiwan), enabling the therapy transducer to generate and output 1-2 cycle histotripsy pulses. A 20 MHz B-mode ultrasound imaging probe (L40-8/12, Ultrasonix, Vancouver, Canada) was co-aligned with the center of the therapy transducer to allow visualization of the focal ablation volume in real time. The ultrasound therapy transducer and the imaging probe were mounted to a motorized 3-axis positioning system (Figure 2-1B) to mechanically scan the therapy focus across a 3D target ablation volume. Water was used as the ultrasound coupling medium by immersing the transducer and imaging probe in a tank of degassed water maintained at 35–37°C by means of a coil heater. The mouse was placed on a custom-built animal platform just over the water tank (Figure 2-1C). To identify the histotripsy focus on ultrasound imaging, test histotripsy pulses were delivered to the water tank by the therapy transducer to generate a “bubble cloud” which appeared as a hyperechoic cavitation zone on ultrasound imaging (Figure 2-1D). The position of the hyperechoic cavitation zone was then marked as the therapy focal position on the ultrasound image.

2.2.5 Histotripsy Ablation

After sedation, the animal was placed decubitus with the tumor submerged in the degassed water such that the therapy transducer was moved by the motorized positioning system to align the therapy transducer focus with the center of the tumor on the ultrasound image. Using a custom MATLAB script, the ultrasound therapy transducer and the imaging probe were scanned using the motorized positioning system, such that a treatment ellipsoid consisting of a grid of uniformly spaced therapy focal zones (~0.5 – 0.75 mm between adjacent focal volumes) would encompass the user-defined target 3D tumor volume (Figure 2-1E). This target volume covered approximately 50% of the original tumor volume for partial ablation or the complete tumor identified on US for entire ablation. One hemisphere of the tumor contacting both the underlying muscle layer and the overlying skin layer was selected for partial ablation. During ablation, histotripsy-induced cavitation was hyperechoic in appearance compared to the surrounding tissue on ultrasound imaging (Figure 2-1F), which was used to monitor the ablation in real-time. At each focal location, 50 histotripsy pulses at 100 Hz PRF (P- >30 MPa) or 0.5 seconds of ablation were delivered. After ablation, the targeted region appeared hypoechoic on ultrasound imaging, enabling real-time feedback to ensure adequate ablation volumes were achieved (Figure 2-1F). Selection of histotripsy parameters (Table 2-2) was based on results of previous in vivo and in vitro work [22, 38]. The choice of PRF, spacing between locations and pulses delivered per location were confirmed to ensure that the intended target tumor region was fractionated to form mostly acellular homogenate in the acute cohort animal groups A and B.

Table 2-2 Histotripsy Ablation Parameters

Pulse Length	1-2 cycles
PRF (Pulse Repetition Frequency)	100 Hz
Estimated Peak Negative Pressure at Focus	>30MPa-
Number of Treatment Locations in Target Zone	2000-3000
Number of Histotripsy Pulses at each Location	50
Treatment Location Spacing within Target Zone	0.5mm-0.7mm (lateral, elevational), 0.75-0.9mm (axial)
Treatment Time	20-40 minutes depending on the tumor size

2.2.6 Magnetic Resonance Imaging for Treatment Evaluation

MRI data was obtained within 1 day prior to histotripsy and within 1-day post-histotripsy, followed by weekly imaging to assess the effects of tumor ablation and characterize variations in imaging appearance. Imaging was performed on a 7.0 T MR scanner using a Direct Drive console (Agilent Technologies, Santa Clara, CA, USA) with a 40 mm inner-diameter transmit-receive radiofrequency (RF) volume coil (Morris Instruments, Ontario, Canada). Prior to and during imaging, the mice were induced and maintained on general anesthesia by inhalation of isoflurane gas (1.5-2.0%) in 1 L/min of oxygen (SurgiVet V704001, Smiths Medical, Waukesha, Wisconsin, USA). Respiration was monitored and animal temperature was maintained at 37±0.5 °C using a rectal temperature probe and a custom-built proportional-integral-derivative (PID) controller (LabVIEW, National Instruments, Austin TX) interfaced with a commercially available small animal system (SA Instruments, Stony Brook, NY). Initial pilot scans were performed to confirm positioning. Thereafter, T2 and T1-weighted fast spin-echo (FSE) sequences and a T2*-weighted gradient-echo (GRE) sequence were used to visualize the tumor in the axial plane (Table 2-3).

Table 2-3 MR Imaging Parameters

Sequence Type	**T2-weighted FSE**	**T1-weighted FSE**	**T2*-weighted GRE**
Slice Thickness	1mm	1mm	1mm
FOV	35 × 35mm	35 × 35mm	35 × 35mm
TR	2000ms	2000ms	250ms
TE	10ms	8.5ms	5ms
Acquisition Time	8 min	8 min	8 min

The overall signal characteristics of the pre-treatment and post-treatment tumor using T1-weighted FSE, T2-weighted FSE and T2*- weighted GRE were recorded and compared to each other to identify potential changes which would differentiate non-viable tumor from viable tumor. MR images were analyzed (Analyze 11.0, AnalyzeDirect, Overland Park, KS) by a radiologist (MML, 13 years of clinical image interpretation experience) in consultation with an imaging scientist (JMG, 20 years of experience in high-field MRI and preclinical small animal models). Tumor (and homogenate post-ablation) volume was quantified by summing area measurements made from the 2D T2-weighted FSE acquisition. Tumor diameter measurements were also made on the T2-weighted sequence in orthogonal anterior-posterior (coronal) and transverse (axial) dimensions. Signal characteristics of the pre-treatment tumor and the post-treatment ablation zone were recorded. Surrounding structures such as the musculature and body wall were evaluated for signs of injury.

2.2.7 Histological Analysis

Post euthanasia, treated tumor, as well as brain and lung tissue samples were harvested and fixed in 10% buffered formalin for histopathology. Fixed tissue samples were submitted to Scientific Solutions, LLC (Fridley, MN) for paraffin processing and embedding as well as staining. Samples were sectioned in 5-micron slices stained with hematoxylin and eosin (H&E). Slides were examined by a board-certified anatomic and clinical pathologist (JS) for histopathologic analysis, under a light microscope Olympus BX43. The Nikon Eclipse 50i imaging microscope was used to capture images.

2.2.8 Statistical Analysis

Experimental data were analyzed using Microsoft Excel (2013). Survival analysis was performed using the Kaplan-Meier method. Survival time data of control and chronic mice was compared with the two-tailed Student's t test, with significance defined as $p < 0.05$. Additionally, a single factor Analysis of Variance (ANOVA) test was performed to determine if there was a statistically significant ($p < 0.05$) difference between the mean survival times of control mice, entirely targeted chronic NSG and NOD-scid mice.

2.3 Results

2.3.1 Clinical Monitoring

All tumor inoculations were well-tolerated with no deaths or complications as a direct result of the subcutaneous tumor injections. All histotripsy procedures were well tolerated without major or minor complications requiring additional care or euthanasia.

2.3.2 Long-term Local Tumor Response to Histotripsy

Effective tumor volume reduction was observed in chronic entirely targeted histotripsy animals as compared to untreated controls (Figure 2-2). MR images revealed that between 2-5 weeks post-ablation, the tumor homogenate completely resolved in all group C mice (Figure 2-3). In 4/6 mice (2/4 NOD-scid and 2/2 NSG mice), no quantifiable tumor volume was detectable on MRI beginning week 3 and until 5-7 weeks post-treatment, after which recurrence was observed. In the remaining 2 NOD-scid mice in group C, recurrence was observed by 3 weeks post-treatment. In the partially targeted NOD-scid mice in group D, the untreated residual tumors continued to grow, and animals were euthanized when they reached tumor endpoints and thus there was no difference in their survival outcomes when compared to the control mice. In control group E, tumor burden continued to increase, and the NSG mice were euthanized at 5-6 weeks and NOD-scid mice were euthanized at 18 weeks post inoculation, based on when they reached tumor endpoints.

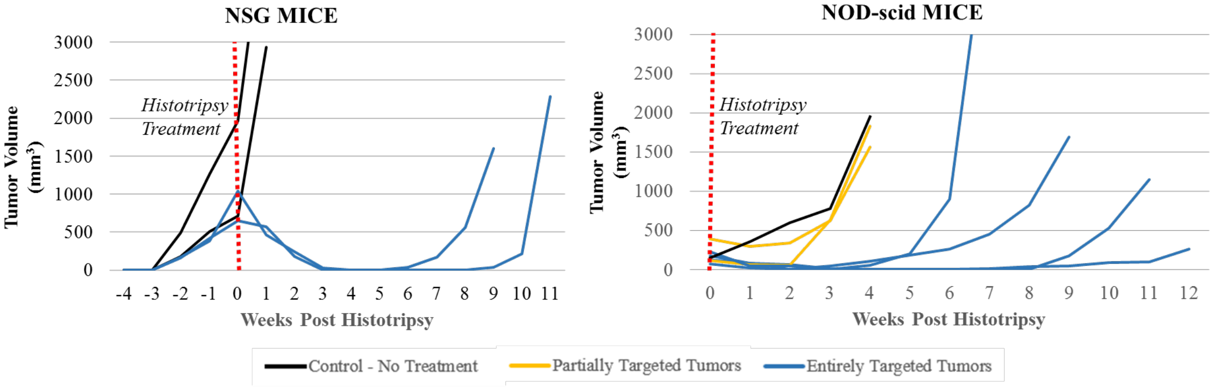

Figure 2-2 ***Treatment Progression and Survival Outcomes in Chronic Cohorts.*** *Volumetric measurements made by MRI show effective tumor volume reduction observed within 3-8 weeks post ablation in the entire ablation group vs. the untreated control in both NSG and NOD-scid mice.*

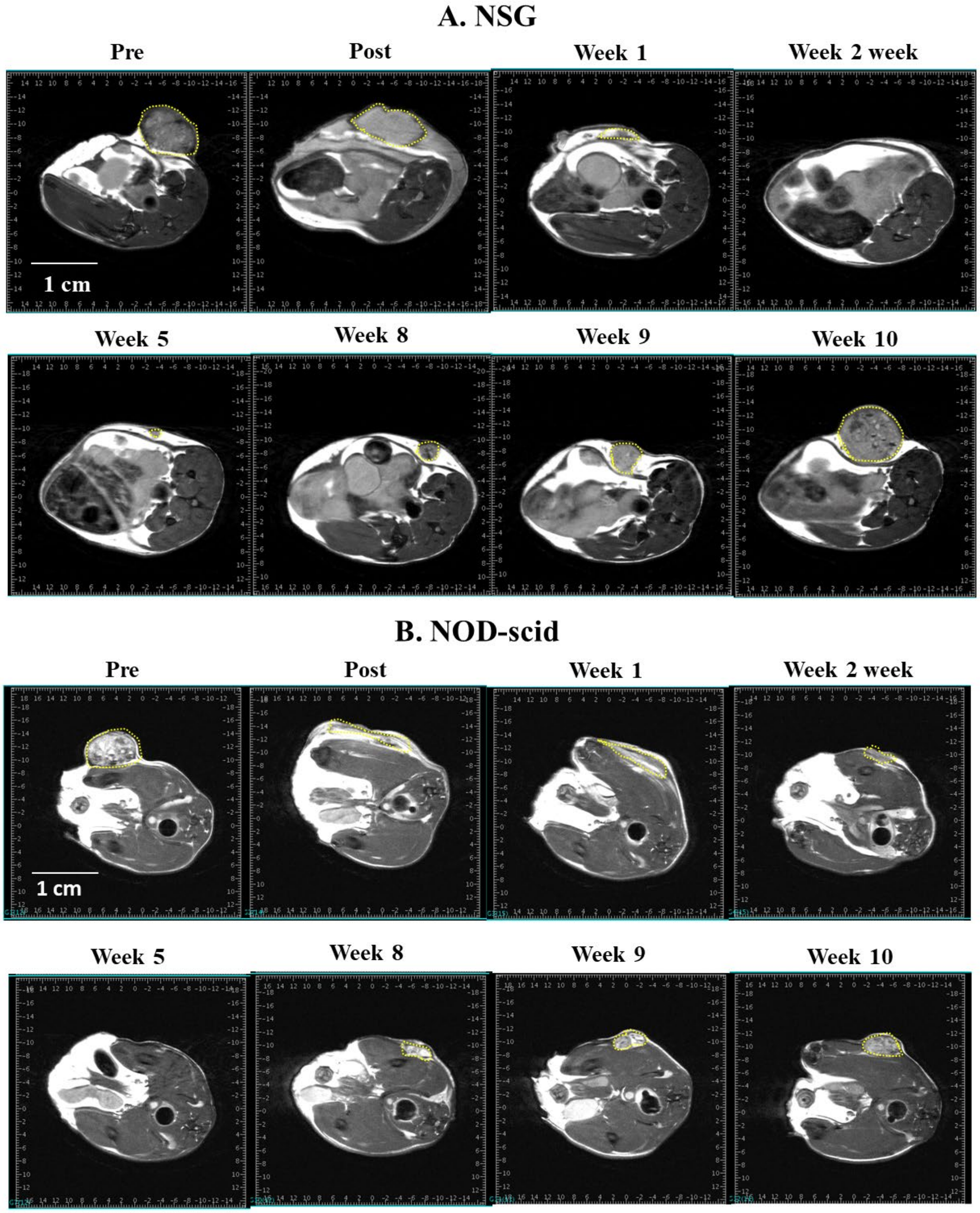

Figure 2-3 ***Long-term response to entire histotripsy ablation evaluated by MRI.*** *Representative T2 weighted MRI images show tumor response (blue arrows) in both chronic (A) NSG and (B) Nod-SCID groups. Pre-treatment imaging demonstrates the heterogenous appearance of the subcutaneous tumor, which extends to just below the dermal layer of the skin. Post-histotripsy the treated tumor now appears hyperintense and changes its shape to conform to the body wall, as expected since the treated tumor cells have become an acellular homogenate with no definable capsule to control the location of the acellular homogenate. 1 week post-histotripsy the ablation volume regresses and remains amorphous. Earlier recurrence is detected for the NSG mouse (5 weeks) in comparison to*

NOD-scid mouse (8 weeks). By 10 weeks, the recurrent tumor has heterogenous imaging appearance near identical to the pre-histotripsy tumor.

2.3.3 MRI Tumor Volume and Signal Characterization

Histotripsy ablation zones were longitudinally evaluated by MRI. Pre-treatment tumors demonstrated heterogeneous hyperintense T2, T2* and T1 signal when compared to the adjacent musculature, albeit varying degrees of heterogeneity (Figure 2-4). After treatment, ablated tumor volumes demonstrated a homogeneous appearance with hyperintense T2, T2*, and T1 signal (Figure 2-4). In cases of partially ablated tumors, MRI was able to distinguish between ablated and untreated regions within one day of histotripsy, providing valuable early feedback on histotripsy imaging appearance with a direct comparison to the tumor appearance (Figure 2-4).

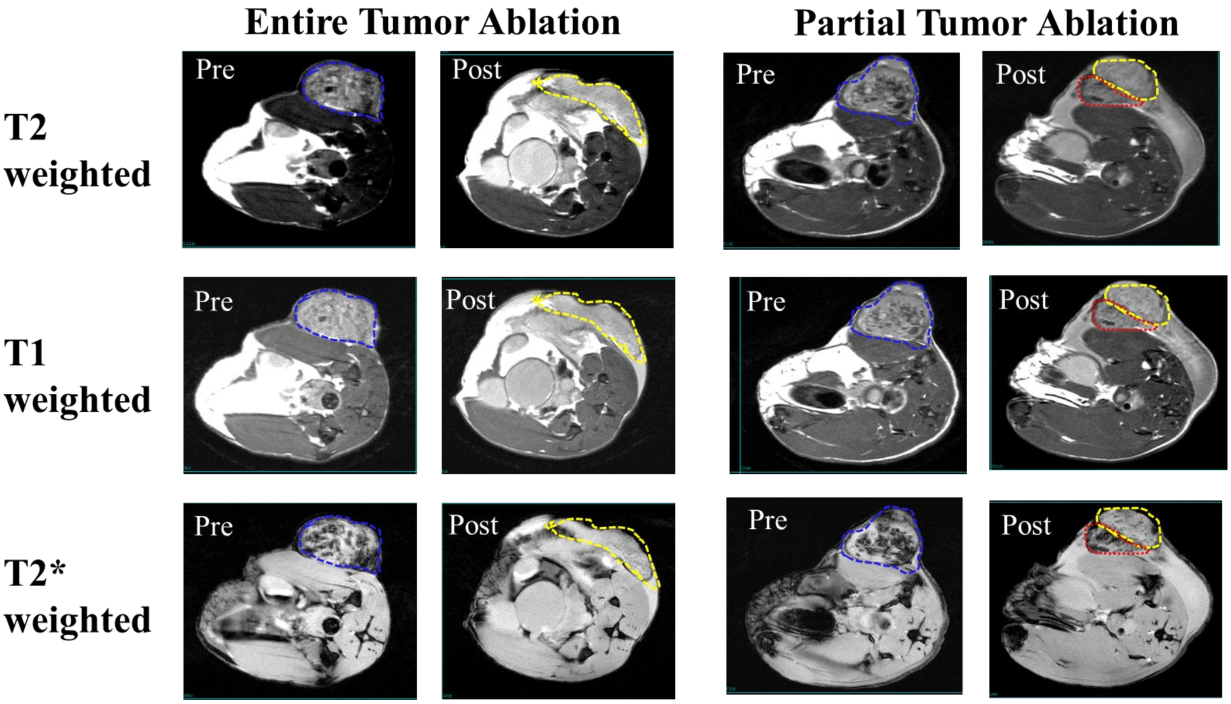

Figure 2-4 ***Characterization of MRI signal pre and post histotripsy****. Pre- histotripsy tumors (blue dashed lines) have a heterogenous hyperintense appearance, with varying degrees of heterogeneity. Within one day post histotripsy, the ablated volume (yellow dashed lines) appears homogeneously hyperintense as compared to the heterogeneous mottled appearance of pre-treatment tumor on T2, T1 and T2* weighted images. In addition, the treated tumor changes configuration to conform to the shape of the body wall, as expected since the tumor becomes a fluid acellular homogenate with no capsule surrounding the treated cavity. In cases of partially targeted tumors, MR can distinguish between ablated (yellow dashed lines) and unablated tumor volume (red dashed lines), providing valuable early feedback on imaging differences between treated and untreated tumor.*

Immediately post-histotripsy the ablated tumor volume was flattened into an oblong shape that conformed to the shape of the body wall. This change in tumor configuration post-treatment was likely related to a combination of the tumor being liquefied and the non-confined location in the subcutaneous tissue, which allowed the fluid homogenate to spread in the subcutaneous tissue space. Although the imaging appearance suggested adequate ablation volume, the post-treatment change in configuration made it difficult to accurately compare volumes between post-treatment and pre-treatment tumors for evaluation of adequacy of ablation and for the detection of residual untreated tumor.

All cases of recurrence were seen between 3-8 weeks post-histotripsy (Figures 2-2, 2-3). Local recurrence was identified within the ablation zone by the re-appearance of an increasing nodular area of heterogeneous T2, T2* and T1 signal intensity which was similar in appearance to the pre-treatment tumor. There were no significant noticeable differences seen visually in the MR appearance of the pre-treatment and post-treatment recurrent tumors.

2.3.4 Histological Analysis

In untreated HCC control tumors in group D, the tumor cells showed sheet-like growth patterns, resembling original human HCC (Figure 2-5A). In partially targeted acute group A, the treated region was completely fractionated into acellular debris with a discrete boundary separating the treatment zone from the residual tumor (Figure 2-5B). In the entirely targeted acute group B, pathology revealed completely fractionated tumor cells within the treatment region on Day 3 post treatment (Figure 2-5C). However, a thin rim of residual viable HCC was identified along the tumor periphery even in entirely ablated tumor group (Figure 2-5D), likely due to the lack of adequate ablation margin along the cutaneous surface of the tumor. These residual tumor cells may have contributed to eventual tumor recurrence. The growth pattern of the recurrent HCC in chronic group C mice was similar to the original HCC tumor architecture with cells arranged in sheet pattern in control group D mice (Figure 2-5E). The main difference in morphological appearance was that recurrent HCC demonstrated prominent regions of tumor necrosis (Figure 2-5F). No metastases were observed in the brain or lungs from the chronic group C (Figures 2-5G, H). These tumor models do not naturally develop metastasis, and our results support that histotripsy did not yield unexpected intrahepatic or systemic metastasis at the locations investigated.

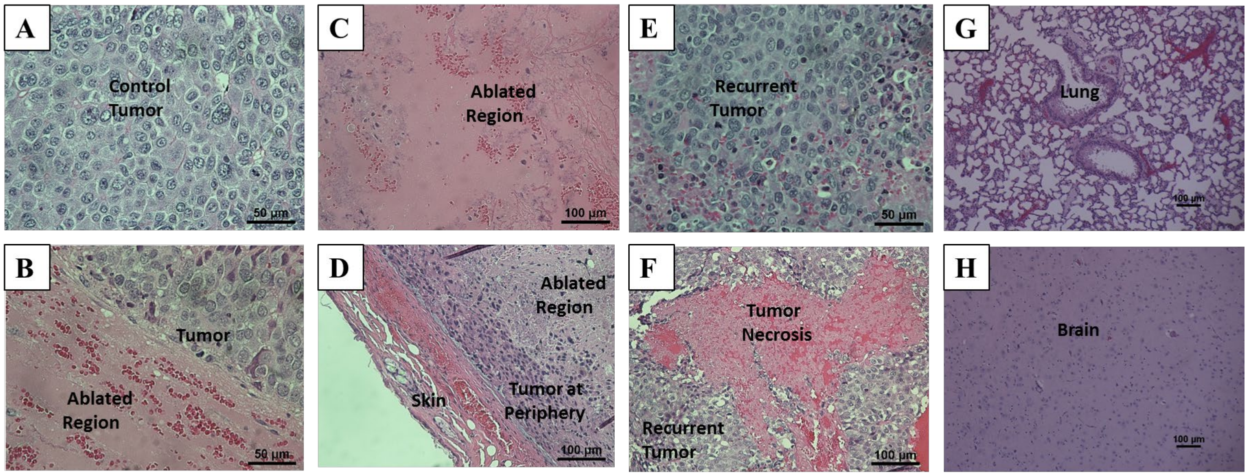

Figure 2-5 ***Histological analysis of harvested tumor and tissue samples.*** *Representative H&E images show (A) Untreated original hepatocellular carcinoma (HCC) tumor cells grow in a trabecular pattern, resembling original human HCC (B) In a partially targeted tumor, the treated region was completely fractionated into acellular debris, with a sharp boundary separating the ablated region from the untreated tumor on Day 3 (C) In an entirely targeted tumor, the vast majority of the HCC tumor cells in the original sites appeared completely liquefied on Day 3 (D) In an entirely targeted tumor, a thin rim of residual HCC (<200µm) was identified at the tumor periphery on Day 3 (E) Recurrent HCC in an entirely ablated survival NSG mouse, showing growth pattern similar to the original HCC (F) Prominent central necrosis observed in one recurrent HCC tumor. No metastasis was observed in the (G) lung and (H) brain at 11 weeks post histotripsy.*

The ablated homogenate region revealed scattered small vessels, fibroblasts, and inflammatory cells (Figure 2-6A-D). Scattered lymphocytes (Figure 2-6A), macrophages (Figure 2-6B), neutrophils (Figure 2-6C), and eosinophils (Figure 2-6D) were amongst the immune cells identified in the homogenate.

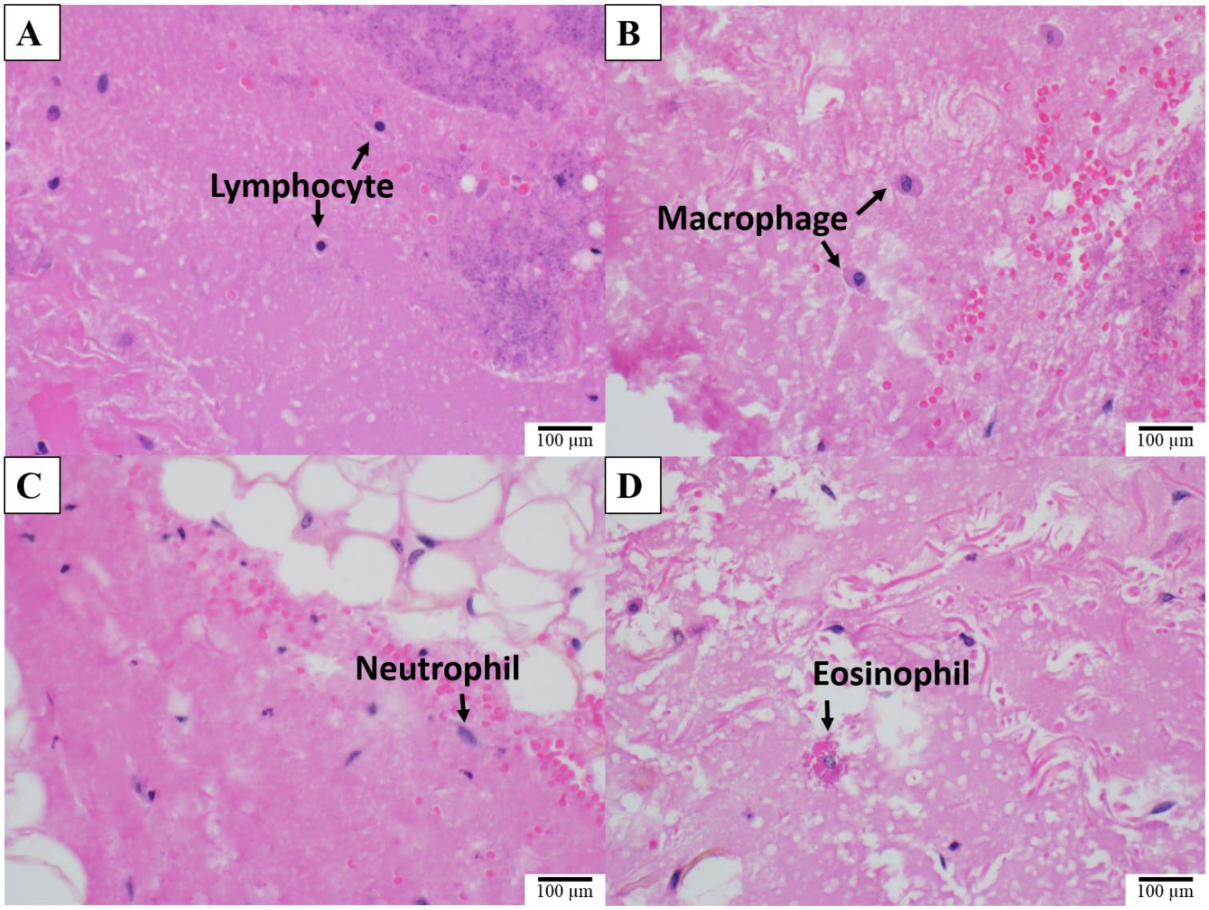

Figure 2-6 ***Immune cells in post treatment homogenate.*** *Histology (H&E staining) of post treatment homogenate reveals infiltration of immune cells such as (A) lymphocytes, (B) macrophages, (C) neutrophils and (D) eosinophils at 3 days post histotripsy as well as scattered residual small vessels, fibroblasts, and other inflammatory cells.*

2.3.5 Survival Outcomes

In general, treated mice in group C survived significantly longer than the control mice in group D ($p < 0.05$) (Figure 2-7). All mice, including controls were euthanized when the tumors measured >1.8 cm, as written in the study protocol secondary to tumor burden on the animal. The survival time in control group D was 5.3 ± 0.33 (mean ± SEM) weeks for NSG mice and 18 weeks for the NOD-scid mouse after tumor inoculation. In treatment group C, the survival time was 15 ± 1 weeks and 20 ± 1.87 weeks after tumor inoculation for the NSG mice and the NOD-scid mice, respectively.

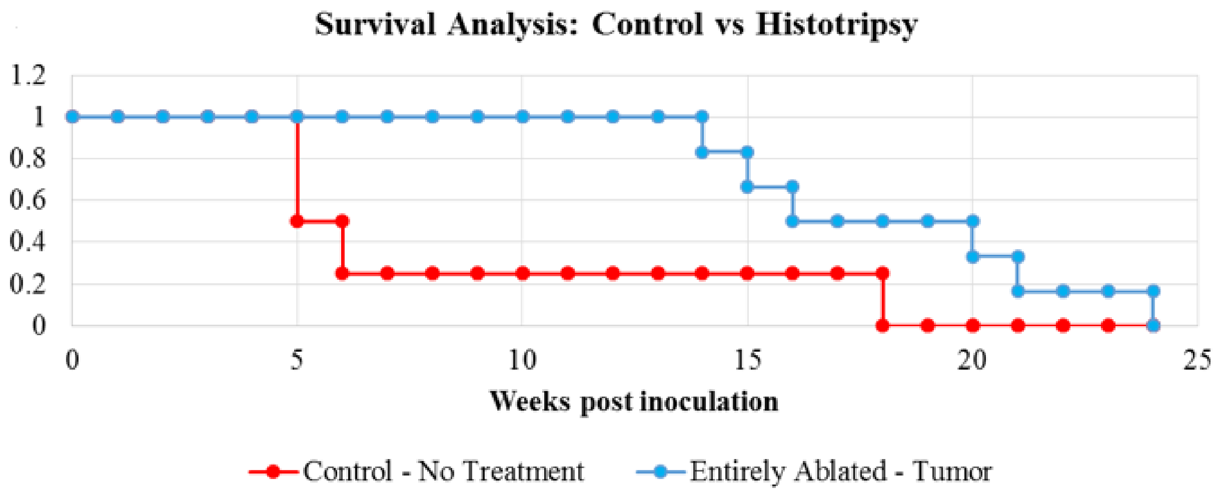

Figure 2-7 ***Survival Analysis.*** *Kaplan – Meier survival demonstrates the survival outcomes for the entirely ablated and the control mice. In general, mice in entire targeted group C survived significantly longer than the untreated control mice group D (p = 0.039).*

2.3.6 Effects on Adjacent Tissue

The ablation volume included up to a 2 mm margin of normal tissue along the far wall of the tumor to ensure adequate margins. However, due to the subcutaneous nature of the tumor model, there was a lack of sufficient ablation margin along the superficial border of the tumor to prevent injury to the overlying skin. Immediately following treatment, a focal area of edema and erythema was noted along the skin surface at the site of treatment. Within 2-3 days post-treatment a focal scab was formed on the surface of the skin at the treatment site, which resolved completely within 2-3 weeks post-treatment (Figure 2-8A).

MR evaluation of the muscle deep to the ablation zone illustrated increased T2 signal within ~50% of the muscle on all but 2 treated mice, which would be consistent with edematous changes within the muscle due to tissue damage. In all cases, this edema resolved by three weeks, without a reduction or change in the overall thickness of the muscle; thus, suggesting that the ablation effects in the muscle were reversible (Figure 2-8B). Two mice had full-thickness edema to the thigh musculature, which eventually resolved without any sequelae of injury and without any atrophy of the muscle as observed on MRI. No significant mobility limitations were observed in the mice post treatment.

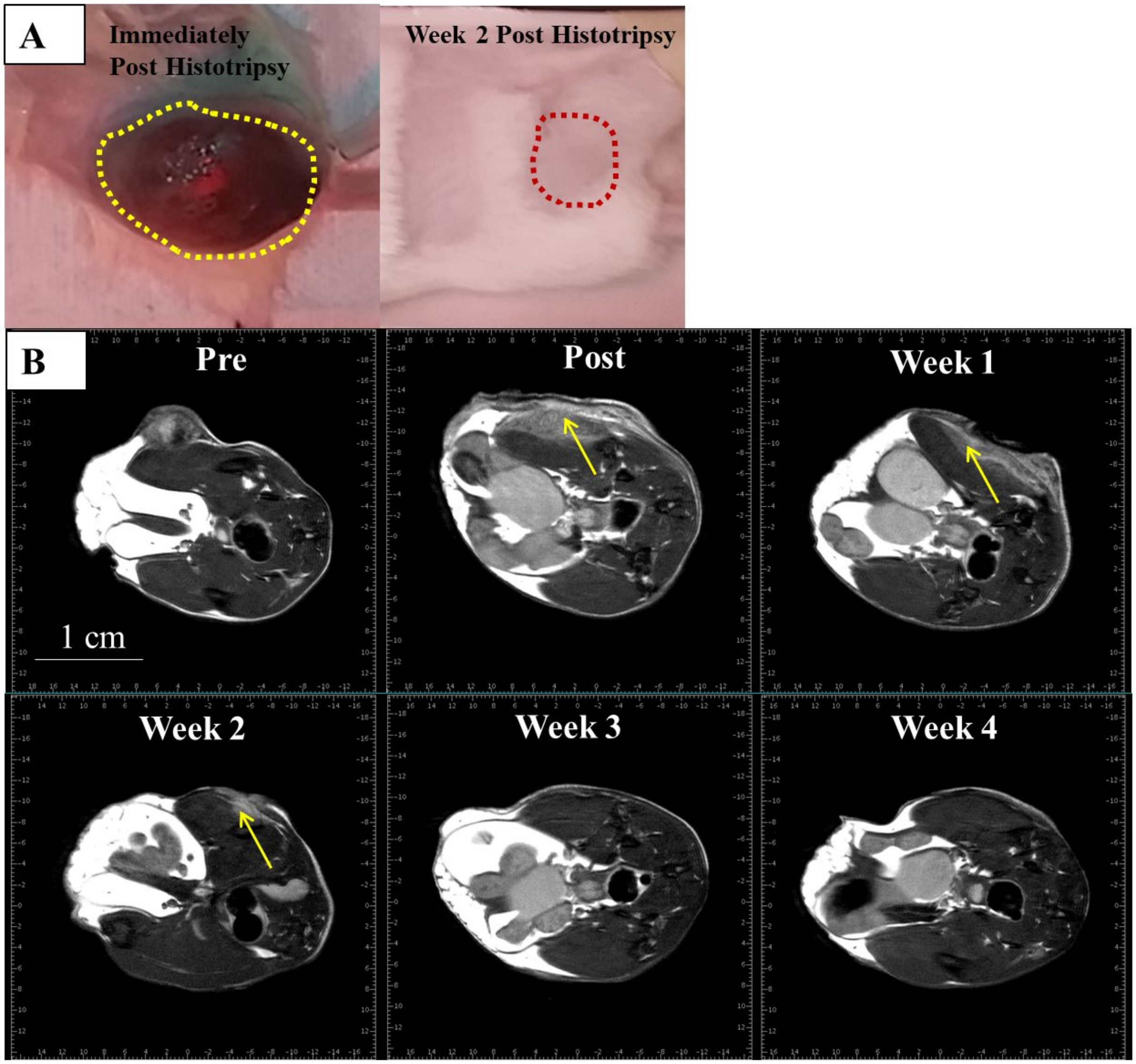

Figure 2-8 ***Effect of histotripsy on adjacent tissue.*** *(A) Immediately post histotripsy, a focal area of edema and erythema was noted along the skin surface at the site of treatment due to lack of margin on the near end of the tumor secondary to the subcutaneous location, which abutted the skin surface. Focal scab was formed on the surface of the skin at the treatment site, which resolved completely within 2-3 weeks post-treatment. (B) Immediate post-treatment imaging demonstrates an increased T2 signal seen within 50% of the muscle just adjacent to the ablation zone, compatible with edema. In all cases, this edema resolved by 3 weeks, without a reduction or change in the overall thickness of the muscle; thus, suggesting that the ablation effects in the muscle region were reversible.*

2.4 Discussion

Our study investigated the response of histotripsy tumor ablation in a subcutaneous HCC tumor xenograft murine model. Xenograft models are being increasingly used for translational oncology research and drug development as they allow for minimal deviation in the stromal composition and histological and molecular heterogeneity of the tumor seen in humans, enabling more accurate pre-clinical assessment of therapeutic responses [39, 40]. In this study, the assessment of the treatment response to histotripsy over time was performed using MR imaging, histology, and caliper measurements. To our knowledge, this is the first study demonstrating histotripsy treatment of tumors with long term (3 month) follow-up in an in vivo murine model. Histotripsy generates well-confined cavitation bubble clouds allowing for real-time monitoring of the ablation zone, as well as resulting in ablation zones with sharply demarcated boundaries between the non-treated tissue and the ablation zone seen both radiographically and histologically.

This is the first study showing that histotripsy resulted in effective tumor burden reduction and significantly extended survival time compared to untreated control. In all mice which underwent entire tumor ablation (group C), the ablated volume was completely absorbed, and no tumor was detected on MRI by week 5 in 4/6 mice. The survival time of the entire ablation group C was significantly longer than the untreated control group D (p=0.039). No local or distant metastasis was detected by MRI or pathology. These results provide new evidence to support the safety and efficacy of using histotripsy for tumor ablation.

MRI or computed tomography (CT) data are the most accepted means to monitor therapeutic response in patients with HCC. For many locoregional therapies, particularly arterial based therapies (TACE/TARE), treatment effectiveness can only be evaluated a few weeks after treatment [41, 42]. In this study, MRI successfully enabled immediate assessment of tumor appearance post-histotripsy ablation. This may offer a significant clinical benefit for histotripsy in the future, as immediate imaging during the time of treatment would allow assessment for complete tumor ablation. In cases of incomplete tumor ablation or inadequate ablation margins detected at the time of treatment, it would allow for rapid re-treatment. Contrast enhanced MRI is commonly used in the clinic for treatment assessment of locoregional therapies [43]. However, given the heterogeneous, and hyperintense MR signal of the viable subcutaneous tumors, no intravenous contrast agents were administered in our study. We used standard T1-weighted FSE, T2-weighted FSE and T2*- weighted GRE sequences which can be easily translated for use in the clinical setting. The major MR imaging finding seen after histotripsy ablation of tumor, is that the heterogeneous, hyperintense appearance of viable HCC tumor is transformed into a relatively homogeneous hyperintense appearance, which pathologically correlates to a relatively acellular homogenate occupying the treatment cavity. The post-ablation homogenate retains the hyperintense appearance as it resolves over time, usually between weeks 3-10 post-treatment. This response to histotripsy contrasts with thermal ablation, in which the treated cavity never fully resorbs, and instead slowly decreases in size over time, remaining as a hypoenhancing area on MR imaging [43-45]. The conversion from heterogeneous signal intensity pre-histotripsy to homogeneous signal intensity post histotripsy may be a reliable metric to evaluate treatment response, although further studies, particularly with radiology-pathology correlation, will be needed to validate this finding.

The change in MRI signal, from heterogeneous to homogeneous, can be attributed to the mechanical breakdown of the tissue structures at the targeted location, as evidenced by histological assessment. In the partial ablation cases, non-ablated tumor regions (>~3mm diameter) are visible on the MR images and correspond to heterogeneous signal similar to the pre-treatment tumors. This was not seen in the cases where the entire tumor was ablated. In addition, the appearance of the recurrent tumor along the ablation margin eventually had imaging characteristics similar to the pre-treated tumor, with an overall heterogeneously hyperintense appearance. The use of alternative imaging sequences, including intravenous contrast agents, may provide valuable information to optimally distinguish healthy tissue, residual tumor tissue, and the homogenate on post-ablation scans. As seen on histology, a thin rim of viable HCC may have remained along the margin of the completely ablated tumors due to the lack of an adequate ablation margin, which was not detected on imaging. Thus, the use of intravenous contrast may be useful in immediate post-ablation imaging to plan retreatment of any identified residual tumor and may thus theoretically improve disease free survival with early detection of local recurrence.

In the current study, the average improvement in survival post inoculation was statistically significantly higher in the complete ablation mice as compared to the control and partial ablation mice. However, given limitations related to tumor location, all mice eventually demonstrated recurrence. Further studies are needed to investigate survival benefits.

This study revealed no irreversible damage to structures adjacent to the ablation zone. In instances where we attempted to define a margin outside the tumor region, post-treatment and weekly follow-up MRI revealed edema in the leg musculature near the treatment region, manifested as a T2-hyperintense signal, which resolved by 3 weeks in all subjects, without permanent damage or resultant atrophy of the musculature. In cases where inflammation was observed on the skin overlying the targeted tumor region, scar tissue was formed and resolved within 2 weeks post treatment. Thus, preliminary studies suggest that histotripsy can be performed relatively safely in a controlled situation, although further work showing the effect of histotripsy on central hepatic structures such as the veins and bile duct, must be performed, though previous large animal studies have indicated no damage to veins near the histotripsy ablation zone while treating liver [46].

In this study, the observation of multiple prominent regions of necrosis in post-histotripsy recurrent tumor compared to the control tumor may be indicative of a histotripsy treatment response in a subcutaneous tumor microenvironment. While in some cancers the development of a necrotic core in untreated tumors has been associated with increased tumor size, high-grade tumor progression, and poor prognosis [47], treatment induced HCC tumor necrosis is a desired outcome for chemotherapy and many local interventional therapies including TACE, RFA, MWA, percutaneous ablation [48-51]. Some studies have shown that when locoregional interventional bridging treatments were utilized for downstaging prior to transplantation, extended post-interventional tumor necrosis was associated with increased recurrence-free long-term survival in patients with HCC [52, 53]. Conversely, some studies have demonstrated that the post-ablation necrosis did not significantly influence the disease-free survival of patients who underwent locoregional therapies, and in fact resulted in longer time to local progression [54, 55]. Given the limited number of animals and the immunocompromised subcutaneous tumor microenvironment in the current study, further investigation is necessary in orthotopic tumor models to fully understand the effect of histotripsy on inducing regulated tumor necrosis and the eventual impact on disease-free survival.

There are a few other limitations of this study, primarily related to the choice of tumor model. First, the subcutaneous tumors did not allow sufficient ablation margin beyond the tumor boundary, and hence viable residual tumor cells post treatment resulted in eventual recurrent tumor. Second, the subcutaneous model cannot replicate the tumor microenvironment as well as an orthotopic model. This limits the evaluation of the invasive characteristics of the tumor and limits the metastatic potential of the tumor. Third, the immunodeficient nature of the murine hosts did not allow us to examine the role of an intact immune system in tumor response to histotripsy. Since the ablated tumor material is left in situ, the presence of an intact immune system may influence the response to histotripsy, especially in cases where the remnants may include viable tumor cells or components of the proteins in the tumor cells. In the next two chapters of this dissertation, we investigate the long-term biological and immunological effects of histotripsy for treatment of HCC in immunocompetent, orthotopic rodent liver tumor models. Additionally, the use of basic MR sequences without intravenous contrast agents precluded the possibility to detect enhancement which might be used to identify residual viable tumor. Future studies with administration of intravenous MR contrast agent after ablation are needed. Finally, as the current therapy system is specifically designed for rodents, the volumetric ablation rate is low due to the necessary requirement of smaller focal zone (higher US frequency). In a large animal or clinical system, the volumetric ablation rate is higher as larger focal zones (lower US frequency) and electronic focal steering are utilized.

Overall, this study demonstrates the potential of histotripsy for non-invasive tumor ablation using a subcutaneous immunocompromised murine model. The study also begins to characterize the MR imaging findings seen after histotripsy treatment of subcutaneous HCC tumors in mice and underscores its importance in the assessment of ablation success. Continued studies of histotripsy in in vivo orthotopic, immunocompetent tumor models will prove beneficial to continue to understand this new ablative technology and its safety and efficacy for potential translation to the clinic.

2.5 References

1. Siegel RL, Miller KD, Jemal A. Cancer statistics, 2019. CA Cancer J Clin. 2019;69(1):7-34. Epub 2019/01/08. doi: 10.3322/caac.21551. PubMed PMID: 30620402.

2. Ferlay J, Soerjomataram I, Dikshit R, Eser S, Mathers C, Rebelo M, et al. Cancer incidence and mortality worldwide: sources, methods and major patterns in GLOBOCAN 2012. Int J Cancer. 2015;136(5):E359-86. Epub 2014/10/09. doi: 10.1002/ijc.29210. PubMed PMID: 25220842.

3. Altekruse SF, Henley SJ, Cucinelli JE, McGlynn KA. Changing hepatocellular carcinoma incidence and liver cancer mortality rates in the United States. Am J Gastroenterol. 2014;109(4):542-53. Epub 2014/02/11. doi: 10.1038/ajg.2014.11. PubMed PMID: 24513805; PubMed Central PMCID: PMCPMC4148914.

4. Inchingolo R, Posa A, Mariappan M, Spiliopoulos S. Locoregional treatments for hepatocellular carcinoma: Current evidence and future directions. World J Gastroenterol. 2019;25(32):4614-28. doi: 10.3748/wjg.v25.i32.4614. PubMed PMID: 31528090; PubMed Central PMCID: PMCPMC6718039.

5. Cho YK, Rhim H, Noh S. Radiofrequency ablation versus surgical resection as primary treatment of hepatocellular carcinoma meeting the Milan criteria: a systematic review. J Gastroenterol Hepatol. 2011;26(9):1354-60. doi: 10.1111/j.1440-1746.2011.06812.x. PubMed PMID: 21679247.

6. Small R, Lubezky N, Ben-Haim M. Current controversies in the surgical management of colorectal cancer metastases to the liver. Isr Med Assoc J. 2007;9(10):742-7. PubMed PMID: 17987765.

7. Tinkle CL, Haas-Kogan D. Hepatocellular carcinoma: natural history, current management, and emerging tools. Biologics. 2012;6:207-19. Epub 2012/07/17. doi: 10.2147/BTT.S23907. PubMed PMID: 22904613; PubMed Central PMCID: PMCPMC3421475.

8. Mazzaferro V, Regalia E, Doci R, Andreola S, Pulvirenti A, Bozzetti F, et al. Liver transplantation for the treatment of small hepatocellular carcinomas in patients with cirrhosis. N Engl J Med. 1996;334(11):693-9. doi: 10.1056/NEJM199603143341104. PubMed PMID: 8594428.

9. Ruers T, Bleichrodt RP. Treatment of liver metastases, an update on the possibilities and results. Eur J Cancer. 2002;38(7):1023-33. PubMed PMID: 11978527.

10. Sawrie SM, Fiveash JB, Caudell JJ. Stereotactic body radiation therapy for liver metastases and primary hepatocellular carcinoma: normal tissue tolerances and toxicity. Cancer Control. 2010;17(2):111-9. doi: 10.1177/107327481001700206. PubMed PMID: 20404794.

11. Livraghi T, Makisalo H, Line PD. Treatment options in hepatocellular carcinoma today. Scand J Surg. 2011;100(1):22-9.

12. Rossi L, Zoratto F, Papa A, Iodice F, Minozzi M, Frati L, et al. Current approach in the treatment of hepatocellular carcinoma. World J Gastrointest Oncol. 2010;2(9):348-59. doi: 10.4251/wjgo.v2.i9.348. PubMed PMID: 21160806; PubMed Central PMCID: PMCPMC2999141.

13. Balogh J, Victor D, Asham EH, Burroughs SG, Boktour M, Saharia A, et al. Hepatocellular carcinoma: a review. J Hepatocell Carcinoma. 2016;3:41-53. Epub 2016/10/05. doi: 10.2147/JHC.S61146. PubMed PMID: 27785449; PubMed Central PMCID: PMCPMC5063561.

14. Poulou LS, Botsa E, Thanou I, Ziakas PD, Thanos L. Percutaneous microwave ablation vs radiofrequency ablation in the treatment of hepatocellular carcinoma. World J Hepatol. 2015;7(8):1054-63. doi: 10.4254/wjh.v7.i8.1054. PubMed PMID: 26052394; PubMed Central PMCID: PMCPMC4450182.

15. Zibari GB, Riche A, Zizzi HC, McMillan RW, Aultman DF, Boykin KN, et al. Surgical and nonsurgical management of primary and metastatic liver tumors. Am Surg. 1998;64(3):211-20; discussion 20-1. PubMed PMID: 9520809.

16. Fukuda H, Ito R, Ohto M, Sakamoto A, Karasawa E, Yamaguchi T, et al. Treatment of small hepatocellular carcinomas with US-guided high-intensity focused ultrasound. Ultrasound Med Biol. 2011;37(8):1222-9. Epub 2011/06/08. doi: 10.1016/j.ultrasmedbio.2011.04.020. PubMed PMID: 21645963.

17. Parsons JE, Cain CA, Abrams GD, Fowlkes JB. Pulsed cavitational ultrasound therapy for controlled tissue homogenization. Ultrasound Med Biol. 2006;32(1):115-29. Epub 2005/12/21. doi: S0301-5629(05)00374-1 [pii]

10.1016/j.ultrasmedbio.2005.09.005. PubMed PMID: 16364803.

18. Roberts WW, Hall TL, Ives K, Wolf JS, Jr., Fowlkes JB, Cain CA. Pulsed cavitational ultrasound: a noninvasive technology for controlled tissue ablation (histotripsy) in the rabbit kidney. J Urol. 2006;175(2):734-8. Epub 2006/01/13. doi: S0022-5347(05)00141-2 [pii]

10.1016/S0022-5347(05)00141-2. PubMed PMID: 16407041.

19. Xu Z, Ludomirsky A, Eun LY, Hall TL, Tran BC, Fowlkes JB, et al. Controlled ultrasound tissue erosion. IEEE Trans Ultrason Ferroelectr Freq Control. 2004;51(6):726-36. Epub 2004/07/13. PubMed PMID: 15244286; PubMed Central PMCID: PMC2669757.

20. Maxwell AD, Cain CA, Hall TL, Fowlkes JB, Xu Z. Probability of cavitation for single ultrasound pulses applied to tissues and tissue-mimicking materials. Ultrasound Med Biol. 2013;39(3):449-65. Epub 2013/02/04. doi: 10.1016/j.ultrasmedbio.2012.09.004. PubMed PMID: 23380152; PubMed Central PMCID: PMCPMC3570716.

21. Maxwell AD, Wang TY, Cain CA, Fowlkes JB, Sapozhnikov OA, Bailey MR, et al. Cavitation clouds created by shock scattering from bubbles during histotripsy. J Acoust Soc Am.

2011;130(4):1888-98. doi: 10.1121/1.3625239. PubMed PMID: 21973343; PubMed Central PMCID: PMCPMC3206907.

22. Vlaisavljevich E, Greve J, Cheng X, Ives K, Shi J, Jin L, et al. Non-Invasive Ultrasound Liver Ablation Using Histotripsy: Chronic Study in an In Vivo Rodent Model. Ultrasound Med Biol. 2016;42(8):1890-902. Epub 2016/05/04. doi: 10.1016/j.ultrasmedbio.2016.03.018. PubMed PMID: 27140521; PubMed Central PMCID: PMCPMC4912895.

23. Zhao G, Cui J, Qin Q, Zhang J, Liu L, Deng S, et al. Mechanical stiffness of liver tissues in relation to integrin beta1 expression may influence the development of hepatic cirrhosis and hepatocellular carcinoma. J Surg Oncol. 2010;102(5):482-9.

24. Umale S, Chatelin S, Bourdet N, Deck C, Diana M, Dhumane P, et al. Experimental in vitro mechanical characterization of porcine Glisson's capsule and hepatic veins. J Biomech. 2011;44(9):1678-83.

25. Vlaisavljevich E, Kim Y, Owens G, Roberts W, Cain C, Xu Z. Effects of tissue mechanical properties on susceptibility to histotripsy-induced tissue damage. Phys Med Biol 2014;59(2):253-70. Epub 2013/12/20. doi: 10.1088/0031-9155/59/2/253. PubMed PMID: 24351722; PubMed Central PMCID: PMCNIHMSID #553779.

26. Vlaisavljevich E, Maxwell A, Warnez M, Johnsen E, Cain C, Xu Z. Histotripsy-induced cavitation cloud initiation thresholds in tissues of different mechanical properties. IEEE Transactions on Ultrasonics, Ferroelectrics, and Frequency Control. 2014;61(2):341-52. Epub 2014/01/30. doi: 10.1109/TUFFC.2014.6722618. PubMed PMID: 24474139; PubMed Central PMCID: PMCNIHMSID # 612783.

27. Vlaisavljevich E, Kim Y, Allen S, Owens G, Pelletier S, Cain C, et al. Image-guided non-invasive ultrasound liver ablation using histotripsy: feasibility study in an in vivo porcine model. Ultrasound Med Biol. 2013;39(8):1398-409. Epub 2013/05/21. doi: 10.1016/j.ultrasmedbio.2013.02.005. PubMed PMID: 23683406; PubMed Central PMCID: PMC3709011.

28. Hall TL, Fowlkes JB, Cain CA. A real-time measure of cavitation induced tissue disruption by ultrasound imaging backscatter reduction. IEEE Trans Ultrason Ferroelectr Freq Control. 2007;54(3):569-75. Epub 2007/03/23. PubMed PMID: 17375825.

29. Allen SP, Hall TL, Cain CA, Hernandez-Garcia L. Controlling cavitation-based image contrast in focused ultrasound histotripsy surgery. Magn Reson Med. 2015;73(1):204-13. Epub 2014/01/29. doi: 10.1002/mrm.25115. PubMed PMID: 24469922.

30. Zhang X, Miller RM, Lin KW, Levin AM, Owens GE, Gurm HS, et al. Real-time feedback of histotripsy thrombolysis using bubble-induced color Doppler. Ultrasound Med Biol. 2015;41(5):1386-401. Epub 2015/01/28. doi: 10.1016/j.ultrasmedbio.2014.12.006. PubMed PMID: 25623821; PubMed Central PMCID: PMCPMC4398659.

31. Vlaisavljevich E, Kim Y, Allen S, Owens G, Pelletier S, Cain C, et al. Image-guided non-invasive ultrasound liver ablation using histotripsy: feasibility study in an in vivo porcine model.

Ultrasound Med Biol. 2013;39(8):1398-409. Epub 2013/05/21. doi: 10.1016/j.ultrasmedbio.2013.02.005. PubMed PMID: 23683406; PubMed Central PMCID: PMCPMC3709011.

32. Smolock AR, Cristescu MM, Vlaisavljevich E, Gendron-Fitzpatrick A, Green C, Cannata J, et al. Robotically Assisted Sonic Therapy as a Noninvasive Nonthermal Ablation Modality: Proof of Concept in a Porcine Liver Model. Radiology. 2018;287(2):485-93. Epub 2018/01/30. doi: 10.1148/radiol.2018171544. PubMed PMID: 29381870.

33. Hall TL, Kieran K, Ives K, Fowlkes JB, Cain CA, Roberts WW. Histotripsy of rabbit renal tissue in vivo: temporal histologic trends. J Endourol. 2007;21(10):1159-66. Epub 2007/10/24. doi: 10.1089/end.2007.9915. PubMed PMID: 17949317.

34. Takenaka K, Prasolava TK, Wang JC, Mortin-Toth SM, Khalouei S, Gan OI, et al. Polymorphism in Sirpa modulates engraftment of human hematopoietic stem cells. Nat Immunol. 2007;8(12):1313-23. Epub 2007/11/04. doi: 10.1038/ni1527. PubMed PMID: 17982459.

35. Shultz LD, Goodwin N, Ishikawa F, Hosur V, Lyons BL, Greiner DL. Human cancer growth and therapy in immunodeficient mouse models. Cold Spring Harb Protoc. 2014;2014(7):694-708. Epub 2014/07/01. doi: 10.1101/pdb.top073585. PubMed PMID: 24987146; PubMed Central PMCID: PMCPMC4411952.

36. Cao X, Shores EW, Hu-Li J, Anver MR, Kelsall BL, Russell SM, et al. Defective lymphoid development in mice lacking expression of the common cytokine receptor gamma chain. Immunity. 1995;2(3):223-38. PubMed PMID: 7697543.

37. DiSanto JP, Müller W, Guy-Grand D, Fischer A, Rajewsky K. Lymphoid development in mice with a targeted deletion of the interleukin 2 receptor gamma chain. Proc Natl Acad Sci U S A. 1995;92(2):377-81. PubMed PMID: 7831294; PubMed Central PMCID: PMCPMC42743.

38. Vlaisavljevich E, Maxwell A, Warnez M, Johnsen E, Cain CA, Xu Z. Histotripsy-induced cavitation cloud initiation thresholds in tissues of different mechanical properties. IEEE Trans Ultrason Ferroelectr Freq Control. 2014;61(2):341-52. Epub 2014/01/30. doi: 10.1109/tuffc.2014.6722618. PubMed PMID: 24474139; PubMed Central PMCID: PMCPMC4158820.

39. Hidalgo M, Amant F, Biankin AV, Budinská E, Byrne AT, Caldas C, et al. Patient-derived xenograft models: an emerging platform for translational cancer research. Cancer Discov. 2014;4(9):998-1013. Epub 2014/07/15. doi: 10.1158/2159-8290.CD-14-0001. PubMed PMID: 25185190; PubMed Central PMCID: PMCPMC4167608.

40. Tentler JJ, Tan AC, Weekes CD, Jimeno A, Leong S, Pitts TM, et al. Patient-derived tumour xenografts as models for oncology drug development. Nat Rev Clin Oncol. 2012;9(6):338-50. Epub 2012/04/17. doi: 10.1038/nrclinonc.2012.61. PubMed PMID: 22508028; PubMed Central PMCID: PMCPMC3928688.

41. Coad JE, Kosari K, Humar A, Sielaff TD. Radiofrequency ablation causes 'thermal fixation' of hepatocellular carcinoma: a post-liver transplant histopathologic study. Clin Transplant. 2003;17(4):377-84. PubMed PMID: 12868996.

42. Marrero JA, Pelletier S. Hepatocellular carcinoma. Clin Liver Dis. 2006;10(2):339-51, ix. doi: 10.1016/j.cld.2006.05.012. PubMed PMID: 16971265.

43. Lee JM, Trevisani F, Vilgrain V, Wald C. Imaging diagnosis and staging of hepatocellular carcinoma. Liver Transpl. 2011;17 Suppl 2:S34-43. doi: 10.1002/lt.22369. PubMed PMID: 21739567.

44. Iannuccilli JD, Grand DJ, Dupuy DE, Mayo-Smith WW. Percutaneous ablation for small renal masses-imaging follow-up. Semin Intervent Radiol. 2014;31(1):50-63. doi: 10.1055/s-0033-1363843. PubMed PMID: 24596440; PubMed Central PMCID: PMCPMC3930654.

45. Patel N, King AJ, Breen DJ. Imaging appearances at follow-up after image-guided solid-organ abdominal tumour ablation. Clin Radiol. 2017;72(8):680-90. Epub 2017/02/23. doi: 10.1016/j.crad.2017.01.014. PubMed PMID: 28237299.

46. Vlaisavljevich E, Owens G, Lundt J, Teofilovic D, Ives K, Duryea A, et al. Non-Invasive Liver Ablation Using Histotripsy: Preclinical Safety Study in an In Vivo Porcine Model. Ultrasound Med Biol. 2017;43(6):1237-51. Epub 2017/03/21. doi: 10.1016/j.ultrasmedbio.2017.01.016. PubMed PMID: 28318889.

47. Lee SY, Ju MK, Jeon HM, Jeong EK, Lee YJ, Kim CH, et al. Regulation of Tumor Progression by Programmed Necrosis. Oxid Med Cell Longev. 2018;2018:3537471. Epub 2018/01/31. doi: 10.1155/2018/3537471. PubMed PMID: 29636841; PubMed Central PMCID: PMCPMC5831895.

48. Haywood N, Gennaro K, Obert J, Sauer PF, Redden DT, Zarzour J, et al. Does the Degree of Hepatocellular Carcinoma Tumor Necrosis following Transarterial Chemoembolization Impact Patient Survival? J Oncol. 2016;2016:4692139. Epub 2016/02/02. doi: 10.1155/2016/4692139. PubMed PMID: 26949394; PubMed Central PMCID: PMCPMC4754482.

49. Shim JH, Kim KM, Lee YJ, Ko GY, Yoon HK, Sung KB, et al. Complete necrosis after transarterial chemoembolization could predict prolonged survival in patients with recurrent intrahepatic hepatocellular carcinoma after curative resection. Ann Surg Oncol. 2010;17(3):869-77. Epub 2009/12/22. doi: 10.1245/s10434-009-0788-7. PubMed PMID: 20033326.

50. Coletta M, Nicolini D, Benedetti Cacciaguerra A, Mazzocato S, Rossi R, Vivarelli M. Bridging patients with hepatocellular cancer waiting for liver transplant: all the patients are the same? Transl Gastroenterol Hepatol. 2017;2:78. Epub 2017/09/27. doi: 10.21037/tgh.2017.09.01. PubMed PMID: 29034351; PubMed Central PMCID: PMCPMC5639014.

51. Louandre C, Ezzoukhry Z, Godin C, Barbare JC, Mazière JC, Chauffert B, et al. Iron-dependent cell death of hepatocellular carcinoma cells exposed to sorafenib. Int J Cancer. 2013;133(7):1732-42. Epub 2013/04/08. doi: 10.1002/ijc.28159. PubMed PMID: 23505071.

52. Kornberg A, Witt U, Matevossian E, Küpper B, Assfalg V, Drzezga A, et al. Extended postinterventional tumor necrosis-implication for outcome in liver transplant patients with advanced HCC. PLoS One. 2013;8(1):e53960. Epub 2013/01/22. doi: 10.1371/journal.pone.0053960. PubMed PMID: 23349774; PubMed Central PMCID: PMCPMC3551930.

53. Allard MA, Sebagh M, Ruiz A, Guettier C, Paule B, Vibert E, et al. Does pathological response after transarterial chemoembolization for hepatocellular carcinoma in cirrhotic patients with cirrhosis predict outcome after liver resection or transplantation? J Hepatol. 2015;63(1):83-92. Epub 2015/01/31. doi: 10.1016/j.jhep.2015.01.023. PubMed PMID: 25646884.

54. Treska V, Mirka H, Fichtl J, Liska V, Skalicky T, Sutnar A. Effects of liver tumor and post-ablation necrosis volume on the result of radiofrequency ablation. Hepatogastroenterology. 2012;59(117):1537-40. doi: 10.5754/hge11730. PubMed PMID: 22172374.

55. Decaens T, Roudot-Thoraval F, Bresson-Hadni S, Meyer C, Gugenheim J, Durand F, et al. Impact of pretransplantation transarterial chemoembolization on survival and recurrence after liver transplantation for hepatocellular carcinoma. Liver Transpl. 2005;11(7):767-75. doi: 10.1002/lt.20418. PubMed PMID: 15973710.

Chapter 3 Effects of Histotripsy on Local Tumor Progression in an In Vivo Orthotopic Rodent Liver Tumor Model

A majority component of this chapter has been published in *BME Frontiers* © 2020 Tejaswi Worlikar et al.

Reprinted with permission from T. Worlikar, M Mendiratta-Lala, E. Vlaisavljevich, et al., "Effects of Histotripsy on Local Tumor Progression in an in vivo Orthotopic Rodent Liver Tumor Model," (in eng), BME Frontiers, vol. 2020, 2020, doi: 10.34133/2020/9830304.

3.1 Introduction

Liver cancer is a leading cause of cancer-related deaths worldwide and amongst the top ten in the US [1, 2]. Hepatocellular Carcinoma (HCC) is the most common primary liver cancer, accounting for >65% of all liver cancers [3]. In the United States, the incidence of HCC has more than tripled since 1980 [4]. Five-year survival rates for liver cancer in the US are reported at only 18%; the second lowest among all cancer types [1]. HCC is most frequently seen in cirrhotic livers, often diagnosed at advanced stages of the disease when patients have become symptomatic and demonstrate concomitant liver dysfunction. However, with improved HCC screening of the cirrhotic population, tumors are identified at an earlier stage, and patients have a variety of locoregional treatment options.

The management of HCC involves a complex decision-making process, considering not only the tumor extent (i.e., size, location, number, vascular invasion, or extrahepatic involvement) and patient comorbidities but also the severity of liver dysfunction, as most treatments for HCC can exacerbate underlying liver disease [5]. Currently, curative treatment options for HCC include liver transplantation, surgical resection, or thermal ablation [6]. However, approximately 80% of HCC patients are not surgical candidates. Patients with HCC eligible for liver transplant require an extensive evaluation and a mandatory waiting period resulting in lengthening wait times for a donor organ [7, 8]. Even then, almost 70% and 20% of patients undergoing resection and transplantation respectively, develop recurrent HCC [9, 10]. Locoregional therapies such as transcatheter arterial chemoembolization (TACE), transarterial radioembolization (TARE), stereotactic body radiotherapy (SBRT), and percutaneous image-guided ablations including radiofrequency ablation (RFA), microwave ablation (MWA) and cryoablation, are commonly used for early or intermediate stage treatment [11, 12]. High intensity focused ultrasound (HIFU) guided by real-time magnetic resonance imaging (MRI) or ultrasound, is a non-invasive thermal ablation method that deposits continuous ultrasound waves or long ultrasound bursts to generate sudden, localized heat to destroy focal tumor by coagulative necrosis. Locoregional therapy has demonstrated improved disease-free and overall survival in patients who cannot undergo resection and is used as a bridge to transplantation or for down-staging borderline-eligible patients for transplant [15]. However, each form of locoregional therapy has different limitations based on tumor location and extent of disease, as well as morbidity based on the degree of underlying liver dysfunction secondary to cirrhosis [4, 16-18].

Histotripsy is the first non-invasive, non-ionizing, non-thermal, mechanical ablation technique that employs acoustic cavitation to destroy target tissue with millimeter accuracy [19, 20]. Using microsecond-duration, low duty cycle (on-time/ total time < 0.1%), high-pressure (P- >15MPa) ultrasound pulses applied from outside the body and focused inside the target tissue, cavitation microbubbles are generated from endogenous nanometer gas pockets in the target tissue with millimeter accuracy [19-21]. The rapid expansion and collapse of cavitation bubbles result in a high strain that disrupts the cellular structure in the target region to form a liquid acellular homogenate [20, 21]. The low duty cycle of the histotripsy pulses (ultrasound on-time/total treatment time << 1%) prevents undesirable thermal effects and may allow homogeneous ablations in highly vascular organs such as the liver [22]. In addition, the structural integrity of large blood vessels, nerves, and bile ducts can be preserved inside the treatment region due to the higher mechanical strength and resistance of collagen-based tissue to histotripsy-induced damage in comparison to non-collagenous tissues such as parenchymal organs and tumors [23-26]. Though histotripsy ablation can be visualized on both ultrasound and MRI [27, 28], we are currently using ultrasound imaging for real-time treatment guidance and MRI for post-treatment monitoring.

In previous studies, we have demonstrated that histotripsy can non-invasively break down non-cancerous liver tissue into liquefied homogenate with no intact cellular structure in a human-scale porcine model and rodent model [22, 25, 29, 30], with the ablated homogenate completely absorbed by the body within a month. In an immunocompromised subcutaneous HCC murine model, histotripsy was able to ablate the target tumor, which was resorbed over time, resulting in an effective reduction of local tumor progression and improvement in survival outcomes [31]. However, due to lack of treatment margin, untreated viable residual tumor at the boundary eventually led to progression. In this longitudinal study, the effect of partial and complete histotripsy tumor ablation on local tumor progression was investigated in an orthotopic immunocompetent rodent HCC model for the first time.

3.2 Materials and Methods

3.2.1 Experimental Design and Technical Design

Orthotopic N1-S1 hepatic tumors were developed in immunocompetent Sprague-Dawley rodent hosts. Liver tumors were targeted for histotripsy ablation either partially (50 - 75% tumor volume) or completely (100% tumor volume), and animals from both groups were monitored for up to 3 months by MRI for local tumor response and examined by histological evaluation at study endpoint. Additionally, MRI and pathology were used to evaluate for distant intra-hepatic metastasis following histotripsy ablation. Primary tumor growth characteristics, tumor response to histotripsy, MR imaging appearance, and survival outcomes were assessed.

The study protocol is shown in Figure 3-1. N1-S1 tumor cells were injected in the inferior liver lobe of 30 Sprague Dawley rats weighing 200-250g. In the survival study, the rats were categorized into three groups based on the tumor volume targeted for ablation: A) partially targeted (n=6), B) entirely targeted (n=9), C) control (n=6). To demonstrate the acute response, a fourth group of rats, D (n=2), was euthanized immediately after histotripsy. MRI and pathology were performed on the acute rats. Five rats did not develop primary tumors and were thus excluded from the study. Two rats developed tumors <5 mm in diameter and were also excluded from the study. Histotripsy ablation (either partial or complete) was performed once the tumor measured a minimum of 5 mm in its largest diameter. Rats in the survival study were monitored weekly post ablation using MRI for up to 3 months or euthanized when the maximum tumor diameter exceeded 25 mm. For the partial ablation groups, approximately 50 - 75% of the tumor volume was targeted for ablation by histotripsy. In the entire tumor ablation group, the entire tumor was targeted for ablation, with an additional small margin (<2 mm) of hepatic parenchyma beyond the tumor boundary included in the target region. The choice of ablation volumes (viable residual tumor intentionally left untargeted versus tumor completely ablated with additional margin of healthy liver tissue) was selected to observe the differences in treatment response and survival outcomes. The control rats received no treatment.

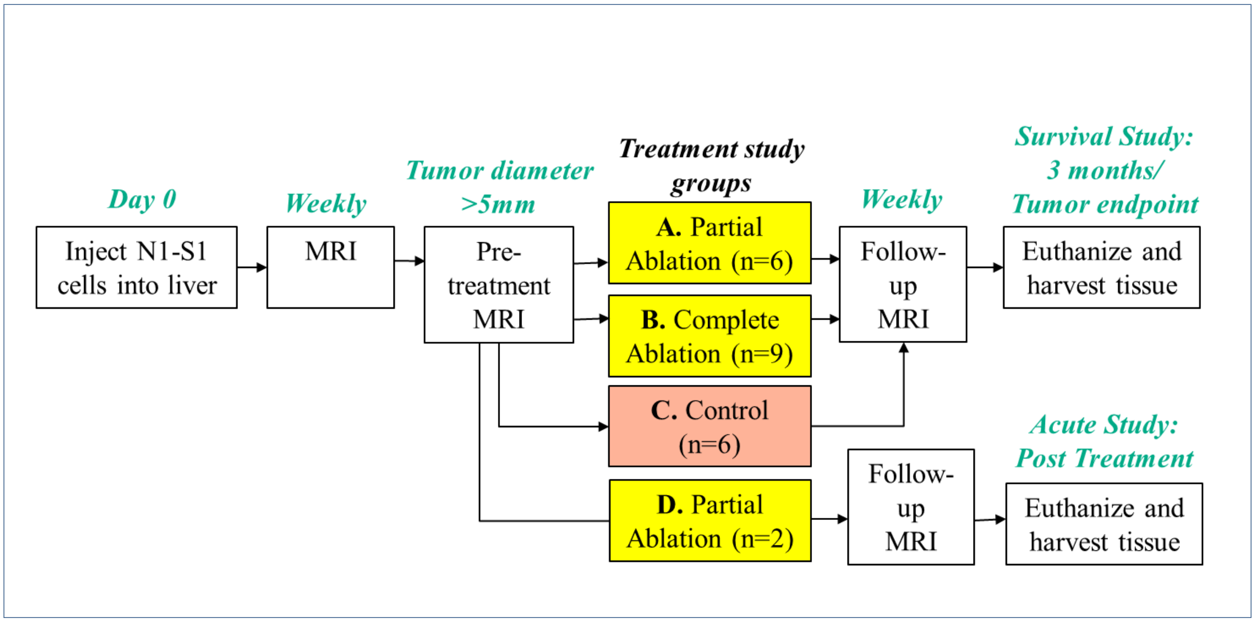

Figure 3-1 ***Study Protocol****: Histotripsy ablation (either partial or entire tumor) was performed once the tumor measured a minimum of 5 mm in the largest diameter. The survival groups A, B, and C were survived and monitored weekly using MRI for up to 3 months post treatment or until the maximum tumor diameter exceeded 25 mm. The acute rats (group D) were euthanized immediately after ablation. For the partial ablation groups A and D, 50 - 75% of the tumor volume was ablated by histotripsy. In the entire tumor ablation group B, the entire tumor with additional margin was targeted for ablation. Animals in control group C received no treatment.*

3.2.2 Cell Preparation

N1-S1 (ATCC® CRL-1604™) cells were obtained directly from the ATCC cell line repository (shipped on 07/09/2018) and were cultivated in Iscove's Modified Dulbecco's Medium (IMDM) containing 4 mM L-glutamine, 4500 mg/L glucose, and 1500 mg/L sodium bicarbonate, supplemented with 10% FBS, 1% antimycotic-antibiotic and 1 mL Gentamicin. The cells were maintained at 37°C in a 5% CO2/95% humidified air atmosphere. The N1-S1 (ATCC® CRL-1604™) cell line has been originally established from a hepatoma induced by feeding 4-dimethylaminoazobenzene to a male rat.

3.2.3 Animals and Study Approval

This study was approved by the Institutional Animal Care and Use Committee at the University of Michigan (UM- IACUC, Protocol Number: PRO00007764). The UM-IACUC has specifically approved the internal orthotopic tumors to grow to a 25 mm maximum diameter size, provided that none of the end-stage illness criteria are reached and the animals are monitored weekly using MR imaging. End stage illness and humane endpoints guidelines were determined as follows: animals exhibiting signs of dehydration, emaciation, cachexia, impaired mobility, systemic infection, or abdominal or thoracic bleeding during or immediately after histotripsy treatment were euthanized. The primary method of euthanasia was exposure to CO2 in compressed gas form followed by a secondary method of euthanasia, which consists of inducing bilateral pneumothoraces to ensure death, in accordance with UM-IACUC guidelines.

Thirty Sprague Dawley rats weighing 200-250g were purchased from Taconic (Hudson, New York) and housed and maintained in specific pathogen-free (SPF) conditions in University of Michigan ULAM (Unit for Laboratory Animal Medicine) housing facility. ULAM technicians provided daily animal husbandry care. Animals were housed in ventilated cages with clean nesting material. Animals were housed in biocontainment housing upon the injection of cyclophosphamide and were moved back to regular SPF housing after 3 days, in accordance with the UM-IACUC protocol. Animals were provided with rodent standard lab diet and autoclaved water bottles.

3.2.4 Orthotopic Tumor Inoculation Procedure

All orthotopic tumor inoculation surgeries were performed in accordance with UM-IACUC approved protocol. Twenty-four hours prior to tumor inoculation, rats were administered 100 mg/kg cyclophosphamide via intraperitoneal injection. Prior to and during surgery, the rats were induced and maintained on general anesthesia by inhalation of isoflurane gas (1.5-2.0%) admixed with 1 L/min of oxygen (SurgiVet V704001, Smiths Medical, Waukesha, Wisconsin, USA). A small animal monitoring system was used to monitor the rectal temperature, heart rate and oxygenation (SpO2) levels throughout the surgery. Core body temperature was maintained between 35-37°C with the use of a heating pad and an overhead heating lamp. Sterile field was maintained during surgery and autoclaved instruments were used. The rats were injected with Carprofen (Rimadyl, Pfizer, NY, USA) analgesic (5 mg/kg) subcutaneously before surgery and once every 24 hours for 2 days after surgery for analgesia. The hair covering the chest and abdomen was removed with an electric clipper. The surgical area was sterilized by scrubbing with chlorhexidine spray, a wet 4x4 gauze, and iodine. To expose the liver, an open laparotomy was performed by making a midline incision through the skin and the abdominal wall. Using forceps and spreader, the left liver lobe was isolated. 2-4 million N1-S1 cells suspended in 0.1 ml Matrigel + PBS (phosphate-buffered saline) were injected into the inferior portion of the left lobe and pressure was applied on the injection site using sterile cotton tip applicators to prevent leakage. The muscle layer was closed using absorbable sutures and the skin layer was closed using staples. Animals were transferred to a recovery cage and were monitored until ambulatory; thereafter, they were returned to their housing cage. Approximately one-week post-surgery, the skin staples were removed. All rats were monitored weekly and tumor diameter measurements were quantified using MRI. Once tumor diameters reached 5 mm in the largest dimension, the rats in the treatment groups were treated with histotripsy.

3.2.5 Animal Preparation for Histotripsy

Prior to and during histotripsy, the rats were induced and maintained on general anesthesia by inhalation of isoflurane gas (1.5-2.0%) in 1 L/min of oxygen (SurgiVet V704001, Smiths Medical, Waukesha, Wisconsin, USA). The hair covering the chest and abdominal region was removed with an electric clipper. Core body temperature was recorded using a rectal probe and was maintained between 35-37°C with an overhead heating lamp. Rats were injected with

Carprofen (Rimadyl, Pfizer, NY, USA) analgesic (5 mg/kg) subcutaneously before delivery of histotripsy treatment and once every 24 hours for 2 days after treatment. Immediately after histotripsy, the rats were transferred to a recovery chamber fitted with an overhead heating lamp and were placed on a heated pad. Once the rats recovered from anesthesia and were mobile, they were transferred back to their housing cages. The rats were monitored weekly for the duration of the study. Tumor dimensions and the treatment response were monitored using MR imaging. Animals were survived up to 3 months or until the tumors reached a diameter of 25 mm in maximum diameter (tumor endpoint).

3.2.6 Rodent Histotripsy Setup

Our lab has designed and built a customized 8 element 1 MHz focused ultrasound therapy transducer specifically for rodent histotripsy therapy [43]. The transducer (f number = 0.6) was designed as a ring configuration scaffold consisting of 8 individually focused lead zirconate titanate elements (20 mm diameter) operating at 1 MHz with a focal distance of 32.5 mm using stereolithographic rapid prototyping techniques as discussed by Kim [44]. The histotripsy transducer was driven by a custom-built high-voltage pulser controlled by a field-programmable gate array (FPGA) development board (DE0-Nano Terasic Technology, HsinChu, Taiwan). The electronical driving signal to the histotripsy therapy transducer was a 1-cycle pulse. The acoustic waveform generated by the histotripsy transducer contained a single dominant negative pressure phase. Histotripsy bubble cloud is produced when the maximum negative amplitude exceeds a distinct pressure threshold (intrinsic threshold) inside the tissue [20, 45]. This intrinsic cavitation threshold depends primarily on the negative pressure phase of the pulse and is not affected by the positive pressure phases of the histotripsy pulses [21]. In free-field, the transducer generated an estimated focal peak negative pressure >30 MPa based on pressure measurements from fiber optic hydrophone [22]. A 20 MHz B-mode ultrasound imaging probe (L40-8/12, Ultrasonix, Vancouver, Canada) was co-aligned with the center of the therapy transducer to allow visualization of the focal ablation volume in real time. The ultrasound therapy transducer and the imaging probe were mounted to a motorized 3-axis positioning system (stepper motor: 17MDSI102S, Anaheim Automation, Anaheim, CA, USA and linear motion system: MS33-100218, Thomson Linear Motor System, Radford, VA, USA) to mechanically scan the therapy focus across a 3D target ablation volume (Figures 3-2A, B). The manufacturer precision for the linear motion system is specified as 5 µm and the stepper motor step size resolution is listed as 0.225o. Water was used as the ultrasound coupling medium by immersing the transducer and imaging probe in a tank of degassed water maintained at 35–37°C by means of a coil heater. The rat was placed on a custom-built animal platform just over the water tank.

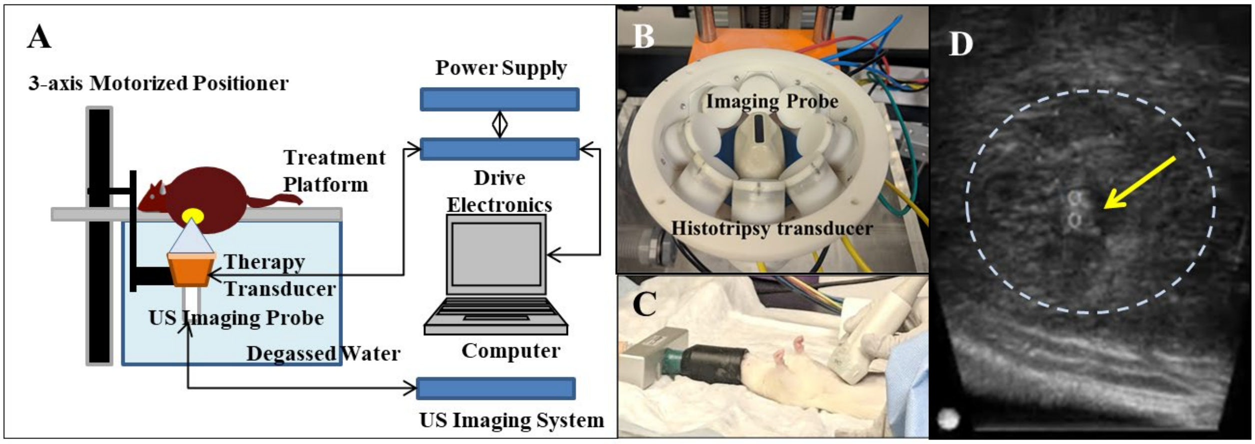

Figure 3-2 ***Histotripsy Setup and Procedure.*** *(A) Histotripsy therapy transducer, driven by custom-built driver electronics, is interfaced with a computer which delivers histotripsy pulses to generate focal cavitation. Single focus is scanned to cover desired target volume by using motorized positioner to control movement of the therapy transducer and the imaging probe. (B) The 1 MHz histotripsy therapy transducer constructed as an 8-element ring configuration with the coaxially aligned imaging probe in the center (C) Ultrasound imaging of the rat liver and tumor was performed prior to placing the rat on the treatment platform to determine tumor location. The tumor location is marked before the rat is placed on the treatment platform, which contains an aperture to allow the tumor region intended for treatment to be immersed in water (ultrasound coupling medium). (D) Generation of hyperechoic cavitation cloud (yellow arrow, two small circles mark the axial extent of the cavitation) in liver tumor (dashed- lines).*

3.2.7 Histotripsy Ablation

To identify the therapy focus on ultrasound imaging, test histotripsy pulses were delivered to the water tank by the therapy transducer to generate a “bubble cloud” (elliptical shape of approximately 1 x 3 mm in water) which appeared as a hyperechoic cavitation zone on ultrasound imaging. The position of the resultant small focal hyperechoic cavitation zone was then marked as the therapy focal position on the ultrasound image.

After sedation, the animal was placed supine and dedicated real-time ultrasound grayscale imaging was performed over the liver to identify the location and size of the tumor (Figure 3-2C). The approximate location was marked with an ‘X’ with a washable marker. Thereafter, the animal was placed prone on the treatment table with the abdominal region submerged in the degassed water. The therapy transducer was then moved by the motorized positioning system to align the therapy transducer focus with the center of the tumor on the ultrasound image. All tumors were measured by real-time ultrasound imaging and correlation was made with the most recent MRI to ensure accurate size measurement and treatment of adequate tumor volumes. The boundaries of the intended treatment region in 3 dimensions (axial, lateral and elevational) were manually determined on ultrasound imaging and an ellipsoid ‘volume’ was generated from these user-defined boundary values using a custom MATLAB script. This treatment ellipsoid encompassed the 3D tumor volume to be targeted for ablation and consisted of a grid of uniformly spaced therapy focal zones (~0.5 – 0.75 mm (lateral, elevational directions) and ~0.75 - 0.9 mm (axial direction) between adjacent focal volumes (Supplementary Figure S3-1). This target volume, as defined on ultrasound imaging, covered approximately 50-75% of the original tumor volume for partial ablation or the complete tumor with additional margin (up to 2 mm) for entire ablation. The transducer focus was mechanically scanned (using the motorized positioning system to move the therapy transducer and the imaging probe) to follow the MATLAB-generated grid of focal locations within the treatment ellipsoid. At each focal location, 50 histotripsy pulses at 100 Hz PRF (p- >30 MPa) were delivered, which equate to 0.5 seconds of ablation time. After ablation, the targeted region appeared hypoechoic on ultrasound imaging, enabling real-time feedback. During ablation, histotripsy-induced cavitation was hyperechoic in appearance compared to the surrounding tissue on ultrasound imaging (Figure 3-2D), which was used to monitor the ablation. Selection of histotripsy parameters (Table 3-1) was based on results of previous in vivo and in vitro work done in our lab [46].

Table 3-1 Histotripsy Ablation Parameters

Histotripsy Pulse Length	1-2 cycles
PRF (Pulse Repetition Frequency)	100 Hz
Estimated Peak Negative Pressure at Focus	>30MPa-
Number of Treatment Locations in Target Volume	2000-3000
Number of Histotripsy Pulses Delivered to each Location	50
Treatment Location Spacing within Target Volume	0.5 - 0.7 mm (lateral, elevational), 0.75 - 0.9 mm (axial)
Treatment Time	10-15 minutes based on the targeted volume

3.2.8 Magnetic Resonance Imaging for Treatment Evaluation

MRI data was obtained within 1 day prior to histotripsy and within 1-day post-histotripsy, followed by weekly imaging to assess the effects of tumor ablation and characterize MR signal variations in tumor appearance. Imaging was performed on a 7.0 T MR small animal scanner using a Direct Drive console (Agilent Technologies, Santa Clara, CA, USA) with a 60 mm inner-diameter transmit-receive radiofrequency (RF) volume coil (Morris Instruments, Ontario, Canada) and 70 mm inner-diameter transmit-receive RF volume coil (Rapid 70, RAPID MR International, Ohio, U.S.A.). Prior to and during imaging, the rats were induced and maintained on general anesthesia by inhalation of isoflurane gas (1.5-2.0%) in 1 L/min of oxygen (SurgiVet

V704001, Smiths Medical, Waukesha, Wisconsin, USA). Respiration was monitored and animal temperature was maintained at 37±0.5 °C using a rectal temperature probe and a custom-built proportional-integral-derivative (PID) controller (LabVIEW, National Instruments, Austin TX) interfaced with a commercially available small animal system (SA Instruments, Stony Brook, NY). Initial pilot scans were performed to confirm positioning. Thereafter, a 2D T2-weighted fast spin-echo (FSE) with respiratory gating was used to visualize the tumor in the coronal plane (Table 2). Intravenous contrast agents were not administered in this study. MRI data was obtained within 1 day prior to histotripsy and within 1 day post-histotripsy, followed by weekly imaging to assess the effects of tumor ablation and characterize variations in imaging appearance. Imaging was performed on a 7.0 T MR scanner using a Direct Drive console (Agilent Technologies, Santa Clara, CA, USA) with a 40 mm inner-diameter transmit-receive radiofrequency (RF) volume coil (Morris Instruments, Ontario, Canada). Prior to and during imaging, the mice were induced and maintained on general anesthesia by inhalation of isoflurane gas (1.5-2.0%) in 1 L/min of oxygen (SurgiVet V704001, Smiths Medical, Waukesha, Wisconsin, USA). Respiration was monitored and animal temperature was maintained at 37±0.5 °C using a rectal temperature probe and a custom-built proportional-integral-derivative (PID) controller (LabVIEW, National Instruments, Austin TX) interfaced with a commercially available small animal system (SA Instruments, Stony Brook, NY). Initial pilot scans were performed to confirm positioning. Thereafter, T2 and T1-weighted fast spin-echo (FSE) sequences and a T2*-weighted gradient-echo (GRE) sequence were used to visualize the tumor in the axial plane (Table 4-2).

Table 3-2 MR Imaging Parameters

TR (ms) *	2000 ms

TEeff (ms)	10 ms
ESP (ms)	10
ETL	8
FOV (mm^2)	60x60
Kzero	2
Data Matrix (zero-filled)	256x256 (512 x 512)
Voxel Size (µm3)	117x117x1000
Slice Thickness (mm)	1
Number of image slices acquired per scan*	15, 20, 21 or 28
Slice Orientation	Coronal
Scan Time (minutes)	~8

*TR = Time to Repetition, TEeff = Effective Echo Time. ESP = echo spacing, ETL = echo train length, FOV = field of view. *In majority of scans (>80%), 21 image slices were acquired. In the only scan acquiring 28 image slices, TR was set to 3000 ms.*

The overall signal characteristics of the pre-treatment and post-treatment tumor using T2-weighted FSE were recorded and compared to each other to identify potential changes which would differentiate non-viable tumor from viable tumor. Tumor volume and post-ablation homogenate volumes were quantified by summing area measurements made from each slice of the 2D T2-weighted FSE acquisition. Tumor diameter measurements were also made on the T2-weighted sequence in orthogonal anterior-posterior (coronal) and superior-inferior (axial) dimensions. Signal characteristics of the pre-treatment tumor and the post-treatment ablation zone were also recorded. Surrounding structures such as the musculature and body wall were evaluated for signs of injury. MR evaluation of the surrounding hepatic parenchyma, overlying histotripsy pathway from the skin to the targeted lesion, and distant sites was also performed to evaluate for local injury or distant metastasis.

3.2.9 Histological Analysis

Post euthanasia, treated tumor, as well as liver tissue samples were harvested and fixed in 10% buffered formalin for histopathological analysis. Fixed tissue samples were submitted to ULAM-IVAC (Unit for Laboratory Animal Medicine – In Vivo Animal Core) for paraffin embedding as well as staining. Samples were sectioned in 5-micron slices and stained with hematoxylin and eosin (H&E). Slides were examined by a board-certified liver pathologist (JS) for histopathologic analysis, under a light microscope (Olympus BX43) which was used to capture images.

3.2.10 Statistical Analysis

Experimental data were analyzed using Microsoft Excel (2013). Pre-treatment timepoint tumor volumes in each survival group (control, partial ablation and complete ablation) were compared with the single-factor ANOVA test, with significance defined as $p < 0.05$. Survival analysis was performed using the Kaplan-Meier method. Survival time data of control and treated rats in each group was compared with the two-tailed Student's t test, with significance defined as $p < 0.05$.

3.3 Results

3.3.1 Clinical Monitoring

All tumor inoculation procedures and histotripsy procedures were well tolerated with no minor or major complications or deaths.

3.3.2 Local Tumor Response to Histotripsy

Effective tumor volume reduction with no recurrence was observed in 9/9 completely ablated animals and 5/6 partially ablated animals (Figure 3-3A). The original untreated tumor demonstrated mild hyperintense signal on T2-weighted MRI when compared to the adjacent uninvolved liver parenchyma. Tumor volumes at the pre-treatment timepoint ranged from 55.26 mm^3 to 2173.05 mm^3 with 636.49 ± 358.52 (mean ± SEM) in the control group, 67.35 mm^3 to 2900.77 mm^3 with 834.18 ± 436.68 in the partial ablation group, and 64.06 mm^3 to 1476 mm^3 with 401.31 ± 148.28 in the entire ablation group. There were no statistically significant differences in the mean tumor volumes of the three groups at the pre-treatment timepoint ($p = 0.58$). Subsequent timepoints are measured from the pre-treatment/ histotripsy timepoint (week 0).

3.3.3 Survival Outcomes

In general, rats in the complete ablation group survived significantly longer than the control rats ($p = 0.039$) (Figure 3-3B). Though animals in the partial ablation group had better survival outcomes than the control group, the difference was not statistically significant ($p = 0.13$) (Figure 3-3B). The survival time was 7.5 ± 2.03 (mean ± SEM) weeks in the control group, 12 ± 0 weeks in complete ablation group, and 10.5 ± 1.5 weeks in partial ablation group. The survival time range was 2-12 weeks for the control group, 3-12 weeks for partial ablation group, and 12 weeks for complete ablation group after histotripsy timepoint. All survival times are reported at the post histotripsy timepoint, which was two weeks post tumor inoculation. 9/9 animals in the complete ablation group, 5/6 animals in partial ablation group, and 3/6 animals in the control group were still surviving at 12 weeks, but euthanized due to reaching the study endpoint per our protocol. Thus, the lack of a significant difference in survival time between the partial ablation and control group is in part due to the study endpoint in our protocol. The remaining 1/6 animals in partial ablation group and 3/6 animals in the control group were euthanized at earlier timepoints due to tumor burden greater than 25 mm in any one dimension.

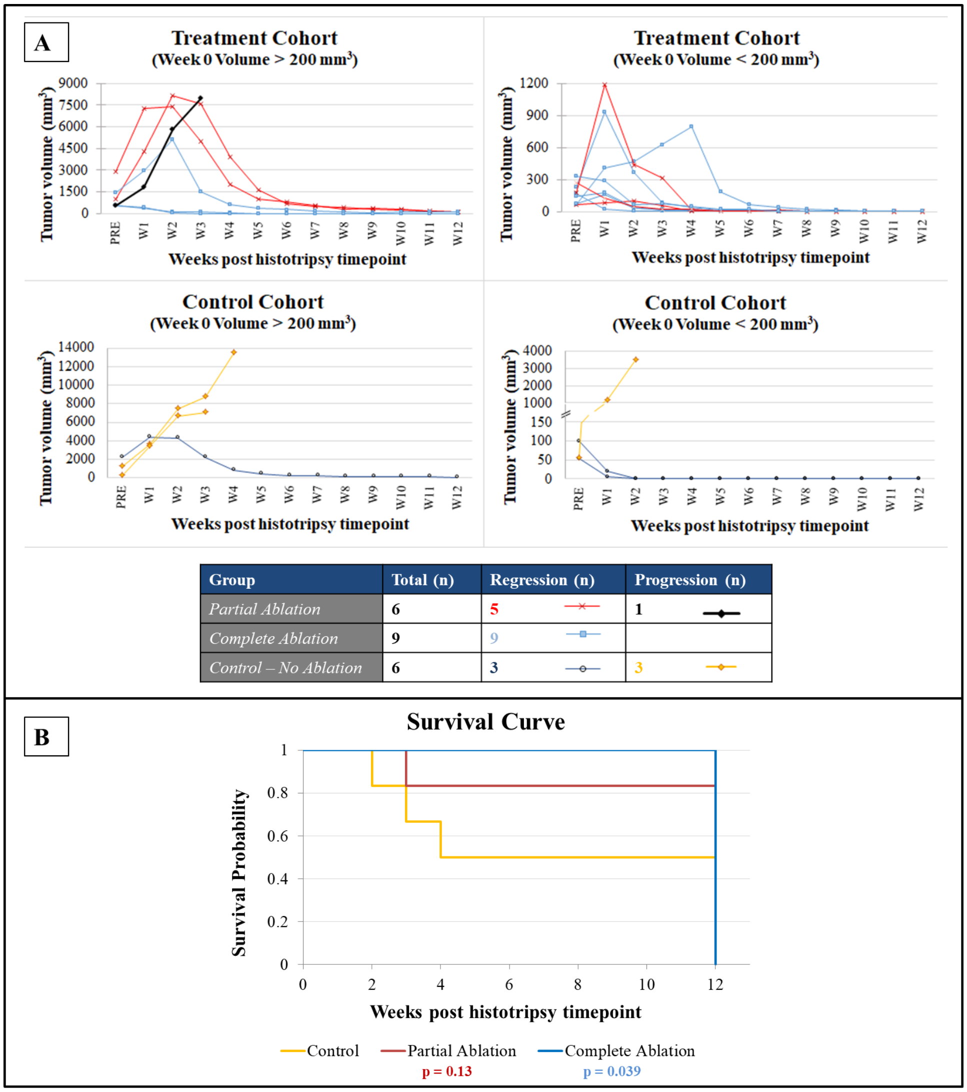

Group	Total (n)	Regression (n)	Progression (n)
Partial Ablation	6	5 —×—	1 —◆—
Complete Ablation	9	9 —■—	
Control – No Ablation	6	3 —○—	3 —◆—

Figure 3-3 ***Histotripsy Tumor Response and Survival Outcomes.*** *(A) Local tumor regression was observed in 9/9 complete ablation cases and 5/6 partial ablation cases irrespective of large tumor volume (>200 mm3) or small tumor volume (<200mm3) as measured at the pre-treatment timepoint (week 0). In contrast, 3/6 control animals demonstrated steady tumor progression while the other 3/6 control animals demonstrated spontaneous regression of their tumors. Individually scaled y-axes are used to more clearly illustrate changes in tumor size. (B) Kaplan Meier survival curve comparing survival outcomes in control, partially ablated, and completely ablated groups. All animals still surviving at 12 weeks were euthanized due to reaching the study endpoint (3 months) in the protocol.*

3.3.4 Tumor Response to Complete Histotripsy Ablation – MRI Observations

Generally, smaller tumors (largest dimension measured < 1 cm) appeared homogeneous, and their appearance became increasingly heterogeneous as the largest dimension measured >1 cm (Figures 3-4, Supplementary Figure S3-2). MRI imaging performed within 6 hours post-ablation demonstrated T2-hypointense signal at the ablation zone (Figure 3-4A). MR imaging performed ~ 1 week after histotripsy ablation demonstrated T2 hyperintense signal within the treatment cavity which mimics that of fluid. The T2 hyperintense appearance persisted for up to 3 weeks post histotripsy, gradually becoming less hyperintense and completely transforming to T2-hypointense signal by week 7 as the treatment cavity decreased in size over time indicating tumor regression (Figures 3-4A, Supplementary Figures S3-2, S3-3). At 8-12 weeks post-histotripsy, a 1-5 mm hypointense area was observed at the original tumor site, indicating fibrous tissue and calcification remnants, as confirmed by histology. Supplementary Figure S3-2 compares the T2W MRI appearance of the post histotripsy lesion at select timepoints with the appearance of viable pre-treatment tumor. Supplementary Figure S3-3 shows imaging observations at all weekly timepoints for the complete ablation case demonstrated in Figure 3-4A.

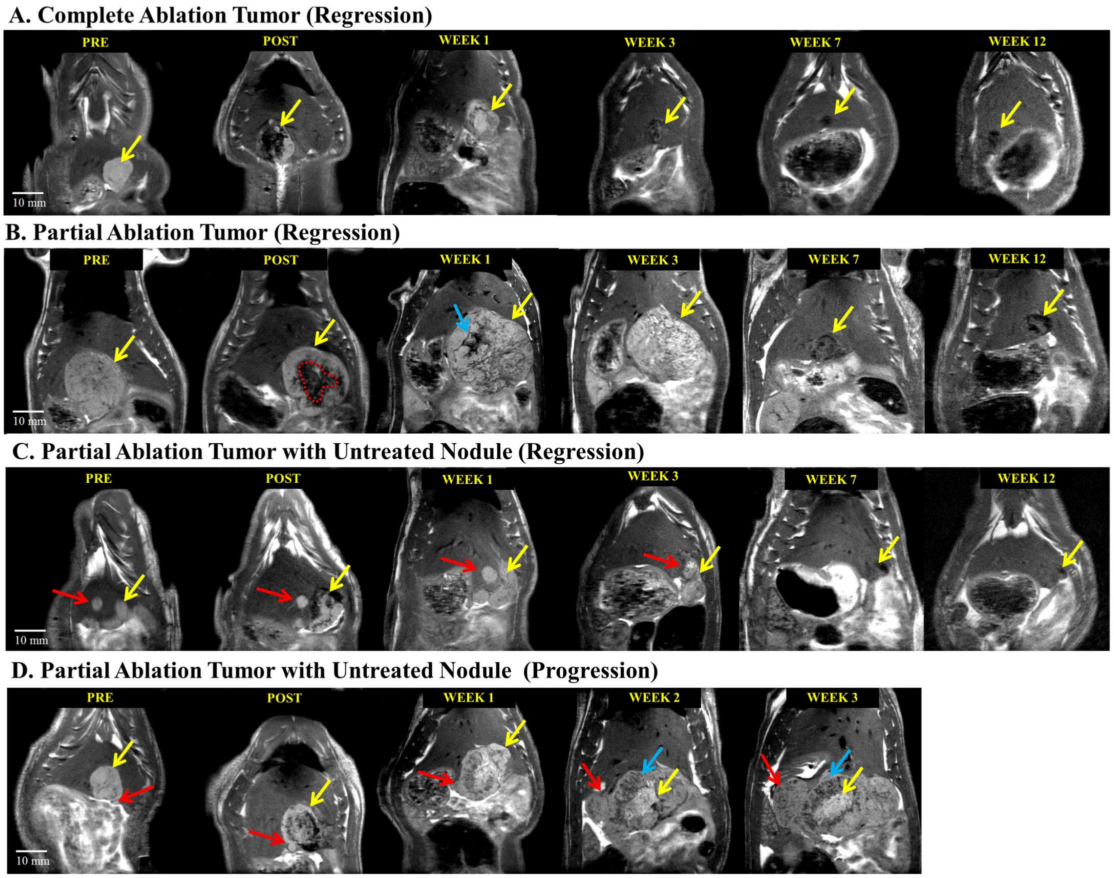

A. Complete Ablation Tumor (Regression)

B. Partial Ablation Tumor (Regression)

C. Partial Ablation Tumor with Untreated Nodule (Regression)

D. Partial Ablation Tumor with Untreated Nodule (Progression)

Figure 3-4 ***Tumor Response to Histotripsy on T2-weighted MRI.*** *The size and appearance of tumor (yellow arrow) in response to complete and partial histotripsy ablation is observed at different timepoints. (A) Complete ablation - pre-treatment (mildly hyperintense), post treatment ablation zone (hypointense), ablation zone at week 1 (mildly hyperintense), week 3 (mildly hypointense, size regression), week 7 (hypointense, size regression) and week 12 (<5 mm hypointense region) (B) Partial ablation - pre-treatment (mildly hyperintense), post treatment ablation zone (hypointense, shown by red dashed lines) and untreated tumor region (mildly hyperintense), lesion at week 1 (mildly hyperintense) with pseudoprogression characteristics (blue arrow), week 3 (mild hyperintense, size regression), week 7 (hypointense, size regression), and week 12 (~5 mm hypointense region). (C) Partial ablation with a separate untreated nodule (red arrow) – ablation zone and untreated nodule at week 1 (mildly hyperintense), week 3 (mildly hyperintense with no size progression), week 7 (hypointense, size regression) and week 12 (<3 mm hypointense region). (D) Partial ablation with adjacent untreated nodule (red arrow) - ablation zone at weeks 1-3 shows a central hyperintense zone (yellow arrow) surrounded by heterogeneous hypointense zone (blue arrow). The untreated nodule (red arrow) increases in size over weeks 1-3 and demonstrates mildly T2-hyperintense signal. In animals demonstrating regression, the hypointense region at the original tumor site observed on ~3 month MRI, indicates near complete resolution of the tumor.*

3.3.5 Tumor Response to Partial Histotripsy Ablation - MRI Observations

For the partially treated tumors, the treatment cavity demonstrated a T2 hypointense signal and the residual untreated tumor demonstrated mild T2 hyperintense signal (Figure 3-4B). The hypointense appearance of the ablation zone seen in the early post-ablation period (<6 hours) allowed for easy delineation between ablated and residual non-ablated tumors. MRI also revealed a transient increase in the size of the lesion when compared to the pre-treatment tumor size at 1 week post histotripsy (Figure 3-4B), presumably due to inflammation derived tumor pseudoprogression. The entire lesion began to regress starting at week 3, resulting in near-complete resolution of the tumor homogenate in weeks 4-12 with a ~5 mm non-tumoral fibrous tissue zone detectable on MRI remaining at the original tumor site at the 3-month timepoint in 5/6 animals (Figure 3-4B and Supplementary Figure S3-4).

Of note, two cases demonstrated a separate small nodular tumor adjacent to the targeted tumor, and the separate small tumor nodule was left untreated. On MRI, the untreated tumor maintained the same appearance after treatment as the pre-treatment tumor. In the first case (Figure 3-4C), both the residual tumor along the margin of the partially ablated tumor and the adjacent untreated nodule responded and regressed starting at week 3, and eventually resulted in near-complete resolution by week 12. However, in the second case (Figure 3-4D), the untreated nodular tumor continued to increase in size and demonstrated signal characteristics similar to the pre-treatment tumor. The treated portion of the tumor demonstrated the expected pseudoprogression at weeks 1-3. The rat was euthanized at week 3 due to increased tumor burden reaching euthanasia limit, and thus the long-term effect of histotripsy on the untreated nodule could not be investigated. Supplementary Figures S3-4 and S3-5 show imaging observations at all weekly timepoints for the partial ablation cases demonstrated in Figures 3-4B, C.

3.3.6 Tumor Response to No Treatment (Control) - MRI Observations

In the control group, tumor burden continued to increase in all animals until two weeks post-inoculation. In three rats, control tumors demonstrated satellite nodules along the periphery of the primary tumor which increased in size. The peripheral satellite nodules also continued to develop which contributed to the progressive increase in tumor burden and the animals were euthanized at by 2-4 weeks (Figure 3-5A). In the other three control animals, tumors developed a diffuse mottled and heterogeneous appearance by week 3 and eventually spontaneously regressed by week 12 (Figure 3-5B). Supplementary Figure S3-6 shows imaging observations at all weekly timepoints for the control tumor demonstrated in Figures 3-5B.

A. Control Tumor (Progression)

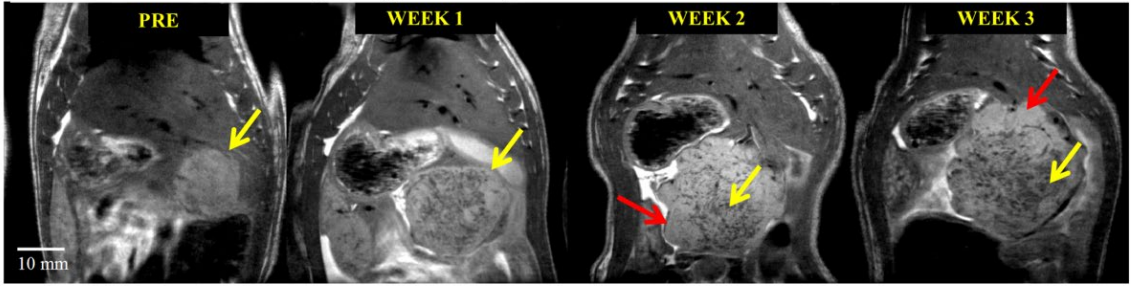

B. Control Tumor (Regression)

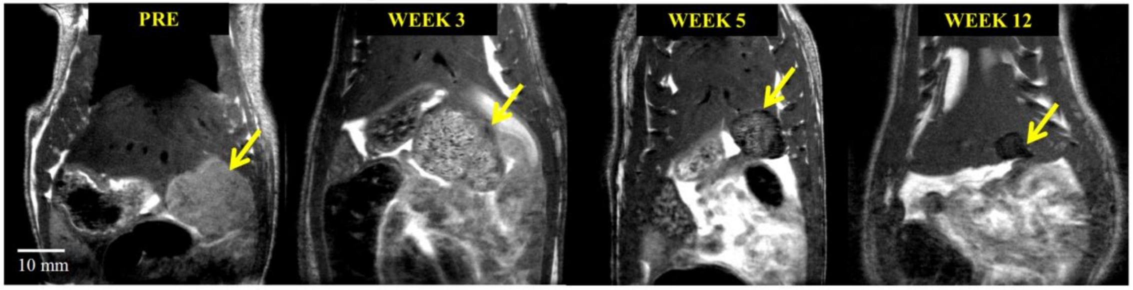

Figure 3-5 ***Control Tumor Evolution on MRI.*** *(A) Control tumor (yellow arrow) demonstrates satellite nodules along the periphery of the primary tumor (red arrow), which eventually contribute to tumor progression. (B) Control tumor (yellow arrow) develops a mottled and heterogeneous appearance, similar to that of pseudoprogression by week 3, and regresses as evidenced by decreasing tumor burden at weeks 5 and 12.*

3.3.7 Effects on Adjacent Tissue

The original ablation volume in the complete treatment cohort (n=9) included up to a 2 mm margin of the normal hepatic parenchyma, to ensure complete ablation of potentially microscopic disease. Post-treatment imaging in all subjects demonstrated ‘pseudoprogression’ of the ablated tumor, in which the entire lesion increased in size, likely a combination of immediate post-treatment edema and the acellular homogenate which was created by histotripsy ablation. This was resolved within 2-3 weeks post-treatment in all subjects demonstrating regression. There was no evidence of immediate post-histotripsy tissue damage along the treatment path outside the treatment zone on MR imaging (i.e., no T2 signal changes). Additionally, there were no gross changes seen on the skin surface in any of the animals treated by histotripsy. Apart from the residual fibrous scar at the treatment zone, there was no imaging or histopathologic evidence of parenchymal atrophy surrounding the ablation zone.

3.3.8 Histological Analysis

In untreated tumors in the control group that did not regress (n=3/6), prominent regions of necrosis were observed at week 3 (euthanasia timepoint) (Figure 3-6A). In the acute study group (n=2), the treated region was composed of extravasated blood cells, fibrin, and inflammatory cells on Day 0 (Figure 3-6B). In the partial ablation survival group, in animals demonstrating regression (n=5/6), histology analysis revealed scar tissue (<5 mm) with scattered dystrophic calcification within the ablated region and a submillimeter rim of inflammatory cells separating the ablated zone from the normal liver at 3 months (euthanasia timepoint) (Figure 3-6C). No residual viable tumor cells were observed. Similar to the partial ablation, in the completely ablated group (n=9/9), the ablation zone also demonstrated scar tissue (<5 mm) with scattered dystrophic calcification and inflammatory cells and no evidence of viable tumor at 3 months (euthanasia timepoint) (Figure 3-6D). These histology observations correlate with the MRI observation of <5 mm T2-hypointense tissue at the original treatment site, indicating complete regression of these tumors to form residual scar tissue. In control rats demonstrating regression, no residual tumor cells were observed, with similar findings of scattered inflammatory cells surrounding scar tissues and calcification at the original tumor site (Figure 3-

6E). In the partial ablation case where the tumor did not regress (n=1/6), the tumor showed necrosis regions at week 3 (Figure 3-6F).

A. Control Tumor, Week 3 (Progression)

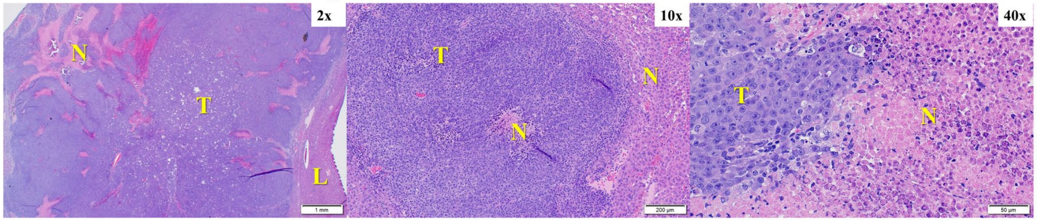

B. Partial Ablation, Day of Treatment

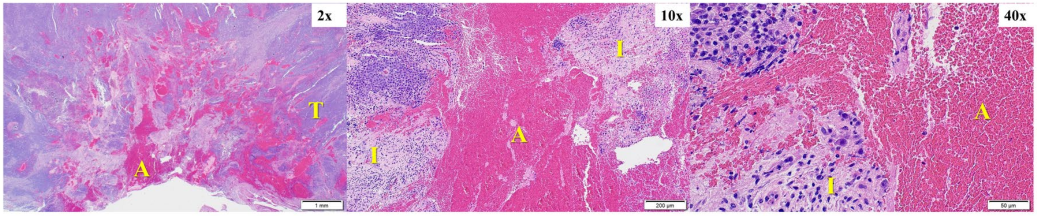

C. Partial Ablation Tumor, Week 12 (Regression)

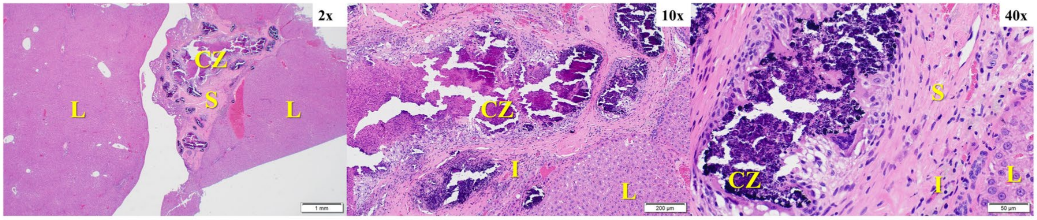

D. Complete Ablation Tumor, Week 12 (Regression)

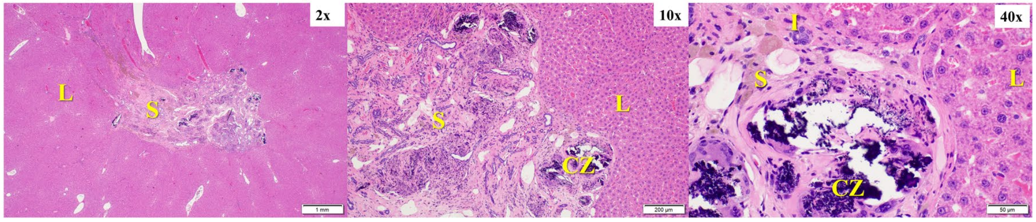

E. Control Tumor, Week 12 (Regression)

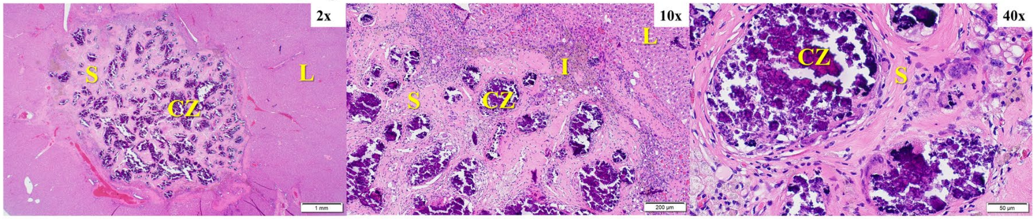

F. Partial Ablation Tumor, Week 3 (Progression)

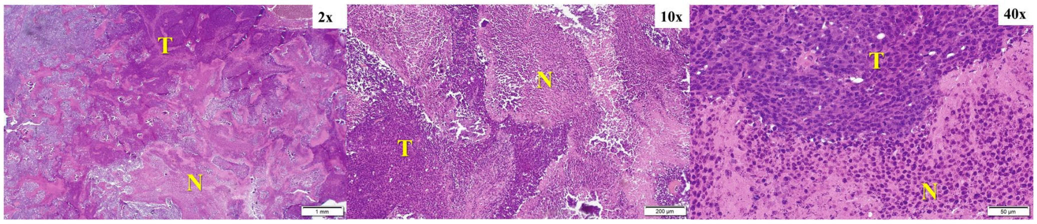

Figure 3-6 ***Representative Histology Images.*** *(A) Control HCC at 3 weeks demonstrating progression, shows viable tumor T with prominent region of necrosis N. (B) Partial ablation on day 0, the ablation zone A is comprised mainly of extravasated red blood cells and fibrin, and is surrounded by regions of inflammatory cells I and regions of viable tumor T. (C) Partial ablation at 12 weeks demonstrating tumor bed completely replaced by scar tissue S and scattered areas of dystrophic calcification CZ within the ablated region with a thin rim of inflammatory cells I*

separating the ablated zone from normal liver L and no evidence of viable tumor. (D) Complete ablation at 3 months demonstrating tumor regression, and replacement by scar tissue S with scattered dystrophic calcification CZ and a thin rim of inflammatory cells I. No evidence of viable residual tumor in the surrounding normal liver L. (E) Control tumor at 3 months demonstrating complete tumor regression, scattered inflammatory cells surrounding scar tissue S and dystrophic calcification CZ at the original tumor site. No evidence of viable residual tumor in the surrounding normal liver L. (F) Partial ablation at 3 weeks demonstrating tumor progression. Viable tumor T is observed with some regions of necrosis N. Timepoints are measured from the histotripsy treatment time as week 0.

3.3.9 Effects on Metastases

No metastases were detected within the liver by gross or microscopic evaluations in any of the ablation groups. However, the N1-S1 tumor model does not naturally develop metastasis, and our results support that histotripsy did not yield unexpected intrahepatic metastasis.

3.4 Discussion

This study evaluated the local tumor progression of orthotopic HCC in response to a single histotripsy treatment in an immune-competent, N1-S1 rodent liver tumor model. The N1-S1 rodent tumor model is one of the most common rodent orthotopic HCC models used for image-guided interventional oncology research [32, 33]. Histotripsy has been studied extensively to treat normal liver tissue in human-scale porcine models [25, 29, 30]. To our knowledge, this is the first study investigating histotripsy ablation of orthotopic, liver tumors in immunocompetent rats with a long term (3 months) follow-up.

Histotripsy ablation responses were evaluated with MRI and histology. Our results demonstrate that histotripsy resulted in effective local tumor burden reduction with no local recurrence in 14/15 treated rats which demonstrated complete regression of the original ablated tumor. The ablated volume was nearly completely resorbed (with only a small focus of residual fibrous scar remaining at original site) in 5/6 rats which underwent partial tumor ablation and 9/9 rats which underwent entire tumor ablation. In these animals, the appearance of the ablated volume had transformed completely to T2-hypointense (indicative of non-tumoral scar tissue) by week 7 and there were no further observable changes in its appearance until the final imaging timepoint at week 12 when it was confirmed by histology that there was no viable tumor. No histotripsy-treated animals demonstrated intrahepatic metastases.

MRI has been utilized to characterize tumor response and to quantify tumor necrosis in pre-clinical animal and human tumor models as well as for the clinical assessment of locoregional therapies [18, 34]. In this study, post-histotripsy MRI results of partially ablated tumors demonstrated clear delineation between treated tumor and residual viable tumor, as seen by differences in their T2 signal. Thus, histotripsy therapeutic response can be assessed by MRI immediately post-ablation, as the signal characteristics of the pre-treatment tumor and the ablated zone are distinct. These characteristics are essential for early post-HCC treatment response evaluation, as the immediate detection of the residual tumor can allow for follow-up re-treatment to ensure adequate ablation. This is a limitation of current practices with some forms of locoregional therapy for HCC (particularly arterial and radiation-based locoregional therapy (TACE, TARE, and SBRT)), in which treatment effectiveness can only be adequately assessed 4-12 weeks post-treatment [35].

MR imaging also demonstrated tumor pseudoprogression (transient increase in the size of the targeted tumor) following histotripsy, seen as an early enlargement of the treatment cavity before subsequently regressing, as evidenced by decreasing the size of the treatment zone and eventual conversion to a small T2 hypointense fibrous nodule. Although the treatment cavity size transiently increased in the early post-treatment time period (up to 3 weeks), the MR imaging appearance of the treatment zone remained distinct from the residual viable tumor, as seen in the partial ablation group. The imaging findings of pseudoprogression are usually seen in tumors treated with systemic immunotherapy (e.g., melanoma, renal cell carcinoma, and squamous cell lung carcinoma), although pseudoprogression has also been reported after locoregional ablation therapies as well as immunological therapies for HCC [36-38]. Previous studies have indicated that an immunologic response to treatment may induce the infiltration of immune mediators and subsequent inflammation within the tumor, which results in the appearance of tumor pseudoprogression [3, 37]. Though histotripsy relies on mechanical cavitation to destroy tumor cells and is not a pure immunologic treatment, the findings of immune cell infiltration surrounding the treatment cavity as seen on histology post-treatment, as well as the increased tumor size 1-3 weeks post histotripsy on MRI evaluation, suggests pseudoprogression may be the initial response to histotripsy, followed by the anti-tumor response resulting in regression of the viable untreated tumor. These results are consistent with the regression of untreated tumors in 5/6 of the partially treated cases. Our recent study has demonstrated that histotripsy ablation of subcutaneous murine B16GP33 melanoma tumors in immunocompetent C57BL/6 murine hosts releases tumor antigens with preserved immunogenicity resulting in a potent local and systemic immunostimulatory response, which reduced distant untreated tumors [39]. In the poorly immunogenic Hepa 1-6 subcutaneous liver tumor model with immunocompetent C57BL/6 murine hosts, histotripsy by itself and in combination with checkpoint inhibition immunotherapy stimulated abscopal immune effects at distant tumor sites [39]. In comparison, in a separate study on immunocompromised mice bearing Hep3B human cell line-derived subcutaneous flank tumors, histotripsy tumor ablation resulted in near-complete resorption of the ablation zone. However, due to a lack of sufficient margin along the skin-ablation zone interface, residual viable tumor cells were observed resulting in eventual tumor recurrence in the immunocompromised mice [31]. Further studies are planned to explore the specific immunomodulation mechanisms in response to histotripsy in orthotopic liver tumor models and directly compare the response in immunocompromised vs immunocompetent hosts.

One confounding result in this study is that 3/6 control rats demonstrated spontaneous regression of their tumors despite lack of treatment, although the other 3 control animals demonstrated steady tumor progression and had to be euthanized due to increased tumor burden. Other studies have also reported that N1-S1 tumors may automatically regress after 5-6 weeks [32]. The presence of an intact immune system may have contributed to the regression of the tumor in otherwise healthy subjects. Further studies, with larger numbers of controls, using more aggressive and highly metastatic HCC tumor models, are needed in order to understand the effects of histotripsy on intrahepatic and distant metastases and the eventual impact on disease-free survival outcomes.

This study revealed no irreversible damage to structures both adjacent to the ablation zone and along the ablation path. In instances of complete ablation where we attempted to define a margin outside the tumor region, post-treatment and weekly follow-up MRI revealed edema in the liver surrounding the treatment region, manifested as a T2-hypointense signal. Despite deliberate ablation of healthy liver tissue to ensure an adequate ablation margin, post-histotripsy imaging revealed no atrophy within the parenchyma adjacent to and upstream from the ablation zone, confirmed with gross pathology and histology. Furthermore, there were no abnormal signals or imaging findings seen on MRI along the cavitation pathway from the surface of the skin to the tumor within the liver, and even deep to the tumor. There was no intrahepatic biliary ductal dilatation within the parenchyma upstream from the ablation zone and no evidence of vascular injury including bleeding or venous thrombosis (although lack of intravenous contrast may have limited evaluation). These findings are supported by previous large animal studies that have indicated no damage to veins near the histotripsy ablation zone or other off-target tissues while treating liver [30].

There are a few other limitations of this study, primarily related to the choice of tumor model. First, N1-S1 cells implanted orthotopically do not fully mimic tumors that develop spontaneously in a cirrhotic liver. Since the N1-S1 cell line is of non-human origin, it does not fully represent human HCC, thus limiting the ability to translate this data to human HCC. Inter-host tumor growth variability was also observed at the pre-treatment timepoint as tumorigenesis is a complex process involving interactions with the immune system. As injection of cyclophosphamide was performed 24h prior to tumor inoculation to support tumor formation by initiating temporary immune suppression [40], there may have been differences in the immunosuppression action across hosts as evidenced by the observed tumor volume heterogeneity at two weeks post-inoculation. Despite this limitation, an immunocompetent rat is necessary in order to study the role of the immune system in the effects of histotripsy on the local tumor. And using a human HCC cell line in an immunocompromised rodent model would limit the investigation of an immune-mediated response to histotripsy. Another limitation of this study is the use of basic MR sequences without intravenous contrast agents or diffusion-weighted imaging (DWI) sequences. Further studies using additional MR sequences to evaluate pre- and post-histotripsy treated tumors at varying time intervals post-ablation are necessary to better understand imaging features post-histotripsy. DWI sequences can help evaluate post-treatment MR signal transformations, allowing clearer differentiation between local tumor progression versus post treatment tissue changes, such as early pseudoprogression [41]. Contrast enhancement on MRI with liver-specific contrast agents may further enhance detection of ablation-induced effects such as vascular obstruction, edema, and tumor necrosis [42].

Overall, this study demonstrated the potential of histotripsy for non-invasive tumor ablation in an immunocompetent rodent HCC model with a high safety profile and low risk of local tumor progression. The study also characterizes the MR imaging observations demonstrating treatment response for up to 3 months following treatment. Local tumor shrinkage was observed in 14/15 (93.3%) treatment rats with no recurrence at 3 months. Additionally, preliminary data showed complete tumor regression despite only partial tumor treatment. The lack of injury to adjacent organs or tissue along the treatment pathway demonstrated a high safety profile for histotripsy. Furthermore, this study suggests a possible immune-mediated response stimulated by histotripsy, resulting in local tumor cell destruction. Research is ongoing to further evaluate the effects of primary tumor histotripsy ablation on distant metastatic tumors. Future studies will continue to investigate the safety, efficacy, and biological effects of histotripsy for potential translation to the clinic.

3.5 References

1. Siegel RL, Miller KD, Jemal A. Cancer statistics, 2020. CA Cancer J Clin. 2020;70(1):7-30. Epub 2020/01/08. doi: 10.3322/caac.21590. PubMed PMID: 31912902.

2. Cancer IAfRo. Global Cancer Observatory (GLOBOCAN): Cancer Today 2018 [07/28/2020]. Available from: https://gco.iarc.fr/today/data/factsheets/cancers/11-Liver-fact-sheet.pdf.

3. Mittal S, El-Serag HB. Epidemiology of hepatocellular carcinoma: consider the population. J Clin Gastroenterol. 2013;47 Suppl:S2-6. doi: 10.1097/MCG.0b013e3182872f29. PubMed PMID: 23632345; PubMed Central PMCID: PMCPMC3683119.

4. Balogh J, Victor D, Asham EH, Burroughs SG, Boktour M, Saharia A, et al. Hepatocellular carcinoma: a review. J Hepatocell Carcinoma. 2016;3:41-53. Epub 2016/10/05. doi: 10.2147/JHC.S61146. PubMed PMID: 27785449; PubMed Central PMCID: PMCPMC5063561.

5. Yang JD, Hainaut P, Gores GJ, Amadou A, Plymoth A, Roberts LR. A global view of hepatocellular carcinoma: trends, risk, prevention and management. Nat Rev Gastroenterol Hepatol. 2019. Epub 2019/08/22. doi: 10.1038/s41575-019-0186-y. PubMed PMID: 31439937.

6. Raza A, Sood GK. Hepatocellular carcinoma review: current treatment, and evidence-based medicine. World J Gastroenterol. 2014;20(15):4115-27. doi: 10.3748/wjg.v20.i15.4115. PubMed PMID: 24764650; PubMed Central PMCID: PMCPMC3989948.

7. Park SJ, Freise CE, Hirose R, Kerlan RK, Yao FY, Roberts JP, et al. Risk factors for liver transplant waitlist dropout in patients with hepatocellular carcinoma. Clin Transplant. 2012;26(4):E359-64. Epub 2012/06/13. doi: 10.1111/j.1399-0012.2012.01668.x. PubMed PMID: 22693962.

8. Bismuth H, Majno PE, Adam R. Liver transplantation for hepatocellular carcinoma. Semin Liver Dis. 1999;19(3):311-22. doi: 10.1055/s-2007-1007120. PubMed PMID: 10518310.

9. Tabrizian P, Jibara G, Shrager B, Schwartz M, Roayaie S. Recurrence of hepatocellular cancer after resection: patterns, treatments, and prognosis. Ann Surg. 2015;261(5):947-55. doi: 10.1097/SLA.0000000000000710. PubMed PMID: 25010665.

10. Zimmerman MA, Ghobrial RM, Tong MJ, Hiatt JR, Cameron AM, Hong J, et al. Recurrence of hepatocellular carcinoma following liver transplantation: a review of preoperative and postoperative prognostic indicators. Arch Surg. 2008;143(2):182-8; discussion 8. doi: 10.1001/archsurg.2007.39. PubMed PMID: 18283144.

11. Ben Ammar M, Nouri-Neuville M, Cornelis FH. Percutaneous image-guided therapies of primary liver tumors: Techniques and outcomes. Presse Med. 2019;48(7-8 Pt 2):e245-e50. Epub 2019/08/22. doi: 10.1016/j.lpm.2019.07.016. PubMed PMID: 31445698.

12. Sawrie SM, Fiveash JB, Caudell JJ. Stereotactic body radiation therapy for liver metastases and primary hepatocellular carcinoma: normal tissue tolerances and toxicity. Cancer Control. 2010;17(2):111-9. doi: 10.1177/107327481001700206. PubMed PMID: 20404794.

13. Wijlemans JW, Bartels LW, Deckers R, Ries M, Mali WP, Moonen CT, et al. Magnetic resonance-guided high-intensity focused ultrasound (MR-HIFU) ablation of liver tumours. Cancer Imaging. 2012;12:387-94. Epub 2012/09/28. doi: 10.1102/1470-7330.2012.9038. PubMed PMID: 23022541; PubMed Central PMCID: PMCPMC3460556.

14. Maloney E, Hwang JH. Emerging HIFU applications in cancer therapy. Int J Hyperthermia. 2015;31(3):302-9. Epub 2014/11/04. doi: 10.3109/02656736.2014.969789. PubMed PMID: 25367011.

15. Heckman JT, Devera MB, Marsh JW, Fontes P, Amesur NB, Holloway SE, et al. Bridging locoregional therapy for hepatocellular carcinoma prior to liver transplantation. Ann Surg Oncol. 2008;15(11):3169-77. Epub 2008/08/12. doi: 10.1245/s10434-008-0071-3. PubMed PMID: 18696158.

16. Livraghi T, Mäkisalo H, Line PD. Treatment options in hepatocellular carcinoma today. Scand J Surg. 2011;100(1):22-9. doi: 10.1177/145749691110000105. PubMed PMID: 21482502.

17. Poulou LS, Botsa E, Thanou I, Ziakas PD, Thanos L. Percutaneous microwave ablation vs radiofrequency ablation in the treatment of hepatocellular carcinoma. World J Hepatol. 2015;7(8):1054-63. doi: 10.4254/wjh.v7.i8.1054. PubMed PMID: 26052394; PubMed Central PMCID: PMCPMC4450182.

18. Rossi L, Zoratto F, Papa A, Iodice F, Minozzi M, Frati L, et al. Current approach in the treatment of hepatocellular carcinoma. World J Gastrointest Oncol. 2010;2(9):348-59. doi: 10.4251/wjgo.v2.i9.348. PubMed PMID: 21160806; PubMed Central PMCID: PMCPMC2999141.

19. Parsons JE, Cain CA, Abrams GD, Fowlkes JB. Pulsed cavitational ultrasound therapy for controlled tissue homogenization. Ultrasound Med Biol. 2006;32(1):115-29. doi: 10.1016/j.ultrasmedbio.2005.09.005. PubMed PMID: 16364803.

20. Xu Z, Ludomirsky A, Eun LY, Hall TL, Tran BC, Fowlkes JB, et al. Controlled ultrasound tissue erosion. IEEE Trans Ultrason Ferroelectr Freq Control. 2004;51(6):726-36. PubMed PMID: 15244286; PubMed Central PMCID: PMCPMC2669757.

21. Maxwell AD, Cain CA, Hall TL, Fowlkes JB, Xu Z. Probability of cavitation for single ultrasound pulses applied to tissues and tissue-mimicking materials. Ultrasound Med Biol. 2013;39(3):449-65. Epub 2013/02/04. doi: 10.1016/j.ultrasmedbio.2012.09.004. PubMed PMID: 23380152; PubMed Central PMCID: PMCPMC3570716.

22. Vlaisavljevich E, Greve J, Cheng X, Ives K, Shi J, Jin L, et al. Non-Invasive Ultrasound Liver Ablation Using Histotripsy: Chronic Study in an In Vivo Rodent Model. Ultrasound Med Biol. 2016;42(8):1890-902. Epub 2016/04/29. doi: 10.1016/j.ultrasmedbio.2016.03.018. PubMed PMID: 27140521; PubMed Central PMCID: PMCPMC4912895.

23. Vlaisavljevich E, Kim Y, Owens G, Roberts W, Cain C, Xu Z. Effects of tissue mechanical properties on susceptibility to histotripsy-induced tissue damage. Phys Med Biol. 2014;59(2):253-70. Epub 2013/12/20. doi: 10.1088/0031-9155/59/2/253. PubMed PMID: 24351722; PubMed Central PMCID: PMCPMC4888779.

24. Umale S, Chatelin S, Bourdet N, Deck C, Diana M, Dhumane P, et al. Experimental in vitro mechanical characterization of porcine Glisson's capsule and hepatic veins. J Biomech. 2011;44(9):1678-83. Epub 2011/04/09. doi: 10.1016/j.jbiomech.2011.03.029. PubMed PMID: 21481399.

25. Vlaisavljevich E, Kim Y, Allen S, Owens G, Pelletier S, Cain C, et al. Image-guided non-invasive ultrasound liver ablation using histotripsy: feasibility study in an in vivo porcine model. Ultrasound Med Biol. 2013;39(8):1398-409. Epub 2013/05/21. doi: 10.1016/j.ultrasmedbio.2013.02.005. PubMed PMID: 23683406; PubMed Central PMCID: PMCPMC3709011.

26. Mancia L, Vlaisavljevich E, Yousefi N, Rodriguez M, Ziemlewicz TJ, Lee FT, et al. Modeling tissue-selective cavitation damage. Phys Med Biol. 2019;64(22):225001. Epub 2019/11/15. doi: 10.1088/1361-6560/ab5010. PubMed PMID: 31639778; PubMed Central PMCID: PMCPMC6925591.

27. Allen SP, Hall TL, Cain CA, Hernandez-Garcia L. Controlling cavitation-based image contrast in focused ultrasound histotripsy surgery. Magn Reson Med. 2015;73(1):204-13. Epub 2014/01/27. doi: 10.1002/mrm.25115. PubMed PMID: 24469922.

28. Hall TL, Fowlkes JB, Cain CA. A real-time measure of cavitation induced tissue disruption by ultrasound imaging backscatter reduction. IEEE Trans Ultrason Ferroelectr Freq Control. 2007;54(3):569-75. Epub 2007/03/23. PubMed PMID: 17375825.

29. Smolock AR, Cristescu MM, Vlaisavljevich E, Gendron-Fitzpatrick A, Green C, Cannata J, et al. Robotically Assisted Sonic Therapy as a Noninvasive Nonthermal Ablation Modality: Proof of Concept in a Porcine Liver Model. Radiology. 2018;287(2):485-93. Epub 2018/01/30. doi: 10.1148/radiol.2018171544. PubMed PMID: 29381870.

30. Vlaisavljevich E, Owens G, Lundt J, Teofilovic D, Ives K, Duryea A, et al. Non-Invasive Liver Ablation Using Histotripsy: Preclinical Safety Study in an In Vivo Porcine Model. Ultrasound Med Biol. 2017;43(6):1237-51. Epub 2017/03/21. doi: 10.1016/j.ultrasmedbio.2017.01.016. PubMed PMID: 28318889.

31. Worlikar T, Vlaisavljevich E, Gerhardson T, Greve J, Wan S, Kuruvilla S, et al. Histotripsy for Non-Invasive Ablation of Hepatocellular Carcinoma (HCC) Tumor in a Subcutaneous Xenograft Murine Model. Conf Proc IEEE Eng Med Biol Soc. 2018;2018:6064-7. doi: 10.1109/EMBC.2018.8513650. PubMed PMID: 30441719.

32. Buijs M, Geschwind JF, Syed LH, Ganapathy-Kanniappan S, Kunjithapatham R, Wijlemans JW, et al. Spontaneous tumor regression in a syngeneic rat model of liver cancer: implications for survival studies. J Vasc Interv Radiol. 2012;23(12):1685-91. doi: 10.1016/j.jvir.2012.08.025. PubMed PMID: 23177115; PubMed Central PMCID: PMCPMC3548324.

33. Thompson SM, Callstrom MR, Knudsen B, Anderson JL, Carter RE, Grande JP, et al. Development and preliminary testing of a translational model of hepatocellular carcinoma for MR imaging and interventional oncologic investigations. J Vasc Interv Radiol. 2012;23(3):385-95. Epub 2012/01/20. doi: 10.1016/j.jvir.2011.11.018. PubMed PMID: 22265247; PubMed Central PMCID: PMCPMC3904802.

34. Lee JM, Trevisani F, Vilgrain V, Wald C. Imaging diagnosis and staging of hepatocellular carcinoma. Liver Transpl. 2011;17 Suppl 2:S34-43. doi: 10.1002/lt.22369. PubMed PMID: 21739567.

35. Marrero JA, Pelletier S. Hepatocellular carcinoma. Clin Liver Dis. 2006;10(2):339-51, ix. doi: 10.1016/j.cld.2006.05.012. PubMed PMID: 16971265.

36. Patel N, King AJ, Breen DJ. Imaging appearances at follow-up after image-guided solid-organ abdominal tumour ablation. Clin Radiol. 2017;72(8):680-90. Epub 2017/02/23. doi: 10.1016/j.crad.2017.01.014. PubMed PMID: 28237299.

37. Taleb B A. Tumour flare reaction in cancer treatments: a comprehensive literature review. Anticancer Drugs. 2019;30(9):953-8. doi: 10.1097/CAD.0000000000000814. PubMed PMID: 31348010.

38. Mamdani H, Wu H, O'Neil BH, Sehdev A. Excellent response to Anti-PD-1 therapy in a patient with hepatocellular carcinoma: case report and review of literature. Discov Med. 2017;23(128):331-6. PubMed PMID: 28715649.

39. Qu S, Worlikar T, Felsted AE, Ganguly A, Beems MV, Hubbard R, et al. Non-thermal histotripsy tumor ablation promotes abscopal immune responses that enhance cancer immunotherapy. J Immunother Cancer. 2020;8(1). doi: 10.1136/jitc-2019-000200. PubMed PMID: 31940590.

40. Diehl R, Ferrara F, Müller C, Dreyer AY, McLeod DD, Fricke S, et al. Immunosuppression for in vivo research: state-of-the-art protocols and experimental approaches. Cell Mol Immunol. 2017;14(2):146-79. Epub 2016/10/10. doi: 10.1038/cmi.2016.39. PubMed PMID: 27721455; PubMed Central PMCID: PMCPMC5301156.

41. Gluskin JS, Chegai F, Monti S, Squillaci E, Mannelli L. Hepatocellular Carcinoma and Diffusion-Weighted MRI: Detection and Evaluation of Treatment Response. J Cancer. 2016;7(11):1565-70. Epub 2016/07/13. doi: 10.7150/jca.14582. PubMed PMID: 27471573; PubMed Central PMCID: PMCPMC4964141.

42. Kim SK, Lim HK, Kim YH, Lee WJ, Lee SJ, Kim SH, et al. Hepatocellular carcinoma treated with radio-frequency ablation: spectrum of imaging findings. Radiographics. 2003;23(1):107-21. doi: 10.1148/rg.231025055. PubMed PMID: 12533646.

43. Vlaisavljevich E, Greve J, Cheng X, Ives K, Shi J, Jin L, et al. Non-Invasive Ultrasound Liver Ablation Using Histotripsy: Chronic Study in an In Vivo Rodent Model. Ultrasound Med Biol. 2016;42(8):1890-902. Epub 2016/05/04. doi: 10.1016/j.ultrasmedbio.2016.03.018. PubMed PMID: 27140521; PubMed Central PMCID: PMCPMC4912895.

44. Kim Y, Maxwell AD, Hall TL, Xu Z, Lin KW, Cain CA. Rapid prototyping fabrication of focused ultrasound transducers. IEEE Trans Ultrason Ferroelectr Freq Control. 2014;61(9):1559-74. doi: 10.1109/TUFFC.2014.3070. PubMed PMID: 25167156.

45. Lin KW, Kim Y, Maxwell AD, Wang TY, Hall TL, Xu Z, et al. Histotripsy beyond the intrinsic cavitation threshold using very short ultrasound pulses: microtripsy. IEEE Trans Ultrason Ferroelectr Freq Control. 2014;61(2):251-65. Epub 2014/01/30. doi: 10.1109/tuffc.2014.6722611. PubMed PMID: 24474132; PubMed Central PMCID: PMCPMC3966303.

46. Vlaisavljevich E, Maxwell A, Warnez M, Johnsen E, Cain CA, Xu Z. Histotripsy-induced cavitation cloud initiation thresholds in tissues of different mechanical properties. IEEE Trans Ultrason Ferroelectr Freq Control. 2014;61(2):341-52. Epub 2014/01/30. doi: 10.1109/tuffc.2014.6722618. PubMed PMID: 24474139; PubMed Central PMCID: PMCPMC4158820.

3.6 Supplementary Figures

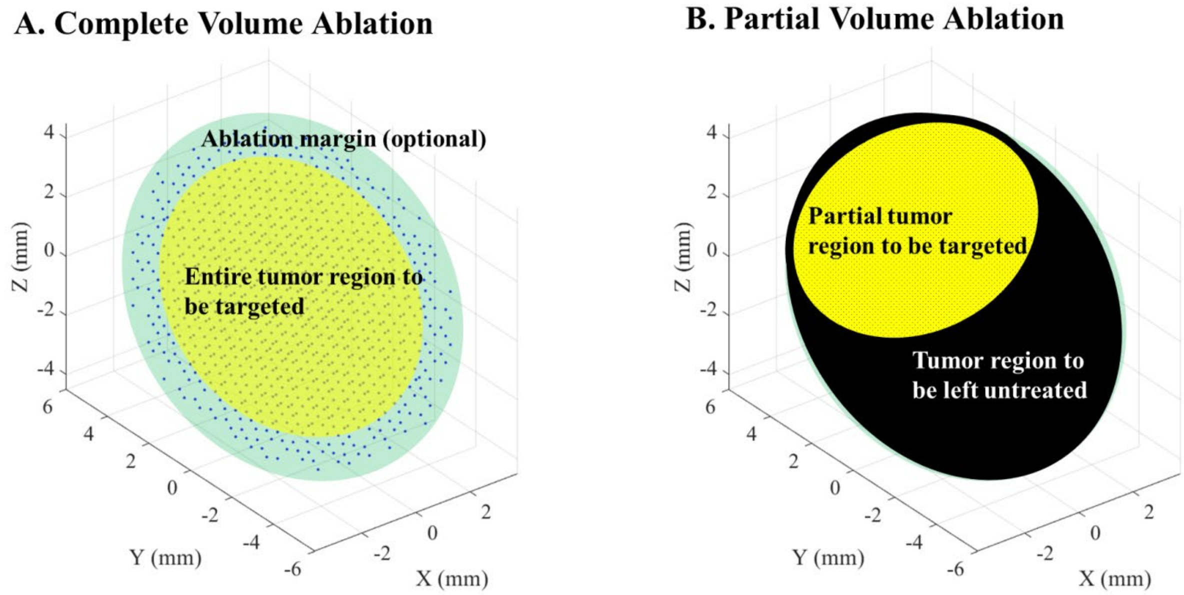

Figure S3-7 ***Generation of treatment ellipsoid for histotripsy targeting and 3D scan path.*** *(A) The treatment ellipsoid (yellow) encompasses the entire 3D tumor volume to be targeted for ablation with additional margin up to 2mm (green) and contains a grid of uniformly spaced therapy focal zones (blue dots), which determines the 3D scan path. (B) For partial ablation cases, only part of the tumor volume (yellow) is targeted for ablation and the rest (black) is left untreated.*

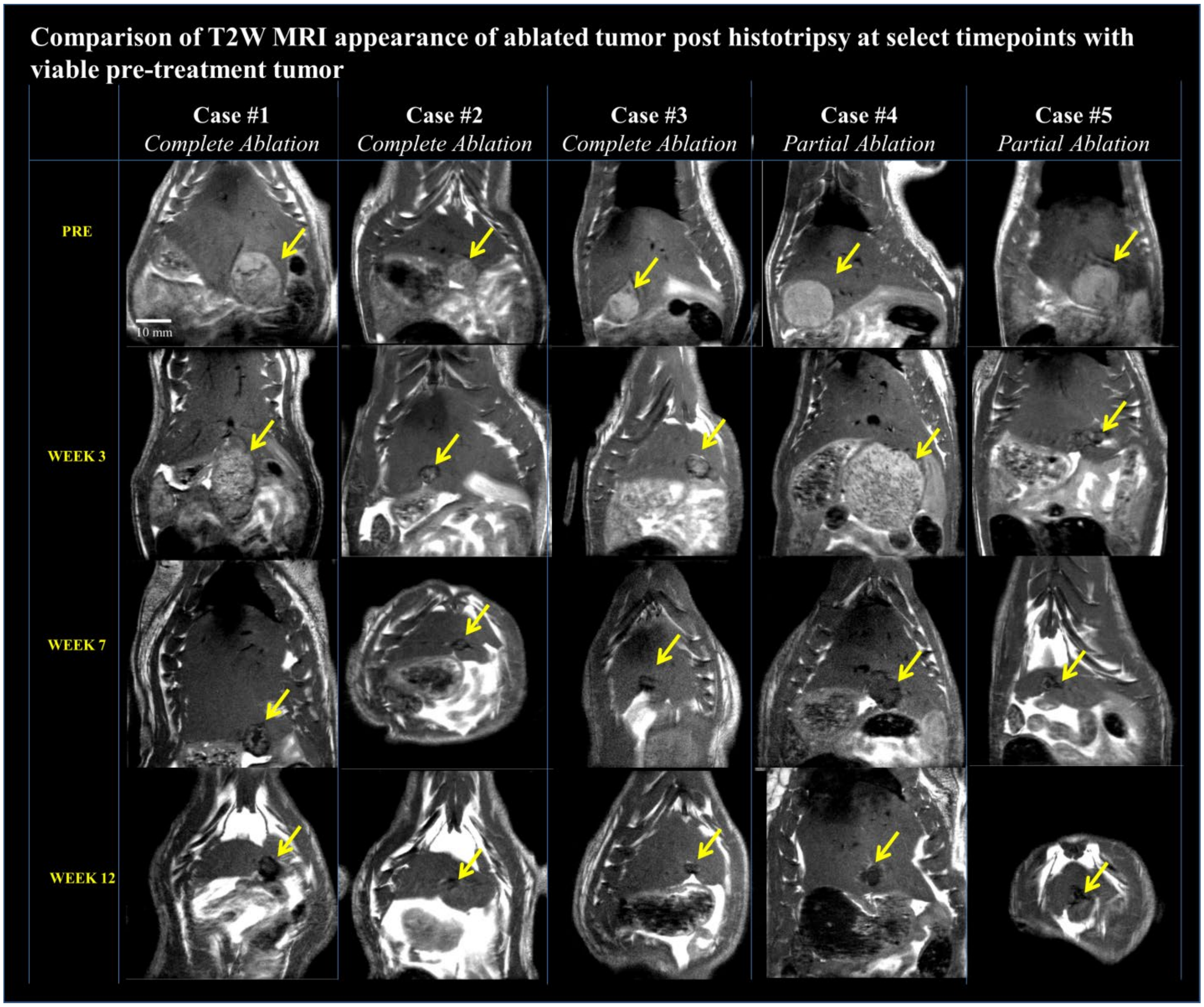

Figure S3-2 ***T2W MRI appearance of histotripsy treated tumor at select timepoints compared to pre-treatment viable tumor for complete and partial ablation cases.*** *At week 3, the lesion begins to regress, resulting in T2 hypointense signal at the ablation site by week 7. The tumor continues to regress until week 12, but there is no further observable change in signal compared to week 7.*

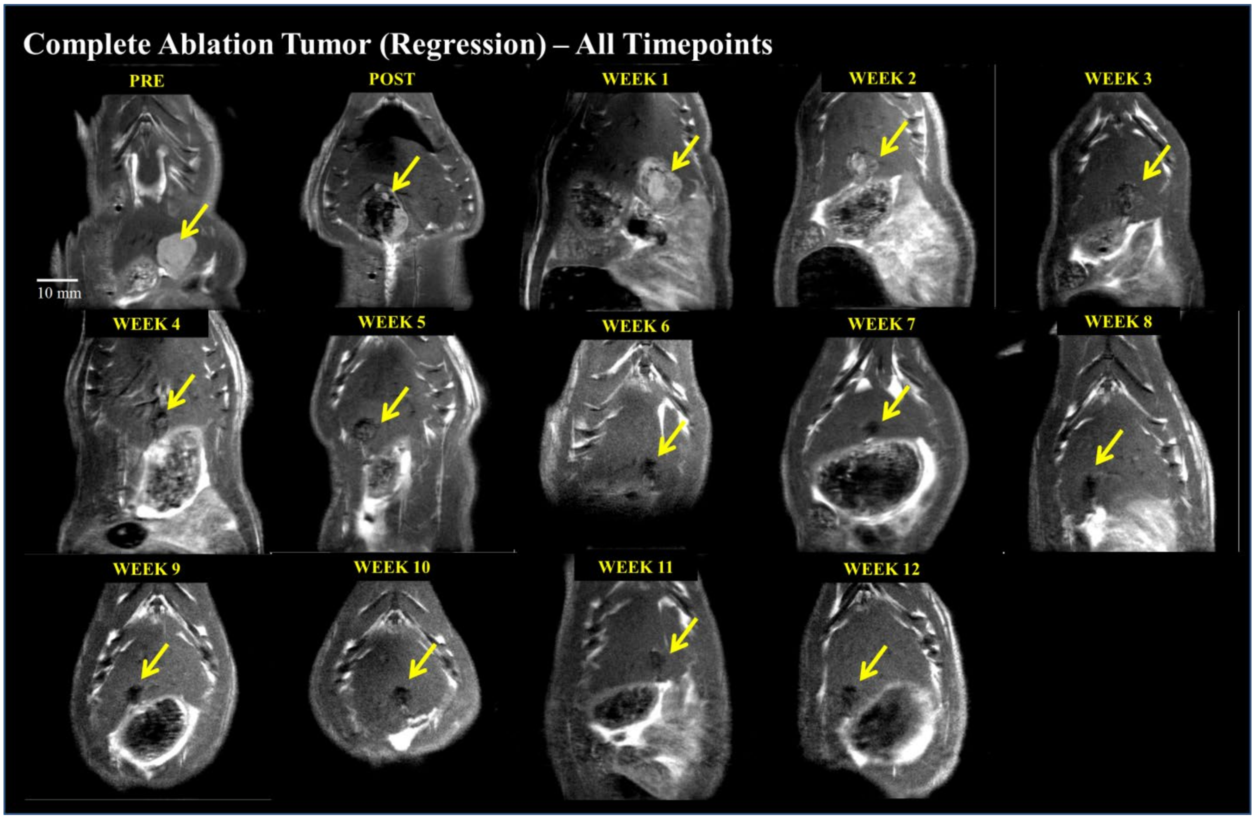

Figure S3-3 ***T2W MRI appearance of histotripsy treated tumor (complete ablation) at all timepoints.*** *Complete ablation - pre-treatment (mildly hyperintense), post treatment ablation zone (hypointense), ablation zone at weeks 1-2 (mildly hyperintense), weeks 3-6 (mildly hypointense, size regression), weeks 7-12 (hypointense, size regression) with <5 mm hypointense region observed at final imaging timepoint. This figure demonstrates all imaging timepoints for the case demonstrated in Figure 4-4A.*

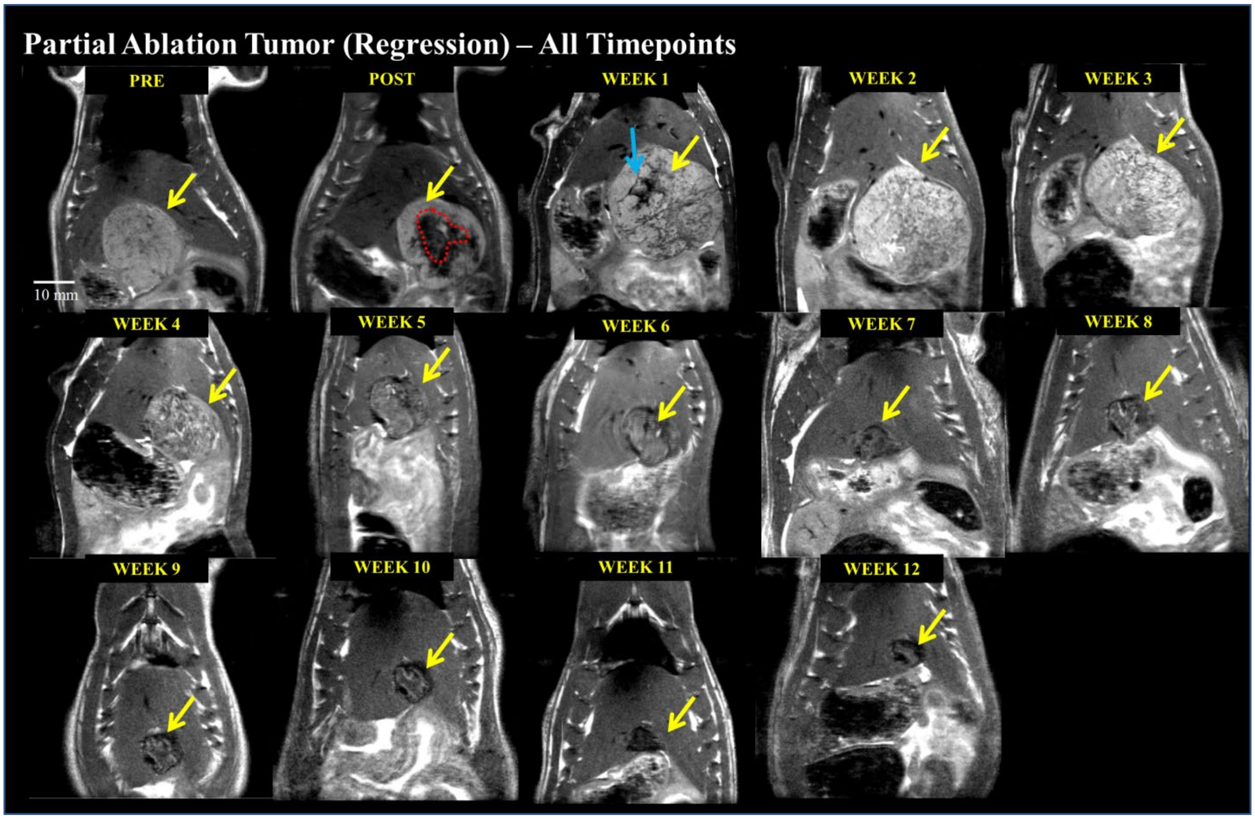

Figure S3-4 ***T2W MRI appearance of histotripsy treated tumor (partial ablation) at all timepoints.*** *Partial ablation - pre-treatment (mildly hyperintense), post treatment ablation zone (hypointense, shown by red dashed lines) and untreated tumor region (mildly hyperintense), the lesion at week 1 (mildly hyperintense) with pseudoprogression characteristics (blue arrow), week 2 (mildly hyperintense), week 3 (mildly hyperintense, size regression), weeks 4-12 (gradual transformation to hypointense, size regression), and week 12 (~5 mm hypointense region). This figure demonstrates all imaging timepoints for the case demonstrated in Figure 4-4B.*

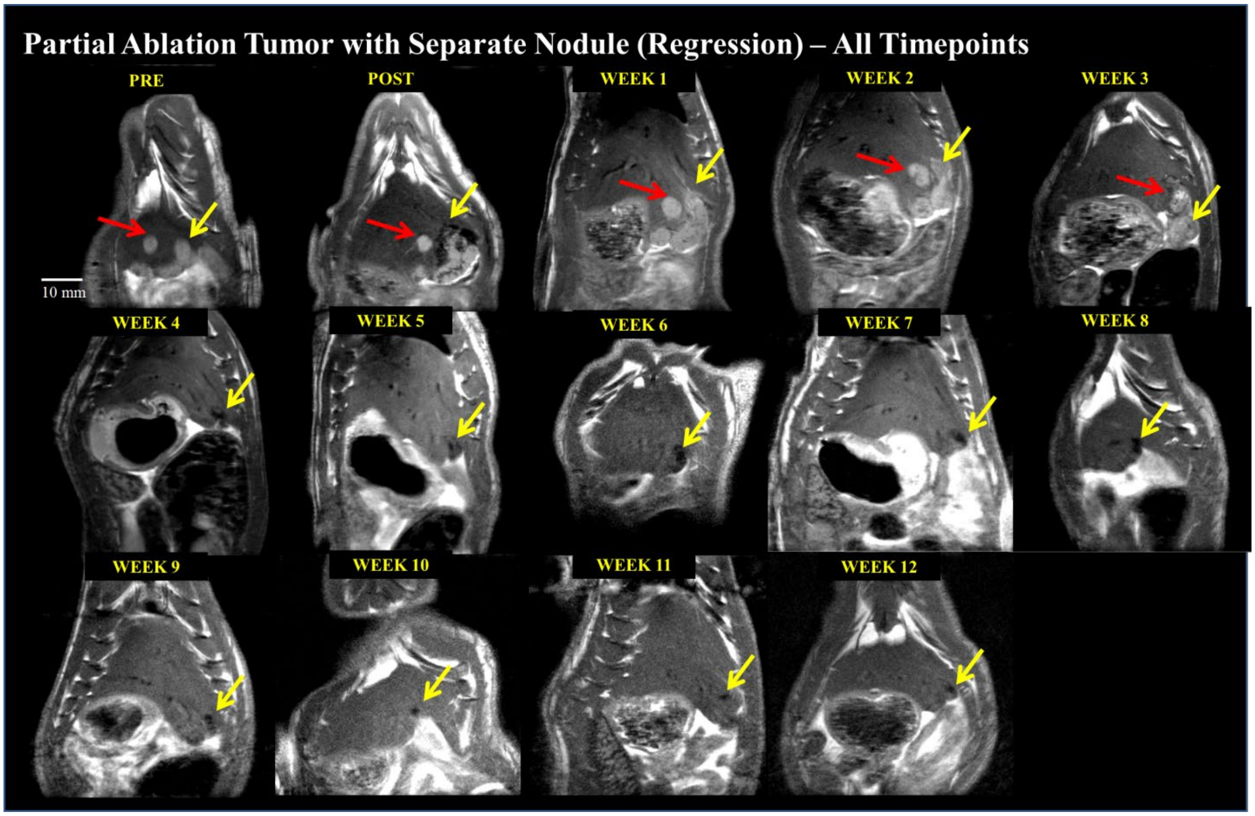

Figure S3-5 ***T2W MRI appearance of histotripsy treated tumor (partial ablation with separate untreated nodule) at all timepoints.*** *Partial ablation with a separate untreated nodule (red arrow) – the lesion consisting of ablation zone and untreated nodule at weeks 1-2 (mildly hyperintense), week 3 (mild hyperintense with no size progression), weeks 4-12 (hypointense, size regression) and week 12 (<3 mm hypointense region). This figure demonstrates all imaging timepoints for the case demonstrated in Figure 4-4C.*

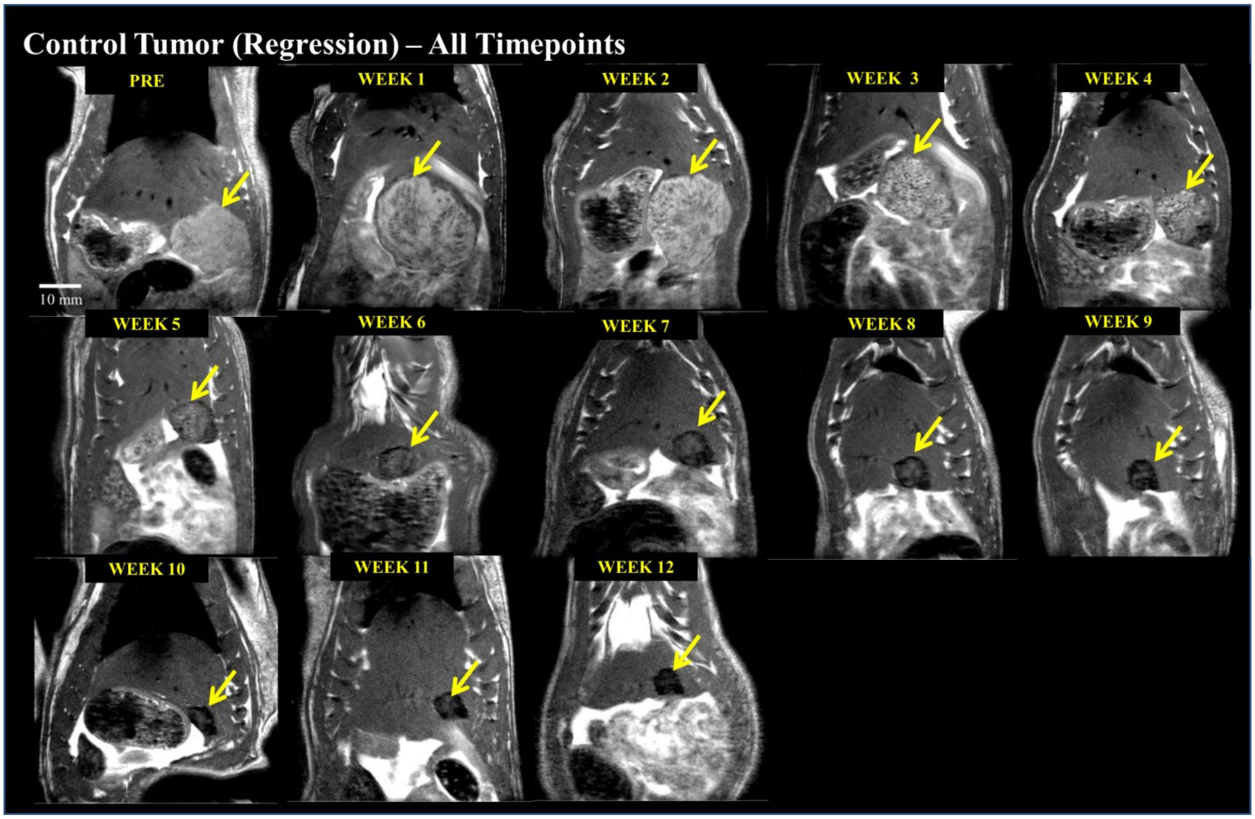

Figure S3-6 ***T2W MRI appearance of control tumor at all timepoints.*** *Control tumor (yellow arrow) develops a mottled and heterogeneous appearance, similar to that of pseudoprogression by week 3, and begins to regress as evidenced by decreasing tumor burden until week 12. By week 7, the appearance of the tumor becomes hypointense and this appearance is maintained until week 12. This figure demonstrates all imaging timepoints for the case demonstrated in Figure 4-5.*

Chapter 4 Impact of Histotripsy on Development of Intrahepatic Metastases in a Rodent Liver Tumor Model

A majority component of this chapter has been published in *Cancers* © 2022 © by the authors.

Reprinted with permission from T. Worlikar, M Zhang, A. Ganguly et al.," Impact of histotripsy on development of intrahepatic metastases in a rodent liver tumor model" (in eng), Cancers 2022, 14, 1612. https://doi.org/10.3390/cancers14071612

4.1 Introduction

Liver cancer is one of the top ten causes of cancer related deaths worldwide and in the United States [1]. Hepatocellular carcinoma (HCC) accounts for 75% of all liver cancer cases, most frequently occurring in patients with chronic liver diseases from etiologies such as hepatitis B and C, alcohol abuse, non-alcoholic steatohepatitis (NASH) and non-alcoholic fatty liver disease (NAFLD) resulting in cirrhosis [2]. The liver is also a frequent site for metastases originating from colorectal cancer, pancreatic cancer, melanoma, lung cancer and breast cancer [3]. Depending on the location, severity and staging of liver cancer, multiple treatment options are currently available including surgical resection, liver transplantation, ablation techniques (including radiofrequency ablation (RFA), micro-wave ablation (MWA), cryoablation, high intensity focused ultrasound (HIFU)), chemotherapy, radiation therapy, targeted drug therapy and immunotherapies [4]. Even with current medical treatments, the 5-year patient survival rate in the United States is only 20%, the second lowest amongst all cancers [1]. Symptoms associated with liver cancer may not show at early stages, placing the patients at an increased risk for nodal and distant metastases which further lowers their 5-year survival rate to an estimated 3-11% [5]. Even after treatment, high prevalence of tumor recurrence and metastasis [6] highlights the clinical need for improving outcomes of liver cancer. In fact, metastasis accounts for >90% of all cancer-associated deaths and metastatic progression is predominantly regulated by the complex signaling pathways between the primary tumor and stromal cells, especially the immune cells [7, 8].

Histotripsy is a novel non-invasive, non-ionizing, and non-thermal ablation technique that mechanically destroys target tissue by controlled acoustic cavitation [9-11]. Using high pressure (P->15MPa), microsecond-length ultrasound pulses at a low duty cycle (ultrasound on-time/total treatment time<1%), endogenous nanometer-scale gas nuclei in the tissue are expanded to over 100 µm followed by collapse within several hundred microseconds, generating high mechanical stress and strain to disrupt the cells in the target tissue. Histotripsy has been shown to completely ablate the target tissue into a liquid consistency acellular homogenate which is resorbed by the body within 2 months leaving mm-length scar tissue [12-14]. Pre-clinical histotripsy investigations have established the feasibility and efficacy of histotripsy for non-invasive ablation in many pre-clinical applications including the ablation of human-scale porcine livers [15-19], and ablation of liver [20-22], kidney [23] and prostate [24] tumors. The mechanical strength of different tis-sue types impacts their resistance to histotripsy-induced damage, which can be exploited by selecting optimal parameters for achieving tumor-selective damage while simultaneously protecting the structural integrity of large blood vessels, nerves, and bile ducts with-in the ablation zone [15, 17, 18, 25].

There has been some evidence suggesting the potent immunostimulatory and systemic effects of histotripsy. In a murine melanoma model, histotripsy ablation of the primary subcutaneous tumor inhibited the development of secondary pulmonary metastases derived from tail vein injection [20]. In an orthotopic rat liver tumor model, histotripsy of the entire tumor volume resulted in complete regression of the tumor in all subjects, and even in 5/6 cases of partial tumor ablation (50-75% tumor volume ablated), the entire tumor regressed completely with no recurrence [22]. Recently, a first-in-human trial demonstrated the feasibility of planned histotripsy ablation of liver tumors with no identified serious adverse events [26]. In all patients (n=8), targeted tumors were locally controlled and in 2 of 8 patients, non-targeted tumors also stabilized [26]. These results suggest that local histotripsy ablation of the entire primary tumor, or even a part of the tumor may systemically influence untargeted tumors. There is insufficient evidence regarding the effects of histotripsy on the risk of recurrence and metastases following tumor debulking. Since histotripsy mechanically disrupts the tumor, it is possible that intact tumor cells may inadvertently detach from the primary tumor and disseminate into lymphatic and/or circulatory system. Our understanding of the immunological response to histotripsy is also limited, especially in cases of partial histotripsy ablation where untargeted tumor volume remains undamaged during treatment, but eventually regresses. This longitudinal study aims to evaluate the effect of partial histotripsy tumor ablation on untargeted local tumor progression, survival outcomes, risk of developing metastases and tumor immune infiltration in an orthotopic, immunocompetent, metastatic rodent HCC model for the first time.

4.2 Materials and Methods

4.2.1 Experimental Design and Technical Design

Orthotopic McA-RH7777 liver tumors were generated in immunocompetent Sprague-Dawley rodent hosts. Once the tumor measured a minimum of 5 mm in its largest dimension, animals were randomized into treatment and control groups. For the survival study, n=11 treatment rats received partial histotripsy ablation (approximately 50-75% of the tumor volume was targeted for ablation by histotripsy) and n=11 control rats received no treatment. Animals were monitored weekly using MRI for up to 3 months or until the animals reached end-stage illness criteria, or the maximum tumor size (25 mm in largest dimension) allowed by ethical standards was reached; therefore, data are not truly absolute for animal survival. At the endpoint (prior to the onset of death), the animals were euthanized, and liver tissue was harvested for histological evaluation. For the early timepoint study, animals were euthanized at day 2 (n=2 control, and n=3 treatment) or day 7 (n=3 control, and n=6 treatment) post histotripsy timepoint and the harvested liver tissue was analyzed to evaluate for intra-hepatic metastasis and immune infiltration at day 2 and day 7 timepoints following histotripsy ablation. An additional cohort of n=3 animals received scant histotripsy ablation (<25% tumor volume targeted by histotripsy) and were euthanized at day 7. The choice of partial ablation (50-75% tumor volume targeted) was repeated from Chapter 3 to observe if similar outcomes can be achieved in a highly metastatic tumor model and to determine if a minimal tumor volume percentage ablation (<25% tumor volume targeted) can achieve meaningful treatment response.

4.2.2 Cell Preparation

McA-RH7777 (ATCC® CRL-1601™) cells were purchased from the ATCC cell line repository. The cells were cultivated in Dulbecco's Modified Eagle's Medium (DMEM) containing 4 mM L-glutamine, 4500 mg/L glucose, and 1500 mg/L sodium bicarbonate, supplemented with 10% FBS and 1 mL Gentamicin. The cells were maintained at 37 °C in a 5% CO2/95% humidified air atmosphere.

4.2.3 Animals and Study Approval

This study was approved by the Institutional Animal Care and Use Committee at the University of Michigan and all procedures were performed in compliance with the ap-proved protocol. Sprague Dawley rats weighing 125-175 g were purchased from Taconic (Hudson, New

York) and housed and maintained in specific pathogen-free (SPF) conditions in University of Michigan ULAM (Unit for Laboratory Animal Medicine) housing facility.

4.2.4 Orthotopic Tumor Implantation

Tumor implantation was performed via laparotomy. Animals were injected with 100 mg/kg cyclophosphamide intraperitoneally 24 hours prior to tumor inoculation. For the inoculation procedure, animals were anesthetized in an induction chamber using isoflurane inhalation (5%, admixed with 1 L/min of oxygen) until loss of withdrawal reflex. After induction, the animals were moved to the surgical area in a supine position and anesthesia then was maintained with 2% isoflurane in 100% oxygen with a flow of 1.5 L/min administered using a nasal-cone connected to a coaxial breathing circuit and vaporizer (SurgiVet V704001, Smiths Medical, Waukesha, Wisconsin, USA). To prevent an-esthesia-related corneal damage, eye lubricant was used. Carprofen (Rimadyl, Pfizer, NY, USA) analgesic (5 mg/kg) was used for analgesia prior to surgery and once every 24 hours for two days post-surgery. The surgical area (chest and abdomen) was shaved and sterilized using chlorhexidine and iodine. Once the animal was draped and prepped for surgery, a midline incision was made through the skin. Blunt dissection was performed to separate the skin and abdominal muscle layer posteriorly and anteriorly to the ends of the incision. To expose the liver, an incision was made in muscle layer and retractor was inserted to keep the incision open. The inferior liver lobe was retracted using forceps. 10 million McA-RH7777 cells were suspended in 100 μL total injection volume constituting of basement membrane matrix (Matrigel, Corning Life Sciences, Corning, NY, USA) and serum free DMEM (Thermofisher Scientific, Waltham, MA, USA) in a 1:1 ratio. The cells were injected into the liver lobe. Pressure was applied on the injection site using sterile cotton tip applicator and a sterile hemostatic compressed sponge was placed on the liver surface to prevent leakage. After 3 minutes, the sponge was removed, and the muscle layer was closed using absorbable sutures. The skin incision was closed using wound staples. Animals were recovered until ambulatory. The wound staples were removed prior to pre-treatment MRI.

4.2.5 Histotripsy Ablation

Our rodent histotripsy setup (Figure 4-1A) consisted of a custom-built 1 MHz therapy transducer, co-aligned with a 20 MHz B-mode ultrasound imaging probe (L40-8/12, Ultrasonix, Vancouver, Canada) mounted to a motorized 3-axis positioning system [22, 27]. The ring configuration transducer (f number = 0.6, focal distance = 32.5 mm) contains 8 individually focused lead zirconate titanate elements (20 mm diameter). The value of peak negative pressure in the tissue is estimated based on pressure measurements from fiber optic hydrophone in free-field [28]. In the free-field medium (degassed water), the pressure measurements from individual transducer elements were summed to calculate the peak negative pressure (P–) of 37.8 MPa and the peak positive pressure (P+) of 43.9 MPa. The peak positive pressure may be underestimated without considering the non-linearity developed when all elements are fired. However, the acoustic waveform at that high pressure with all elements fired simultaneously could not be measured due to instantaneous cavitation generation. The spatial peak temporal peak intensity (I_{SPTP}) was estimated to be ~130 kW/cm^2, spatial peak pulse average intensity (I_{SPPA}) was estimated to be ~24 kW/cm^2 and spatial peak temporal average (I_{SPTA}) was estimated to be ~8 W/cm^2. The transducer and imaging probe were immersed in a tank of degassed water maintained at 35–37°C. For histotripsy treatment, animals were anesthetized by inhalation of isoflurane gas (1.5-2.0%) in 1 L/min of oxygen (SurgiVet V704001, Smiths Medical, Waukesha, Wisconsin, USA). The chest and abdominal regions were shaved with an electric clipper. Carprofen (Rimadyl, Pfizer, NY, USA) analgesic (5 mg/kg) was used for analgesia prior to histotripsy and once every 24 hours for two days post-ablation. The animal was placed on a custom-built platform over the tank such that the liver region was submerged in the de-gassed water, which is the coupling medium (Figure 4-1A). Under ultrasound guidance, the therapy transducer was positioned to co-localize the focal zone of the therapy transducer focus with the tumor core. The entire tumor volume was visualized by scanning the imaging probe mounted on the motorized positioning system to determine the limits of the in-tended target volume. In the scant histotripsy ablation cohort, <25% tumor volume was targeted for ablation. In all other animals receiving histotripsy, 50-75% tumor volume was targeted, similar to partial ablation volume percentage selected in Chapter 3. The desired fraction of tumor volume was targeted for histotripsy ablation by mechanically scanning the histotripsy focus to cover the targeted volume by using the motorized positioning system with continuous motion. At each focal location within the target volume, the therapy transducer delivered 1-2 cycle length histotripsy pulses (with a single high amplitude negative pressure phase) at 100 Hz PRF and generated peak negative pressure (P-) exceeding 30 MPa. P- >30 MPa exceeds the intrinsic threshold of the soft-tissue target (typically P->26MPa) to generate inertial cavitation; this is the mechanism of intrinsic threshold histotripsy [28]. During histotripsy, the generated cavitation appeared hyperechoic compared to the surrounding liver parenchyma on ultrasound imaging (Figure 4-1B). Post histotripsy-ablation, the targeted region appeared hypoechoic, indicative of tumor tissue disruption (Figure 4-1B). After treatment, animals were recovered until ambulatory. Total ablation time ranged from 3-5 minutes, at 100 Hz PRF equated to total 18,000–30,000 pulses delivered to the intended target volume (ranging from 30 mm^3 to 100 mm^3). Histotripsy parameters were determined based on previous in vivo and in vitro work done in our lab [22].

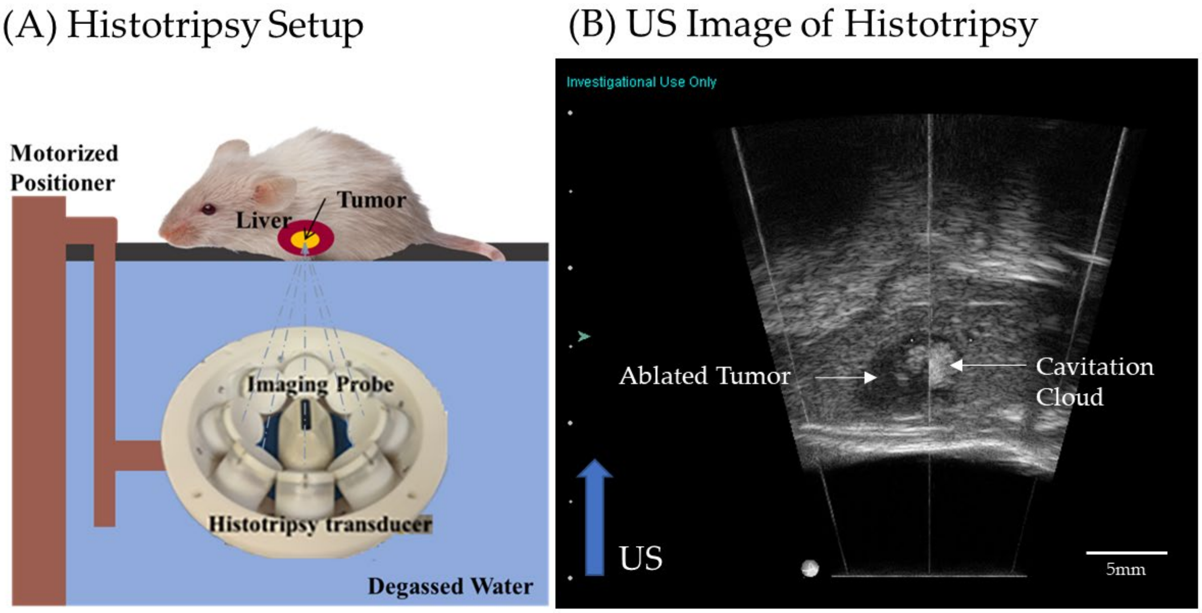

Figure 4-1A) ***Histotripsy Setup.*** *The rodent histotripsy treatment setup consisted of an 8 element 1MHz therapy transducer delivering 1-2 cycle pulses at P-> 30 MPa and 100 Hz PRF. A coaxially aligned 20MHz imaging probe was used for real time ultrasound-guidance. Both transducers were mounted to a motorized positioning system and immersed in a tank of degassed water (coupling medium). The animal was placed in a prone position on a platform to allow the intended target region to submerge. B) Generation of hyperechoic cavitation cloud in liver tumor. The ablated tumor region appears hypoechoic compared to surrounding liver parenchyma.*

4.2.6 Magnetic Resonance Imaging

To assess tumor development, MRI was obtained within 1-day prior to histotripsy (pre-treatment timepoint) and within 1-day post-histotripsy (post-treatment timepoint). Weekly MRI was also used for monitoring ablation response. A 7.0 T MR small animal scanner using a Direct Drive console (Agilent Technologies, Santa Clara, CA, USA) was used with a 60 mm inner-diameter transmit-receive radiofrequency (RF) volume coil (Morris Instruments, Ontario, Canada). During imaging, rats were anesthetized using isoflurane inhalation (1.5-2.0% in 1 L/min of oxygen) and temperature was monitored using rectal probes. Respiratory gating was used during image acquisition. A custom-built proportional-integral-derivative (PID) controller (LabVIEW, National Instruments, Austin TX) was interfaced with a commercially available small animal system (SA Instruments, Stony Brook, NY) to monitor respiration. Animal position in the scanner was confirmed with pilot scans. To visualize the tumor, a 2D T2-weighted fast spin-echo (FSE) in the coronal plane was used with the following parameters: [TR/TEeff =2500/10 ms, FOV=60mm x60 mm, slice thickness = 1 mm, matrix (zero-filled) = 256 x 256 (512 x 512), resulting in a voxel size of 117 µm x 117 µm x 1000 µm and total scan time ~5 minutes].

4.2.7 Histological Analysis

After euthanasia, treated tumor, as well as liver tissue samples were harvested and fixed in 10% buffered formalin for histopathological analysis. Fixed tissue samples were submitted to ULAM-IVAC (Unit for Laboratory Animal Medicine – In Vivo Animal Core, Ann Arbor, MI, USA) for paraffin embedding. Paraffin block samples were submitted to McClinchey Histology Labs, Inc. (Stockbridge, MI, USA) for sectioning in 4-micron thick slices and preparing unstained slides, Masson's trichrome stained slides, and hematoxylin and eosin (H&E) slides. Slides were examined under high resolution microscope (KEYENCE BZ-X800, Keyence, Itasca, IL, USA) which was used to capture images.

4.2.8 Histological Analysis

For multicolor immunofluorescence antigen retrieval, the tissue sections were deparaffinized by passing 2X times in Xylene. The samples were then washed in Xylene Ethanol followed by pure ethanol and were then gradually rehydrated by passing through 70%, 50%, 30% ethanol, and distilled water for 3 minutes each. Masked epitopes from the sections were recovered by heat induced antigen retrieval buffer by using water bath at 90°C for 30 minutes. Two methods of heat-induced antigen retrieval were performed. Citrate buffer pH 6 (Abcam, Waltham, MA, USA) and/or Tris-EDTA pH 9 (Abcam) were used depending on the nature of the antibody. For CD11b, CD8 and NK1.1 staining, after antigen retrieval, sections were transferred to PBS (Phosphate Buffered Saline, Thermofisher Scientific) for 30 minutes, and then the sections were blocked in 5% BSA (Bovine Serum Albumin). After washing with PBS, the samples were incubated with a rabbit IgG specific for CD8a for 1 hour at 37°C. For visualization of CD8a, the sections were incubated in Alexa 555 labeled Goat anti Rabbit IgG for 1 hour at 37°C. For visualization of CD11b and NK1.1, the sections were incubated with 1:100 diluted anti-CD11B antibody (clone M/170, Biolegend, San Diego, CA, USA) directly conjugated with Alexa 488 and anti-NK1.1 antibody (Biolegend) directly conjugated with Alexa 647 over-night at 4°C.

For E-cadherin, N-cadherin, and vimentin staining, the sections were first incubated in 1:100 dilution of Anti-vimentin mouse IgG, clone V9 (MilliporeSigma, Burlington, MA, USA) at 37°C, and secondary antibody staining was performed using Alexa 488 goat anti-mouse IgG. After each secondary antibody incubation, samples were washed for 30 minutes in PBS to eliminate cross reactivity for next cycle of antibody staining. Sections were then incubated with 1:100 anti-N-cadherin antibody, clone 6A9.2 (MilliporeSigma) for 1 hour at 37°C. Secondary antibody staining was performed using 1:100 Alexa 555 goat anti-mouse for visualization. After PBS wash, the sections were incubated with anti-E cadherin antibody [4A2] (Abcam) for 1 hour at 37°C. After washing with PBS, the sections were counterstained with Alexa 647 goat anti-mouse IgG, for visualization. After the final step of washing, the sections were quenched by using tissue autofluorescence quenching kit (Vector Biolabs, Malvern, PA, USA) and mounted using mounting media containing 4′,6-diamidino-2-phenylindole (DAPI, 1:10,000; MilliporeSigma).

4.2.9 Statistical Analysis

Statistical analysis was performed using SAS (version 9.4). The difference between treatment and controls was assessed using one-way ANOVA. For survival data, Kaplan–Meier curves were generated. The survival time (defined as the time taken for animals to reach the tumor endpoint criteria, i.e., tumor burden greater than 25 mm in any single dimension) was compared between control and treated rats using the log-rank test. $p < 0.05$ was considered significant.

4.3 Results

4.3.1 Tumor Response to Histotripsy and Survival Outcomes

All animals tolerated the orthotopic liver tumor inoculation procedure without complication. Seven to nine days after inoculation, MRI imaging indicated a minimum tumor diameter of 5 mm in all animals. Histotripsy was performed successfully in all treatment cohort animals with no complications, and the post-procedure monitoring revealed no clinical issues.

In the survival cohort, 81.8% (n=9/11) treatment animals experienced tumor burden reduction following partial histotripsy ablation and had tumor free survival for the remainder of the study (Table 4-1). In comparison, 100% (n=11/11) untreated control animals demonstrated increased tumor burden and intrahepatic metastasis and had to be euthanized within 1-3 weeks post treatment timepoint. Histotripsy-treated animals had statistically significant improved survival outcomes compared to controls with a p-value < 0.0001 (Figure 4-2).

Table 4-1McA-RH7777 tumor measurements

Group	ID	Survival (Week)	Week 0 (mm^3)	Week 1 (mm^3)	Week 2 (mm^3)	Week 3 (mm^3)	Week 4 (mm^3)	Week 5 (mm^3)	Week 6 (mm^3)	Week 7 (mm^3)	Week 8 (mm^3)	Week 9 (mm^3)	Week 10 (mm^3)	Week 11 (mm^3)	Week 12 (mm^3)
Histotripsy	H1	12	40.27	17.55	0	0	0	0	0	0	0	0	0	0	0
	H2	12	157.50	66.40	3.55	0	0	0	0	0	0	0	0	0	0
	H3	12	48.92	1.05	0	0	0	0	0	0	0	0	0	0	0
	H4	12	161.23	60.20	6.00	0	0	0	0	0	0	0	0	0	0
	H5	12	150.90	102.0	81.64	0	0	0	0	0	0	0	0	0	0
	H6	12	120.41	38.68	0	0	0	0	0	0	0	0	0	0	0
	H7	6	50.63	111.3	71.11	97.04	302.57	2490	7967	-	-	-	-	-	-
	H8	6	42.91	127.5	175.08	2032	1329.8	1950	6487	-	-	-	-	-	-
	H9	12	57.61	57.27	20.93	0	0	0	0	0	0	0	0	0	0
	H10	7	51.28	34.16	2.198	0	0	0	0	0	-	-	-	-	-
	H11	7	67.95	37.68	0	0	0	0	0	0	-	-	-	-	-
Control	C1	3	73.85	1094	1441	2747	-	-	-	-	-	-	-	-	-
	C2	1	233.35	11528	-	-	-	-	-	-	-	-	-	-	-
	C3	1	164.06	4391	-	-	-	-	-	-	-	-	-	-	-
	C4	1	193.63	4729	-	-	-	-	-	-	-	-	-	-	-
	C5	1	67.25	1421	-	-	-	-	-	-	-	-	-	-	-
	C6	1	278.62	2555	-	-	-	-	-	-	-	-	-	-	-
	C7	1	156.71	8937	-	-	-	-	-	-	-	-	-	-	-
	C8	2	55.16	454	2905	-	-	-	-	-	-	-	-	-	-
	C9	2	64.52	3727	4391	-	-	-	-	-	-	-	-	-	-
	C10	2	28.88	587.5	9107	-	-	-	-	-	-	-	-	-	-
	C11	1	39.25	1198	-	-	-	-	-	-	-	-	-	-	-

Note: Tumor measurements are made on MRI images in 3 dimensions, which is used to estimate tumor burden. If no tumor is detected on MRI '0' is recorded. Week 0 is the histotripsy timepoint (7–9 days post inoculation). n = 2/11 histotripsy animals still surviving at 7 weeks with no observable tumor were euthanized due to COVID shutdown (ID H10 and H11).

The survival time in the control group was 1.45 ± 0.69 (mean ± SEM) weeks. In the treatment group, the survival time was 10 ± 0.84 weeks. All survival times are reported post histotripsy timepoint, which was two weeks post tumor inoculation. The survival time range was 1-3 weeks (control group) and 6-12 weeks (treatment group) after histotripsy timepoint. n=7/11 animals in partial ablation group A were alive at 12 weeks with no observable tumor and were euthanized due to study endpoint per our protocol. In these animals, even with partial ablation of the tumor, we observed complete regression of both ablated and untargeted tumor. n=2/11 animal in the treatment group were euthanized at 6 weeks due to tumor burden greater than 25 mm in any one dimension. 2/11 histotripsy animals with complete regression and no metastases were euthanized early at 7 weeks due to research shutdown during COVID.

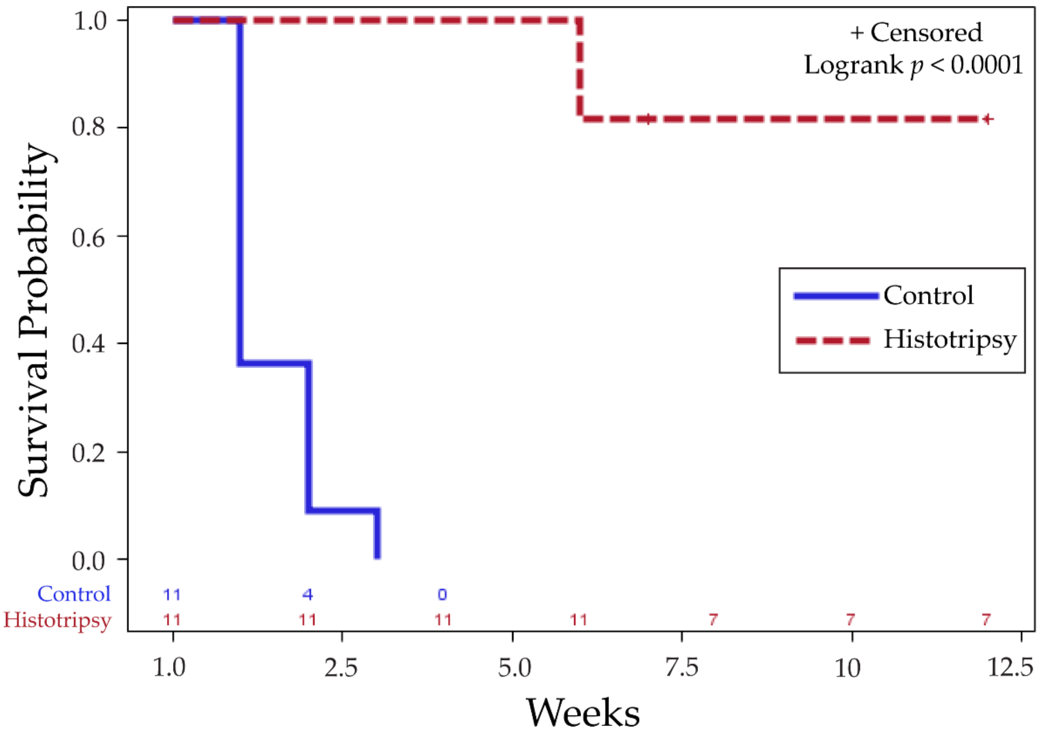

Figure 4-2 ***Survival Outcomes.*** *Kaplan Meier survival curve indicates significant difference in survival outcomes of histotripsy-treated animals vs untreated controls for tumor progression (p < 0.0001). '+ Censored' indicates that observations are right censored as n=2/11 histotripsy animals still surviving at 7 weeks with no observable tumor were euthanized due to COVID shutdown.*

4.3.2 Radiology Observations

At the histotripsy timepoint (7-9 days post tumor inoculation), untreated tumor appeared hyperintense on T2-weighted MRI compared to the adjacent normal liver tissue (Figure 4-3A). The tumor volume was 86.25 ± 15.12 mm3 (mean ± SEM) in the histotripsy group and 123.20 ± 25.87 mm3 (mean ± SEM) in control group. The difference was not statistically significant (p = 0.232). Subsequent timepoints are measured from the histotripsy timepoint (week 0).

In all control animals, a multi-nodular primary tumor along with multiple secondary metastatic nodules was observed by 1-3 weeks (Figure 4-3A), and the animals had to be euthanized due to increased tumor burden.

In the treatment group, the ablated tumor region demonstrated a hyperintense appearance (if the imaging was performed >6 hours after treatment) (Figure 4-3B) or demonstrated a hypointense appearance (if the imaging was performed within 4 hours of treatment) (Figure 4-3C). The untargeted tumor region showed appearance similar to the control tumor. In 9/11 animals, both ablated and unablated tumors began to demonstrate regression at 1 week post treatment and there was no detectable tumor on MRI by 3 weeks (Figure 4-3B). In these animals, no recurrence or metastasis was observed until the study endpoint was reached. Of note, local tumor progression and metastases was observed in 2/11 animals, leading to increased tumor burden and the animals were euthanized at 6 weeks post treatment (Figure 4-3C). There was no off-target ablation damage to skin or surrounding organs in any histotripsy animals.

A. Control tumor progression and metastases

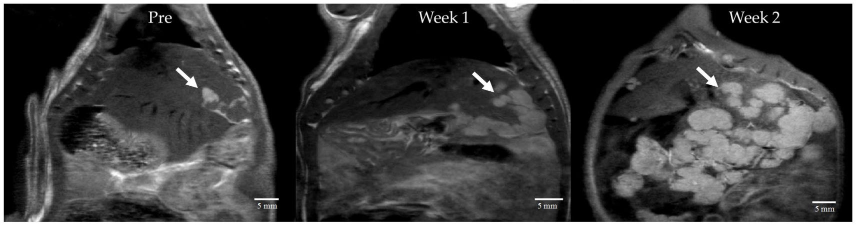

B. Histotripsy-treated tumor regression

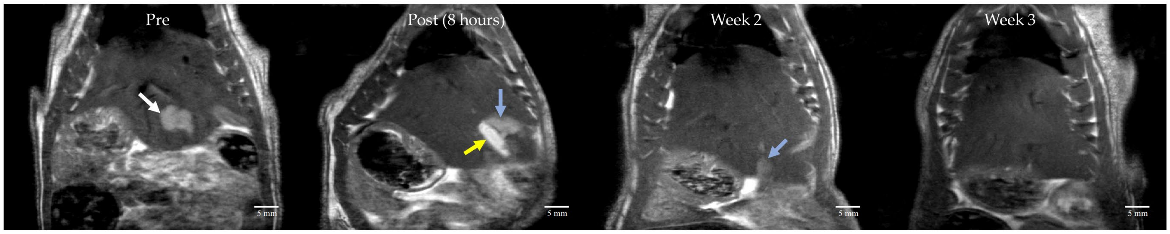

C. Histotripsy-treated tumor progression and metastases

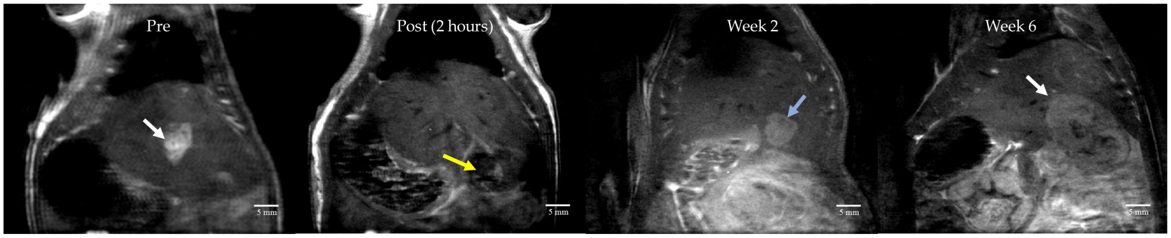

Figure 4-3 ***Representative T2- weighted MR images*** *for (A) untreated control, (B) histotripsy-treated tumor showing complete regression, and (C) histotripsy-treated tumor with local tumor progression. (A) Untreated control tumor appeared hyperintense compared to surrounding liver parenchyma at pre-treatment timepoint, developed metastases at week 1 which grew aggressively by week 2. White arrows show the tumor location. (B) Post-ablation, the ablated region appears hyperin-tense (yellow arrow) compared to untargeted tumor (blue arrow) likely due to edema (image acquired 8 hours post treatment). By week 2, tumor appeared to regress (blue arrow) and was undetectable week 3 onwards. (C) Post-ablation, the ablated region (yellow arrow) appears hy-pointense (image acquired within 2 hours post treatment). At week 2, the tumor did not show signs of size regression (blue arrow). Local tumor progression and metastases were observed by week 6 (white arrow).*

4.3.3 Histology Observations in Survival Groups

In control animals, multinodular local tumor progression was observed on H&E staining (Figure 4-4A). In these cases, aggressive tumor growth occupied most of the liver lobe, both at the site of the original tumor as well as Intrahepatic metastases (Figure 4-4A). In treated animals demonstrating complete tumor regression, there was ~1mm residual scar tissue with scattered dystrophic calcification at the site of the original tumor and no evidence of viable tumor cells on H&E staining (Figure 4-4B). These histology observations correlate with the MRI observation of no detectable tumor at the original treatment site, indicating complete regression of these tumors with resultant formation of focal scar tissue. In treated animals demonstrating tumor progression, collagenous tissue with regions of dystrophic calcification was observed in the ablation cavity (Figure 4-4C). The local tumor progression of the residual, untargeted tumor had a similar appearance to the control tumor.

A. Control tumor (Intrahepatic metastases), Week 1

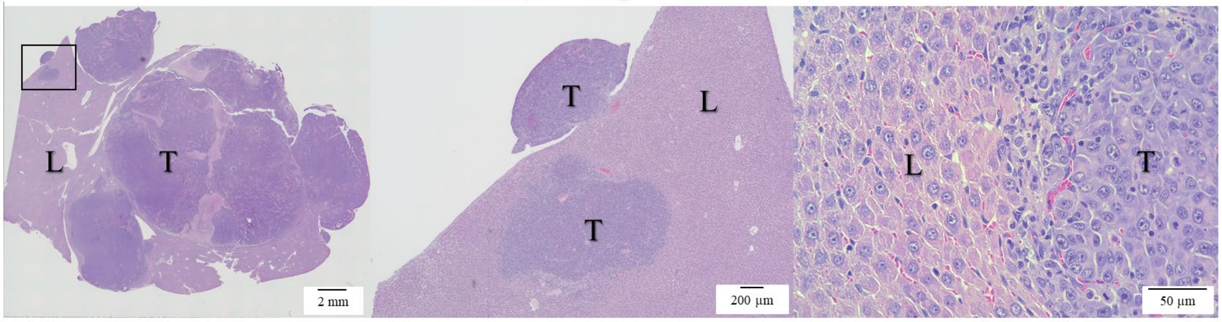

B. Histotripsy-treated tumor (Complete regression), Week 12

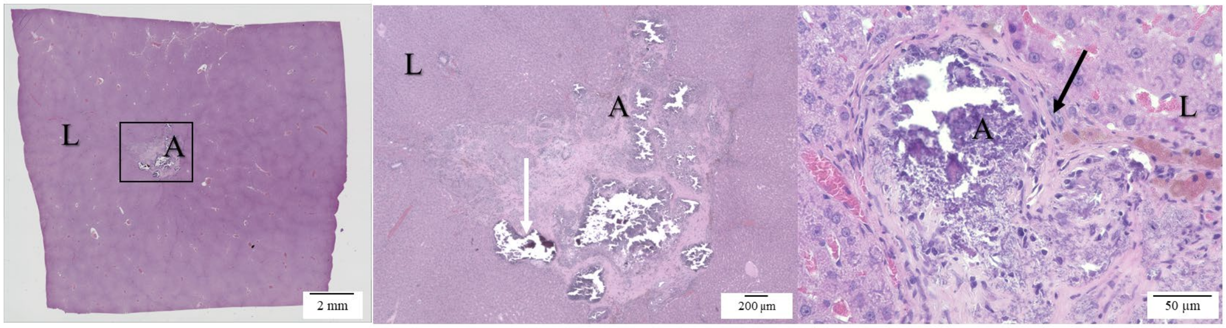

C. Histotripsy-treated tumor (Local tumor progression), Week 6

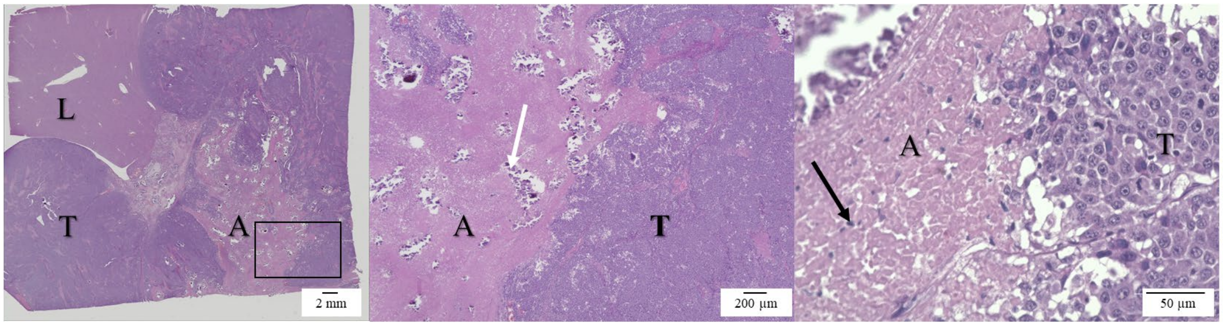

Figure 4-4 ***H&E-stained representative images*** *for (A) untreated control, (B) histotripsy-treated tumor showing complete regression, and (C) histotripsy-treated tumor with local tumor progression (L: Liver, A: Ablation Zone, T: Tumor). For each row, the first panel shows a low-magnification view of the entire tissue section, with an identified region of interest (ROI), the second and third panel show the ROI at higher magnifications. (A) Control tumor – Week 1: Intra-hepatic tumor progression and metastases are observed in the untreated control. Tumor growth occupied most of the liver lobe. (B) Histotripsy treated tumor – Week 12: In a treated tumor demonstrating regression, ~1mm scar tissue with scattered dystrophic calcification in the ablation zone (white arrow) and inflammatory cells (black arrow) within and surrounding the ablation zone are observed. (C) Histotripsy treated tumor – Week 6: In a treated tumor demonstrating local tumor progression, multinodular tumor growth is observed. Collagenous tissue with scattered dystrophic calcification is observed in the ablation zone (white arrow). A few inflammatory cells are seen in the ablation zone (black arrow).*

4.3.4 Histology Observations in Early Timepoint Groups

Trichrome staining of the control tumor on day 2 revealed nodular tumor extensions from the primary nodule as well as areas of collagen deposition in the tumor core, indicative of necrotic regions (Figure 4-5A). In comparison, at day 2 post-histotripsy, there is a thin rim of immune cells surrounding the periphery of the ablated tumor and liver (Figure 4-5B). There are intact tumor cells adjacent to the ablation zone indicative of the untargeted, residual tumor. The core of the ablation zone shows blood products.

Control tumor at day 7 shows invasive appearance at tumor periphery and multiple secondary tumor nodules (Figure 4-5C). In comparison, at day 7 post histotripsy, there is evidence of homogenate resorption with fibrotic or scar tissue beginning to form (Figure 4-5D). Inflammatory cells are scattered within the scar tissue and there is no evidence of intact tumor cells. On day 7 after scant histotripsy, collagenous deposition is observed, but there is no evidence of dystrophic calcification (Figure 4-5E). While there is evidence of blood products at the core, inflammatory cells are mainly confined to the ablation zone periphery. The appearance of the ablation zone is similar to the day 2 appearance post-histotripsy. These results suggest that the process of homogenate resorption and formation of scar tissue may be protracted in the scant histotripsy cohort as compared to the histotripsy cohort.

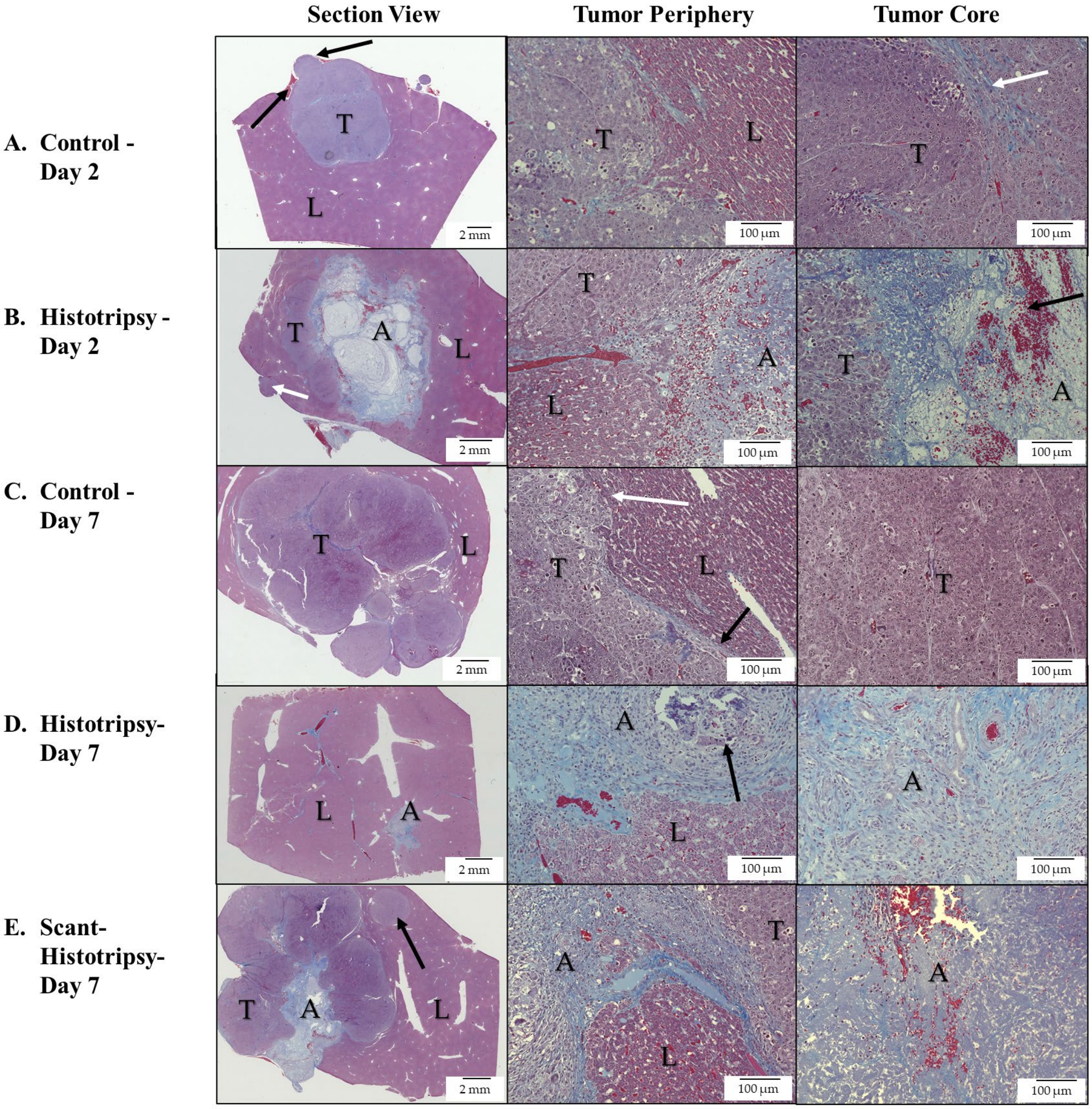

Figure 4-5 ***Trichrome-stained representative images*** *for (A) untreated control tumor (Day 2), (B) histotripsy-treated tumor (Day 2), (C) untreated control tumor (Day 7), (D) histotripsy-treated tumor (Day 7), and (E) scant histotripsy-treated (<25% tumor volume ablated) tumor (Day 7). All days are measured from the histotripsy-treatment timepoint. (L: Liver, A: Ablation Zone, T: Tumor). (A) Control - Day 2: Nodular tumor extensions from the primary nodule are observed (black arrows), areas of collagen deposition are observed in the tumor core (white arrow). (B) Histotripsy - Day 2: The ablation zone can be distinguished from the untreated residual tumor region. A metastatic nodule is observed (white arrow). The ablation zone consists of mostly acellular debris with scattered red and white blood cells (black arrow). (C) Control - Day 7: Local tumor progression of the primary tumor and multiple metastatic nodules is observed, colonizing most of the liver lobe. Tumor cells at the periphery demonstrate invasive characteristics (white arrow), at the location where a thin rim of collagenous tissue separating the tumor from normal liver is breached (black arrow). (D) Histotripsy - Day 7: Tumor is replaced by scar tissue with areas of dystrophic calcification (black arrow), substantial infiltration of inflammatory cells, and few red blood cells. No viable tumor cells are observed. (E) Scant Histotripsy - Day 7: Local tumor progression of the primary tumor and a*

metastatic nodule (black arrow) are observed with an area of scar tissue within the ablation zone. The ablation zone contains red blood cells and collagen. Inflammatory cells are observed mainly at the periphery of the ablation zone, but not at the core of the ablation zone.

4.3.5 Observations from Immunofluorescence Staining of Immune Cells

To determine the immune effects of histotripsy, infiltration of CD11b+ cells, CD8+ T cells and NK cells was compared in histotripsy treated tumors vs control tumors. At the core and the periphery of the control tumor, there is minimal immune infiltration on day 2 (Figure 4-6A). On day 2, increased immune infiltration of CD11b+ and NK cells is observed at the ablation zone periphery compared to control tumor periphery (Figure 4-6B). NK cells are also detected in the ablation zone on day 2 (Figure 4-6B).

On day 7, there is some infiltration of CD8+ T cells at the core and periphery of the control tumor as compared to day 2 (Figure 4-6C). CD8+ T-cell infiltration is also observed at the boundaries of histotripsy ablation zone, while NK cell and CD8+ cells are detected in the ablation zone core on day 7 (Figure 4-6D). In case of scant histotripsy ablation, reduced immune infiltration of CD8+ and NK cells is observed at the boundary of untreated tumor and normal liver in comparison to day 2 and day 7 post histotripsy (Figure 4-6E). Similarly, within the scant histotripsy ablation zone, the immune infiltration is insubstantial (Figure 4-6E). Overall, increased immune infiltration is observed in histotripsy tumors compared to controls on day 2 and day 7 post treatment timepoint. It is possible that there is a mini-mum tumor fraction threshold that should be ablated to generate meaningful immune effects as evidenced by the diminished immune infiltration observed in scant histotripsy (<25% volume ablation) vs histotripsy treated tumors (50-75% volume ablation).

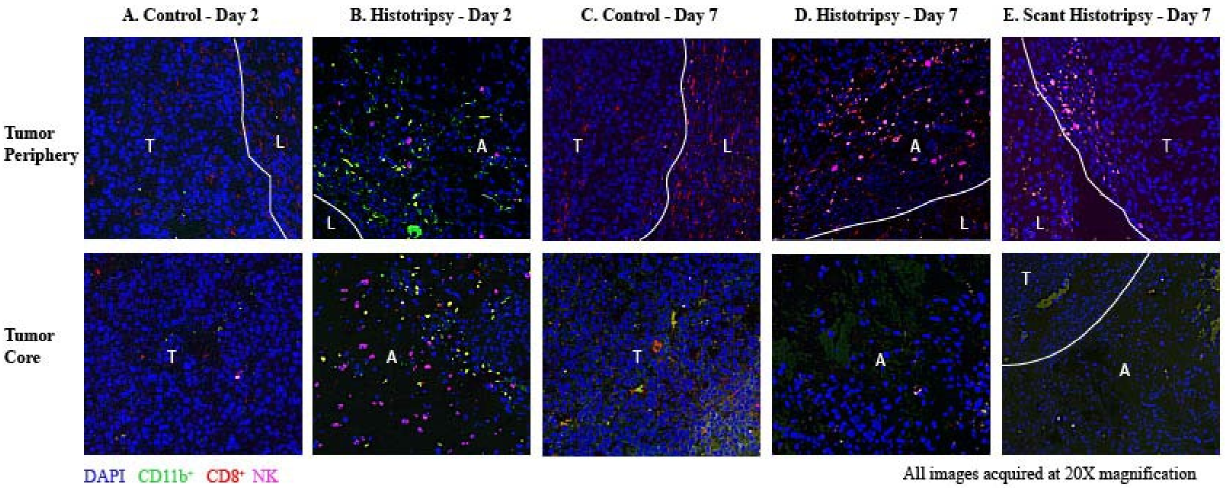

Figure 4-6 ***Representative multiplex immunohistochemistry images at 20X magnification showing immune cell infiltration*** *in (A) untreated control (Day 2), (B) histotripsy-treated tumor (Day 2), (C) untreated control (Day 7), (D) histotripsy-treated tumor (Day 7) and (E) scant histotripsy-treated (<25% tumor volume ablated) tumor (Day 7) at the tumor periphery (top) and tumor core (bottom). All days are measured from the histotripsy-treatment timepoint. (L: Liver, A: Ablation Zone, T: Tumor). The samples were stained for DAPI (blue), CD11b (green), CD8 (red) and NK (pink). (A) Control - Day 2: There is minimal immune infiltration at the core of the untreated control tumor. (B) Histotripsy - Day 2: At the periphery, increased infiltration of CD11b+ and NK cells is observed, NK cells are also observed at the core of the ablation zone. (C) Control - Day 7: There is some infiltration of CD8+ cells at the periphery, but no substantial infiltration is observed at the tumor core. (D) Histotripsy – Day 7: NK and CD8+ cells infiltrated the tumor periphery and were also detected at the core of the ablation zone. (E) Scant Histotripsy - Day 7: Some CD8+ and NK cells are observed at the un-targeted tumor-liver interface, but no substantial infiltration is observed in the ablation zone.*

4.3.6 Observations for Immunofluorescence Staining for Epithelial and Mesenchymal markers

To explore the impact of histotripsy on the risk of metastases, immunohistochemical expression of mesenchymal markers, i.e., loss of E-cadherin and gain of N-cadherin and vimentin was compared in histotripsy treated tumors vs control tumors. The plasma membranes of hepatocytes express N-cadherin (Figure 4-7). There is weak expression of vimentin in the untreated control tumor (Figure 4-7A). At day 2 post ablation, vimentin is upregulated at the ablation zone periphery (Figure 4-7B). At day 7, vimentin is also upregulated at the periphery of the control tumor (Figure 4-7C). At day 7 post ablation, vimentin up-regulation appears to have shifted inwards, towards the core of the ablation zone, while E-cadherin expression is upregulated at the periphery (Figure 4-7D). At day 7 post scant histotripsy, vimentin is weakly expressed at the perimeter of the untreated tumor as compared to the control tumor at day 7 (Figure 4-7E). Vimentin expression is also up-regulated near the edge of the ablation zone at the ablation zone-untreated tumor boundary on day 7 post scant histotripsy (Figure 4-7F).

The upregulation of mesenchymal marker vimentin could be associated with either tissue healing or metastasis. Since there was evidence of scar tissue formation but no in-tact tumor cells on histology at day 7 post histotripsy, the expression of vimentin at the periphery of the ablation zone on day 2 and in the ablation zone on day 7 suggests that tis-sue healing is the likely process. The similarity between the boundaries of the ablation zones on day 7 post scant histotripsy and day 2 post histotripsy further supports the premise that the process of homogenate resorption and tissue healing may be protracted in scant histotripsy. Vimentin upregulation at the control tumor periphery and untreated tumor in scant histotripsy on day 7, may be linked to metastatic invasion. The invasive appearance of control tumor on day 7 histology, as well as eventual development of metastases in all control animals and n=2 histotripsy animals with local tumor progression support this proposition.

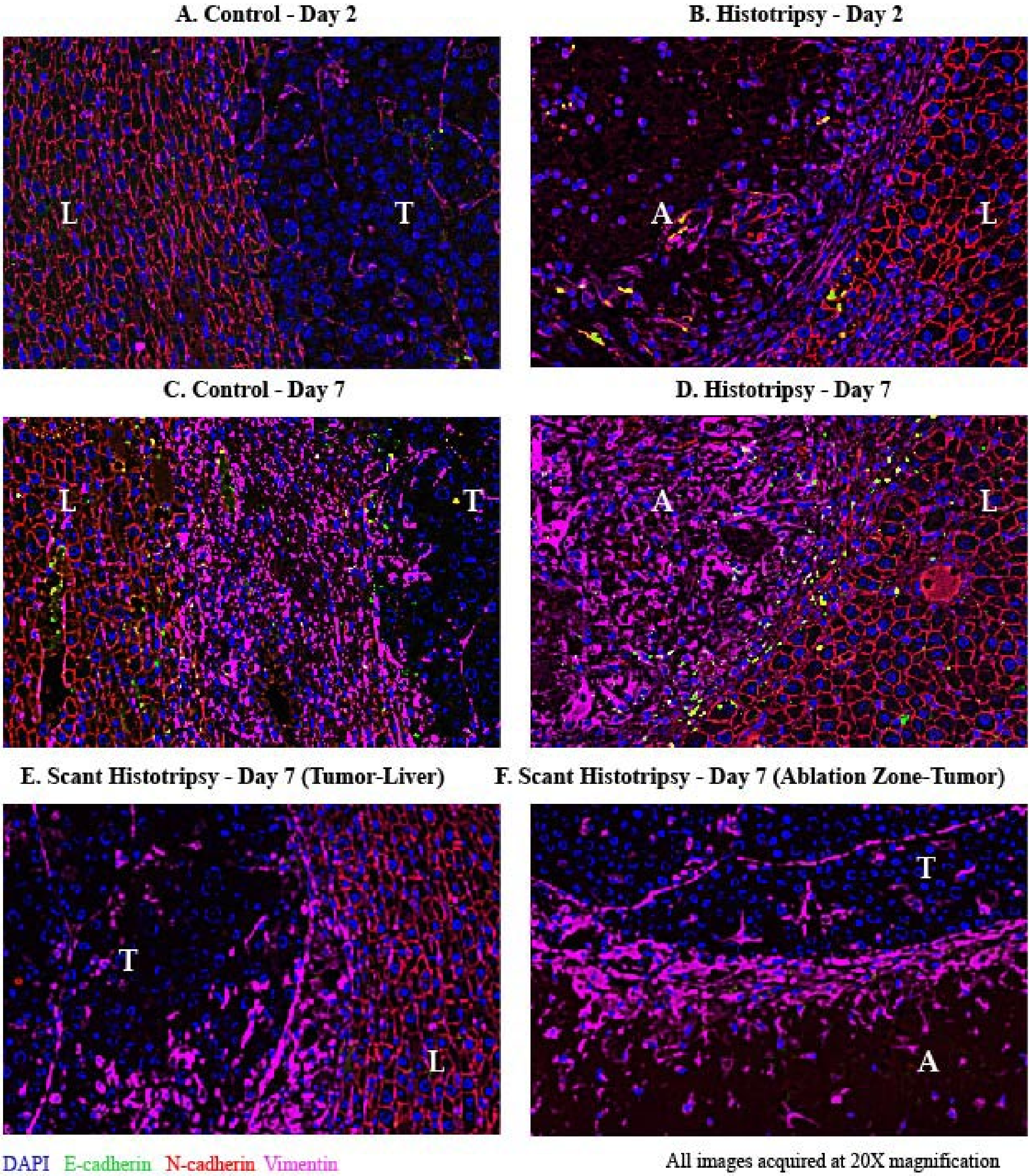

A. Control - Day 2

B. Histotripsy - Day 2

C. Control - Day 7

D. Histotripsy - Day 7

E. Scant Histotripsy - Day 7 (Tumor-Liver)

F. Scant Histotripsy - Day 7 (Ablation Zone-Tumor)

DAPI E-cadherin N-cadherin Vimentin

All images acquired at 20X magnification

Figure 4-7 ***Representative multiplex immunohistochemistry images showing epithelial and mesenchymal markers*** *in (A) untreated control (Day 2), (B) histotripsy-treated tumor (Day 2), (C) untreated control (Day 7), (D) histotripsy-treated tumor (Day 7), and (E-F) scant histotripsy treated (<25% tumor volume ablated) tumor (Day 7). All days are measured from the histotripsy-treatment timepoint. The samples were stained for DAPI (blue), E-cadherin (green), N-cadherin (red) and vimentin (pink). (L: Liver, A: Ablation Zone, T: Tumor). In all panels, N-cadherin is expressed at the plasma membrane of hepatocytes. (A) Control - Day 2: Vimentin is weakly expressed within the control tumor. (B) Histotripsy - Day 2: Vimentin expression is upregulated at the ablation zone periphery. (C) Control - Day 7: Vimentin expression is upregulated at the control tumor periphery. (D) Histotripsy - Day 7: Vimentin is up-regulated within the ablation zone, E-cadherin is ex-pressed at the ablation zone periphery. (E)*

Scant Histotripsy - Day 7: Vimentin is expressed at the untreated tumor-liver interface. (F) Scant Histotripsy - Day 7: Vimentin is expressed in the periphery of the ablation zone at the ablation zone-untreated tumor interface.

4.4 Discussion

Previous histotripsy investigations have demonstrated the feasibility and efficacy of histotripsy for non-invasive ablation in the liver [15, 16, 19, 22, 27]. In this study, we evaluated the development of metastatic HCC after partial histotripsy tumor ablation in an immune-competent, McA-RH7777 rodent liver tumor model. The McA-RH7777 rodent tumor model is a well-established rat orthotopic HCC model used for image-guided interventional oncology research [29, 30]. Even with partial ablation of the tumor volume, >80% histotripsy-treated animals demonstrated local tumor regression, with no local recurrence or metastasis and had significantly improved survival as compared to 100% control animals demonstrating local tumor progression and intra-hepatic metastases. The formation of scar tissue was observed in histotripsy-treated animals with no viable tumor cells observable as early as day 7 post histotripsy, indicating the resorption of the ablation zone had begins early post-treatment. These results suggest that histotripsy does not increase the risk of developing metastases post ablation. Increased immune infiltration was also observed in treated tumors at day 2 and day 7 post-histotripsy as compared to control tumors, which may have triggered an anti-tumor immune response contributing to the complete regression of partially ablated tumors, while preventing metastases in the immunocompetent rodent hosts.

Metastasis is a complex process consisting primarily of five essential steps- 1) invasion, where tumor cells detach from ECM and infiltrate adjacent tissue, 2) intravasation, where tumor cells enter the circulatory system 3) survival in the circulatory system, 4) extravasation; where tumor cells exit the circulatory system and infiltrate a distant site and 5) colonization; where tumor cells grow and proliferate at the new site [31]. The seed and soil theory of metastasis was first proposed by Stephen Paget in 1889, which suggests that the metastatic growth of cancer cells (the ‘seed’) is dependent on the competence of the distant organ (the ‘soil’) [32]. HCC is a highly invasive cancer favoring proximal intrahepatic metastasis, likely due to the dense hepatic vasculature and immunosuppressive polarization of the liver [33]. In this study, we focused investigation on the first step of the metastatic cascade, invasion which is induced by epithelial-to-mesenchymal transition (EMT) of tumor cells where they lose epithelial characteristics and concomitantly acquire mesenchymal characteristics. EMT is a biologic process that allows epithelial cells to transform into a mesenchymal cell phenotype, allowing them to migrate and infiltrate and can be classified into three biological subtypes. Of these, ‘type 2’ is associated with wound healing and organ fibrosis, and ‘type 3’ is associated with tumor progression and metastases [34]. EMT is characterized by the downregulation of epithelial markers such as E-cadherin and the up-regulation of mesenchymal markers such as N-cadherin and vimentin. In type 3 EMT, carcinoma cells at the invasive front of primary tumors can acquire mesenchymal phenotype [35]. In our study, vimentin upregulation observed in at the periphery of control tumor on day 7, but not on day 2 is likely indicative of a type 3 EMT process. This premise is supported by the more invasive appearance of tumor observed on day 7 trichrome staining as well as the eventual invasive metastatic progression observed in all control tumors at later timepoints. In contrast, type 2 EMT is initiated as a reparative-associated process in response to tissue injury or inflammation and ceases once the inflammatory offense is withdrawn, such as with wound healing and fibrosis [36]. However, within the liver, the contribution of type 2 EMT to fibrosis is still controversial [37-39]. In general, vimentin is upregulated in the wound healing process; cytoskeletal vimentin is released extracellularly after tissue injury and binds to mesenchymal leader cells located at the wound edge to facilitate healing [40].

In our study, vimentin was observed at the histotripsy-treated tumor boundary on day 2 and within tumor on day 7. This evidence suggests that the expression of vimentin is likely linked to the formation of fibrous tissue as part of the wound healing process in response to histotripsy ablation. Upregulation of E-cadherin observed at the tumor boundary on day 7 is likely indicative of re-epithelialization of the ‘wound’ caused by histotripsy ablation; re-epithelialization is a necessary and essential requirement for successful wound closure [41]. Since EMT may be involved in both tissue healing and metastasis processes, further investigation of the metastatic cascade is necessary. Intravasation of tumor cells generate circulating tumor cells (CTCs), however, it has been estimated that only <0.01% of CTCs will develop distant metastatic lesions after surviving stress, immune attack and anoikis in a hostile circulatory system environment [42]. Additional studies are on-going to assess the circulating tumor cells (CTCs) which will provide an insight into whether the mechanical disruption caused by histotripsy increases CTCs as compared to untreated controls.

The immune microenvironment also affects the metastatic potential of the disseminating cells. Cancer therapies such as radiation, chemotherapy and thermal ablation destroy tumor and surrounding tissues via necrosis, which can trigger an inflammatory immune response. However, this response can be either pro-tumor or anti-tumor depending on the tumor microenvironment and the expression of immune mediators and modulators [43-46]. Our previous study demonstrated that subcutaneous histotripsy ablation of melanoma tumors in murine hosts releases tumor antigens with preserved immunogenicity initiating both local (upregulation of intratumoral NK cells, dendritic cells, neutrophils, B cells, CD4+ T cells and CD8+ T cells), and systemic immune response as evidenced by abscopal immune effects [20]. In the current study, we observed increased immune infiltration of CD11b+ and NK cells in histotripsy-treated orthotopic liver tumor boundary compared to control tumor at day 2 timepoint. At day 7 timepoint CD8+ T cells were also seen infiltrating the tumor region from the periphery. CD11b+ myeloid cells as well as NK cells contribute to anti-tumor innate immunity, while CD8+ cells contribute to adaptive immune-mediated responses [47-49]. Studies have shown that enhanced T-cell response generated by immunotherapy can prevent metastasis in early-stage cancer patients [50]. In a human colorectal cancer study, absence of metastasis correlated with increased expression of T cell proliferation and antigen presentation functions [51]. There is increasing evidence that ablative therapies can either positively or negatively impact tumor progression and metastasis by regulating both adaptive and innate immunity [52-55]. A murine study reported that RFA of the liver induced a strong, time-dependent immune response (presence of neutrophils, activated myofibroblasts, and macrophages) at the necrotic zone boundary [56]. In a study involving colorectal cancer patients, incomplete RFA (presence of remnant tumor after therapy) was shown to promote tumor progression and was associated with earlier development of metastases [57]. Another study reported in-creased metastatic potential of residual carcinoma after transarterial embolization using the McA-RH7777 model [30]. The first-in-human histotripsy study reported intrahepatic abscopal effects (reduction in non-targeted tumor lesions) following histotripsy ablation of a single liver tumor lesion in a colorectal cancer patient with progressive, multiple meta-static disease [26]. Our previous study using the N1-S1 liver orthotopic tumor model had demonstrated that complete histotripsy ablation cohort had a 100% regression rate, however in the partial ablation cohort (50-75% tumor ablation), only 80% animals demonstrated regression [22]. Similar results were observed in the current study; when at least 50% tumor volume was ablated, >80% of the tumors completely regressed and no clinical recurrence/metastases was detected, indicating an anti-tumor immune response. However, in the scant histotripsy cohort (<25% tumor ablation), tumor progression was observed suggesting that the anti-tumor immune response was too weak as evidenced by the diminished immune infiltration. There is likely a minimal tumor volume percentage threshold that needs to be ablated to generate sufficient histotripsy response to cause the entire tumor (both ablated and unablated regions) to regress.

One of the primary limitations of our study is that only small subset of immune cells was analyzed. Future studies will focus extensively on quantitation of additional intra-tumoral and peripheral immune cell subsets using flow cytometry assays. Tumor progression and metastasis are influenced by several molecular mechanisms and factors. The orthotopic implantation of McA-RH7777 cells using cyclophosphamide for temporary immune suppression to promote tumor uptake [58] does not fully represent spontaneously developing tumors in the human liver. This study also did not utilize any immunomodulating drugs in combination with histotripsy. Although histotripsy alone resulted in complete regression of the tumor in >80% animals, it would be worthwhile to explore the response of histotripsy in combination with immunotherapies since ablation-induced immune responses have been historically reported as inadequate in eliminating established tumors. The exact mechanism of cell death of the untargeted residual tumor following partial ablation is also unknown and is likely a combination of immunogenic cell death mechanisms; further investigations are currently ongoing. Another limitation is that tumors in this study were treated at an early stage before metastases were radiologically visible. Future studies will utilize immunomodulatory adjuvants with histotripsy ablation to treat tumors in different stages of disease progression, including after the development of intrahepatic metastases and monitor their response.

4.5 References

1. R. L. Siegel, K. D. Miller, H. E. Fuchs, and A. Jemal, "Cancer Statistics, 2021," (in eng), CA Cancer J Clin, vol. 71, no. 1, pp. 7-33, 01 2021, doi: 10.3322/caac.21654.

2. D. Anwanwan, S. K. Singh, S. Singh, V. Saikam, and R. Singh, "Challenges in liver cancer and possible treatment approaches," (in eng), Biochim Biophys Acta Rev Cancer, vol. 1873, no. 1, p. 188314, 01 2020, doi: 10.1016/j.bbcan.2019.188314.

3. J. de Ridder, J. H. de Wilt, F. Simmer, L. Overbeek, V. Lemmens, and I. Nagtegaal, "Incidence and origin of histologically confirmed liver metastases: an explorative case-study of 23,154 patients," (in eng), Oncotarget, vol. 7, no. 34, pp. 55368-55376, 08 23 2016, doi: 10.18632/oncotarget.10552.

4. L. Kulik and H. B. El-Serag, "Epidemiology and Management of Hepatocellular Carcinoma," (in eng), Gastroenterology, vol. 156, no. 2, pp. 477-491.e1, 01 2019, doi: 10.1053/j.gastro.2018.08.065.

5. American Cancer Society, "Cancer Facts & Figures 2021," 2021.

6. N. Portolani et al., "Early and late recurrence after liver resection for hepatocellular carcinoma: prognostic and therapeutic implications," (in eng), Ann Surg, vol. 243, no. 2, pp. 229-35, Feb 2006, doi: 10.1097/01.sla.0000197706.21803.a1.

7. K. Leone, C. Poggiana, and R. Zamarchi, "The Interplay between Circulating Tumor Cells and the Immune System: From Immune Escape to Cancer Immunotherapy," (in eng), Diagnostics (Basel), vol. 8, no. 3, Aug 30 2018, doi: 10.3390/diagnostics8030059.

8. P. S. Steeg, "Tumor metastasis: mechanistic insights and clinical challenges," (in eng), Nat Med, vol. 12, no. 8, pp. 895-904, Aug 2006, doi: 10.1038/nm1469.

9. Z. Xu et al., "Controlled ultrasound tissue erosion," (in eng), IEEE Trans Ultrason Ferroe-lectr Freq Control, vol. 51, no. 6, pp. 726-36, Jun 2004.

10. J. E. Parsons, C. A. Cain, G. D. Abrams, and J. B. Fowlkes, "Pulsed cavitational ultrasound therapy for controlled tissue homogenization," (in eng), Ultrasound Med Biol, vol. 32, no. 1, pp. 115-29, Jan 2006, doi: 10.1016/j.ultrasmedbio.2005.09.005.

11. W. W. Roberts, T. L. Hall, K. Ives, J. S. Wolf, Jr., J. B. Fowlkes, and C. A. Cain, "Pulsed cavi-tational ultrasound: a noninvasive technology for controlled tissue ablation (histotripsy) in the rabbit kidney," (in eng), J Urol, vol. 175, no. 2, pp. 734-8, Feb 2006, doi: 10.1016/s0022-5347(05)00141-2.

12. Y. N. Wang, T. Khokhlova, M. Bailey, J. H. Hwang, and V. Khokhlova, "Histological and biochemical analysis of mechanical and thermal bioeffects in boiling histotripsy lesions induced by high intensity focused ultrasound," (in eng), Ultrasound Med Biol, vol. 39, no. 3, pp. 424-38, Mar 2013, doi: 10.1016/j.ultrasmedbio.2012.10.012.

13. F. Winterroth et al., "Examining and analyzing subcellular morphology of renal tissue treated by histotripsy," (in eng), Ultrasound Med Biol, vol. 37, no. 1, pp. 78-86, Jan 2011, doi: 10.1016/j.ultrasmedbio.2010.10.002.

14. T. L. Hall, K. Kieran, K. Ives, J. B. Fowlkes, C. A. Cain, and W. W. Roberts, "Histotripsy of rabbit renal tissue in vivo: temporal histologic trends," (in eng), J Endourol, vol. 21, no. 10, pp. 1159-66, Oct 2007, doi: 10.1089/end.2007.9915.

15. E. Vlaisavljevich et al., "Image-guided non-invasive ultrasound liver ablation using histotripsy: feasibility study in an in vivo porcine model," (in eng), Ultrasound Med Biol, vol. 39, no. 8, pp. 1398-409, Aug 2013, doi: 10.1016/j.ultrasmedbio.2013.02.005.

16. A. R. Smolock et al., "Robotically Assisted Sonic Therapy as a Noninvasive Nonthermal Ablation Modality: Proof of Concept in a Porcine Liver Model," (in eng), Radiology, vol. 287, no. 2, pp. 485-493, 05 2018, doi: 10.1148/radiol.2018171544.

17. E. A. Knott et al., "Robotically-Assisted Sonic Therapy for Renal Ablation in a Live Porcine Model: Initial Preclinical Results," (in eng), J Vasc Interv Radiol, vol. 30, no. 8, pp. 1293-1302, Aug 2019, doi: 10.1016/j.jvir.2019.01.023.

18. K. C. Longo et al., "Robotically Assisted Sonic Therapy (RAST) for Noninvasive Hepatic Ablation in a Porcine Model: Mitigation of Body Wall Damage with a Modified Pulse Sequence," (in eng), Cardiovasc Intervent Radiol, vol. 42, no. 7, pp. 1016-1023, Jul 2019, doi: 10.1007/s00270-019-02215-8.

19. E. Vlaisavljevich et al., "Non-Invasive Liver Ablation Using Histotripsy: Preclinical Safety Study in an In Vivo Porcine Model," (in eng), Ultrasound Med Biol, vol. 43, no. 6, pp. 1237-1251, Jun 2017, doi: 10.1016/j.ultrasmedbio.2017.01.016.

20. S. Qu et al., "Non-thermal histotripsy tumor ablation promotes abscopal immune responses that enhance cancer immunotherapy," (in eng), J Immunother Cancer, vol. 8, no. 1, Jan 2020, doi: 10.1136/jitc-2019-000200.

21. T. Worlikar et al., "Histotripsy for Non-Invasive Ablation of Hepatocellular Carcinoma (HCC) Tumor in a Subcutaneous Xenograft Murine Model," (in eng), Conf Proc IEEE Eng Med Biol Soc, vol. 2018, pp. 6064-6067, 07 2018, doi: 10.1109/EMBC.2018.8513650.

22. T. Worlikar et al., "Effects of Histotripsy on Local Tumor Progression in an in vivo Orthotopic Rodent Liver Tumor Model," (in eng), BME Frontiers, vol. 2020, 2020, doi: 10.34133/2020/9830304.

23. N. R. Styn, T. L. Hall, J. B. Fowlkes, C. A. Cain, and W. W. Roberts, "Histotripsy of renal implanted VX-2 tumor in a rabbit model: investigation of metastases," (in eng), Urology, vol. 80, no. 3, pp. 724-9, Sep 2012, doi: 10.1016/j.urology.2012.06.020.

24. G. R. Schade et al., "Histotripsy focal ablation of implanted prostate tumor in an ACE-1 ca-nine cancer model," (in eng), J Urol, vol. 188, no. 5, pp. 1957-64, Nov 2012, doi: 10.1016/j.juro.2012.07.006.

25. L. Mancia, E. Vlaisavljevich, Z. Xu, and E. Johnsen, "Predicting Tissue Susceptibility to Me-chanical Cavitation Damage in Therapeutic Ultrasound," (in eng), Ultrasound Med Biol, vol. 43, no. 7, pp. 1421-1440, Jul 2017, doi: 10.1016/j.ultrasmedbio.2017.02.020.

26. J. Vidal-Jove, X. Serres-Creixams, T. J. Ziemlewicz, and J. M. Cannata, "Liver Histotripsy Mediated Abscopal Effect-Case Report," (in eng), IEEE Trans Ultrason Ferroelectr Freq Control, vol. 68, no. 9, pp. 3001-3005, 09 2021, doi: 10.1109/TUFFC.2021.3100267.

27. E. Vlaisavljevich et al., "Non-Invasive Ultrasound Liver Ablation Using Histotripsy: Chronic Study in an In Vivo Rodent Model," (in eng), Ultrasound Med Biol, vol. 42, no. 8, pp. 1890-902, Aug 2016, doi: 10.1016/j.ultrasmedbio.2016.03.018.

28. A. D. Maxwell, C. A. Cain, T. L. Hall, J. B. Fowlkes, and Z. Xu, "Probability of cavitation for single ultrasound pulses applied to tissues and tissue-mimicking materials," (in eng), Ultrasound Med Biol, vol. 39, no. 3, pp. 449-65, Mar 2013, doi: 10.1016/j.ultrasmedbio.2012.09.004.

29. W. Zhang et al., "Establishment and characterization of McA-RH7777 cells using virus-mediated stable overexpression of enhanced green fluorescent protein," (in eng), Exp Ther Med, vol. 16, no. 4, pp. 3149-3154, Oct 2018, doi: 10.3892/etm.2018.6580.

30. G. Z. Wang et al., "Increased metastatic potential of residual carcinoma after transarterial embolization in rat with McA-RH7777 hepatoma," (in eng), Oncol Rep, vol. 31, no. 1, pp. 95-102, Jan 2014, doi: 10.3892/or.2013.2820.

31. F. van Zijl, G. Krupitza, and W. Mikulits, "Initial steps of metastasis: cell invasion and en-dothelial transmigration," (in eng), Mutat Res, vol. 728, no. 1-2, pp. 23-34, 2011 Jul-Oct 2011, doi: 10.1016/j.mrrev.2011.05.002.

32. S. Paget, "The distribution of secondary growths in cancer of the breast. 1889," (in eng), Cancer Metastasis Rev, vol. 8, no. 2, pp. 98-101, Aug 1989.

33. F. van Zijl et al., "Epithelial-mesenchymal transition in hepatocellular carcinoma," (in eng), Future Oncol, vol. 5, no. 8, pp. 1169-79, Oct 2009, doi: 10.2217/fon.09.91.

34. R. Kalluri and R. A. Weinberg, "The basics of epithelial-mesenchymal transition," (in eng), J Clin Invest, vol. 119, no. 6, pp. 1420-8, Jun 2009, doi: 10.1172/JCI39104.

35. T. Brabletz et al., "Variable beta-catenin expression in colorectal cancers indicates tumor progression driven by the tumor environment," (in eng), Proc Natl Acad Sci U S A, vol. 98, no. 18, pp. 10356-61, Aug 28 2001, doi: 10.1073/pnas.171610498.

36. G. D. Marconi et al., "Epithelial-Mesenchymal Transition (EMT): The Type-2 EMT in Wound Healing, Tissue Regeneration and Organ Fibrosis," (in eng), Cells, vol. 10, no. 7, 06 23 2021, doi: 10.3390/cells10071587.

37. K. Yu, Q. Li, G. Shi, and N. Li, "Involvement of epithelial-mesenchymal transition in liver fibrosis," (in eng), Saudi J Gastroenterol, vol. 24, no. 1, pp. 5-11, 2018 Jan-Feb 2018, doi: 10.4103/sjg.SJG_297_17.

38. M. Zeisberg et al., "Fibroblasts derive from hepatocytes in liver fibrosis via epithelial to mesenchymal transition," (in eng), J Biol Chem, vol. 282, no. 32, pp. 23337-47, Aug 10 2007, doi: 10.1074/jbc.M700194200.

39. Y. L. Zhao, R. T. Zhu, and Y. L. Sun, "Epithelial-mesenchymal transition in liver fibrosis," (in eng), Biomed Rep, vol. 4, no. 3, pp. 269-274, Mar 2016, doi: 10.3892/br.2016.578.

40. J. L. Walker, B. M. Bleaken, A. R. Romisher, A. A. Alnwibit, and A. S. Menko, "In wound re-pair vimentin mediates the transition of mesenchymal leader cells to a myofibroblast pheno-type," (in eng), Mol Biol Cell, vol. 29, no. 13, pp. 1555-1570, 07 01 2018, doi: 10.1091/mbc.E17-06-0364.

41. I. Pastar et al., "Epithelialization in Wound Healing: A Comprehensive Review," (in eng), Adv Wound Care (New Rochelle), vol. 3, no. 7, pp. 445-464, Jul 01 2014, doi: 10.1089/wound.2013.0473.

42. A. F. Chambers, A. C. Groom, and I. C. MacDonald, "Dissemination and growth of cancer cells in metastatic sites," (in eng), Nat Rev Cancer, vol. 2, no. 8, pp. 563-72, Aug 2002, doi: 10.1038/nrc865.

43. S. I. Grivennikov, F. R. Greten, and M. Karin, "Immunity, inflammation, and cancer," (in eng), Cell, vol. 140, no. 6, pp. 883-99, Mar 19 2010, doi: 10.1016/j.cell.2010.01.025.

44. J. Vakkila and M. T. Lotze, "Inflammation and necrosis promote tumour growth," (in eng), Nat Rev Immunol, vol. 4, no. 8, pp. 641-8, 08 2004, doi: 10.1038/nri1415.

45. M. J. Smyth, G. P. Dunn, and R. D. Schreiber, "Cancer immunosurveillance and immuno-editing: the roles of immunity in suppressing tumor development and shaping tumor immuno-genicity," (in eng), Adv Immunol, vol. 90, pp. 1-50, 2006, doi: 10.1016/S0065-2776(06)90001-7.

46. W. W. Lin and M. Karin, "A cytokine-mediated link between innate immunity, inflamma-tion, and cancer," (in eng), J Clin Invest, vol. 117, no. 5, pp. 1175-83, May 2007, doi: 10.1172/JCI31537.

47. M. C. Schmid et al., "Integrin CD11b activation drives anti-tumor innate immunity," (in eng), Nat Commun, vol. 9, no. 1, p. 5379, 12 19 2018, doi: 10.1038/s41467-018-07387-4.

48. B. Farhood, M. Najafi, and K. Mortezaee, "CD8," (in eng), J Cell Physiol, vol. 234, no. 6, pp. 8509-8521, 06 2019, doi: 10.1002/jcp.27782.

49. J. Wu and L. L. Lanier, "Natural killer cells and cancer," (in eng), Adv Cancer Res, vol. 90, pp. 127-56, 2003, doi: 10.1016/s0065-230x(03)90004-2.

50. J. Fares, M. Y. Fares, and Y. Fares, "Immune checkpoint inhibitors: Advances and impact in neuro-oncology," (in eng), Surg Neurol Int, vol. 10, p. 9, 2019, doi: 10.4103/sni.sni_366_18.

51. B. Mlecnik et al., "The tumor microenvironment and Immunoscore are critical determinants of dissemination to distant metastasis," (in eng), Sci Transl Med, vol. 8, no. 327, p. 327ra26, Feb 24 2016, doi: 10.1126/scitranslmed.aad6352.

52. H. Takaki, F. Cornelis, Y. Kako, K. Kobayashi, N. Kamikonya, and K. Yamakado, "Thermal ablation and immunomodulation: From preclinical experiments to clinical trials," (in eng), Di-agn Interv Imaging, vol. 98, no. 9, pp. 651-659, Sep 2017, doi: 10.1016/j.diii.2017.04.008.

53. R. Slovak, J. M. Ludwig, S. N. Gettinger, R. S. Herbst, and H. S. Kim, "Immuno-thermal ab-lations - boosting the anticancer immune response," (in eng), J Immunother Cancer, vol. 5, no. 1, p. 78, 10 17 2017, doi: 10.1186/s40425-017-0284-8.

54. L. Qian, Y. Shen, J. Xie, and Z. Meng, "Immunomodulatory effects of ablation therapy on tumors: Potentials for combination with immunotherapy," (in eng), Biochim Biophys Acta Rev Cancer, vol. 1874, no. 1, p. 188385, 08 2020, doi: 10.1016/j.bbcan.2020.188385.

55. S. P. Haen, P. L. Pereira, H. R. Salih, H. G. Rammensee, and C. Gouttefangeas, "More than just tumor destruction: immunomodulation by thermal ablation of cancer," (in eng), Clin Dev Immunol, vol. 2011, p. 160250, 2011, doi: 10.1155/2011/160250.

56. N. Rozenblum et al., "Radiofrequency Ablation: Inflammatory Changes in the Periablative Zone Can Induce Global Organ Effects, including Liver Regeneration," (in eng), Radiology, vol. 276, no. 2, pp. 416-25, Aug 2015, doi: 10.1148/radiol.15141918.

57. L. Shi et al., "Inflammation induced by incomplete radiofrequency ablation accelerates tu-mor progression and hinders PD-1 immunotherapy," (in eng), Nat Commun, vol. 10, no. 1, p. 5421, 11 28 2019, doi: 10.1038/s41467-019-13204-3.

58. R. Diehl et al., "Immunosuppression for in vivo research: state-of-the-art protocols and ex-perimental approaches," (in eng), Cell Mol Immunol, vol. 14, no. 2, pp. 146-179, Feb 2017, doi: 10.1038/cmi.2016.39.

Chapter 5 Histotripsy Ablation Stimulates Abscopal Immune Responses to Enhance Cancer Immunotherapy

A majority component of this chapter has been published in *Journal for Immunotherapy of Cancer* © 2020 BMJ Publishing Group Ltd & Society for Immunotherapy of Cancer.

Reprinted, with permission, from S. Qu, T. Worlikar, A.E. Felsted et al., "Non-thermal histotripsy tumor ablation promotes abscopal immune responses that enhance cancer immunotherapy," (in eng), J Immunother Cancer, vol. 8, no. 1, Jan 2020, doi: 10.1136/jitc-2019-000200.

5.1 Introduction

Histotripsy is a novel non-invasive, non-ionizing, non-thermal ablation method that destroys target tissue through precise control of acoustic cavitation [1-3]. Microsecond-length, high-amplitude ultrasound pulses (<2 cycles) generate cavitation from endogenous gas pockets in the target tissue[1, 2, 4]. The rapid expansion and collapse of the cavitation microbubbles (within a few hundred microseconds) produces high strains and disrupts cells in the target region into a liquid acellular homogenate [2, 5]. The low duty cycle of the ultrasound pulses (on-time/ (on- + off- time) < 0.1%) prevents undesirable thermal effects to safely achieve homogeneous cell disruption even in vascular organs [6]. Our previous study has demonstrated that histotripsy can destroy the target tumor tissue to form acellular debris, which is resorbed over time, resulting in effective reduction of local tumor progression and improvement in survival outcomes [7]. It is hypothesized that histotripsy-mediated mechanical disruption of tumor cells may release tumor antigens which can be recognized by the immune system to stimulate anti-tumor response.

Cancer immunotherapy encompasses treatments such as targeted antibodies, cancer vaccines, adoptive cell transfer, tumor-infecting viruses, checkpoint inhibitors, and cytokines to stimulate the patient’s immune system to recognize and eliminate tumor cells [8]. Specifically, immune checkpoint inhibitors (ICIs) are antibodies that target inhibitory receptors (e.g., CTLA-4, PD-1, LAG-3, TIM-3) and ligands (PD-L1) expressed on T lymphocytes, antigen presenting cells and tumor cells [9, 10]. Since tumors express varying levels of immunogenicity, ICI treatment is more likely to be effective when there either is pre-existing anti-tumor immunity or T cell infiltration in the tumor microenvironment [10]. Various studies have evaluated the role of radiation and thermal ablation therapies in promoting immunogenic effects in “cold” tumors (such as enhanced release of tumor antigens, and T cell infiltration), and their combination with ICI to amplify the anti-tumor response [11, 12]. It is theorized that ablation and radiation may promote pro-inflammatory events within the tumor microenvironment and expose previously concealed tumor antigens to immune recognition, potentiating the effect of ICI, even sensitizing previously resistant tumors to immunotherapy [13-18]. However, these modalities have not yet independently demonstrated sufficient tumoral release of inflammatory or immunogenic subcellular components to promote strong tumor-directed adaptive immune responses [19, 20]. Since histotripsy can mechanically ablate cells without denaturing them, we hypothesize that histotripsy may be capable of promoting stronger inflammatory and immunostimulatory effects not possible with other thermal ablation modalities and could be a robust adjuvant to cancer immunotherapy. In this study, we use a murine model of subcutaneous tumor ablation to demonstrate that histotripsy is uniquely capable of promoting local, regional, and systemic anti-tumor adaptive immune responses that can significantly augment the efficacy of ICI-based immunotherapy.

5.2 Materials and Methods

5.2.1 Experimental Design

The murine experiments were prospectively reviewed and approved by the University of Michigan and VA Ann Arbor Healthcare Animal Care and Use Committees. C57BL/6 mice (Mus musculus) aged 6–8 weeks old were purchased from Taconic (Hudson, New York) and housed and maintained in specific pathogen-free conditions. Each experiment involved the use of 4–23 mice per experimental group, and experimental group sizes are noted in the figure legends.

Mice were inoculated by subcutaneous flank injection with 10^6 B16GP33 or 4×10^6 Hepa1-6 cells suspended in phosphate buffered saline (PBS) to generate tumors. Pulmonary tumors were established by inoculating mice by tail vein injection with 2×105 B16GP33 cells suspended in PBS. Pulmonary metastases were quantified after euthanasia by counting the number of pigmented tumors identified along the surfaces of all lobes. Interobserver variability was mitigated by averaging the counts of three independent observers. Ten days after tumor inoculation, mice in treatment cohort were treated with histotripsy, where ~80% tumor volume was targeted for ablation. The choice of targeted tumor volume was based on previous study in Chapter 3 where up to ~75% target tumor partial ablation was able to induce regression. If the entire tumor volume is targeted for ablation, then the extent of residual viable tumor may not be sizeable enough to evaluate the impact of immune response vs the impact of tumor debulking effects on tumor response to histotripsy. In this study, we wanted to be able to specifically study the levels of immune infiltration in the untargeted viable tumor volume. In checkpoint inhibition cohorts, checkpoint inhibition immunotherapy (administration of 200 µg CTLA-4 mAb) was performed on days 3, 6 and 9 after B16GP33 tumor inoculation or days 3, 6, 9 and 12 after Hepa1-6 tumor inoculation, based on previous literature on CTLA-4 blockade monotherapy in various murine tumor models [21]. On days 3 and 10 after histotripsy ablation, mice were euthanized, and tumors were harvested for flow cytometric analysis. Additionally, end stage illness and humane endpoints guidelines were determined as follows: animals exhibiting signs of dehydration, emaciation or cachexia, impaired mobility, systemic infection, or abdominal or thoracic bleeding during or immediately after histotripsy treatment were to be euthanized.

5.2.2 Cell Preparation

B16F10 (CRL-6475™) and Hepa1-6 (CRL-1830™) cell lines were obtained from ATCC. B16GP33 cell line was established by transfecting B16F10, a poorly immunogenic melanoma cell line arising in C57BL/6 mice, with a plasmid encoding GP33, a class I major histocompatibility (MHC)-restricted lymphocytic choriomeningitis virus (LCMV) glycoprotein as previously published[22-27]. B16GP33 cell line was maintained by culturing with 200 ug/mL G418 in RPMI-1640 medium (Gibco, Life Technologies Corporation, Grand Island, NY) with 10% fetal bovine serum (HyClone, GE Healthcare Life Sciences), 2 mM L-glutamine (Gibco, Life Technologies Corporation, Grand Island, NY), 100 U/ml penicillin (Gibco, Life Technologies Corporation, Grand Island, NY) and 100 ug/ml streptomycin (Gibco, Life Technologies Corporation, Grand Island, NY). Hepa 1–6 cell lines were maintained by culturing in Dulbecco’s modified Eagle’s medium (DMEM) (Gibco, Life Technologies) with 10% fetal bovine serum (HyClone, GE Healthcare Life Sciences).

5.2.3 Animal Preparation

Prior to and during histotripsy, the mice were induced and maintained on general anesthesia by inhalation of isoflurane gas (1.5-2.0%) in 1 L/min of oxygen (SurgiVet V704001, Smiths Medical, Waukesha, Wisconsin, USA). The hair covering the subcutaneous tumor region was removed with an electric clipper. Depilatory cream was not used to avoid any unintentional immune effects. Core body temperature was recorded using a rectal probe and was maintained between 35-37 °C with an overhead heating lamp. The mice were injected with Bupivacaine analgesic (2 mg/kg) subcutaneously before delivery of histotripsy treatment and then as needed every 4-12 hours after histotripsy therapy. Immediately after histotripsy, the mice were transferred to a recovery chamber fitted with an overhead heating lamp and were placed on a heated pad. Once the mice recovered from anesthesia and were mobile, they were transferred back to their housing cages.

5.2.4 Experimental Setup

Our lab has designed and built a custom 8 element 1 MHz focused ultrasound therapy transducer specifically for rodent histotripsy therapy [6, 7]. The histotripsy transducer was driven by a custom-built high-voltage pulser controlled by a field-programmable gate array (FPGA) development board (DE0-Nano Terasic Technology, HsinChu, Taiwan), enabling the therapy transducer to generate, and output 1-2 cycle histotripsy pulses. A 20 MHz B-mode ultrasound imaging probe (L40-8/12, Ultrasonix, Vancouver, Canada) was co-aligned with the center of the therapy transducer to allow visualization of the focal ablation volume in real time. The ultrasound therapy transducer and the imaging probe were mounted to a motorized 3-axis positioning system to mechanically scan the therapy focus across a 3D target ablation volume. Water was used as the ultrasound coupling medium by immersing the transducer and imaging probe in a tank of degassed water maintained at 35–37°C by means of a coil heater. The mouse was placed on a custom-built animal platform just over the water tank.

5.2.5 Histotripsy Ablation

After sedation, the animal was placed decubitus with the tumor submerged in the degassed water. To identify the histotripsy focus on ultrasound imaging, test histotripsy pulses were delivered to the water tank by the therapy transducer to generate a “bubble cloud” which appeared as a hyperechoic cavitation zone on ultrasound imaging. The position of the hyperechoic cavitation zone was then marked as the therapy focal position on the ultrasound image. Using a custom MATLAB script, the ultrasound therapy transducer and the imaging probe were scanned using the motorized positioning system, such that a treatment ellipsoid consisting of a grid of uniformly spaced therapy focal zones (~0.4 – 0.7 mm between adjacent focal volumes) would encompass the user-defined target 3D tumor volume. This target volume covered approximately 80% of the original tumor volume. During ablation, histotripsy-induced cavitation was hyperechoic in appearance compared to the surrounding tissue on ultrasound imaging, which was used to monitor the ablation in real-time. At each focal location, 50 histotripsy pulses at 100 Hz PRF (P- >30 MPa) or 0.5 seconds of ablation were delivered. After ablation, the targeted region appeared hypoechoic on ultrasound imaging, enabling real-time feedback to ensure adequate ablation volumes were achieved. Selection of histotripsy parameters was based on results of previous in vivo and in vitro work [7].

5.2.6 Checkpoint inhibition immunotherapy

Checkpoint inhibition immunotherapy was performed by treating tumor-bearing mice with intraperitoneal injections of 200 μg anti-CTLA-4 mAb (R&D Systems, Minneapolis, MN) on days 3, 6 and 9 after B16GP33 tumor inoculation or days 3, 6, 9 and 12 after Hepa1-6 tumor inoculation.

5.2.7 Sham therapy and in vitro CD8+ T cell stimulation to determine neoantigen

Sham therapy consisted of isoflurane anesthesia alone. Sham-ablated tumors were explanted and placed in 1.5 mL tubes and subjected to five cycles of rapid freezing in liquid nitrogen for 2 min, followed by rapid thawing in a 60°C water bath for 2 min. The sham freeze–thaw process represents a commonly used homogenization procedure for achieving subcellular fractionation. Sham-ablated and in vivo histotripsy-ablated tumors were liquefied consistently and exposed to 10^6 CD8+ T cells harvested from the spleen of C57BL/6 mice 8 days after LCMV infection (at which time only 5%–10% of circulating CD8+ T cells are specific for the LCMV GP33) in the presence of 10 U interleukin (IL)-2 and brefeldin A at 37°C for 5 hours. CD8+ T cells were also exposed to media alone as negative controls and to 0.01 μg/mL GP33 peptide alone as positive controls.

5.2.8 Flow cytometry

Tumors, tumor draining lymph nodes (TDLN), non-tumor draining lymph nodes (NTDLN), and spleens were harvested and processed into single-cell suspensions on sterile fine mesh screens. Tumor infiltrating lymphocytes (TIL) were isolated from dissociated tumors using Histopaque (Sigma Aldrich, St, Louis, MO) centrifugation. Lymphocytes from each sample were stained with APC-labeled MHC class I (Dd) tetramers loaded with MHC class I-restricted GP33 peptide (NIH Tetramer Facility Core, Atlanta, GA), Pacific Blue-labeled anti-CD8 mAb, BV510-labeled anti-CD4 mAb, PerCP/Cy5.5-labeled anti-CD19 mAb, PE/Cy7-labeled anti-CD11c mAb, AF488-labeled anti-Ly6G mAb, BV650-labeled anti-NK1.1 mAb, and PE-labeled anti-CD25 mAb. All extracellular antibodies were purchased from BioLegend (San Diego, CA), except for anti-CD8 (BD Biosciences, San Diego, CA) and anti-Ly6G (eBioscience, San Diego, CA). Fluorescence data were acquired on a BD LSRFortessa Flow Cytometer (BD Biosciences, San Jose, CA) and analyzed using FlowJo software (Tree Star Inc., Ashland, OR).

5.2.9 Immunohistochemistry

Tumors were washed with PBS and preserved in 10% formalin for 24–48 hours and in 70% ethanol until paraffin embedding. Sections of 4.5 µm thickness were deparaffinized in xylene for 6 min, then washed in 50% xylene in ethanol and 100% ethanol, and rehydrated by sequential transfer to 95%, 70%, and 50% ethanol, and ultimately to distilled water for 3 min each before staining. Samples were washed in PBS, blocked in 1% bovine serum albumin for 30 min, and incubated with rabbit polyclonal anti-CD8a antibody to CD8a antibody (synaptic system) at 4°C overnight. Samples were then washed and blocked in goat serum, incubated with biotin-conjugated goat antirabbit IgG for 45 min, washed for 30 min in PBS, then incubated with horseradish peroxidase (HRP)-conjugated avidin. Samples were developed using the CN/DAB Substrate Kit (Thermo Fisher, Waltham, Massachusetts) for 5 min as per vendor instructions, then counterstained with hematoxylin for 10 s, and washed and mounted. Samples were visualized using a 10× or 20× objective on a Nikon Eclipse E400 microscope, and images were captured using a DXM1200F camera using the software provided by the vendor (Nikon, Melville, New York). At least 10 images from each tumor sample were obtained for each magnification. Cells were counted using ImageJ software after appropriate background subtraction.

5.2.10 Immunofluorescence

Formalin-fixed paraffin-embedded tumor sections were deparaffinized and rehydrated as above. Heat-mediated antigen retrieval was performed in Tris buffer containing 1% Triton X (for CD8 staining) or citrate buffer (for calreticulin (CRT) staining) in a boiling water bath for 20 min. Sections were blocked in 5% bovine serum albumin (BSA) in PBS for 30 min, then primary antibody staining was performed with a primary rabbit IgG antibody against CD8, or rabbit IgG against CRT directly conjugated to Alexa 647 and rabbit IgG against Erp72 directly conjugated to Alexa 555 (Abcam, Cambridge, England) overnight at 4°C overnight. Secondary antibody staining (for CD8 staining) was performed with Alexa 488-labelled goat antirabbit IgG for 1 hour. Sections were washed and mounted using Prolong Gold Antifade Mountant with 4’6-diamidino-2-phenylindone (DAPI) (Thermo Fisher), and a minimum of five overlapping optical fields from two independent samples were captured. Images were acquired using a Keyence BZ-800 microscope (Keyence, Osaka, Japan) under 10× objective with a 1× digital zoom, or under 40× objective with a 1× digital zoom. Images were imported to ImageJ and the threshold was adjusted using the color threshold tool.

5.2.11 HMGB1 assays

Serum levels of HMGB1 were measured by enzyme-linked immunosorbent assay (ELISA) (Tecan, Männedorf, Switzerland), according to manufacturer’s instructions. Intratumoral levels of HMGB1 were measured by immunofluorescence using tumor samples snap frozen in liquid nitrogen. Tumors were prepared on round cover glass and fixed in 4% PFA at room temperature for 15 min after PBS washing. Slides were permeabilized in 0.3% Triton X-100 for 10 minutes followed by blocking solution (5% BSA in PBS) for 30 min at room temperature. Samples were stained in antibody reaction buffer (1% BSA and 0.3% Triton X-100 in PBS, pH 7.4) with a primary antibody for HMGB1 overnight at 4oC followed by secondary antibodies for 1 hour at room temperature. F-actin was stained with rhodamine phalloidin (Invitrogen). Hoechst 33342 (Life Technologies) was used for nuclear staining. All slides were scanned under the same conditions for magnification, exposure time, lamp intensity, and camera gain. Confocal images were acquired using an Olympus Fluoview 1000 microscope (Olympus, Tokyo, Japan). All images were quantitated as previously described with HMGB1 staining intensity normalized to nuclei using MetaMorph software (Molecular Devices, Downingtown, PA) [28].

5.2.12 Statistical Analysis

Experimental data were analyzed using SPSS V.23 statistical software. Two groups of independent samples were compared using the two-tailed Student's t-test. Analysis of variance was applied to assess the statistical significance in tumor growth kinetics. Differences in survival between groups were assessed using the log-rank test. Significance was defined as $p<0.05$, and error bars represent SEM.

5.3 Results

5.3.1 Local Tumor Response to Histotripsy

Histotripsy ablation significantly inhibited tumor growth without producing significant alterations in body weight (Figure 5-1 A, B).

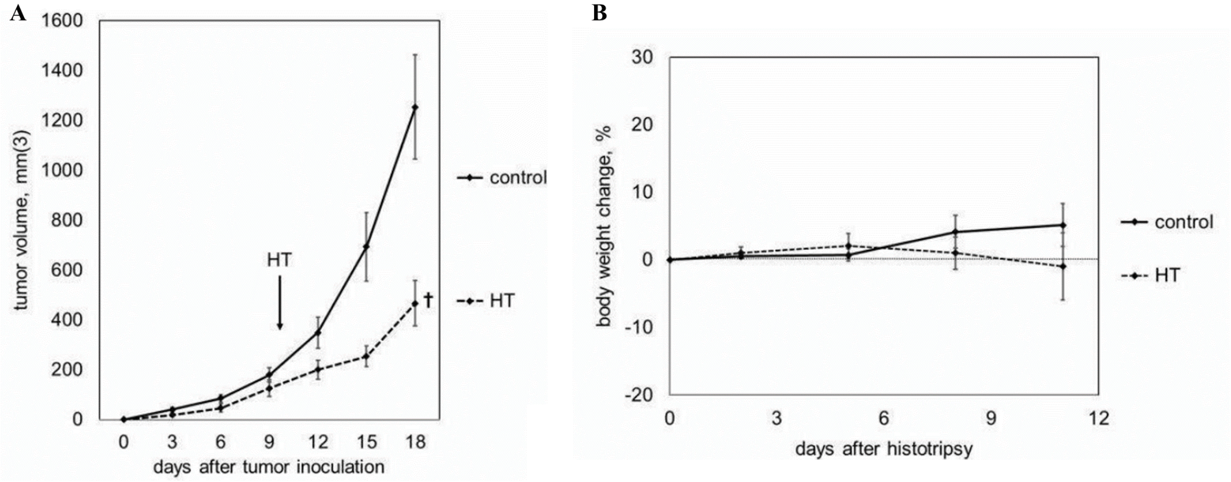

Figure 5-1 ***Response to Histotripsy.*** *(A) Histotripsy ablation resulted in suppression of local tumor growth. (B) No significant differences in body weight were observed following histotripsy ablation.*

5.3.2 Histotripsy promotes local intratumoral innate and adaptive immune responses

We examined the effect of histotripsy on intratumoral lymphocyte infiltration. As shown in Figure 5-2 A-D, a significant upregulation of intratumoral natural killer (NK) cells, dendritic cells (DCs), neutrophils, B cells, CD4+ T cells and CD8+ T cells was observed following histotripsy ablation. In addition, histotripsy was also associated with significant intratumoral infiltration of melanoma antigen-specific CD8+ T cells (Figure 5-2E).

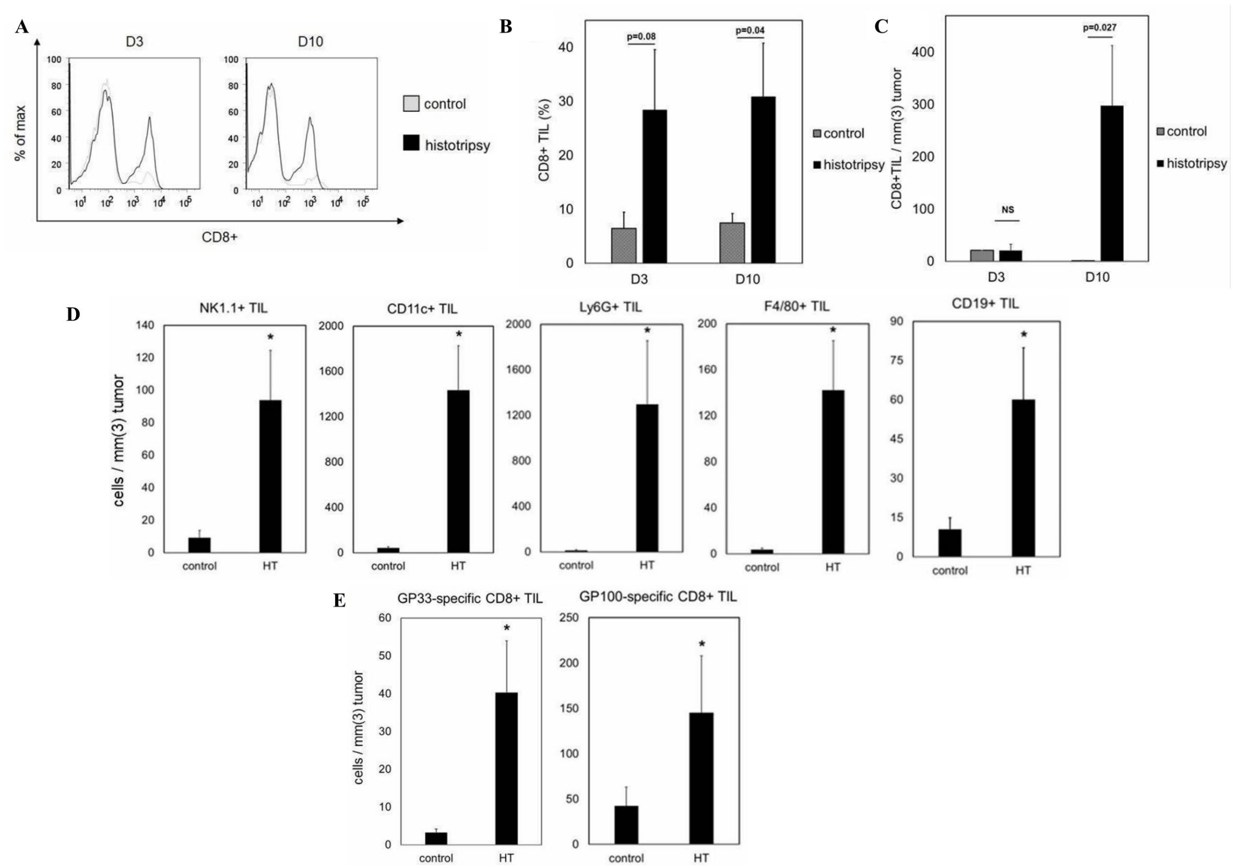

Figure 5-2 ***Histotripsy promotes intratumoral CD8+ T cell infiltration.*** *(A, B) Fluorescence-activated cell sorting (FACS) analysis of tumor-infiltrating lymphocytes (TIL) on day 3 (D3) and day 10 (D10) after treatment (gated on viable lymphocytes) demonstrated higher percentages of intratumoral CD8+ T cell infiltration after histotripsy by day 10. (C) Stimulation of CD8+ TIL remained significant on day 10 when cell numbers were normalized to tumor volume. (D) FACS analysis of TIL on day 10 after treatment also identified marked increases in intratumoral populations of NK1.1+ natural killer cells, CD11c+ dendritic cells, Ly6G+ neutrophils, F4/80+ macrophages, and CD19+ B cells after histotripsy. (E) Staining with major histocompatibility complex (MHC) tetramers loaded with the minor melanoma antigen GP33 and the major melanoma antigen GP100 identified significant increases in intratumoral populations of melanoma antigen-specific CD8+T cells. (n=4–8 per group; *p<0.05 vs control by t-test).*

5.3.3 Non-thermal histotripsy is capable of releasing immunogenic tumor neoantigens

To explore the ability of histotripsy to release intact tumor antigens capable of stimulating CD8+ T cell responses, subcutaneous B16F10 and B16GP33 melanoma tumors were explanted immediately after sham or histotripsy ablation performed 10 days after inoculation. Figure 5-3 demonstrates that the activation of CD8+ T cells (as indicated by intracellular interferon gamma (IFNγ) expression) was only observed after exposure to B16GP33 melanoma tumors treated with histotripsy. The magnitude of this CD8+ T cell stimulation approached the level of stimulation seen with direct exposure to GP33 peptide (positive control), indicating that non-thermal disruption of tumors by histotripsy was capable of releasing preserved tumor antigens capable of stimulating CD8+ T cell responses. The absence of CD8+ T cell stimulation by B16F10 tumors (which do not express GP33) treated with histotripsy confirmed the antigen-specific nature of this response.

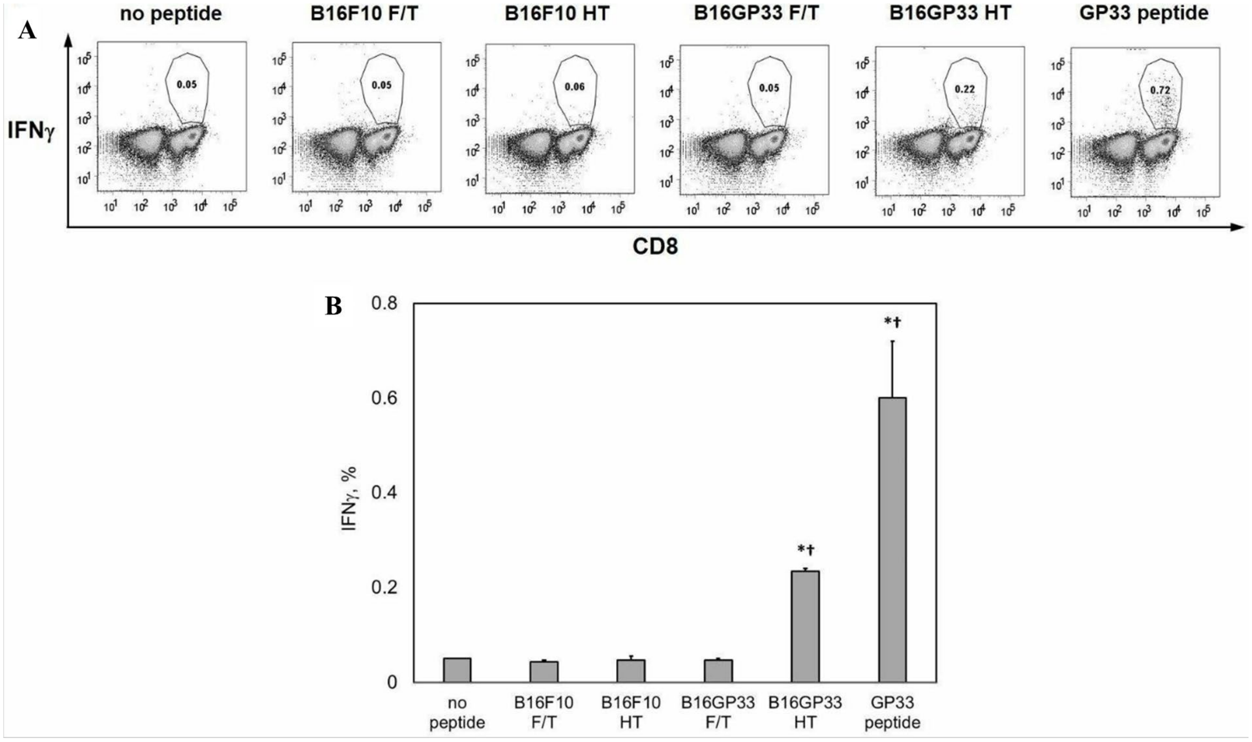

Figure 5-3 ***Non-thermal histotripsy is capable of releasing immunogenic tumor neoantigens.*** *C57BL/6 mice were inoculated with B16F10 or B16GP33 subcutaneous tumors, then treated with sham or histotripsy ablation (HT) on day 10. Tumors were excised and sham-treated tumors were liquefied using three freeze–thaw (F/T) cycles consisting of 2 min in liquid nitrogen and 2 min in a 60°C water bath. Liquefied tumors were exposed to CD8+ T*

*cells isolated from the spleens of C57BL/6 mice 8 days after LCMV infection (at which time small populations of GP33-specific effector CD8+ T cells exist) in the presence of interleukin-2 and brefeldin A. Negative controls consisted of CD8+ T cells alone (no peptide) and positive controls consisted of CD8+ T cells exposed to 0.01 µg/mL GP33 peptide (GP33 peptide). After 5-hour incubation, individual (A) and group (B) fluorescence-activated cell sorting (FACS) analyses of intracellular IFNγ expression (gated on viable lymphocytes) demonstrated that exposure to histotripsy-treated B16GP33 tumors was the only experimental condition capable of stimulating GP33-specific CD8+ T cells in vitro. The magnitude of this stimulation was approximately half of that seen with direct exposure to GP33 peptide (n=4 per group, *$p<0.05$ vs negative control by t-test; †$p<0.05$ vs all other experimental groups by analysis of variance). IFNγ, interferon gamma; LCMV, lymphocytic choriomeningitis virus.*

5.3.4 Regional and systemic tumor-specific CD8+ T cell responses

We examined the effect of histotripsy ablation on other lymphoid compartments beyond the treated tumor. Ten days after sham or histotripsy ablation of B16GP33 melanoma tumors, ipsilateral inguinal lymph nodes were harvested as TDLN, and contralateral axillary lymph nodes were harvested as NTDLN. Flow cytometric analysis (FACS) identified slightly higher numbers of CD8+ T cells specific for the weakly immunogenic tumor antigen GP33 within TDLN but not NTDLN after histotripsy, but this did not reach statistical significance (Figure 5-4A, B). However, analysis of splenocytes did identify significantly higher numbers of circulating GP33-specific CD8+ T cells after histotripsy as compared with controls, radiation, and radiofrequency ablation (Figure 5-4C, D). Analysis of CD4+/CD25+/FoxP3+ cells demonstrated a favorable skewing of tumor-specific CD8+ T cell: regulatory T cell ratios after histotripsy (Figure 5-4E).

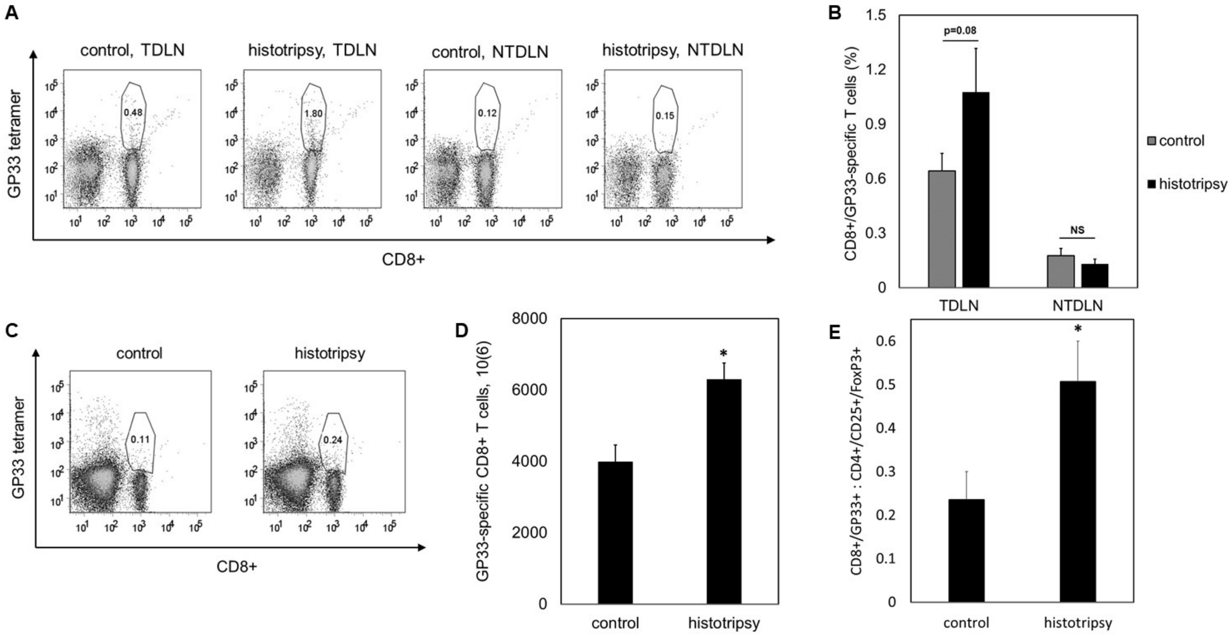

Figure 5-4 ***Histotripsy promotes regional and systemic tumor-specific CD8+ T cell responses.*** *C57BL/6 mice were inoculated with B16GP33 subcutaneous tumors expressing very low levels of GP33 peptide, then treated with no therapy (control) or histotripsy ablation on day 10, tumors were harvested 10 days later. (A, B) FACS analyses demonstrated a trend toward larger percentages of CD8+ T cells with TCR specificity for the melanoma neoantigen GP33 in tumor-draining lymph nodes (TDLN) but not non-tumor-draining lymph nodes (NTDLN) after histotripsy. (C, D) FACS analyses of splenocytes (gated on viable lymphocytes) demonstrated higher numbers of circulating CD8+ T cells with T cell receptor (TCR) specificity for the minor melanoma antigen GP33 after histotripsy. (E) Histotripsy was also associated with a higher ratio of circulating melanoma-specific CD8+ T cells to regulatory CD4+ T cells (n=4 per group, *p<0.05 vs control by t-test).*

5.3.5 Abscopal intratumoral CD8+ T cell responses

Because of the unique ability of histotripsy to trigger significant local and systemic tumor-directed CD8+ T cell responses, we evaluated the effect of histotripsy on distant tumor sites. Ten days after inoculation with bilateral subcutaneous flank B16GP33 melanoma tumors, C57BL/6 mice were treated with no therapy or histotripsy ablation of unilateral tumors. Ten days after treatment, contralateral (non-treated) tumors were harvested for lymphocyte assays. FACS identified significantly higher levels of abscopal CD8+ T cell infiltration into distant tumor sites after contralateral histotripsy ablation (Figure 5-5A). Comparison between bilateral tumors using immunohistochemistry confirmed minimal infiltration of CD8+ T cells in control mice (Figure 5-5B). CD8+ T cell infiltration on days 3, 5 and 7 after histotripsy was analyzed by immunohistochemistry. In control tumors, CD8+ T cell numbers were low and decreased over time; in histotripsy-ablated tumors, CD8+ T cell numbers increased dramatically from day 3 to day 5 and remained high on day 7. The abscopal effect in contralateral tumors after histotripsy was characterized by a more gradual increase in CD8+ T cell numbers (Figure 5-5C). Whereas tumors treated with histotripsy ablation exhibited brisk CD8+ T cell infiltration along the periphery of ablation zones, abscopal CD8+ T cell infiltration in contralateral tumors after histotripsy ablation was qualitatively different, exhibiting a more diffuse and homogeneous pattern (Figure 5-5D, E). Of note, the ability of unilateral histotripsy ablation to promote distant CD8+ TIL was associated with a small but significant inhibition of contralateral tumor growth (Figure 5-5F). Furthermore, despite the presence of a contralateral untreated tumor, survival studies indicated that the abscopal impact of unilateral histotripsy ablation was associated with a statistically significant survival advantage to mice bearing bilateral B16GP33 melanoma tumors (Figure 5-5G).

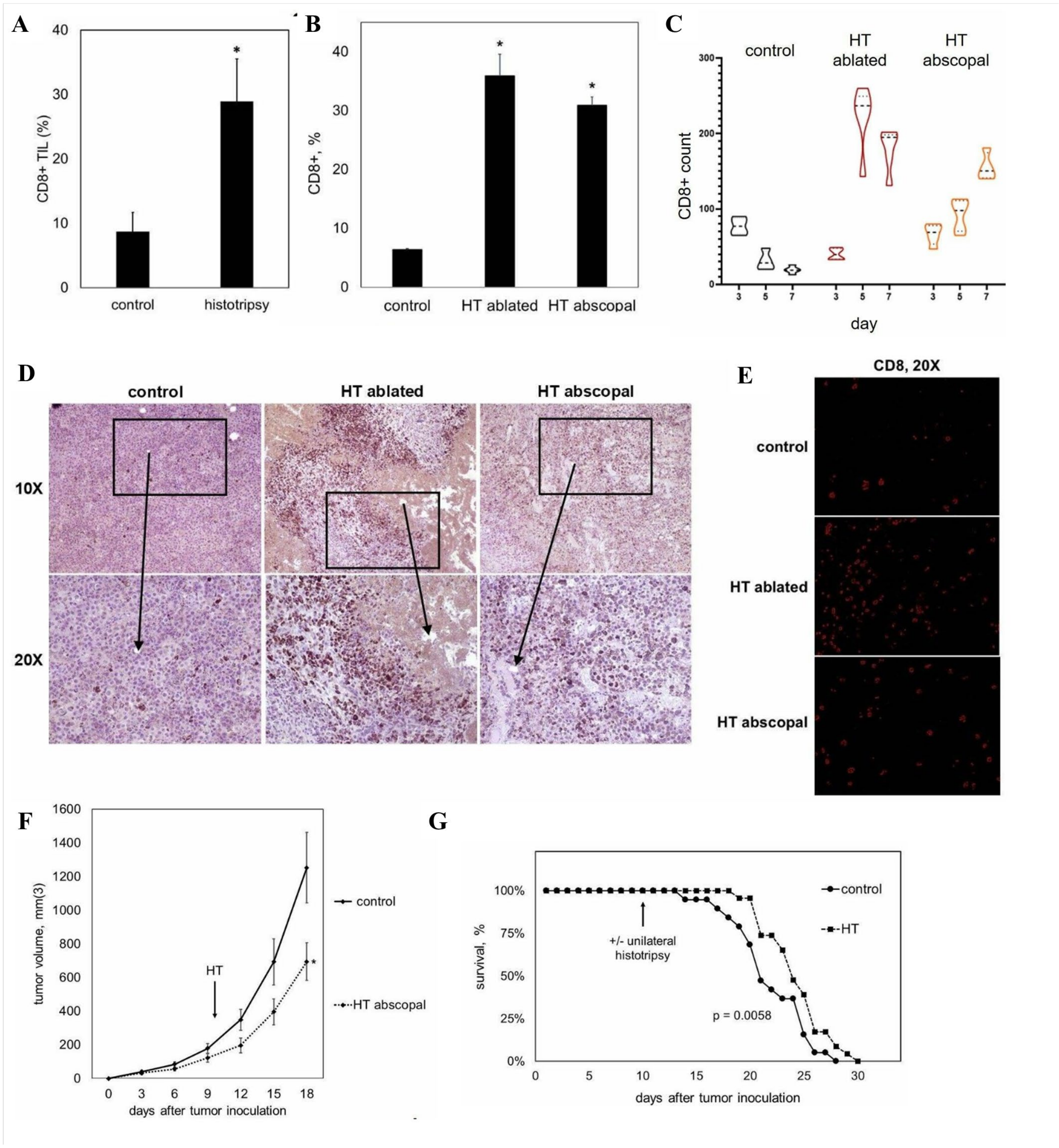

Figure 5-5 ***Histotripsy promotes abscopal CD8+ T cell responses****. Seven days after bilateral B16GP33 melanoma tumor inoculation, C57BL/6 mice were treated with unilateral sham or subtotal histotripsy tumor ablation. FACS analysis of TIL populations 10 days after treatment identified (A) significantly stronger intratumoral CD8+ T cell infiltration in contralateral, untreated tumors after histotripsy. (B) FACS analysis of histotripsy-ablated (HT ablated) and contralateral non-ablated tumors (HT abscopal) identified comparable levels of intratumoral CD8+ T cell infiltration (C) Quantitation of CD8+ T cells using immunohistochemistry (defined as the average number of CD8+ T cells per 500 µm2 area for a minimum of five non-overlapping fields from two independent samples) on days 3, 5 and 7 after sham or histotripsy ablation showed small and diminishing CD8+ T cell numbers over time in*

*control tumors, rapidly increasing CD8+ T cell numbers in histotripsy-ablated tumors, and gradually increasing CD8+ T cell numbers in contralateral non-ablated tumors. (D) Immunohistochemistry and (E) immunofluorescence staining of CD8 confirmed similar levels of CD8+ T cell infiltration between histotripsy-ablated (HT ablated) and contralateral non-ablated tumors (HT abscopal), but with different patterns of infiltration. Whereas CD8+ T cells were largely localized to peripheral areas that surrounded ablation zones in histotripsy-ablated tumors, CD8+ T cell infiltration was more diffuse and homogeneous in contralateral non-ablated tumors. (F) Comparison of tumor growth between treated and contralateral non-treated tumors showed that histotripsy was associated with a modest but significant abscopal inhibition of contralateral tumor growth. (G) This abscopal inhibition of contralateral tumor growth by histotripsy was associated with significant prolongation of survival (n=4 per group and 23 per group in survival experiments, *p<0.05 vs control by t-test; †p<0.05 vs all other groups by analysis of variance).*

5.3.6 Histotripsy inhibits the development of distant metastases

Given the evidence of abscopal immune stimulation, we investigated the ability of local histotripsy ablation to inhibit growth of distant tumors. C57BL/6 mice were inoculated with unilateral subcutaneous injections of B16GP33 melanoma cells on day 0 and with intravenous injections of B16GP33 melanoma cells on day 3 to establish flank and pulmonary melanoma tumors, respectively. On day 10, mice were treated with sham ablation or histotripsy ablation of flank tumors; on day 20, mice were euthanized for visual quantitation of pulmonary metastases. Significantly fewer pulmonary metastases were observed in mice treated with histotripsy ablation of flank tumors (Figures 5-6A, B). Immunohistochemical analysis demonstrated smaller tumor size and marked CD8+ T cell infiltration among pulmonary metastases after flank tumor histotripsy ablation (Figures 5-6C).

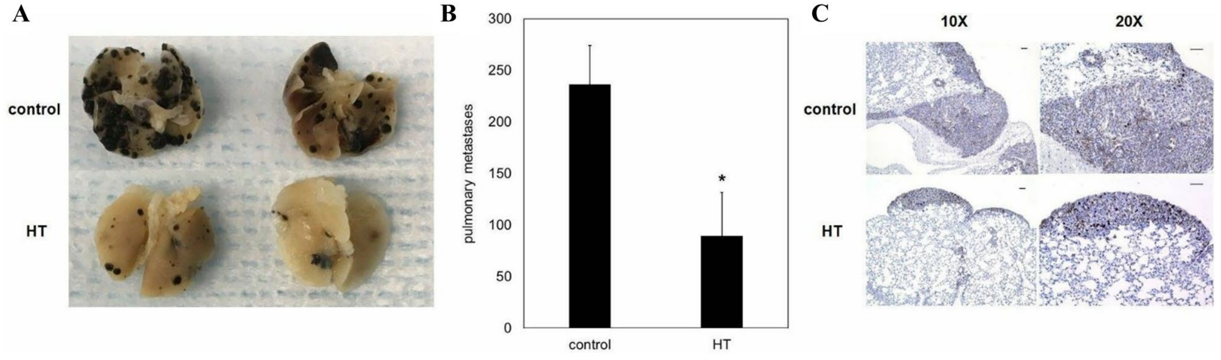

Figure 5-6 ***Histotripsy inhibits the development of distant pulmonary metastases.*** *C57BL/6 mice were inoculated with flank and intravenous inoculations of B16GP33 melanoma on days 0 and 3, respectively. Sham (control) or histotripsy (HT) of flank tumors was performed on day 10, and pulmonary metastases were quantified by visual inspection on day 20. Representative specimens (A) and group data (B) demonstrated significantly fewer pulmonary*

*metastases in mice treated with flank tumor histotripsy ablation. (C) Immunohistochemical analysis demonstrated smaller tumor size and more concentrated CD8+ T cell infiltration among pulmonary metastases in mice treated with histotripsy (n=4 per group, *p<0.05 vs control by t-test; black bars indicate 50 µm).*

5.3.7 Systemic inflammatory changes and local release of HMGB1

We hypothesized that the immunostimulatory effects of histotripsy could be associated with an ability to promote the release of intratumoral HMGB1. As illustrated in Figure 5-2, histotripsy tumor ablation was followed by an intense inflammatory infiltrate of NK cells, DCs, neutrophils and macrophages. FACS of splenocytes on day 10 after histotripsy demonstrated a significant increase in circulating NK cells and a trend toward higher percentages of circulating neutrophils (Figures 5-7A-C). One day after histotripsy treatment, immunofluorescence assays identified apoptotic changes within treated tumors, as evidenced by nuclear condensation; this was associated with marked translocation of CRT from the endoplasmic reticulum to the plasma membrane as compared with untreated controls (Figures 5-7D). On days 1 and 7 after histotripsy treatment, immunofluorescence assays demonstrated a significant extranuclear translocation of HMGB1 within the intratumoral microenvironment compared with untreated controls (Figures 5-7E, F). By day 7 after histotripsy treatment, ELISA (Figure 5-7G) measured significant increases in serum levels of HMGB1 compared with untreated controls.

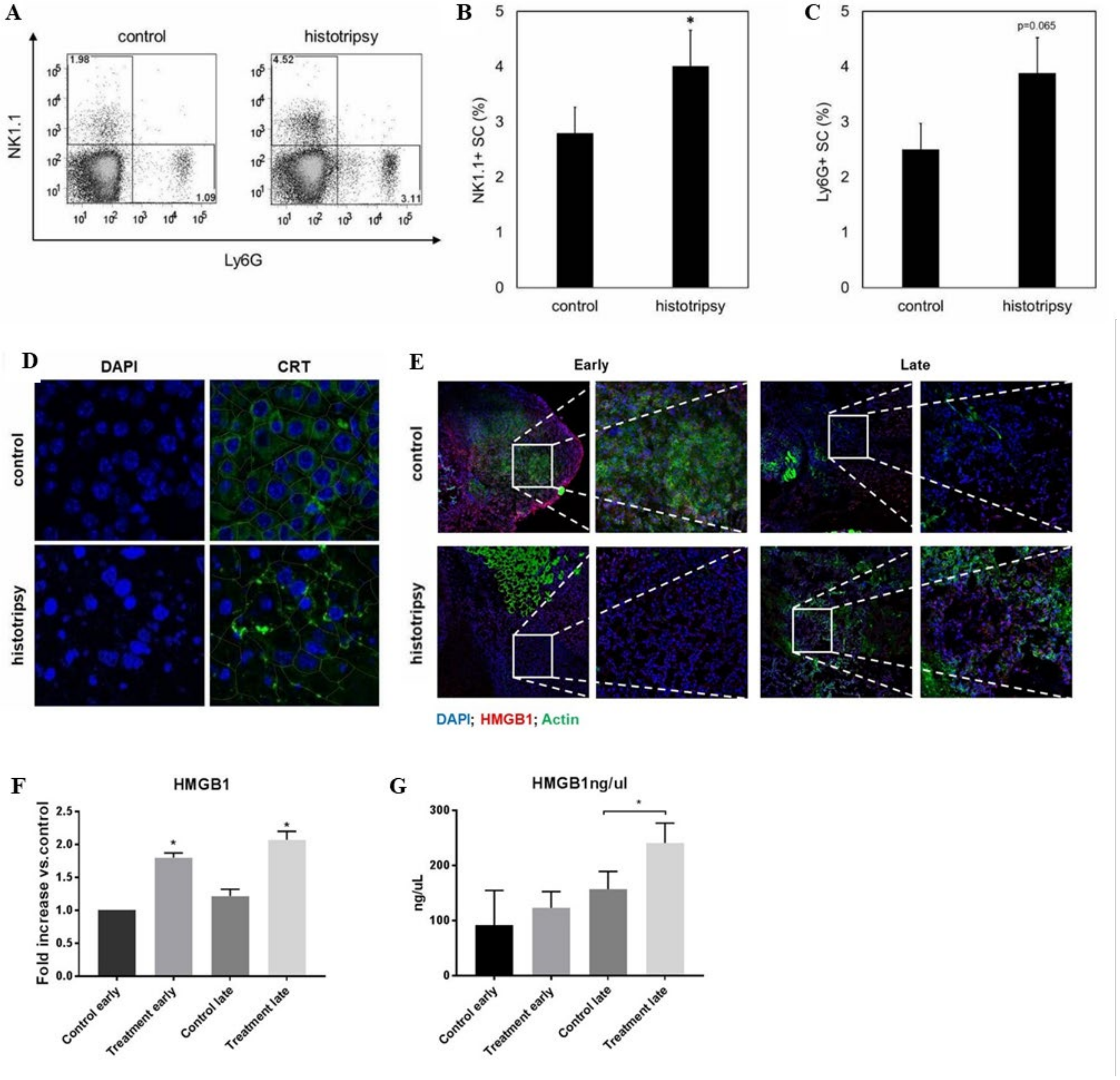

Figure 5-7 ***Histotripsy promotes local and systemic inflammatory events.*** *(A-C) FACS analyses demonstrated significantly larger populations of circulating NK1.1+ natural killer cells and a trend toward larger populations of Ly6G+ neutrophils ten days after histotripsy. (D) Immunofluorescence analyses of tumors confirmed colocalization of CRT with the endoplasmic reticulum protein ERp72 (data not shown); 1 day after histotripsy ablation, DAPI staining identified marked nuclear condensation and translocation of calreticulin (CRT) to the plasma membrane (outlined in green) consistent with apoptosis induction. (E, F) Immunofluorescence analyses of tumors (40X magnification) showed significant increases in levels of extracellular high mobility group box protein 1 (HMGB1) on days 1 (early) and 7 (late) after histotripsy. (G) By day 7 after histotripsy, enzyme-linked immunosorbent assays of serum identified significantly higher levels of circulating HMGB1. (n=3 per group, * p<0.05 vs. control)*

5.3.8 Efficacy of checkpoint inhibition immunotherapy

We tested the ability of histotripsy-associated antitumor immune stimulation to work cooperatively with conventional immunotherapy. C57BL/6 mice were inoculated with bilateral subcutaneous B16GP33 melanoma tumors, then treated with sham or intraperitoneal injections of anti-CTLA-4 mAb on days 6, 9, and 12, and sham or histotripsy ablation on day 10. The systemic ability of checkpoint inhibition to control tumor growth was slightly stronger than the abscopal effect of histotripsy ablation (Figure 5-8A). When used together, the addition of contralateral histotripsy significantly augmented the therapeutic efficacy of checkpoint inhibition. Checkpoint inhibition, unilateral histotripsy, and combination therapy were all associated with significant increases in CD8+ tumor-infiltrating lymphocytes in contralateral, non-ablated tumors (Figures 5-8B, C). However, when quantified as numbers of infiltrating CD8+ T cells normalized to tumor volume, the addition of unilateral histotripsy significantly increased CD8+ TIL concentration compared with checkpoint inhibition alone. To verify that histotripsy was able to potentiate immune responses against less immunogenic tumors, C57BL/6 mice were inoculated with bilateral subcutaneous Hepa1-6 hepatocellular carcinoma tumors, then treated with sham or intraperitoneal injections of anti-CTLA-4 mAb on days 3, 6, 9 and 12, and sham or histotripsy ablation on day 10. As shown in Figure 5-8D, contralateral histotripsy stimulated abscopal antitumor immune effects that produced a similar enhancement of checkpoint inhibition immunotherapeutic efficacy in this more poorly immunogenic tumor model.

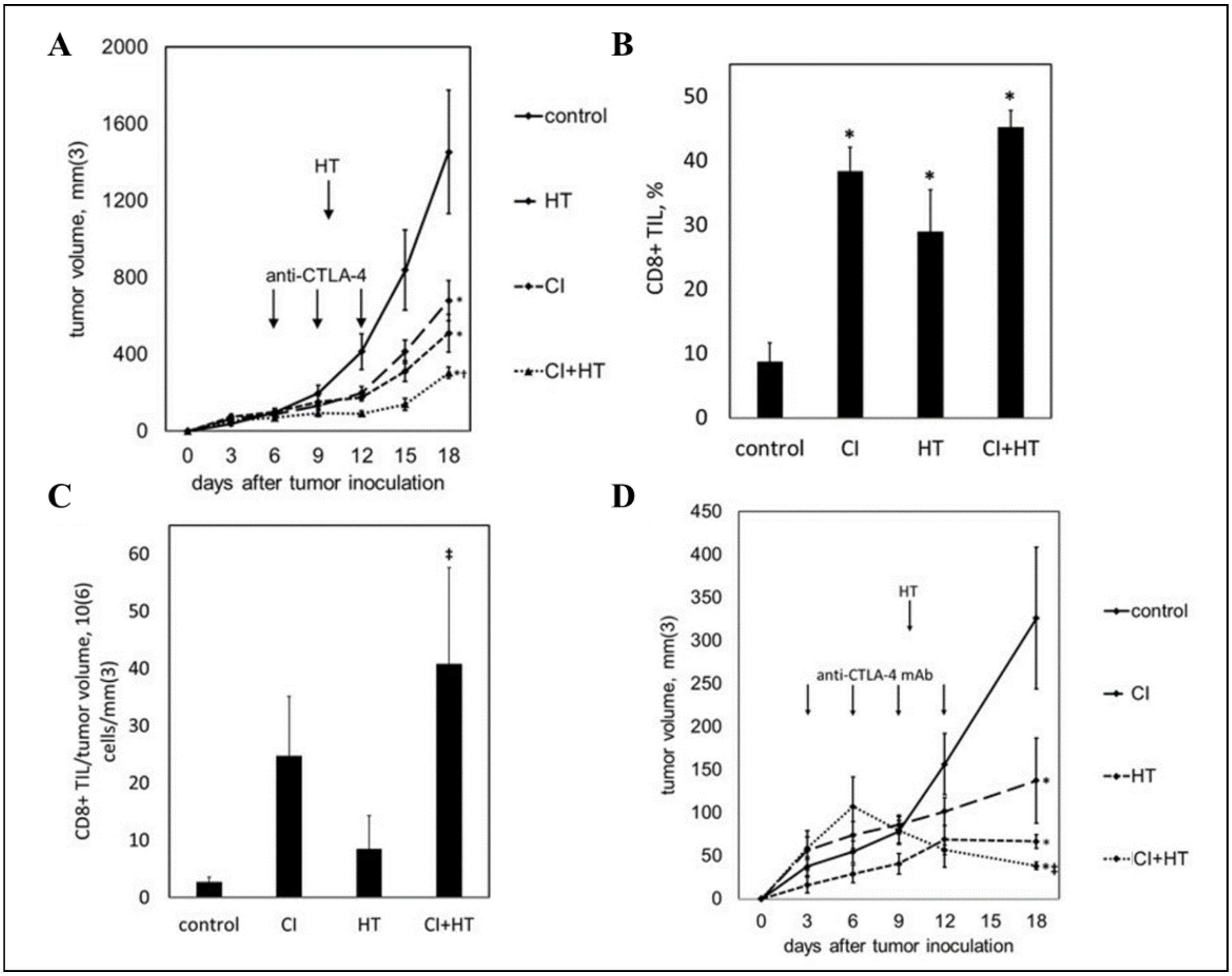

Figure 5-8 ***Histotripsy augments the therapeutic efficacy of checkpoint inhibition.*** *C57BL/6 mice bearing bilateral B16GP33 tumors were treated with or without anti-CTLA-4 mAb on days 3, 6 and 9, and with or without unilateral histotripsy tumor ablation on day 10. (A) Serial tumor measurements demonstrated optimal suppression of non-ablated tumors in mice receiving combination therapy. (B) When measured as a percentage of TIL, intratumoral CD8+ T cells were increased in non-ablated tumors in all treatment groups; (C) however, when measured as cell numbers normalized to tumor volume, significant increases in intratumoral CD8+ T cell responses were only observed in non-ablated tumors after combination therapy. (D) C57BL/6 mice bearing bilateral Hepa1-6 tumors were treated with or without anti-CTLA-4 mAb on days 3, 6, 9 and 12, and with or without unilateral tumor ablation on day 10. Serial tumor measurements demonstrated optimal suppression of non-ablated tumors in mice receiving combination therapy. (n=4 per group; *p<0.05 vs control by t-test; †p<0.05 vs histotripsy by t-test; ‡p<0.05 vs all other groups by analysis of variance).*

5.4 Discussion

Checkpoint inhibitors can bypass tumor-associated immune suppression in relatively immunogenic malignancies like melanoma and lung cancer to improve prognosis of patients [26, 27, 29-33]. However, overall response rates with checkpoint inhibition are limited, and the success of immunotherapy has not been fully translated to patients with less immunogenic cancers [34-37]. Efforts to increase the impact of checkpoint inhibition may require immunomodulatory interventions that can magnify tumor immunogenicity. The ability of radiation therapy and thermal ablation to trigger tumor-directed immune responses has been explored for years, but the magnitude of their immunostimulation and their ability to meaningfully impact cancer immunotherapy remain undetermined [13-18, 38]. Promising studies have also suggested that high-intensity focused ultrasound (HIFU), which uses ultrasonic waves to induce thermal injury, may be capable of promoting local inflammatory and immunostimulatory effects [39, 40]. However, like thermal ablation, HIFU relies on the induction of denaturing heat that could theoretically blunt the immunogenicity of the post-treatment tumor microenvironment.

We observed that histotripsy ablation of subcutaneous melanoma tumors resulted in a marked upregulation of intratumoral CD8+ T cell infiltration. The immunostimulatory potency of histotripsy may be related to its ability to promote immunogenic cell death. Unlike thermal ablation, which exerts its effect through heat-based denaturation and necrosis, histotripsy causes cell membrane disruption while preserving the integrity of subcellular components that could have immunogenic or proinflammatory effects on their release from tumor cells. This may explain why non-thermal histotripsy mediates immunostimulatory effects not seen with thermal radiofrequency ablation. The unique ability of histotripsy to markedly upregulate circulating numbers of CD8+ T cells specific for the minor tumor antigen GP33 suggests that histotripsy may facilitate cross-presentation of tumor antigens [41-43]. Indeed, the induction of inflammatory and antigen-presenting cell populations within the ablated tumor and the therapeutically favorable skewing of tumor-specific CD8+ effector:CD4+ regulatory T cells within the systemic circulation suggest that the local immunostimulatory effects of histotripsy may be potent enough to globally reorient the systemic immune system toward tumor antigen recognition. Radiation therapy has been proposed as a means to promote apoptotic immunogenic cell death [18, 38, 44]. It is recognized that proapoptotic conditions of cell death in which danger associated molecular patterns (DAMPs) like CRT, HMGB1, heat shock proteins, and nucleic acids are released from dying cells are highly inflammatory, inducing the migration and activation of phagocytes and antigen-presenting cells that subsequently promote tumor antigen presentation to the adaptive immune system. In contrast, largely pronecrotic conditions of cell death in which involution of dying cells is not accompanied by the release of DAMPs or exposure of tumor antigens lead to a tolerogenic, non-immunogenic cell death [45-47]. Indeed, we observed evidence of both local and systemic inflammatory responses following histotripsy, manifested by increases in intratumoral NK, DC, neutrophil, B and T cell populations, as well as elevated levels of circulating NK cells. We also observed a striking early translocation of CRT from the cytosolic endoplasmic reticulum to the plasma membrane, and translocation of HMGB1 out of the nucleus immediately after histotripsy ablation, followed by significant increases in circulating HMGB1 levels. These phenomena suggest that the ability of histotripsy to promote release of DAMPs from dying tumor cells may be involved in the stimulation of innate and adaptive immune responses against tumor. Ongoing work in our laboratory is directed at dissecting the potentially causative role that release of HMGB1 or other DAMPs may have in histotripsy immunostimulation.

Because of this ability of histotripsy to generate systemic immune responses against tumor, we used a two-tumor model to demonstrate that unilateral histotripsy tumor ablation is capable of stimulating abscopal CD8+ TIL responses within contralateral, untreated tumors. Previous studies in various animal models have demonstrated the induction of measurable abscopal immune responses following thermal ablation and radiation [13-18, 38, 44], we observed strong systemic effect with histotripsy. Within the tumor microenvironment, we observed qualitative differences in the patterns of intratumoral CD8+ T cell infiltration between treated and distant tumors. Whereas TIL populations were heavily concentrated along the periphery of ablation zones in treated tumors, TILs were localized more diffusely at distant tumor sites. The ability of subtotal (unilateral) histotripsy ablation to promote tumor-directed immune responses at both treated and untreated tumor sites resulted in a retardation of distant tumor growth. Despite the presence of contralateral tumors that were left completely untreated, this retardation was sufficient to promote statistically significant prolongation of survival. The potency of histotripsy-mediated abscopal effects was further illustrated by the ability of local histotripsy ablation to concomitantly inhibit distant pulmonary metastases. Importantly, we found that the immunostimulatory impact of histotripsy could work cooperatively with checkpoint inhibition immunotherapy, imparting a significant improvement in tumor control beyond that seen with checkpoint inhibition alone. Moreover, histotripsy-mediated abscopal immune responses were capable of potentiating checkpoint inhibition immunotherapy against more poorly immunogenic tumors like hepatocellular carcinoma.

Our observation that histotripsy immunostimulation could work cooperatively to enhance the efficacy of checkpoint inhibition immunotherapy against melanoma and hepatocellular carcinoma has important clinical implications. Contemporary checkpoint inhibitors like anti-CTLA-4 and anti-PD-1 monoclonal antibodies have, alone or in combination, yielded remarkable responses and prolonged survival for a subset of patients whose advanced melanoma and lung cancer had until only recently been largely untreatable. Recent studies have also suggested the therapeutic efficacy of CTLA-4 blockade for malignancies like hepatocellular carcinoma [47-49]. However, a sizeable majority of patients with these diseases remain unresponsive to checkpoint inhibition, and the remarkable benefits of immunotherapy have not been widely translated to patients with other, less immunogenic malignancies. It has become well established that responsiveness to checkpoint inhibition correlates with markers of tumor immunogenicity, as reflected by mutation and neoantigen frequency [50, 51]. Checkpoint inhibitors are unlikely to be able to add meaningful impact in a setting of poorly immunogenic tumors that do not trigger endogenous immune responses on their own.

There are a few other limitations of this study, primarily related to the choice of tumor model. The subcutaneous liver cancer model (Hepa 1-6) cannot replicate the tumor microenvironment as well as an orthotopic model. Melanoma and HCC tumors may have varying levels of tumor immunogenicity, so the strength of immune responses may vary across tumor types. Since subtotal histotripsy ablation was performed, it is possible that the level of immune response may also be influenced by the ratio of ablated tumor volume to the total tumor burden. Although the checkpoint inhibitor dosing in this study was chosen based on literature, optimal dosing for maximizing therapeutic response in combination with histotripsy still needs to be determined. Finally, the histotripsy-mediated immune response beyond 10 days post ablation was not characterized in this study, it is possible that it may decline over time and strategies such as re-ablation or additional immunotherapy dosing could be needed to maintain optimal levels of anti-tumor immunity. To address all these concerns, future studies will focus on in-depth immune investigations in immunocompetent, orthotopic tumor models.

5.5 References

1. J. E. Parsons, C. A. Cain, G. D. Abrams, and J. B. Fowlkes, "Pulsed cavitational ultrasound therapy for controlled tissue homogenization," (in eng), Ultrasound Med Biol, vol. 32, no. 1, pp. 115-29, Jan 2006, doi: 10.1016/j.ultrasmedbio.2005.09.005.

2. Z. Xu et al., "Controlled ultrasound tissue erosion," (in eng), IEEE Trans Ultrason Ferroelectr Freq Control, vol. 51, no. 6, pp. 726-36, Jun 2004, doi: 10.1109/tuffc.2004.1308731.

3. W. W. Roberts, T. L. Hall, K. Ives, J. S. Wolf, Jr., J. B. Fowlkes, and C. A. Cain, "Pulsed cavitational ultrasound: a noninvasive technology for controlled tissue ablation (histotripsy) in the rabbit kidney," (in eng), J Urol, vol. 175, no. 2, pp. 734-8, Feb 2006, doi: S0022-5347(05)00141-2 [pii]10.1016/S0022-5347(05)00141-2.

4. A. D. Maxwell, C. A. Cain, T. L. Hall, J. B. Fowlkes, and Z. Xu, "Probability of cavitation for single ultrasound pulses applied to tissues and tissue-mimicking materials," (in eng), Ultrasound Med Biol, vol. 39, no. 3, pp. 449-65, Mar 2013, doi: 10.1016/j.ultrasmedbio.2012.09.004.

5. A. D. Maxwell et al., "Cavitation clouds created by shock scattering from bubbles during histotripsy," (in eng), J Acoust Soc Am, vol. 130, no. 4, pp. 1888-98, Oct 2011, doi: 10.1121/1.3625239.

6. E. Vlaisavljevich et al., "Non-Invasive Ultrasound Liver Ablation Using Histotripsy: Chronic Study in an In Vivo Rodent Model," (in eng), Ultrasound Med Biol, vol. 42, no. 8, pp. 1890-902, 08 2016, doi: 10.1016/j.ultrasmedbio.2016.03.018.

7. T. Worlikar et al., "Histotripsy for Non-Invasive Ablation of Hepatocellular Carcinoma (HCC) Tumor in a Subcutaneous Xenograft Murine Model," (in eng), Conf Proc IEEE Eng Med Biol Soc, vol. 2018, pp. 6064-6067, 07 2018, doi: 10.1109/EMBC.2018.8513650.

8. Y. Yang, "Cancer immunotherapy: harnessing the immune system to battle cancer," (in eng), J Clin Invest, vol. 125, no. 9, pp. 3335-7, Sep 2015, doi: 10.1172/JCI83871.

9. J. A. Marin-Acevedo, E. O. Kimbrough, and Y. Lou, "Next generation of immune checkpoint inhibitors and beyond," (in eng), J Hematol Oncol, vol. 14, no. 1, p. 45, 03 19 2021, doi: 10.1186/s13045-021-01056-8.

10. J. B. Jacob, M. K. Jacob, and P. Parajuli, "Review of immune checkpoint inhibitors in immuno-oncology," (in eng), Adv Pharmacol, vol. 91, pp. 111-139, 2021, doi: 10.1016/bs.apha.2021.01.002.

11. J. Peng, A. K. Lalani, and A. Swaminath, "Cytoreductive stereotactic body radiotherapy (SBRT) and combination SBRT with immune checkpoint inhibitors in metastatic renal cell carcinoma," (in eng), Can Urol Assoc J, vol. 15, no. 8, pp. 281-286, Aug 2021, doi: 10.5489/cuaj.6963.

12. O. Dahl, J. E. Dale, and M. Brydøy, "Rationale for combination of radiation therapy and immune checkpoint blockers to improve cancer treatment," (in eng), Acta Oncol, vol. 58, no. 1, pp. 9-20, Jan 2019, doi: 10.1080/0284186X.2018.1554259.

13. G. Li, K. F. Staveley-O'Carroll, and E. T. Kimchi, "Potential of Radiofrequency Ablation in Combination with Immunotherapy in the Treatment of Hepatocellular Carcinoma," (in eng), J Clin Trials, vol. 6, no. 2, Apr 2016, doi: 10.4172/2167-0870.1000257.

14. M. S. Sabel, G. Su, K. A. Griffith, and A. E. Chang, "Rate of freeze alters the immunologic response after cryoablation of breast cancer," (in eng), Ann Surg Oncol, vol. 17, no. 4, pp. 1187-93, Apr 2010, doi: 10.1245/s10434-009-0846-1.

15. F. Ahmad et al., "Changes in interleukin-1β and 6 after hepatic microwave tissue ablation compared with radiofrequency, cryotherapy and surgical resections," (in eng), Am J Surg, vol. 200, no. 4, pp. 500-6, Oct 2010, doi: 10.1016/j.amjsurg.2009.12.025.

16. K. F. Chu and D. E. Dupuy, "Thermal ablation of tumours: biological mechanisms and advances in therapy," (in eng), Nat Rev Cancer, vol. 14, no. 3, pp. 199-208, Mar 2014, doi: 10.1038/nrc3672.

17. M. H. den Brok et al., "In situ tumor ablation creates an antigen source for the generation of antitumor immunity," (in eng), Cancer Res, vol. 64, no. 11, pp. 4024-9, Jun 2004, doi: 10.1158/0008-5472.CAN-03-3949.

18. S. S. Park et al., "PD-1 Restrains Radiotherapy-Induced Abscopal Effect," (in eng), Cancer Immunol Res, vol. 3, no. 6, pp. 610-9, Jun 2015, doi: 10.1158/2326-6066.CIR-14-0138.

19. M. A. O'Brien, D. G. Power, A. J. Clover, B. Bird, D. M. Soden, and P. F. Forde, "Local tumour ablative therapies: opportunities for maximising immune engagement and activation," (in eng), Biochim Biophys Acta, vol. 1846, no. 2, pp. 510-23, Dec 2014, doi: 10.1016/j.bbcan.2014.09.005.

20. A. Mehta, R. Oklu, and R. A. Sheth, "Thermal Ablative Therapies and Immune Checkpoint Modulation: Can Locoregional Approaches Effect a Systemic Response?," (in eng), Gastroenterol Res Pract, vol. 2016, p. 9251375, 2016, doi: 10.1155/2016/9251375.

21. J. F. Grosso and M. N. Jure-Kunkel, "CTLA-4 blockade in tumor models: an overview of preclinical and translational research," (in eng), Cancer Immun, vol. 13, p. 5, 2013.

22. A. J. Russ et al., "Suppression of T-cell expansion by melanoma is exerted on resting cells," (in eng), Ann Surg Oncol, vol. 18, no. 13, pp. 3848-57, Dec 2011, doi: 10.1245/s10434-011-1667-6.

23. A. J. Russ et al., "Melanoma-induced suppression of tumor antigen-specific T cell expansion is comparable to suppression of global T cell expansion," (in eng), Cell Immunol, vol. 271, no. 1, pp. 104-9, 2011, doi: 10.1016/j.cellimm.2011.06.011.

24. L. Wentworth, J. V. Meyers, S. Alam, A. J. Russ, M. Suresh, and C. S. Cho, "Memory T cells are uniquely resistant to melanoma-induced suppression," (in eng), Cancer Immunol Immunother, vol. 62, no. 1, pp. 149-59, Jan 2013, doi: 10.1007/s00262-012-1326-1.

25. A. Contreras et al., "Enhanced local and systemic anti-melanoma CD8+ T cell responses after memory T cell-based adoptive immunotherapy in mice," (in eng), Cancer Immunol Immunother, vol. 65, no. 5, pp. 601-11, May 2016, doi: 10.1007/s00262-016-1823-8.

26. D. A. Mahvi et al., "Ctla-4 blockade plus adoptive T-cell transfer promotes optimal melanoma immunity in mice," (in eng), J Immunother, vol. 38, no. 2, pp. 54-61, 2015 Feb-Mar 2015, doi: 10.1097/CJI.0000000000000064.

27. A. Contreras et al., "Co-transfer of tumor-specific effector and memory CD8+ T cells enhances the efficacy of adoptive melanoma immunotherapy in a mouse model," (in eng), J Immunother Cancer, vol. 6, no. 1, p. 41, 05 29 2018, doi: 10.1186/s40425-018-0358-2.

28. E. Vlaisavljevich, Y. Kim, G. Owens, W. Roberts, C. Cain, and Z. Xu, "Effects of tissue mechanical properties on susceptibility to histotripsy-induced tissue damage," (in eng), Physics in Medicine and Biology, vol. 59, no. 2, pp. 253-70, Jan 20 2014, doi: 10.1088/0031-9155/59/2/253.

29. H. Huang et al., "Histones activate the NLRP3 inflammasome in Kupffer cells during sterile inflammatory liver injury," (in eng), J Immunol, vol. 191, no. 5, pp. 2665-79, Sep 01 2013, doi: 10.4049/jimmunol.1202733.

30. F. S. Hodi et al., "Improved survival with ipilimumab in patients with metastatic melanoma," (in eng), N Engl J Med, vol. 363, no. 8, pp. 711-23, Aug 19 2010, doi: 10.1056/NEJMoa1003466.

31. J. D. Wolchok et al., "Nivolumab plus ipilimumab in advanced melanoma," (in eng), N Engl J Med, vol. 369, no. 2, pp. 122-33, Jul 11 2013, doi: 10.1056/NEJMoa1302369.

32. J. Larkin et al., "Combined Nivolumab and Ipilimumab or Monotherapy in Untreated Melanoma," (in eng), N Engl J Med, vol. 373, no. 1, pp. 23-34, Jul 02 2015, doi: 10.1056/NEJMoa1504030.

33. J. Brahmer et al., "Nivolumab versus Docetaxel in Advanced Squamous-Cell Non-Small-Cell Lung Cancer," (in eng), N Engl J Med, vol. 373, no. 2, pp. 123-35, Jul 09 2015, doi: 10.1056/NEJMoa1504627.

34. H. Borghaei et al., "Nivolumab versus Docetaxel in Advanced Nonsquamous Non-Small-Cell Lung Cancer," (in eng), N Engl J Med, vol. 373, no. 17, pp. 1627-39, Oct 22 2015, doi: 10.1056/NEJMoa1507643.

35. R. J. Motzer et al., "Nivolumab versus Everolimus in Advanced Renal-Cell Carcinoma," (in eng), N Engl J Med, vol. 373, no. 19, pp. 1803-13, Nov 05 2015, doi: 10.1056/NEJMoa1510665.

36. R. E. Royal et al., "Phase 2 trial of single agent Ipilimumab (anti-CTLA-4) for locally advanced or metastatic pancreatic adenocarcinoma," (in eng), J Immunother, vol. 33, no. 8, pp. 828-33, Oct 2010, doi: 10.1097/CJI.0b013e3181eec14c.

37. B. Lee et al., "Emerging biomarkers for immunomodulatory cancer treatment of upper gastrointestinal, pancreatic and hepatic cancers," (in eng), Semin Cancer Biol, vol. 52, no. Pt 2, pp. 241-252, 10 2018, doi: 10.1016/j.semcancer.2017.12.009.

38. W. Ngwa, O. C. Irabor, J. D. Schoenfeld, J. Hesser, S. Demaria, and S. C. Formenti, "Using immunotherapy to boost the abscopal effect," (in eng), Nat Rev Cancer, vol. 18, no. 5, pp. 313-322, 05 2018, doi: 10.1038/nrc.2018.6.

39. V. A. Khokhlova et al., "Histotripsy methods in mechanical disintegration of tissue: towards clinical applications," (in eng), Int J Hyperthermia, vol. 31, no. 2, pp. 145-62, Mar 2015, doi: 10.3109/02656736.2015.1007538.

40. G. R. Schade, Y. N. Wang, S. D'Andrea, J. H. Hwang, W. C. Liles, and T. D. Khokhlova, "Boiling Histotripsy Ablation of Renal Cell Carcinoma in the Eker Rat Promotes a Systemic Inflammatory Response," (in eng), Ultrasound Med Biol, vol. 45, no. 1, pp. 137-147, 01 2019, doi: 10.1016/j.ultrasmedbio.2018.09.006.

41. A. L. Marzo et al., "Tumor antigens are constitutively presented in the draining lymph nodes," (in eng), J Immunol, vol. 162, no. 10, pp. 5838-45, May 15 1999.

42. O. Preynat-Seauve, E. Contassot, P. Schuler, V. Piguet, L. E. French, and B. Huard, "Extralymphatic tumors prepare draining lymph nodes to invasion via a T-cell cross-tolerance process," (in eng), Cancer Res, vol. 67, no. 10, pp. 5009-16, May 15 2007, doi: 10.1158/0008-5472.CAN-06-4494.

43. E. Contassot, O. Preynat-Seauve, L. French, and B. Huard, "Lymph node tumor metastases: more susceptible than primary tumors to CD8(+) T-cell immune destruction," (in eng), Trends Immunol, vol. 30, no. 12, pp. 569-73, Dec 2009, doi: 10.1016/j.it.2009.08.001.

44. S. C. Formenti et al., "Radiotherapy induces responses of lung cancer to CTLA-4 blockade," (in eng), Nat Med, vol. 24, no. 12, pp. 1845-1851, 12 2018, doi: 10.1038/s41591-018-0232-2.

45. D. V. Krysko, A. D. Garg, A. Kaczmarek, O. Krysko, P. Agostinis, and P. Vandenabeele, "Immunogenic cell death and DAMPs in cancer therapy," (in eng), Nat Rev Cancer, vol. 12, no. 12, pp. 860-75, Dec 2012, doi: 10.1038/nrc3380.

46. S. Ladoire et al., "Cell-death-associated molecular patterns as determinants of cancer immunogenicity," (in eng), Antioxid Redox Signal, vol. 20, no. 7, pp. 1098-116, Mar 01 2014, doi: 10.1089/ars.2012.5133.

47. L. Bezu et al., "Combinatorial strategies for the induction of immunogenic cell death," (in eng), Front Immunol, vol. 6, p. 187, 2015, doi: 10.3389/fimmu.2015.00187.

48. B. Sangro et al., "A clinical trial of CTLA-4 blockade with tremelimumab in patients with hepatocellular carcinoma and chronic hepatitis C," (in eng), J Hepatol, vol. 59, no. 1, pp. 81-8, Jul 2013, doi: 10.1016/j.jhep.2013.02.022.

49. D. Agdashian et al., "The effect of anti-CTLA4 treatment on peripheral and intra-tumoral T cells in patients with hepatocellular carcinoma," (in eng), Cancer Immunol Immunother, vol. 68, no. 4, pp. 599-608, Apr 2019, doi: 10.1007/s00262-019-02299-8.

50. A. Snyder et al., "Genetic basis for clinical response to CTLA-4 blockade in melanoma," (in eng), N Engl J Med, vol. 371, no. 23, pp. 2189-2199, Dec 04 2014, doi: 10.1056/NEJMoa1406498.

51. S. Champiat, C. Ferté, S. Lebel-Binay, A. Eggermont, and J. C. Soria, "Exomics and immunogenics: Bridging mutational load and immune checkpoints efficacy," (in eng), Oncoimmunology, vol. 3, no. 1, p. e27817, Jan 01 2014, doi: 10.4161/onci.27817.

Chapter 6 Investigation of Repeat Histotripsy Ablation

6.1 Introduction

Liver cancer is one of the top ten causes of cancer related deaths worldwide and in the United States [1]. Although many treatment options are available, including radiofrequency ablation (RFA), micro-wave ablation (MWA), Transarterial chemoembolization (TACE), cryoablation, high intensity focused ultrasound (HIFU)), chemotherapy, radiation therapy, targeted drug therapy and immunotherapies, HCC continues to have a high recurrence rate [2, 3]. Approximately 50-80% of patients experience recurrence within a few years following treatment [4]. There is currently ongoing interest in neoadjuvant and adjuvant treatment strategies aimed at decreasing recurrence rates.

Histotripsy non-invasively destroys soft tissue through precise control of acoustic cavitation [5-7]. Our previous study in immunocompromised mice has demonstrated that histotripsy can destroy the target tumor tissue to form acellular debris, which is resorbed over time, resulting in effective reduction of local tumor progression and improvement in survival outcomes, eventually tumor recurrence was observed [8]. We have also demonstrated that histotripsy can mechanically ablate cells to promote anti-tumor inflammatory and immunostimulatory effects in immunocompetent mice [9]. Histotripsy can be theoretically repeated as necessary to control local tumor progression, however, the tolerability and the biological effects of repeat histotripsy procedures in local control have not been studied yet. The aim of this study is to compare the safety, efficacy, local tumor control and survival outcomes for single and repeat histotripsy using immunocompetent and immunocompromised murine HCC models.

6.2 Materials and Methods

6.2.1 Experimental Design

This study was approved by the Institutional Animal Care and Use Committee at the University of Michigan (UM-IACUC). Human-derived xenograft murine subcutaneous HCC tumor model was developed in immune-compromised NSG (NOD-Prkdcscid IL2rγnull) murine hosts. A mouse-derive subcutaneous HCC tumor model was developed in immunocompetent C3H murine hosts. Animals were monitored for up to 3 months by MRI for local tumor regression or progression. The primary tumor growth characteristics, response to histotripsy, tumor recurrence and survival outcomes were compared between the two histotripsy doses.

HepG2 HCC tumor cells were injected subcutaneously in the flanks of 24 NSG female mice aged 6-7 weeks to generate tumors. The mice were categorized into three groups based on the tumor volume targeted for ablation: A) single histotripsy (n=8), B) repeat histotripsy (n=8), and C) control (n=8). Three weeks after inoculation, the mice in single and repeat treatment groups were treated with histotripsy. The mice in control group did not receive histotripsy or other treatment. One week after initial histotripsy treatment, mice in the repeat treatment group mice received repeat histotripsy treatment.

HCA-1 tumor cells were injected subcutaneously in the flanks of 21 C3H female mice aged 6-7 weeks to generate tumors. The mice were categorized into three groups based on the tumor volume targeted for ablation: A) single histotripsy (n=7), B) repeat histotripsy (n=7), and C) control (n=7). Four weeks after inoculation, the mice in single and repeat treatment groups were treated with histotripsy. The mice in control group did not receive histotripsy or other treatment. One week after initial histotripsy treatment, mice in the repeat treatment group mice received repeat histotripsy treatment.

The choice of performing the repeat histotripsy treatment at 1 week post initial treatment was based on the observations of adaptive immune response to histotripsy observed at 1 week post treatment in previous studies [9]. While this study focuses on the tolerability and survival outcomes, we plan to investigate if repeat treatments can sustain favorable anti-tumor immune response over time to control local tumor growth as compared to single treatment.

6.2.2 Cell Preparation

HepG2 (ATCC® HB-8064™) cells derived from human HCC tumors were cultivated in DMEM (+Glutamine, +Earle's Salts) media supplemented with 10% FBS, and 1 mL Gentamicin. HCA-1 cells obtained from Duda Laboratory (Harvard University, Massachusetts) were cultivated in DMEM (+Glutamine, +Earle's Salts) media supplemented with 10% FBS, and 1 mL Gentamicin. The cells were maintained at 37 °C in a 5% CO2/95% humidified air atmosphere.

6.2.3 Animals

NSG mice were injected with 5 million HepG2 cells subcutaneously into the right flank to generate xenograft tumors. All mice were monitored weekly and tumor diameter measurements were quantified using calipers. C3H mice were injected with 7-8 million HCA-1 cells subcutaneously into the right flank to generate xenograft tumors.

Prior to and during histotripsy, the mice were induced and maintained on general anesthesia by inhalation of isoflurane gas (1.5-2.0%) in 1 L/min of oxygen (SurgiVet V704001, Smiths Medical, Waukesha, Wisconsin, USA). The hair covering the subcutaneous tumor region was removed with an electric clipper. Core body temperature was recorded using a rectal probe and was maintained between 35-37 °C with an overhead heating lamp. The mice were injected with Carprofen analgesic (5 mg/kg) subcutaneously before delivery of histotripsy treatment and 24 and 48 hours after histotripsy therapy. Immediately after histotripsy, the mice were transferred to a recovery chamber fitted with an overhead heating lamp and were placed on a heated pad. Once the mice recovered from anesthesia and were mobile, they were transferred back to their housing cages.

End stage illness and humane endpoints guidelines were determined as follows: animals exhibiting signs of dehydration, emaciation or cachexia, impaired mobility, systemic infection, or abdominal or thoracic bleeding during or immediately after histotripsy treatment were to be euthanized.

6.2.4 Experimental Setup

Our lab has designed and built a custom 8 element 1 MHz focused ultrasound therapy transducer specifically for rodent histotripsy therapy [8, 10]. The histotripsy transducer was driven by a custom-built high-voltage pulser controlled by a field-programmable gate array (FPGA) development board (DE0-Nano Terasic Technology, HsinChu, Taiwan), enabling the therapy transducer to generate, and output 1-2 cycle histotripsy pulses. A 20 MHz B-mode ultrasound imaging probe (L40-8/12, Ultrasonix, Vancouver, Canada) was co-aligned with the center of the therapy transducer to allow visualization of the focal ablation volume in real time. The ultrasound therapy transducer and the imaging probe were mounted to a motorized 3-axis positioning system to mechanically scan the therapy focus across a 3D target ablation volume. Water was used as the ultrasound coupling medium by immersing the transducer and imaging probe in a tank of degassed water maintained at 35–37°C by means of a coil heater. The mouse was placed on a custom-built animal platform just over the water tank.

6.2.5 Histotripsy Ablation

After sedation, the animal was placed decubitus with the subcutaneous tumor submerged in the degassed water. To identify the histotripsy focus on ultrasound imaging, test histotripsy pulses were delivered to the water tank by the therapy transducer to generate a "bubble cloud" which appeared as a hyperechoic cavitation zone on ultrasound imaging. The position of the hyperechoic cavitation zone was then marked as the therapy focal position on the ultrasound image. Using a custom MATLAB script, the ultrasound therapy transducer and the imaging probe were scanned using the motorized positioning system, such that a treatment ellipsoid consisting of a grid of uniformly spaced therapy focal zones (~0.5 – 0.7 mm between adjacent focal volumes) would encompass the user-defined target 3D tumor volume. The entire tumor volume was targeted for ablation without any additional treatment margin to avoid off-target damage to skin and muscle. At each focal location, 50 histotripsy pulses at 100 Hz PRF (P- >30 MPa) or 0.5 seconds of ablation were delivered. Treatment times ranged from 5-15 minutes depending on tumor volume dimensions. After ablation, the targeted region appeared hypoechoic on ultrasound imaging, enabling real-time feedback to ensure adequate ablation volumes were achieved. Histotripsy parameters were chosen on the basis of previous in vivo and in vitro work [8, 11].

6.2.6 Magnetic Resonance Imaging for Treatment Evaluation

MRI data was obtained within 1 day prior to histotripsy and within 1 day post-histotripsy, followed by weekly imaging to assess the effects of tumor ablation and characterize variations in imaging appearance. Imaging was performed on a 7.0 T MR scanner using a Direct Drive console (Agilent Technologies, Santa Clara, CA, USA) with a 40 mm inner-diameter transmit-receive radiofrequency (RF) volume coil (Morris Instruments, Ontario, Canada). Prior to and during imaging, the mice were induced and maintained on general anesthesia by inhalation of isoflurane gas (1.5-2.0%) in 1 L/min of oxygen (SurgiVet V704001, Smiths Medical, Waukesha, Wisconsin, USA). Respiration was monitored and animal temperature was maintained at 37±0.5 °C using a rectal temperature probe and a custom-built proportional-integral-derivative (PID) controller (LabVIEW, National Instruments, Austin TX) interfaced with a commercially available small animal system (SA Instruments, Stony Brook, NY). Initial pilot scans were performed to confirm positioning. Thereafter, T2, T1-weighted fast spin-echo (FSE) sequences and a T2*-weighted gradient-echo (GRE) sequence were used to visualize the tumor in the axial plane (Table 6-1). Tumor diameter measurements were also made on the MRI images. Surrounding structures such as the musculature and body wall were evaluated for signs of injury.

Table 6-1 MR Imaging Parameters

Sequence Type	**T2-weighted FSE**	**T1-weighted FSE**	**T2*-weighted GRE**
Slice Thickness	1mm	1mm	1mm
FOV	40 × 40mm	40 × 40mm	40 × 40mm
TR	2000ms	2000ms	250ms
TE_{eff}	21.3ms	7.18ms	5ms
Acquisition Time	~2 min	~2 min	~2 min

6.2.7 Statistical Analysis

Experimental data were analyzed using MATLAB (v2016). Survival analysis was performed using the Kaplan-Meier method. Analysis of variance (ANOVA) was applied to assess the statistical significance in tumor growth kinetics. Differences in survival between control, single dose of histotripsy and repeat histotripsy ablation cohorts were assessed using the log-rank test. Significance was defined as $p < 0.05$.

6.3 Results

6.3.1 Clinical Monitoring

All tumor inoculations were well-tolerated with no deaths or complications as a direct result of the subcutaneous tumor injections. All histotripsy procedures were well tolerated without major or minor complications requiring additional care or euthanasia.

6.3.2 Local Tumor Response

Histotripsy of HepG2 tumors in immunocompromised mice inhibited tumor growth for 1-2 weeks following treatment as compared to controls (Figure 6-1A). A second treatment of histotripsy stabilized tumor volumes for an additional 1-2 weeks, however eventually tumor progression was observed, similar to single histotripsy. Histotripsy of HCA-1 tumors in immunocompetent mice inhibited tumor growth for 1-2 weeks following treatment as compared to controls (Figure 6-1B). A second treatment of histotripsy stabilized tumor volumes for an additional 1-2 weeks, however eventually tumor progression was observed, similar to single histotripsy.

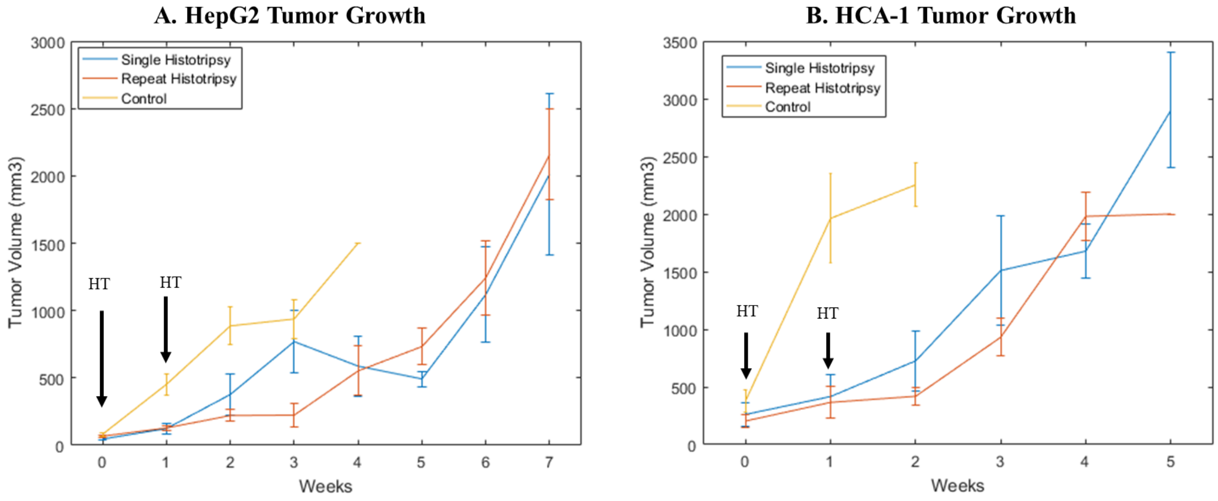

Figure 6-1 ***Response to Histotripsy.*** *Histotripsy ablation resulted in suppression of local tumor growth in both (A) HepG2 and (B) HCA-1 tumor models as compared to control. Histotripsy was performed at week 0. For the repeat histotripsy group, the second treatment was performed at week 1.*

6.3.3 Survival Outcomes

Histotripsy treated animals had statistically significant improved survival compared to controls in the HepG2 tumor model (Figure 6-2A). All the control mice in the HepG2 group were euthanized by 4 weeks post treatment timepoint due to increased tumor burden. n=8/8 repeat histotripsy mice survived up to 7 weeks, in comparison, only n=3/8 single histotripsy mice survived up to 7 weeks. However, the difference between histotripsy groups is not statistically significant.

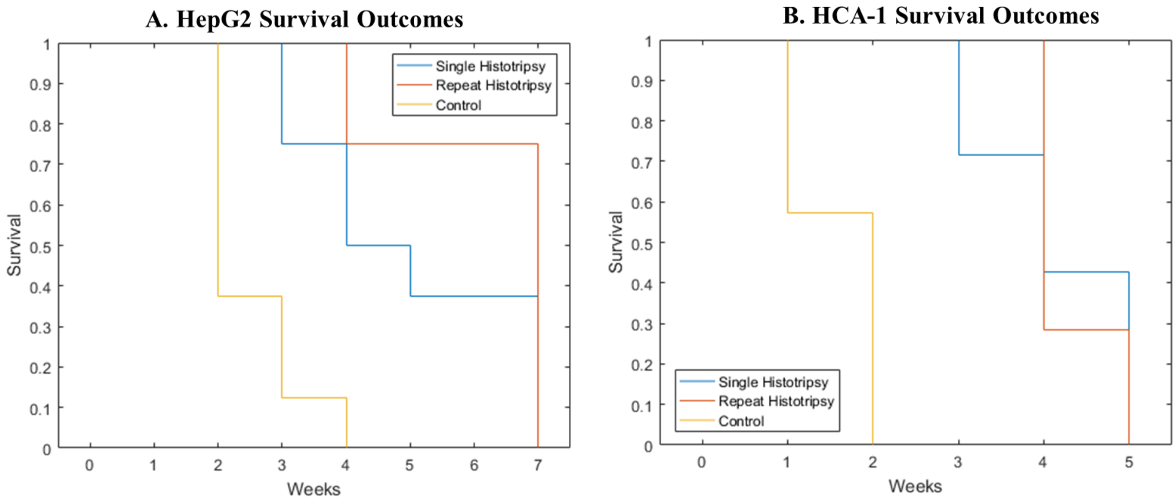

Figure 6-2 ***Survival Outcomes.*** *Kaplan Meier survival curve indicates significant difference in survival outcomes of histotripsy-treated animals vs untreated controls in both (A) HepG2 and (B) HCA-1 tumor models (p < 0.0001). The difference between histotripsy groups is not statistically significant*

All the control mice in the HCA-1 group were euthanized by 2 weeks post treatment timepoint due to increased tumor burden. Histotripsy treated animals had statistically significant improved survival compared to controls in HCA-1 tumor model (Figure 6-2B). n=7/7 repeat histotripsy mice survived more than 4 weeks, in comparison, only n=5/7 single histotripsy mice survived more than 4 weeks. However, the difference between histotripsy groups is not statistically significant.

6.3.4 Radiological Observations in HepG2 tumor model

At the histotripsy timepoint (3 weeks post tumor inoculation), untreated tumor appeared hyperintense on T1-weighted MRI compared to the adjacent muscle. The tumor volume was 45.59 ± 10.01 mm^3 (mean ± SEM) in the single histotripsy group, 67.43 ± 7.64 mm^3 (mean ± SEM) in the repeat histotripsy group, and 81.45 ± 12.73 mm^3 (mean ± SEM) in control group. The difference was not statistically significant ($p > 0.05$). Subsequent timepoints are measured from the histotripsy timepoint (week 0).

Effective tumor volume stabilization was observed in histotripsy animals as compared to untreated controls (Figures 6-3, 6-4). On T2* MR imaging, tumor is hypointense compared to the muscle and becomes hyperintense post treatment, indicating liquification of tumor post histotripsy. Although the ablated tumor homogenate did not completely resolve post histotripsy, tumor progression was arrested for at least one week following histotripsy treatment in both treatment groups.

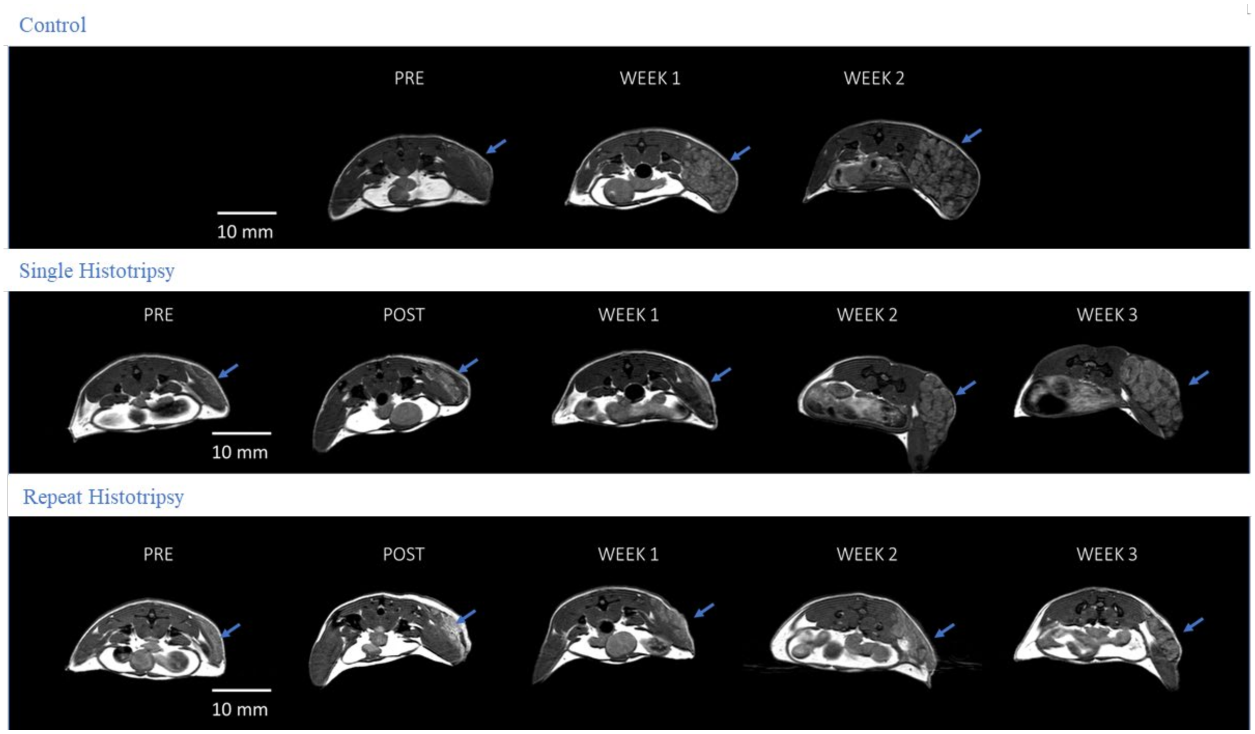

Figure 6-3 ***Comparison of HepG2 tumor progression on T1-weighted MRI****. Representative T1 weighted MRI images show tumor response. In the repeat histotripsy group, tumor was treated again at week 1 timepoint. Local tumor control is observed 1-2 weeks following histotripsy treatment, however local tumor progression is observed in the control animal.*

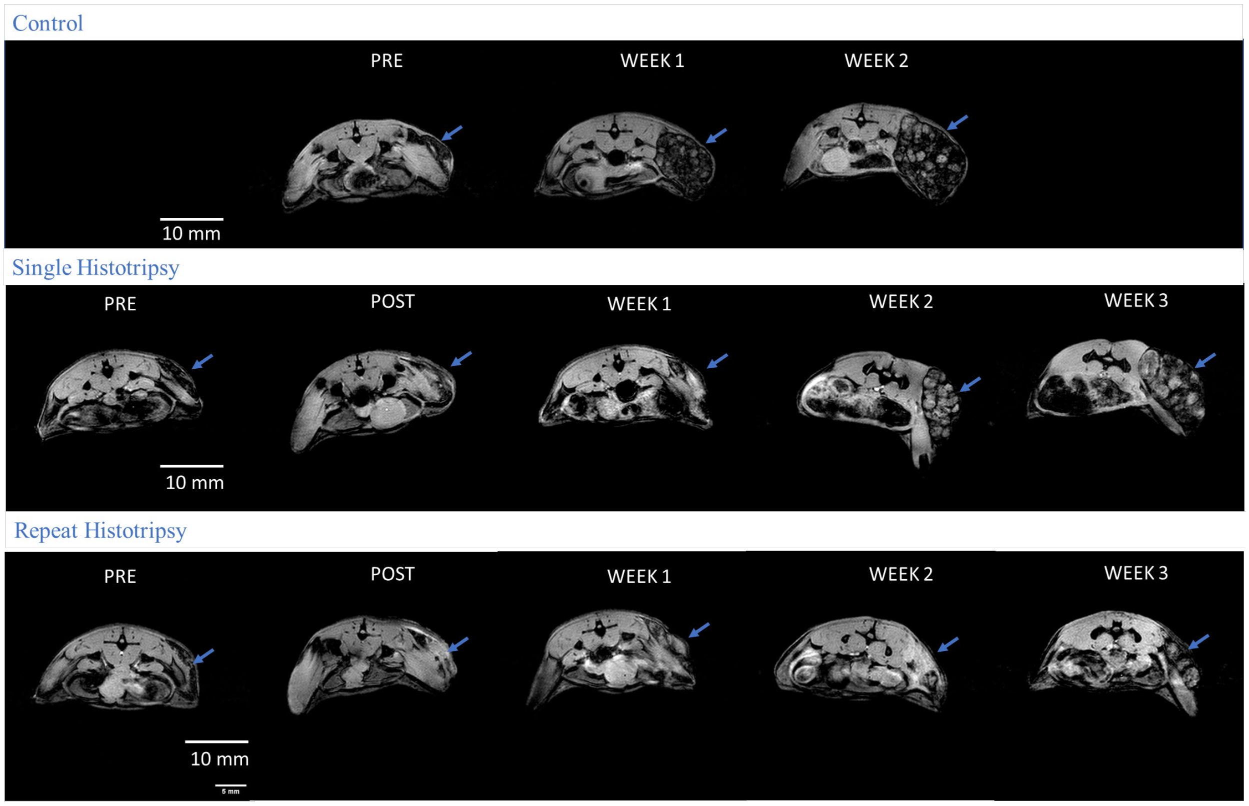

Figure 6-4 ***Comparison of HepG2 tumor progression on T2*-weighted MRI.*** *Representative T2* weighted MRI images show tumor response. In the repeat histotripsy group, tumor was treated again at week 1 timepoint. Local tumor control is observed 1-2 weeks following histotripsy treatment, however local tumor progression is observed in the control animal.*

6.3.5 Radiological Observations in HCA-1 tumor model

At the histotripsy timepoint (4 weeks post tumor inoculation), untreated tumor appeared hyperintense on T2-weighted MRI compared to the adjacent muscle (Figure 6-6). The tumor volume was 261.17 ± 102.05 mm^3 (mean ± SEM) in the single histotripsy group, 204.17 ± 60.91 mm^3 (mean ± SEM) in the repeat histotripsy group, and 376.94 ± 97.26 mm^3 (mean ± SEM) in control group. The difference was not statistically significant ($p > 0.05$). Subsequent timepoints are measured from the histotripsy timepoint (week 0).

Effective tumor volume stabilization was observed in histotripsy animals as compared to untreated controls (Figures 6-5). Although the ablated tumor homogenate did not complete resolve post histotripsy, local tumor progression was controlled for at least one week following histotripsy treatment in both treatment groups.

Control

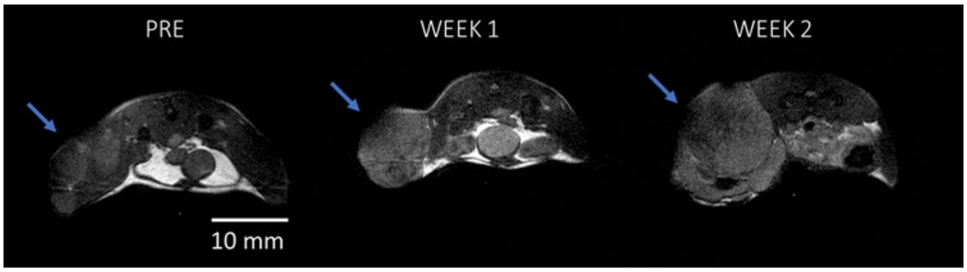

Single Histotripsy

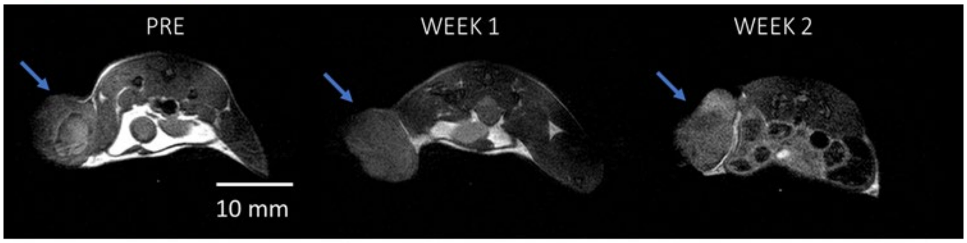

Repeat Histotripsy

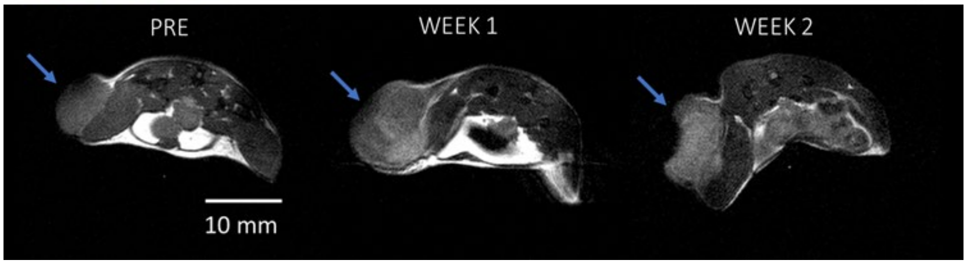

Figure 6-5 ***Comparison of HCA-1 tumor progression on T2-weighted MRI.*** *Representative T2 weighted MRI images show tumor response. In the repeat histotripsy group, tumor was treated again at week 1 timepoint. In both single and repeat histotripsy cases, tumor volume appears stabilized at 2 weeks, whereas tumor progression is observed in the control case.*

6.4 Discussion

This study investigates the response of single and repeat histotripsy tumor ablation in both immunocompetent and immunocompromised HCC murine tumor models using MR imaging. Cirrhotic patients at risk of HCC are known to be systemically immunocompromised [12]. We have used the human-derived HCC xenograft model for more accurate pre-clinical assessment of histotripsy tumor responses in immunocompromised hosts, while using the mouse-derived HCC model to study the response in an intact immune system. Our results indicate that histotripsy controlled local tumor progression as compared to controls in both models, although complete tumor regression was not observed. This study also demonstrates that repeat histotripsy is well tolerated and contributes to local tumor control. Theoretically it may be possible to repeat histotripsy procedures more than once to effectively control and even reduce the tumor burden over time. However, the impact of repeat procedures on immunomodulation remains to be investigated. Ablation has traditionally been used as a curative therapy or bridging therapy to downstage tumors[13]. Histotripsy may be useful an effective adjuvant to downstage tumors in combination with other therapies.

In the HCA-1 tumor study, tumors were treated at a later timepoint (4 weeks post inoculation), and the pre-treatment tumor volumes were higher compared to the HepG2 study. Promisingly, the histotripsy procedures of larger tumor volumes (relative to mouse dimensions) were well tolerated, and no safety concerns were observed. Although local tumor growth is initially inhibited in treated animals as compared to controls, eventually tumor growth is observed. Previous studies have shown that histotripsy promotes local inflammatory and immunostimulatory effects within two weeks following histotripsy, however these effects have not been investigated longer-term[9]. Repeat ablation has the potential to extend the anti-tumor inflammatory and immunostimulatory benefits and should be further investigated to establish optimal treatment timing and dosage for maximizing tumor reduction.

There are some limitations of this study. First, the subcutaneous tumors did not allow sufficient ablation margin beyond the tumor boundary. Second, the subcutaneous model cannot replicate the tumor microenvironment as well as an orthotopic model. Overall, this study demonstrates the feasibility of multiple histotripsy procedures for non-invasive tumor ablation using human-derived and mouse-derived HCC murine models.

6.5 References

1. R. L. Siegel, K. D. Miller, H. E. Fuchs, and A. Jemal, "Cancer Statistics, 2021," (in eng), *CA Cancer J Clin,* vol. 71, no. 1, pp. 7-33, 01 2021, doi: 10.3322/caac.21654.

2. L. Kulik and H. B. El-Serag, "Epidemiology and Management of Hepatocellular Carcinoma," (in eng), *Gastroenterology,* vol. 156, no. 2, pp. 477-491.e1, 01 2019, doi: 10.1053/j.gastro.2018.08.065.

3. P. Tabrizian, G. Jibara, B. Shrager, M. Schwartz, and S. Roayaie, "Recurrence of hepatocellular cancer after resection: patterns, treatments, and prognosis," (in eng), *Ann Surg,* vol. 261, no. 5, pp. 947-55, May 2015, doi: 10.1097/SLA.0000000000000710.

4. R. D. Kim, A. I. Reed, S. Fujita, D. P. Foley, K. L. Mekeel, and A. W. Hemming, "Consensus and controversy in the management of hepatocellular carcinoma," (in eng), *J Am Coll Surg,* vol. 205, no. 1, pp. 108-23, Jul 2007, doi: 10.1016/j.jamcollsurg.2007.02.025.

5. J. E. Parsons, C. A. Cain, G. D. Abrams, and J. B. Fowlkes, "Pulsed cavitational ultrasound therapy for controlled tissue homogenization," (in eng), *Ultrasound Med Biol,* vol. 32, no. 1, pp. 115-29, Jan 2006, doi: 10.1016/j.ultrasmedbio.2005.09.005.

6. Z. Xu *et al.*, "Controlled ultrasound tissue erosion," (in eng), *IEEE Trans Ultrason Ferroelectr Freq Control,* vol. 51, no. 6, pp. 726-36, Jun 2004, doi: 10.1109/tuffc.2004.1308731.

7. W. W. Roberts, T. L. Hall, K. Ives, J. S. Wolf, Jr., J. B. Fowlkes, and C. A. Cain, "Pulsed cavitational ultrasound: a noninvasive technology for controlled tissue ablation (histotripsy) in the rabbit kidney," (in eng), *J Urol,* vol. 175, no. 2, pp. 734-8, Feb 2006, doi: S0022-5347(05)00141-2 [pii]10.1016/S0022-5347(05)00141-2.

8. T. Worlikar *et al.*, "Histotripsy for Non-Invasive Ablation of Hepatocellular Carcinoma (HCC) Tumor in a Subcutaneous Xenograft Murine Model," (in eng), *Conf Proc IEEE Eng Med Biol Soc,* vol. 2018, pp. 6064-6067, 07 2018, doi: 10.1109/EMBC.2018.8513650.

9. S. Qu *et al.*, "Non-thermal histotripsy tumor ablation promotes abscopal immune responses that enhance cancer immunotherapy," (in eng), *J Immunother Cancer,* vol. 8, no. 1, Jan 2020, doi: 10.1136/jitc-2019-000200.

10. E. Vlaisavljevich *et al.*, "Non-Invasive Ultrasound Liver Ablation Using Histotripsy: Chronic Study in an In Vivo Rodent Model," (in eng), *Ultrasound Med Biol,* vol. 42, no. 8, pp. 1890-902, 08 2016, doi: 10.1016/j.ultrasmedbio.2016.03.018.

11. E. Vlaisavljevich, Y. Kim, G. Owens, W. Roberts, C. Cain, and Z. Xu, "Effects of tissue mechanical properties on susceptibility to histotripsy-induced tissue damage," (in eng), *Physics in Medicine and Biology,* vol. 59, no. 2, pp. 253-70, Jan 20 2014, doi: 10.1088/0031-9155/59/2/253.

12. P. Tandon and G. Garcia-Tsao, "Bacterial infections, sepsis, and multiorgan failure in cirrhosis," (in eng), *Semin Liver Dis,* vol. 28, no. 1, pp. 26-42, Feb 2008, doi: 10.1055/s-2008-1040319.

13. A. Facciorusso, G. Serviddio, and N. Muscatiello, "Local ablative treatments for hepatocellular carcinoma: An updated review," (in eng), *World J Gastrointest Pharmacol Ther,* vol. 7, no. 4, pp. 477-489, Nov 2016, doi: 10.4292/wjgpt.v7.i4.477.

Chapter 7 Summary and Future Work

7.1 Summary

This dissertation demonstrates the safety, efficacy, and biological effects of histotripsy for tumor ablation *in vivo* with a primary emphasis on liver cancer. The works begins with the development of subcutaneous human-derived HCC murine tumor models to demonstrate the safety, feasibility, and tumor burden reduction effects of histotripsy. Next, the immunomodulatory effects of histotripsy are investigated in murine melanoma and HCC models. This is followed by development of orthotopic HCC models in immunocompetent hosts to demonstrate the safety and feasibility of targeting liver tumors. Most significantly, these studies demonstrate that histotripsy is capable of controlling local tumor growth and even promoting complete local tumor regression without increasing the risk of metastasis. Though this work has investigated histotripsy primarily in liver cancer models, the insights can be easily translated for treatment of other solid tumors (e.g., melanoma, breast cancer, pancreatic cancer). The aim of this work is to provide a scientific basis to facilitate clinical translation of histotripsy as a liver cancer treatment modality.

The first study evaluated the safety and feasibility and survival benefits of histotripsy for in vivo tumor ablation [1]. Results showed that non-invasive histotripsy ablation reduced local tumor progression of subcutaneous human-derived HCC tumor and improved survival outcomes in immunocompromised mice. This study also characterized the radiological features correlating to the histotripsy tumor response.

The second study evaluated the safety, feasibility, and tumor volume reduction effects of histotripsy for liver cancer ablation in an orthotopic, immune-competent in vivo rat HCC model [2]. For the first time, it was demonstrated that complete as well as partial histotripsy ablation of tumors can result in complete tumor regression with no recurrence.

The third study evaluated the effects of partial histotripsy tumor ablation on tumor response, risk of metastases and immune infiltration in an orthotopic, immunocompetent, metastatic rodent hepatocellular carcinoma (HCC) model [3]. Results showed that histotripsy significantly improved survival outcomes with no increased risk of metastasis compared to controls and demonstrated that augmented tumor immune infiltration may have contributed to the eventual regression even with partial treatment of tumors.

The fourth study evaluated the anti-tumor immune response generated by histotripsy ablation of subcutaneous murine melanoma and HCC tumors [4]. Histotripsy stimulated potent local intratumoral infiltration of innate and adaptive immune cell populations, promoted abscopal immune responses at untreated tumor sites and inhibited growth of pulmonary metastases. Histotripsy was capable of releasing tumor antigens with retained immunogenicity and was able to amplify the efficacy of checkpoint inhibition immunotherapy.

The fifth study compared the tumor response and survival outcomes with single and repeat histotripsy treatment in human-derived and mouse-derived HCC murine models. One week after the initial histotripsy treatment, animals received a repeat histotripsy treatment. Results showed that both single and repeat histotripsy treatment significantly improved survival outcomes over controls.

Overall, the results of this dissertation provide significant insight into the physical processes underlying histotripsy tumor ablation and will help to guide the future development of histotripsy therapy for clinical applications such as the treatment of liver cancer. Histotripsy is a promising alternative that can overcome the limitations of current locoregional ablation therapies for safe and effective non-invasive liver tumor ablation. Additionally, since histotripsy mechanically ablates cells without denaturing them, we have shown that histotripsy is capable of releasing tumor antigens which can be recognized by the immune system to stimulate strong anti-tumor response as a robust adjuvant to cancer immunotherapy. Clinically, histotripsy may be a suitable downstaging treatment modality either alone or in combination with other therapies in early and intermediate-stage HCC patients, enabling them to meet the criteria for curative HCC options such as resection and transplantation. Histotripsy may also be useful for treating cases of recurrent HCC as the procedure can be theoretically repeated on-demand. Finally, histotripsy has the potential to be clinically adopted for the treatment of other solid tumors in addition to liver cancer. Future work will aim to build upon the studies detailed in this dissertation in order to further our understanding of the biological processes involved in histotripsy tumor ablation and to promote the clinical translation of histotripsy.

7.1 Future Work

7.1.1 Investigation of histotripsy mediated tumor cell-death mechanism

Cancer cell death is a multi-factorial, complex process. The type of cell death induced can have significant biological and physiological consequences in terms of local and systemic tumor treatment efficacy[5]. It can significantly impact treatment efficacy, cancer recurrence, and inflammation [6-9]. Histotripsy is hypothesized to cause immunological cell death of tumor; however, the exact mechanism is not well understood. In previous studies, even partial ablation of tumor triggered complete regression of the entire tumor lesion (including both ablated and residual tumor). The four major types of cell death, apoptosis, necrosis, pyroptosis and necroptosis can be evaluated by their markers such as cleaved caspase-3, phosphydylserine/annexin V binding (apoptosis), RIP-1 activation, NF-kB & TNF signaling (necrosis), leaved caspase-1,-11, Gasdermin D, inflammasome activation (pyroptosis) and RIPK3 and MLKL activation (necroptosis)[5]. However, since proteins and biochemical pathways can be involved in more than one cell death mechanisms, the conclusive determination of a definitive type of cell death is difficult [10, 11]. A recently discovered mechanism, ferroptosis could also play an important role in liver cancer histotripsy as it involves iron-dependence [12, 13]. Additionally, other studies have shown that liver cancer cells may be able to be eliminated in a ferroptosis-dependent manner [14, 15]. Studies are currently ongoing to determine the immunological cell death mechanisms and immune response following histotripsy.

7.1.2 Investigation of risk of metastasis

Metastasis is a complex process consisting primarily of five essential steps- 1) invasion, where tumor cells detach from ECM and infiltrate adjacent tissue, 2) intravasation, where tumor cells enter the circulatory system 3) survival in the circulatory system, 4) extravasation; where tumor cells exit the circulatory system and infiltrate a distant site and 5) colonization; where tumor cells grow and proliferate at the new site [16]. Previously, we focused investigation on the first step of the metastatic cascade, invasion which is induced by epithelial-to-mesenchymal transition (EMT) of tumor cells where they lose epithelial characteristics and concomitantly acquire mesenchymal characteristics [4, 17]. The second step of the cascade, intravasation of tumor cells generates circulating tumor cells (CTCs), however, it has been estimated that only <0.01% of CTCs will develop distant metastatic lesions after surviving stress, immune attack and anoikis in a hostile circulatory system environment [18]. Additional studies are on-going to assess the circulating tumor cells (CTCs) which will provide an insight into whether the mechanical disruption caused by histotripsy increases CTCs as compared to untreated controls.

7.1.3 Investigation of immune effects and abscopal responses in orthotopic models

The immune microenvironment also affects the metastatic potential of the disseminating cells. Cancer therapies such as radiation, chemotherapy and thermal ablation destroy tumor and surrounding tissues via necrosis, which can trigger an inflammatory immune response. However, this response can be either pro-tumor or anti-tumor depending on the tumor microenvironment and the expression of immune mediators and modulators[19-22]. Our previous study demonstrated that subcutaneous histotripsy ablation of melanoma tumors in murine hosts releases tumor antigens with preserved immunogenicity initiating both local and systemic immune response as evidenced by abscopal immune effects [4]. However, subcutaneous models do not fully mimic the tumor microenvironment. Previous studies have shown that histotripsy promotes local inflammatory and immunostimulatory effects within two weeks following histotripsy[4], however these effects have not been investigated longer-term. Currently, we are studying the impact of histotripsy ablation of liver lesion on distant intrahepatic lesions. Future investigation will also be focused on in-depth analysis of the immune response in orthotopic tumor models, with and without underlying cirrhosis at different timepoints post histotripsy.

7.1.4 Histotripsy parameter optimization

Previous studies have demonstrated that there is likely a minimal tumor volume percentage threshold that needs to be ablated to generate sufficient histotripsy response to cause the entire tumor (both ablated and unablated regions) to regress [1]. Our study presented in Chapter 6 has also shown that repeat histotripsy ablation can be advantageous over single histotripsy ablation for controlling tumor growth and improving survival outcomes. Overall, varying responses to single histotripsy ablation were observed in different tumor models presented in this dissertation – underscoring the importance of determining optimal histotripsy parameters based on tumor type to maximize therapeutic efficacy. Eventually, the standardization of dosimetry for histotripsy would be beneficial as currently different research groups use different parameters which impedes comparative studies. Currently, studies are ongoing to optimize histotripsy parameters and evaluate the impact of factors such as percentage of tumor volume targeted for ablation, number of treatment pulses delivered, and focal peak negative pressure on tumor response.

7.2 References

1. T. Worlikar et al., "Histotripsy for Non-Invasive Ablation of Hepatocellular Carcinoma (HCC) Tumor in a Subcutaneous Xenograft Murine Model," (in eng), Conf Proc IEEE Eng Med Biol Soc, vol. 2018, pp. 6064-6067, 07 2018, doi: 10.1109/EMBC.2018.8513650.

2. T. Worlikar et al., "Effects of Histotripsy on Local Tumor Progression in an in vivo Orthotopic Rodent Liver Tumor Model," (in eng), BME Frontiers, vol. 2020, 2020, doi: 10.34133/2020/9830304.

3. T Worlikar et al., “Impact of Histotripsy on Development of Intrahepatic Metastases in a Rodent Liver Tumor Model”. Cancers. 2022; 14(7):1612. https://doi.org/10.3390/cancers14071612

4. S. Qu et al., "Non-thermal histotripsy tumor ablation promotes abscopal immune responses that enhance cancer immunotherapy," (in eng), J Immunother Cancer, vol. 8, no. 1, Jan 2020, doi: 10.1136/jitc-2019-000200.

5. R. M. Brock, N. Beitel-White, R. V. Davalos, and I. C. Allen, "Starting a Fire Without Flame: The Induction of Cell Death and Inflammation in Electroporation-Based Tumor Ablation Strategies," (in eng), Front Oncol, vol. 10, p. 1235, 2020, doi: 10.3389/fonc.2020.01235.

6. D. Hanahan and R. A. Weinberg, "Hallmarks of cancer: the next generation," (in eng), Cell, vol. 144, no. 5, pp. 646-74, Mar 04 2011, doi: 10.1016/j.cell.2011.02.013.

7. A. Baroja-Mazo et al., "The NLRP3 inflammasome is released as a particulate danger signal that amplifies the inflammatory response," (in eng), Nat Immunol, vol. 15, no. 8, pp. 738-48, Aug 2014, doi: 10.1038/ni.2919.

8. J. Zhang, C. L. Wolfgang, and L. Zheng, "Precision Immuno-Oncology: Prospects of Individualized Immunotherapy for Pancreatic Cancer," (in eng), Cancers (Basel), vol. 10, no. 2, Jan 30 2018, doi: 10.3390/cancers10020039.

9. S. Aizawa, G. Brar, and H. Tsukamoto, "Cell Death and Liver Disease," (in eng), Gut Liver, vol. 14, no. 1, pp. 20-29, 01 15 2020, doi: 10.5009/gnl18486.

10. T. Vanden Berghe, W. J. Kaiser, M. J. Bertrand, and P. Vandenabeele, "Molecular crosstalk between apoptosis, necroptosis, and survival signaling," (in eng), Mol Cell Oncol, vol. 2, no. 4, p. e975093, 2015 Oct-Dec 2015, doi: 10.4161/23723556.2014.975093.

11. D. Frank and J. E. Vince, "Pyroptosis versus necroptosis: similarities, differences, and crosstalk," (in eng), Cell Death Differ, vol. 26, no. 1, pp. 99-114, 01 2019, doi: 10.1038/s41418-018-0212-6.

12. J. Li et al., "Ferroptosis: past, present and future," (in eng), Cell Death Dis, vol. 11, no. 2, p. 88, 02 03 2020, doi: 10.1038/s41419-020-2298-2.

13. X. Zhang et al., "Ferroptosis is governed by differential regulation of transcription in liver cancer," (in eng), Redox Biol, vol. 24, p. 101211, 06 2019, doi: 10.1016/j.redox.2019.101211.

14. F. Q. Wu et al., "ADRB2 signaling promotes HCC progression and sorafenib resistance by inhibiting autophagic degradation of HIF1α," (in eng), J Hepatol, vol. 65, no. 2, pp. 314-24, 08 2016, doi: 10.1016/j.jhep.2016.04.019.

15. C. Louandre et al., "Iron-dependent cell death of hepatocellular carcinoma cells exposed to sorafenib," (in eng), Int J Cancer, vol. 133, no. 7, pp. 1732-42, Oct 2013, doi: 10.1002/ijc.28159.

16. F. van Zijl, G. Krupitza, and W. Mikulits, "Initial steps of metastasis: cell invasion and endothelial transmigration," (in eng), Mutat Res, vol. 728, no. 1-2, pp. 23-34, 2011 Jul-Oct 2011, doi: 10.1016/j.mrrev.2011.05.002.

17. F. van Zijl et al., "Epithelial-mesenchymal transition in hepatocellular carcinoma," (in eng), Future Oncol, vol. 5, no. 8, pp. 1169-79, Oct 2009, doi: 10.2217/fon.09.91.

18. A. F. Chambers, A. C. Groom, and I. C. MacDonald, "Dissemination and growth of cancer cells in metastatic sites," (in eng), Nat Rev Cancer, vol. 2, no. 8, pp. 563-72, Aug 2002, doi: 10.1038/nrc865.

19. S. I. Grivennikov, F. R. Greten, and M. Karin, "Immunity, inflammation, and cancer," (in eng), Cell, vol. 140, no. 6, pp. 883-99, Mar 19 2010, doi: 10.1016/j.cell.2010.01.025.

20. J. Vakkila and M. T. Lotze, "Inflammation and necrosis promote tumour growth," (in eng), Nat Rev Immunol, vol. 4, no. 8, pp. 641-8, 08 2004, doi: 10.1038/nri1415.

21. M. J. Smyth, G. P. Dunn, and R. D. Schreiber, "Cancer immunosurveillance and immunoediting: the roles of immunity in suppressing tumor development and shaping tumor immunogenicity," (in eng), Adv Immunol, vol. 90, pp. 1-50, 2006, doi: 10.1016/S0065-2776(06)90001-7.

22. W. W. Lin and M. Karin, "A cytokine-mediated link between innate immunity, inflammation, and cancer," (in eng), J Clin Invest, vol. 117, no. 5, pp. 1175-83, May 2007, doi: 10.1172/JCI31537.